Structure and connectivity of water molecules at the interfaces of nanoconfined systems

Simona Dalla Bernardina

NNT : 2015SACLS103

THESE DE DOCTORAT
DE
L'UNIVERSITE PARIS-SACLAY
PREPAREE A
"SYNCHROTRON SOLEIL"

ECOLE DOCTORALE N° 571

Sciences chimiques : molécules, matériaux, instrumentation et biosystèmes

Spécialité de doctorat Chimie

Par

Mme Simona Dalla Bernardina

Structure and connectivity of water molecules at the interfaces of nanoconfining systems

Thèse présentée et soutenue à Gif sur Yvette, le 17 novembre 2015 :

Composition du Jury :

M. Mercury Lionel	Professeur, Université d'Orléans	Rapporteur
M. Mermet Alain	Professeur, Université Lyon 1	Rapporteur
Mme Alba-Simionesco Christiane	Directrice de recherche, LLB	Examinatrice
Mme Bleuzen Anne	Professeur, Université Paris-Sud	Examinatrice
Mme Filabozzi Alessandra	Professeur, Université Roma 2	Examinatrice
M. San Miguel Alfonso	Professeur, Université Lyon 1	Examinateur
Mme Roy Pascale	Directrice de recherche, synchrotron SOLEIL	Directrice de thèse
M. Brubach Jean-Blaise	Synchrotron SOLEIL	Encadrant de thèse

université PARIS-SACLAY
ÉCOLE DOCTORALE
Sciences chimiques : molécules, matériaux, instrumentation et biosystèmes

Titre : Structure et connectivité de molécules d'eau aux interfaces de systèmes nanoconfinants

Mots clés : Eau, Nanopores, Spectroscopie infrarouge, Liaison hydrogène, Confinement, Hydratation

La compréhension des mécanismes d'absorption de l'eau, ainsi que l'arrangement moléculaire adopté par le réseau de molécules d'eau lors du confinement à l'échelle nanométrique, est crucial que ce soit pour l'optimisation de plusieurs applications, telles que la production d'énergie propre, la purification et le dessalement de l'eau, ou pour élucider certains processus complexes qui ont lieu dans les systèmes biologiques. Dans le cadre de cette thèse, l'hydratation contrôlée de trois systèmes poreux modèles suivie par spectroscopie infrarouge montre les effets de la nature des surfaces et des limitations stériques qui, en altérant les liaisons hydrogène entre les molécules d'eau, déclenche la formation de réseaux atypiques. La brillance de la source de rayonnement synchrotron infrarouge, exploitée par la ligne de lumière AILES au sein du synchrotron SOLEIL, a permis l'étude d'échantillons très absorbants en permettant de mettre en évidence la faible contribution de monocouches de molécules d'eau voire même de chaînes linéaires. L'effet d'une surface hydrophile est étudié en mesurant l'absorbance d'une lamelle de Vycor poreux à l'équilibre avec une pression de vapeur d'eau donnant lieu à la formation d'un réseau d'eau bi-dimensionnel. Les interactions fortes entre l'eau interfaciale et la surface hydrophile provoquent plusieurs transitions structurales du réseau d'eau expliquant ainsi les observations par d'autres techniques. Des similitudes et des différences surprenantes ont été observés entre l'hydratation d'une surface hydrophile et celle d'un système hydrophobe dans des conditions de confinement extrême : les nanotubes de carbone à paroi unique ayant un diamètre de quelques Angstrom. Nos mesures ont montré que l'établissement d'un réseau de molécules d'eau unique peut être à l'origine du déplacement rapide des molécules d'eau à l'intérieur des nanotubes de carbone. Enfin, l'étude des mécanismes d'adsorption de la membrane Nafion, membrane modèle dans les piles à combustible à membrane échangeuse de protons, a permis de clarifier les processus en jeu lors de l'ionisation et la formation d'espèces protonique.

Title : Structure and connectivity of water molecules at the interfaces of nanoconfining systems

Keywords : Water, Nanopores, Infrared spectroscopy, Hydrogen bond, Confinement, Hydration

Understanding the water absorption mechanisms, and the molecular arrangement adopted by the water molecules upon confinement at the nanoscale is crucial both for technological applications, such as clean energy production, purification and desalination of water, and to unveil some of the complex processes occurring in biological systems. In this thesis, the controlled hydration of three porous model systems monitored by infrared spectroscopy shows the effects of surfaces forces and steric limitations that triggers the formation atypical networks by altering the hydrogen bonds established between water molecules. The brightness of the infrared synchrotron radiation source on the AILES beamline at synchrotron SOLEIL allowed to highlight the low contribution coming from water molecules arranged as monolayer or linear chains in highly infrared absorbent matrices. The effect of a hydrophilic surface was examined by measuring the absorbance of a porous Vycor slab at equilibrium with the water vapor pressure needed to obtain a two- dimensional water network. The strong interfacial interactions between water and the hydrophilic surface cause several structural transitions on the water network elucidating the observations made by other techniques. Surprising similarities and differences are observed between the hydration of a hydrophilic surface and that of a hydrophobic system under extreme confinement: single-wall carbon nanotubes having a diameter of several Angstroms. Our measurements have shown that the arrangement of a peculiar water network may be the origin of the enhanced water flux in carbon nanotubes. Finally, the study of the adsorption mechanisms of the Nafion membrane, the benchmark electrolyte in proton exchange membrane fuel cells, has shed new light on the processes involved in the ionization and the formation of protonic species, accountable for the remarkable ionic conductivity typical of these membranes. This approach may be also extended to more complex systems, such as water molecules networks in biological systems.

Université Paris-Saclay
Espace Technologique / Immeuble Discovery
Route de l'Orme aux Merisiers RD 128 / 91190 Saint-Aubin, France

Acknowledgements

This manuscript is the result of passionate team work and enriching collaborations over the three years of my PhD. For this reason, I want to express my heartfelt thanks to whom, in one way or another, contributed to the accomplishment of this thesis.

My deepest gratitude goes to my supervisors Pascale Roy and Jean-Blaise Brubach for having me under their guidance and letting me into an exciting topic for my research. I enjoyed spending time with them, always kind, brilliant and passionate about our work. They taught me to face problems with unwavering enthusiasm making me realize that patience and determination are important requirements for experimental researchers, and for life in general.

I want to convey a special thanks to Patrick Judeinstein for his invaluable collaboration in all projects on confined water, which are the foundations of this manuscript, and the enjoyable time spent with him during experiments. I am grateful to Jean-Marc Zanotti for his contribution to the development of the hydration setup and for his helpful discussions on Vycor porous glass.

My sincere gratitude also extends to Sandrine Lyonnard and Armel Guillermo for the pleasant collaboration on the study of Nafion membrane and their kindness during my visits in Grenoble.

I am also thankful to Pascale Launois, Erwan Paineau and Stéphan Rouzière for the fruitful collaboration dedicated to the astonishing hydration of hydrophobic carbon nanotubes. Undoubtedly, the hardship we had to face during this study is proportional to the value of our results.

I would like to take this opportunity to thank Stephanie Blanchandin and Karine Chaouchi for their generous help at the chemistry laboratory.

These acknowledgements would not be complete without mentioning those who are or have been part of the AILES beamline for their support and the refreshing conversations around coffee and meals: Laurent Manceron, Olivier Pirali, Mylene Chapuis, Maxime Deutsch, Sebastien Gruet, Mbaye Faye, Frederico Alabarse, Alexandr Kalinko Alexandre Voute and especially Stefano Tammaro that, more than anyone else, helped and supported me during these years. I would not have been able to undertake this wonderful French journey without him and now we are ready to move toward our next adventure.

TABLE OF CONTENT

"Water never waits.

It changes shape and floes around things, and

finds the secret paths no one else thought about..."

Arthur Golden

INTRODUCTION

The importance of water for the world as we know it, and for life itself, had been already acknowledged in ancient Greece by Thales of Miletus (600 BC) who held the idea that water was the originating principle of nature. Through centuries, the interest on water did not lessen but rather rose up. Indeed, progresses in science and technology allowed to disclose the unique properties of water originating in particular from the extended three-dimensional hydrogen bonding network established between water molecules [1—5]. Such three-dimensional structure, being perturbed when water is trapped in confined environments or when it is bonded to an interface, can promote drastic changes in its structure [6—9], its phase transitions [10—15] and its dynamical properties [5], [9], [16—18].

Water confined and at interfaces plays a key role in countless reactions. Water leads the protein folding, hydrates membranes and large biomolecules. It is in contact with interfaces in catalytic reactions, during ions transportation and when it acts as polar solvent. Its adsorption into porous rock formations or conducting polymers is exploited for several applications, such as wastewater purification or clean energy production. Each surface induces specific effects on the water structure and the hydrogen bond network that are governed by wall forces and steric limitations.

Understanding the mechanism of water sorption in hydrophilic or hydrophobic nanostructures, as well as the molecular arrangement adopted upon nanoscale confinement, could lead to significant improvements in food science, geology, biology, environmental and energy science. This is why, nowadays an extremely high number of experimental studies and numerical simulations are dedicated to water confined and at various interfaces.

In this thesis, the effects of confinement on the structure and the hydrogen bonding of water molecules are investigated by means of Fourier Transform infrared (FTIR) spectroscopy. FTIR spectroscopy is a powerful tool to address these issues since it is suited to identify changes in water molecules structure and bond strengths. Indeed, it provides information about intramolecular vibrations, in the mid infrared (MIR: O-H stretching, 3000—3700 cm^{-1}; HOH bending angle,

~1650 cm^{-1}), and intermolecular modes, in the far infrared (FIR: frustrated rotations, 300—900 cm^{-1}; hindered translations of hydrogen bond, 30—300 cm^{-1}). The use of the synchrotron infrared source at the AILES beamline of SOLEIL allows to study highly absorbent sample with a high signal to noise ratio, and the wide spectral range available is well adapted to follow the inter- and intramolecular modes of bulk and confined water molecules.

For this purpose, a specific hydration cell was designed to follow *in situ* the adsorption (desorption) of water molecules in (out) nanoporous matrices with a fine control on the water vapor pressure and the temperature applied to the sample. With this setup, stepwise hydration measurements were performed on three nanoporous media, a porous Vycor glass, the Nafion membrane and single walled carbon nanotubes (SWNTs), which differ in nature (being hydrophilic, hydrophobic or amphiphilic), in pore size (from 1 to 5 nm) and in shape (cylindrical and swelling pores). We selected those samples to determine the effects of wall forces and steric limitations on confined water but also for their technological interest in several applications, such as water purification and desalinization as well as clean power sources fuel cells.

As will be described, strong deviations from bulk water are observed for water trapped in all samples.

Water affinity for hydrophilic Vycor's pores walls was exploited to study interfacial water at different temperatures, from T=70 K to T=300 K. In particular, we will present a comparison with liquid and solid bulk water revealing that at low temperature (T<150 K) the two-dimensional water network in Vycor's pores is arranged as amorphous ice. Transitions in the water network are observed as temperature is increased, at T~150 K and T~220 K.

In Nafion membrane, the benchmark electrolyte in fuel cells, we will show that the intermolecular arrangement between ionic groups, proton species and water molecules at different hydration levels, allowed to identify a three-step hydration process. Combining FIR and MIR data, we were able to assess that the ionization process and the resulting formation of the hydronium ion, H_3O^+, is a kinetically-driven process. Once this step is reached, the process leading to the formation of protonic species is governed by water vapor pressure.

Finally, we will present a study revealing the kinetics of water adsorption within single walled carbon nanotubes (SWNTs). This investigation is based on an

unprecedented infrared study of such nanotubes hydration, under controlled water vapor pressure. For water trapped into the hydrophobic cylindrical pores, this study shows the presence of a large amount of dangling OH bonds facing the carbon walls during all the hydration process. Moreover, we will show that small nanotubes (1—1.2 nm diameter) accommodate water in ordered ring structures even at room temperature.

This thesis is organized as follows:

- In Chapter One, we review the physicochemical properties of water and introduce the interest of interfacial and confined water studies. Moreover, a description of the infrared spectroscopy technique is reported.
- Chapter Two is dedicated to the description of the synchrotron radiation and the main elements of the AILES beamline, in particular the infrared source and the spectrometer based mainly on a Michelson interferometer. Section 2—3 includes an article published in Vibrational Spectroscopy "New experimental set-ups for studying nanoconfined water on the AILES beamline at Soleil" that report the description of the hydration cell, conceived and developed to water adsorption and desorption measurements.
- In Chapter Three, we present a study on bulk water in gaseous, liquid and ambient pressure solid states which is exploited for comparisons with the confined and interfacial water studies.
- In Chapter Four, a manuscript submitted to Nature Communication "Competing coexisting phases in 2D water" is reported. Here we analyze a monolayer of water on porous Vycor glass in a wide range of temperature. Experimental results support a percolation model for the low temperature two-dimensional water network.
- Chapter Five presents an article published in The Journal of Physical Chemistry C "Mechanism of ionization, hydration, and intermolecular H-bonding in proton conducting nanostructures ionomers" where the complex processes taking place inside the Nafion membrane are described as a function of the level of hydration.
- In Chapter Six, we report a manuscript submitted to Nano Letters "Water in carbon nanotubes: the peculiar hydrogen bond network revealed by infrared spectroscopy" where we provide a description of the organization of water trapped in SWNTs with diameter size between 1 and 2 nm.
- A section opening up to future directions will conclude this thesis.

CHAPTER 1

BACKGROUND

The first section of this chapter reviews the physicochemical properties of water and the peculiar hydrogen bond network established between water molecules. A description of water confined and at interface is given and a brief overview on literature is reported.

We describe the three systems (porous Vycor glass, Nafion membrane and single walled carbon nanotubes) used as confining media in this thesis to unveil and understand the properties of water in environments differing in nature (hydrophilic, hydrophobic or amphiphilic), in pore size (from 1 to 5 nm) and in shape (cylindrical and swelling pores).

Basic principles of quantum theory are introduced to describe infrared spectroscopy which is the main investigation technique of data presented in this manuscript.

1—1 THE WATER MOLECULE: GENERAL PROPERTIES

Properties of water have always intrigued scientists of many different disciplines. This small molecule is nearly ubiquitous, it plays a key role in countless reactions and it is vital for life itself. Hence, it is not surprising that water has attracted considerable attention and it has therefore been a subject of investigation for centuries. In the last decades, interfacial and confined water caught much attention because of its involvement in many biological and geological reactions as well as industrial operations.

In this Section we will describe the water molecule structure and the peculiar hydrogen bond which is accountable for many of the unique properties of water.

1—1.1 THE STRUCTURE

Water appears like a simple molecule composed of three atoms: two hydrogen atoms covalently bonded to one oxygen atom (Figure 1.1.1). Its composition was discovered by Henry Cavendish in 1781 but its molecular formula, $\boldsymbol{H_2O}$, was suggested for the first time in 1804 by Joseph Louis Gay-Lussac and Alexander von Humboldt. Its molecular diameter, about 2.75 Å, has been estimated from crystal data by interpolation of the effective ionic radii of O^{2-}, OH^- and H_3O^+ [19].

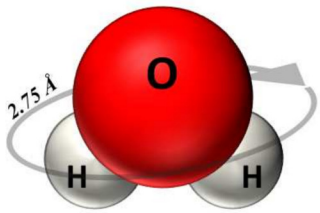

Figure 1.1.1 – Graphical depiction of the water molecule. The hydrogen atoms (H) in grey, the oxygen atom (O) in red.

Water possesses three symmetry operations, in addition to identity (labelled E). Indeed, as illustrated in Figure 1.1.2, the molecule looks the same *(i)* after a rotation of 180° around an axis of symmetry labelled C_2 (where C_n is a rotation through the angle $360°/n$) and *(ii)* after reflections through any of the two planes

perpendicular to each other, labelled σ_v and $\sigma_{v'}$, both containing the rotation axis of symmetry.

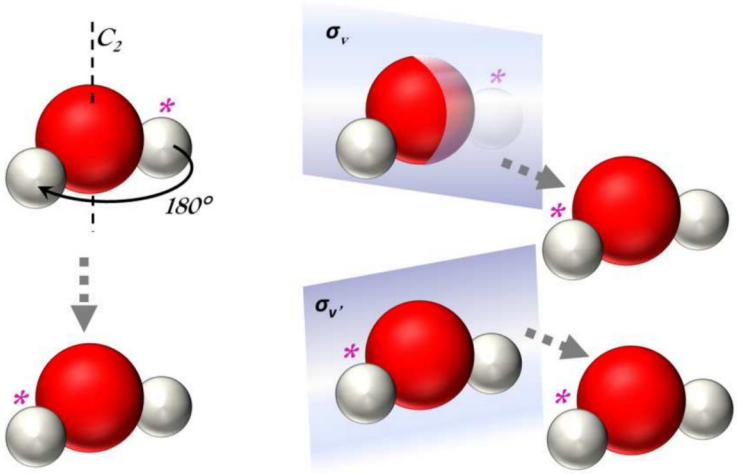

Figure 1.1.2 – Symmetry operation of water. The axis of symmetry, C_2, and the two planes of symmetry, σ_v and $\sigma_{v'}$,are represented.

The shape of the molecule can be determined by the Valence-Shell Electron-Pair Repulsion (VSEPR) theory. The hydrogen atom holds one proton in the nucleus and one electron in atomic orbital *1s.* The oxygen atom holds eight electrons: two in the orbital *1s*, two in the orbital *2s* and four in the orbitals *2p*. According to the atomic orbital model, orbitals represent the probability to find the electron in a delimited region around the nucleus (see Section 1—6.2). In particular, orbitals *n-s* assume a spherical shape centered around the nucleus and the radius increases with *n*, while orbitals $n\text{-}p_{x,y,z}$ each form two ellipsoids with a point of tangency at the nucleus along the orthogonal axes x, y, and z. In the oxygen atom, the combination of the orbitals *2s* and $2p_x$, $2p_y$, $2p_z$ produces four lobe-shaped hybrid orbitals sp^3.

The water molecule is formed when two hydrogen atoms bind covalently to the oxygen, which occurs when the electrons of the *1s* orbital of the hydrogen atoms and the electrons of two of the four hybrid sp^3 orbitals of the oxygen atom are shared. The other two hybrid sp^3 orbitals remain as lone pairs. According to the VSEPR theory, hybrid orbitals arrange themselves around the nucleus assuming a tetrahedral structure as a consequence of the repulsion between negative charged electrons. Nevertheless, the presence of two lone pairs in the water molecule slightly deforms the structure so that the angle formed by the hydrogen atoms and

the oxygen nucleus is 104.5° instead of 109° like in a pure tetrahedral structure. Hence, water assumes a bent (or V-shaped) geometry, Figure 1.1.3.

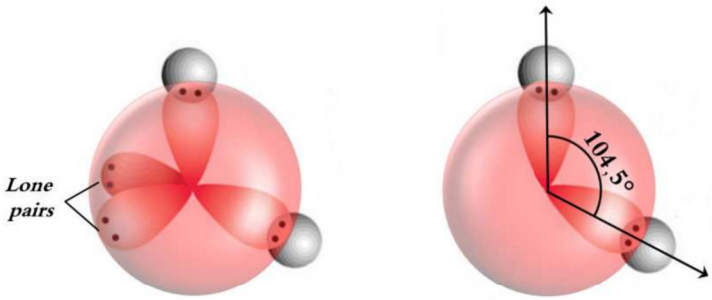

Figure 1.1.3 – Electronic distribution in water molecule. On the left: tetrahedral structure of the molecular orbitals with electrons involved in the covalent bond and the lone pairs. On the right: angle formed by the hydrogen atoms and the oxygen bent by the presence of lone pairs.

1—1.2 POLARITY

In the water molecule, a partial negative charge lies near the oxygen atom, while two partial positive charges are closer to the hydrogen atoms. Such charge distribution induces an internal polarity even though the whole molecule results electrically neutral. Polarity is quantified by the molecular dipole moment, defined as:

$$\bar{\mu} = q \cdot \bar{r} \tag{1.1.1}$$

where q is the magnitude of the charge, in Coulombs, from either end of the dipole and $\bar{r}$ is the distance between the centers of positive and negative charges, in meters. Generally it is expressed in Debye (D), where $1\ D = 3.33 \cdot 10^{-30}\ C\ m$.

Polarity plays a key role in the formation of an unusual and important bond among water molecules, the hydrogen bond, as further discussed in Section 1—1.3. The dipole moment for a gas phase water monomer along its axis of symmetry, C_2, is 1.8546 Debye [20], Figure 1.1.4, but this value significantly increases when the molecule is surrounded and bonded to other water molecules. Calculations performed using Effective Fragment Potential (EFP) method [21] suggest that the enhancement of the dipole moment arises primarily from decreases in the angles

between the lone pair dipole vectors. This angle decreases when the number of hydrogen bonds involving that oxygen increases.

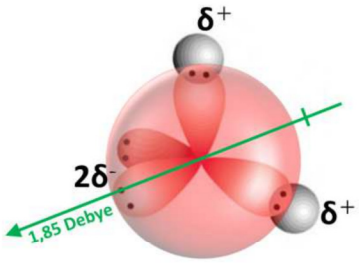

Figure 1.1.4 – Polarity of water. Molecular dipole moment of a water monomer.

1—1.3 THE HYDROGEN BOND

Many of the unique properties of water are attributed to the hydrogen bond. Weaker than ionic and covalent bonds but stronger than Van der Waals interaction, the hydrogen bond causes high viscosity, maximum density at T=4 °C when water is not yet in its solid state, the increase of fusion (T=0 °C) and boiling (T=100 °C) temperatures (which allow changes of state at typical temperatures and pressures on Earth). Indeed, water seems similar in mass and size to methane, CH_4, but its melting and boiling points are much higher because of the hydrogen bond network established between water molecules. Without the hydrogen bonding, water would be a gas at room temperature just like methane, whose boiling point is at T=-161 °C. Typical bond energies for inter-molecular and intra-molecular bonding are reported in Table 1.1.

Described for the first time by Latimer and Rodebush in 1920 [22], the hydrogen bonding (H-bond) occurs when a hydrogen atom is attracted to two electronegative atoms. The hydrogen atom is then covalently bonded to a highly electronegative atom that attracts the electron cloud and leaves a positive charge around the hydrogen atom. This charge acts as hydrogen bond *donor*. The positive charge density attracts a lone pair of electrons of another electronegative atom, which is therefore an a*cceptor*, and it results in a H-bond (Figure 1.1.5).

Table 1.1 – Typical intra- and inter-molecular bonding energies.

Type of bond	TYPICAL BOND ENERGIES *(kJ·mol^{-1})*
Ionic bond	**700-4000**
Covalent Triple bond	**800-1000**
Covalent Double bond	**500-700**
Covalent Single bond	**200-500**
Ion-Dipole interaction	**40-600**
Hydrogen Bonds *(inter-molecular)*	**10-40**
Van der Waals (inter-molecular)	**5-25**
He-He (weakest bond)	**~ 8·10^{-6}**

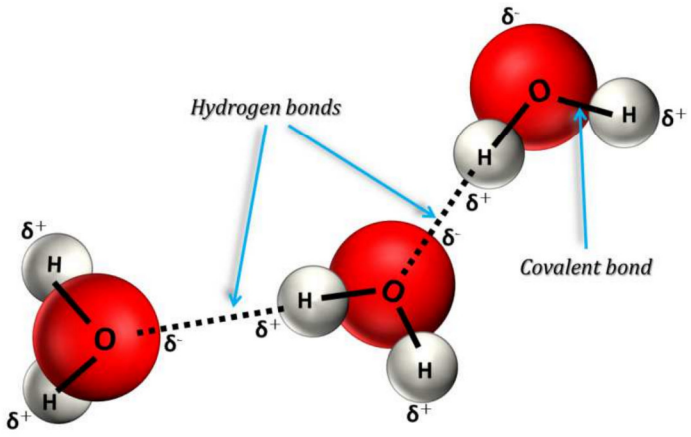

Figure 1.1.5 – Hydrogen bond in liquid water. Water molecules attracted via hydrogen bond induced by partial negative oxygen and partial positive hydrogen atoms.

The hydrogen bond is highly directional and it is stronger when the three atoms involved assume an approximately linear arrangement. Such directionality limits the number of neighboring water molecules to about four. The hydrogen bond strength is also determined by the electronegative atoms involved in the bond [23]. It can be as strong as a covalent bond in the case of fluorine (HF_2^-: ~163 KJ/mol) or weak as Van der Waals forces if iodine atoms are involved (HI_2^-: ~2 KJ/mol). In liquid water, where two oxygen atoms are attracted via the hydrogen atom, the energy of the bond is about 23.3 KJ/mol [24].

Hydrogen bonding weakens the covalent bonds in the molecule and reduces the repulsion between electron orbitals. Consequently, the O-H length and the HOH

angle values increase with the number of established H-bonds. Notably, their values are slightly greater in solid than in liquid phase which, in turn, are slightly greater than in gaseous (isolated) water molecules. Moreover, as reported is Section 1—1.2, reducing the angle between the lone pair of the oxygen atom, which is a consequence of the established H-bond, causes an increase of water polarity. This encourages the formation of further H-bonds resulting in a cooperative behavior. The water molecule acting as hydrogen bond donor increases its negative density on the oxygen atom promoting the acceptance of H-bond but discouraging, at the same time, a further donation. Vice versa, the water molecule involved in the H-bond with an acceptor oxygen atom experiences a reduction in the electron density and encourages the hydrogen atom donation [25].

Bond lengths and angles are affected by the molecules environment but typical values for H_2O and D_2O are reported in Table 1.2. It is important to note that these values are highly dependent from the specific method used to estimate them. Nevertheless a general trend is evident: the O-H length value increases from 0.957 to 1.025 Å and the HOH angle opens from 104.4° to 109.5° during water changes of phases, from gaseous monomer to ice with four H-bonds established.

Table 1.2 – Typical values of bond lengths and angles for H_2O and D_2O in different states (references are in square brackets).

	Numerical Simulation		**Experimental values**	
H_2O	*O-H distance (Å)*	*HOH angle*	*O-H distance (Å)*	*HOH angle*
Isolated	**0.957854**[26]	**104.500°**[26]	**0.95718**[27]	**104.474°**[27]
Liquid	**0.961**[28]	**106.3°**[29]	**0.976**[30]	**105°**[30]
Ice	**0.967**[29]	**108.4°**[29]	**0.985**[31]	**106.6°**[31]
D_2O	*O-D distance (Å)*	*DOD angle*	*O-D distance (Å)*	*DOD angle*
Isolated	**0.957835**[26]	**104.490°**[26]	**0.9572**[2]	**104.52°**[2]
Liquid	**1.020**[32]	**104.6°**[32]	**0.970**[33]	**106.1°**[33]
Ice	**1.025**[32]	**105.4°**[32]	**0.985**[34]	**109.5°**[35]

The formation of hydrogen bonds between water molecules governs the overall structure and dynamic of water [36]. It confers an unusual behavior to water and differentiates it from other simple molecular liquids. Liquid water structure expands when temperature decreases as hydrogen bonded structure establishes, unlike simple liquids that contract under cooling down. Indeed, the maximum density does not occur at T=273 K, when water is in its solid state, but rather at T=277 K when water is still a liquid [36—38]. Moreover, the evaporation is affected by the hydrogen bonding. The energy required to break H-bonds is higher than the energy needed to hinder Van der Waals interactions, hence evaporation of liquid water occurs for higher temperature than for other liquids (precisely at T=373 K with a pressure of 1.01 bar).

The crucial role water plays in chemistry and biology is a consequence of its H-bond network [39]. It is implicated in various phenomena such as high efficiency proton transfer [40—43] or protein transportation [44, 45] among many others. Unfortunately it is hard to obtain information on the local dynamics of networks in liquid water since it is highly stochastic, as it breaks and reforms continuously. The average number of H-bonds established with the neighboring water molecules in the liquid state, n_{h_liquid}, has been predicted by Stanley and Texeira [46] and afterwards determined by molecular dynamics simulations [47] and X-ray diffusion [48]. According to these studies, n_{h_liquid} is estimated between 2 and 2.5 hydrogen bonds per water molecule. Such a huge decrease compared to ice (n_{h_ice} $\sim$ 3.6 at T=273 K) is due to thermal energy that induces vibrations on molecules causing the breaking of the H-bond, when two water molecules move away from each other, or the formation of a new one, when two water molecules get closer. Actually, the H-bond life time is very short (of the order of picosecond) and highly depends on temperature [49]. If we could get a snapshot of the liquid water network we could expect to find a portion of water molecule slightly connected forming zero or 1 H-bond, another portion highly connected forming 3 or 4 H-bonds, and the remaining molecules between these two extremes.

1—2 INTERFACIAL AND CONFINED WATER

In many biological and geological systems as well as in some technological devices, water is present. Few layers of water molecules may lie on hydrophilic and hydrophobic surfaces as well as in tiny pores with diameters of the order of nanometer (corresponding to a few molecular diameters). Such interfacial or confined water presents different properties compared to bulk water. Indeed, water structure [6—9], phase transitions [10—15] and dynamical properties [9], [16—18] are affected by wall forces and steric limitations through their molecular structure and their shape. Despite the difficulties to deduce general properties of water near boundaries, considerable attention is devoted to the study of these systems since confined or interfacial water plays a key role in many important processes such as protein folding, molecular and ionic transport, corrosion and many other phenomena [50—52]. A great effort is still underway, but to date, properties of confined water are far from being completely understood.

In this Section we focus on the nanoscale environment and the phenomenon of the capillary condensation that induces the transition vapor-liquid in tiny pores. Typical adsorption functions will be presented. Finally, a few examples on the anomalous behavior of water confined in mesoporous materials, such as MCM-41, Vycor and carbon nanotubes, will be reported.

1—2.1 CONFINING SYSTEMS

Porous materials are exploited to study the structure and the dynamics of confined water at low-dimensional levels.

Infinite numbers of confining systems are possible, but the main categories are illustrated in Figure 1.2.1:

(i) A few layers film of water molecules may be trapped in lamellar structures, as it has been observed in lamellar bilayers of aerosol-OT (AOT) surfactants [53] or in mono- and di-hydrate tungsten oxide WO_3 [54].

(ii) When a surfactant in a bulk organic solvent interacts with a small amount of water, the water molecules gather together surrounded by the polar surfactant head groups forming spherical reverse micelles, as in the case of AOT surfactants [55].

(iii) Water may also be trapped in porous materials along pores, or channel, which are classified according to their size by the International Union of Pure and Applied Chemistry (IUPAC) as *macropores* of diameter larger than 50 nm, *mesopores* of diameter between 2-50 nm and *micropores* of diameter less than 2 nm.

(iv) There are also porous systems whose pore size changes according to the amount of adsorbed water molecules, as it is observed in perfluorinated sulfonic acid (PFSA) membranes (like Nafion) [56, 57].

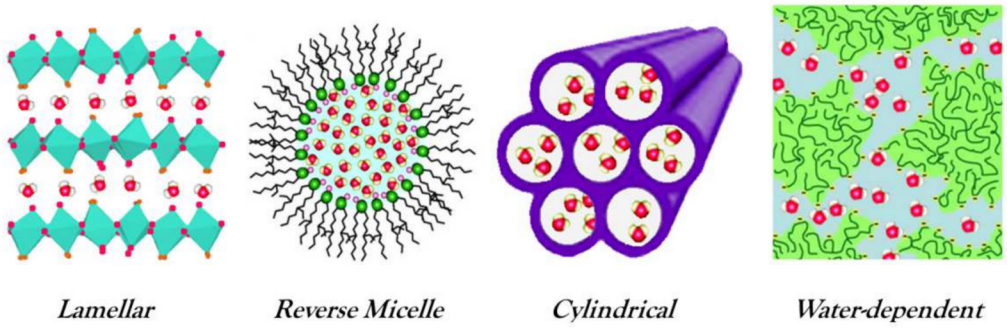

Figure 1.2.1 – Water confined in nanospaces. From left to right: water monolayer in tungsten oxide, water reverse micelle in AOT surfactant, water in regular cylindrical pores of MCM-41 and in Nafion channels.

For water molecules in a nanoscale environment it is relevant to consider some isotope effect, giving distinct behaviors to confined H_2O and D_2O. Deuterium, D, is a stable isotope of hydrogen discovered in 1931 by Harold Urey. Unlike the hydrogen atom, which contains only one proton, deuterium has a proton and a neutron in the nucleus so its mass is double of the hydrogen mass. Few and recent studies have investigated the mixture of light (H_2O) and heavy (D_2O) water observing an isotopic preference at air/water surfaces [58, 59]. An interesting effect was also observed in the hydration of cement where the slower reaction

kinetics and the higher activation energy in the presence of D_2O remain unexplained [60].

In addition to its fundamental interest, the understanding of the confinement is sought for many industrial and geophysical operations. Many rock and soil formations are porous, and the flow, diffusion and selective adsorption of water, aqueous solutions, pollutants, oil and gas in soils and rocks are exploited for several applications [61, 62]. Materials with regular pores are finding application in the fabrication of nanomaterials (conducting polymers, optoelectronic devices, metal wires, etc...). Micro- and mesoporous materials are widely used in the chemical, oil and gas, food and pharmaceutical industries for pollution control, mixture separation, catalyst supports for chemical reactions, etc... Improving the understanding of the effects of confinement on the equilibrium composition of reacting mixtures, and on adsorption and diffusion rates, could lead to significant improvements in these industrial processes [10].

1—2.2 WATER CONDENSATION IN MESOPORES

In Section 1—1.2 it has been stressed that polarity in water promotes cohesion between molecules: polar water molecules are attracted to each other and form hydrogen bond networks. When liquid water is not constrained between the walls of a receptacle, it aggregates in spherical droplets, this shape allowing the minimum number of water molecules at the surface. Molecules inside the droplet are surrounded by other molecules that exert attractive forces, such as Van der Waals forces, from all directions. Molecules on the surface are attracted toward the droplet because they are only partially surrounded and the interactive force is applied from the inside (this causes the droplet to assume a shape with the smallest surface area for a given volume). Along the surface, molecules are bound together and act as a thin film producing a surface tension, Figure 1.2.2.

When liquid water is in equilibrium with its gaseous phase, the rate of condensation is equal to the rate of evaporation. The vapor exerts a pressure equal to the surface tension, both dependent on temperature. At T=25 °C, the saturation water vapor pressure is p_0=31.7 mbar (at sea level). Generally, different values of vapor pressure p are expressed in terms of relative humidity (RH) according to the formula:

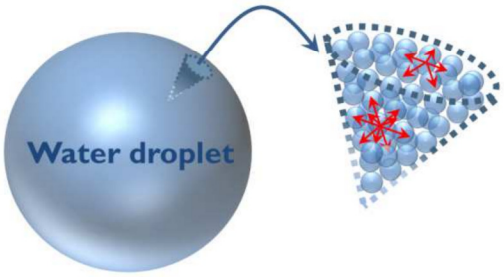

Figure 1.2.2 – Attractive forces in a water droplet. Attractive forces, red arrows, experienced by a water molecule, depicted as small spheres, inside the droplet and on the surface.

$$RH = \frac{p}{p_0} \cdot 100 \tag{1.2.1}$$

Pure water vapor requires a sufficient vapor pressure (several hundred percent of relative humidity) in order to condense into water droplet, having to overcome a strong free energy barrier.

In the atmosphere, cloud droplets are observed to form below this saturation pressure because water molecules nucleate on micron and sub-micron sized solid particles, present in significant concentration in the atmosphere. In this case, hydrogen bonds induce adhesion between surface particles and water that favors condensation.

When isolated water molecules approach a surface, they experience Van der Waals attraction. They bind to the surface and to neighboring molecules and the vapor-liquid transition begins. Between vapor and liquid phase, the droplet surface exerts a surface tension, σ_{lv}, defined as the work required to increase the surface unit area of liquid. The interaction force between the surface and the vapor, σ_{wv}, the surface and the liquid, σ_{wl}, as well as the liquid-vapor surface tension, σ_{wv}, determine the droplet shape, see Figure 1.2.3.

To describe the force equilibrium, we use the **Young's equation**:

$$\sigma_{lv} \cos(\theta) + \sigma_{wl} = \sigma_{wv} \,. \tag{1.2.2}$$

The terms $\sigma_{lv} \cos(\theta)$ being the adhesion tension and θ, the angle between the wall and the droplet interface, describe the wettability of the pore walls.

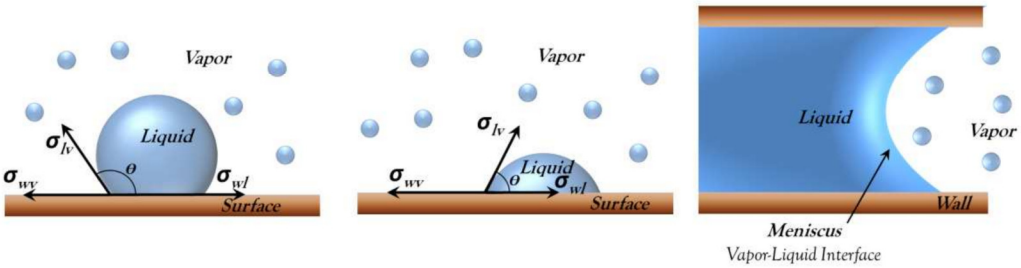

Figure 1.2.3 – Water condensation on a pore wall. Wall-vapor interaction, σ_{wv}, wall-liquid, σ_{wl}, and the surface tension, σ_{wv}, depend on the wettability of the pore walls. A hydrophobic surface, with $\theta>90°$, on the left; a hydrophilic surface, with $\theta>90°$, on the right.

From Eq. (1.2.2):

$$\cos(\theta) = \frac{\sigma_{wv}-\sigma_{wl}}{\sigma_{lv}} \tag{1.2.3}$$

if $\theta < 90°$ the liquid wets the surface and the wall-vapor energy interaction is larger than the wall-liquid interaction ($\sigma_{wv} > \sigma_{wl}$), if $\theta > 90°$ the liquid do not wet the surface and $\sigma_{wv} < \sigma_{wl}$.

This description is still valid for isolated water molecules adsorbed into tiny pores. In this case, multilayers of molecules keep condensing on the pore walls until layers fusion in the center of the pore and form a meniscus at the liquid-vapor interface (Figure 1.2.3). A pressure difference on the interface, called capillary pressure p_c, arises from the difference between vapor, p_v, and liquid, p_l, pressure:

$$p_c = \Delta P = p_v - p_l\,. \tag{1.2.4}$$

To estimate these pressures in a simple way, we can consider a spherical water droplet, with radius R, surrounded by water vapor. On its surface, a capillary pressure ΔP is applied. If ΔP induces a change in the droplet's volume dV, the work made by the pressure can be expressed as:

$$\Delta W_p = P \cdot dV = \Delta P \cdot 4\pi r R^2 dR. \tag{1.2.5}$$

The volume change induces a change in the droplet surface:

$$dS = (4\pi R^2 - 4\pi(R-dR)^2) = (4\pi R^2 - 4\pi(R^2 - dR^2 + 2RdR)) \approx 8\pi R dR\ . \tag{1.2.6}$$

Consequently, the produced surface tension, defined as the work required to increase the surface unit area of the liquid, is:

$$\Delta W_s = \sigma_{\mathrm{vl}} \cdot dS = \sigma_{\mathrm{vl}} \cdot 8\pi R dR\,. \tag{1.2.7}$$

The system is at the equilibrium when the two forces (1.2.5) and (1.2.7) are equal:

$$\Delta P \cdot 4\pi r R^2 dR = \sigma_{\mathrm{vl}} \cdot 8\pi R dR\,. \tag{1.2.8}$$

This occurs when the capillary pressure is:

$$p_c = \Delta P = p_v - p_l = \frac{2\sigma_{vl}}{R}. \tag{1.2.9}$$

Equation (1.2.9), known as **Young-Laplace equation**, implies that the curvature, *R*, of the surface is related to the pressure difference between vapor and liquid water. In the case of droplets immersed in their vapor, $\Delta P > 0$ because *R* has a positive sign. If we consider instead bubbles in a liquid or the meniscus formed during capillary condensation we have to assign a negative value to *R* because in concave surfaces the radius is measured on the vapor side, consequently $\Delta P < 0$. For a flat surface $R \to \infty$, hence $\Delta P = 0$.

The pressure changes due to the curvature effects when a flat surface is curved induce a change in the molar Gibbs free energy given by the fundamental equation:

$$dG = VdP - SdT\,. \tag{1.2.10}$$

At constant temperature, the variation of the Gibbs free energy per mole of liquid, upon curving in a spherical drop, is:

$$\Delta G = G^c - G = \int_0^{\Delta P} V_m dP = \Delta P \cdot V_m = \frac{2\sigma_{\mathrm{vl}}}{R} \cdot V_m \tag{1.2.11}$$

where *G* is the molar Gibbs free energy of the vapor in equilibrium with a flat surface, and depends on the vapor pressure p_0, while G^c is the molar Gibbs free energy for a liquid with a curved surface:

$$G = G^0 + R_{gas}T \cdot ln(p_0) \tag{1.2.12}$$

$$G^c = G^0 + R_{gas}T \cdot ln(p_0^c)\,. \tag{1.2.13}$$

Hence, the variation of the Gibbs free energy can be also written:

$$\Delta G = G^c - G = R_{gas}T \cdot \ln\left(\frac{p_0^c}{p_0}\right) \quad (1.2.14)$$

By combining Eq. 1.2.11 and Eq. 1.2.14, we obtain the pressure exerted by the vapor on a spherical surface of radius R:

$$\ln\left(\frac{p_0^c}{p_0}\right) = \frac{2\sigma_{vl}V_m}{R \cdot R_{gas}T} \quad (1.2.15)$$

Eq. 1.2.15 is the **Kelvin equation** that relates the vapor pressure to the curvature of the liquid. We can also obtain the pressure applied to the meniscus in the vapor-liquid interface of water in mesopores:

$$\ln\left(\frac{p_0^c}{p_0}\right) = -\frac{2\sigma_{vl}V_m}{R \cdot R_{gas}T} \ . \quad (1.2.16)$$

The negative sign has to be used because the radius of the meniscus is measured on the vapor side. The same has to be done for vapor bubbles in the liquid.

An important implication of the Kelvin equation is that it is used to quantitatively describe the phenomenon of the capillary condensation which occurs when water molecules are adsorbed into mesopores. At a given pressure p_0^c, once the meniscus is formed in the pore, condensation continues until the radius of the liquid, *R=Rp/cos(Θ)* in Figure 1.2.4, has reached the value given by the Kelvin equation. Then, **liquids are strongly adsorbed into porous materials as a consequence of the capillary condensation** [63].

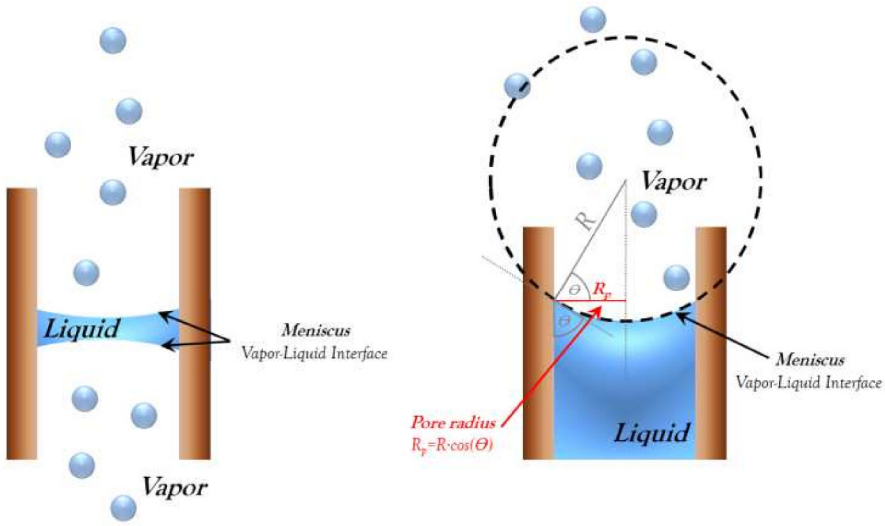

Figure 1.2.4 – Schematic illustration of capillary condensation. (Left) Vapor water molecules are adsorbed on pore walls and a meniscus at water-liquid interface is formed, (Right) water condensation continues until the curvature of the meniscus is *R*, as given by the Kelvin equation (Eq. 1.2.16).

By writing the Kelvin equation as a function of the pore radius, the equilibrium pressure is directly related to the contact angle Θ, see Figure 1.2.4, and the wettability of the pore walls:

$$\ln\left(\frac{p_0^c}{p_0}\right) = -\frac{2\cdot\sigma_{vl}\cos(\Theta)\cdot V_m}{R\cdot R_{gas}T} \quad . \tag{1.2.17}$$

If $\Theta < 90°$ condensation occurs below the saturation vapor pressure p_0 because $ln(p^c_0/p_0) < 1$. On the contrary, if $\Theta < 90°$ condensation occurs above p_0.

1—2.3 ADSORPTION

The amount of molecules adsorbed to an interface is described by adsorption functions $\Gamma=f(P,T)$. In general, when adsorption is dominated by physical interaction rather than chemical bonding, it is called *physisorption.* This is characterized by low interaction energies (~20-40 KJ/mol), so adsorbed molecules are still relatively free to diffuse on the surface and the molecular structure at the interface is not modified. When the adsorption energy is of the order of chemical binding energies(~100-400 KJ/mol), the adsorption is called *chemisorption* and molecules are adsorbed in specific binding sites, causing changes in the molecular structure.

Depending on the physicochemical conditions, different adsorption vs pressure functions can be observed. Adsorption is generally measured at constant temperature and described by functions called **adsorption isotherms**: $\Gamma=f(P)$. When the adsorption of a vapor in equilibrium with its liquid is under investigation, the amount of vapor adsorbed is plotted as a function of the partial vapor pressure P/P_0 or the relative humidity $RH=P/P_0 \cdot 100$.

A classification of adsorption isotherms as suggested by [63] and [64], is shown in Figure 1.2.5.

The simplest case is that of a linear increase *(type A)* and is described by the Henry equation:

$$\Gamma=k_H \cdot P \tag{1.2.18}$$

with k_H constant.

Type *(B)* describes the adsorption on heterogeneous surfaces which present regions with low affinity together with sites of high affinity. The steep increase at low pressures shows that the high affinity sites are occupied as a first step. The isotherm is described by the Freundlich equation:

$$\Gamma = k_F \cdot P^q \tag{1.2.19}$$

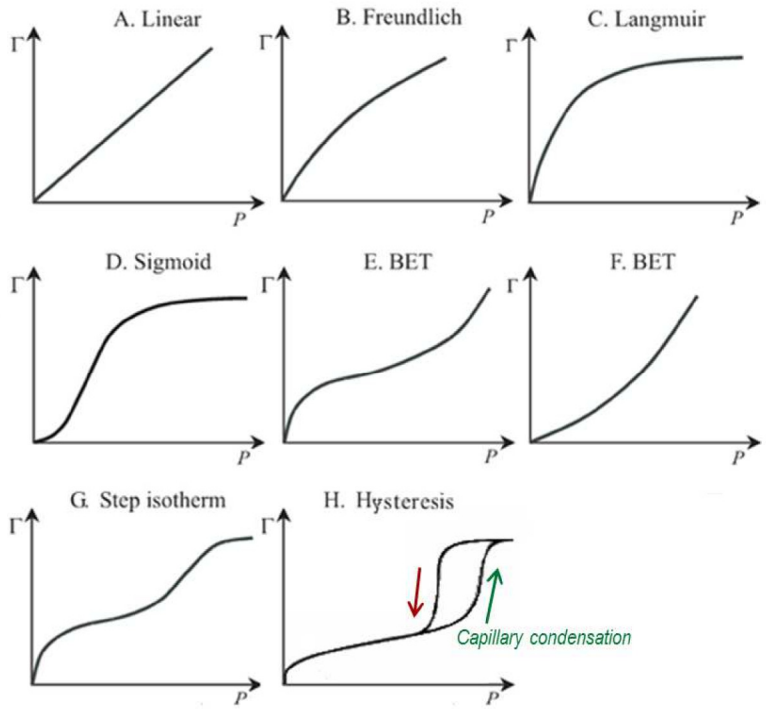

Figure 1.2.5 – Classification of the most common adsorption isotherms. Plots of typical adsorption isotherm functions versus pressure, from [63] and [64].

with both k_F and q constant and $q<1$.

Type *(C)* describes the adsorption on a surface for which only one monolayer can be adsorbed. It is described by the Langmuir equation:

$$\theta = \frac{k_L P}{1+k_L P}, \tag{1.2.20}$$

with $\theta = \Gamma / \Gamma_{monolayer}$ and k_L constant. This type of isotherm can be observed on various surfaces including the walls of nanoporous materials, in those cases where isotherm saturates when pores are filled.

The sigmoidal isotherm *(D)* is observed during adsorption on flat and homogeneous surfaces where cooperative effects take place. Adsorption is boosted when molecules can interact with a neighboring adsorbed molecule. This is common in macropores (diameter larger than 50 nm). These pores being large, the gaseous molecules are virtually adsorbed on flat surfaces.

Types *(E)* and *(F)* are extensions of the Langmuir theory proposed by Brunauer, Emmett and Teller, so they are called BET isotherms. They describe the adsorption of multilayers but assume a Langmuir adsorption for each layer according to the equation:

$$\frac{n}{n_{mon}} = \frac{C}{\left(1-\frac{P}{P_0}\right)\cdot\left[1+\frac{P}{P_0}\cdot(C-1)\right]}\cdot\frac{P}{P_0} \qquad (1.2.21)$$

where n is the number of moles adsorbed per unit area, n_{mon} is the number of adsorbed moles in one full monolayer per unit area, P_0 is the equilibrium vapor pressure and C takes into account the adsorption (and desorption) to (and from) layers. In *(E)* the first step describes the adsorption of one monolayer, increasing pressure further, the molecules are adsorbed on a molecular layer already formed. In *(F)* the binding of the first monolayer to the surface is weaker than the binding to already adsorbed molecules.

Type *(G)* is a step isotherm which may be observed in porous materials. At low pressure a single layer of molecules adsorbs to the surface (as in Langmuir adsorption), at intermediate pressures multilayers are formed and saturation occurs at high pressure when pores are filled.

Type *(H)* shows the hysteresis between adsorption and desorption often occurring in pores. Capillary condensation enhances the filling of mesopores as it is clearly observed by the sudden rise in the adsorption isotherm. The desorption isotherm, which lies above, represents the vaporization of molecules. A hysteresis is observed because evaporation occurs only for the molecules that have access to the vapor phase (desorption is hindered for pores surrounded by other liquid-filled pores), so the process is delayed.

The amount of molecules adsorbed on pores and surfaces can be experimentally measured with different methods. Among them, the **quartz crystal microbalance** (QCM) allows to measure the mass of the adsorbed molecule upon the variation in mass of the material. Quartz has piezoelectric properties so it can be deformed by

an external voltage. Notably, it can oscillate at its resonance frequency by applying an appropriate AC voltage across the electrodes, opportunely placed on the top and the bottom of the crystal. Since the resonance frequency is highly sensitive to the oscillating mass, it can be affected by the slight variation of the mass upon adsorption.

1—2.4 EFFECTS OF CONFINEMENT

In this Section, we illustrate the anomalous behavior of water upon nanoscale confinement through a few examples. There are many parameters that come into play (such as surface forces, pore geometry and size, molecular structure of the pore surface, pore connectivity, etc...) and a great effort is still required to unveil all the peculiarities of confined water.

Many studies on water confined in porous silica materials, such as MCM-41 or Vycor glass, report a lowering in the freezing and melting points of water resulting from the reduction in the number of neighboring molecules [65]. It also depends on surfaces forces and curvature effects. It was observed that, while decreasing temperature, the interaction with the pore surface prevents up to three layers of water molecules to assume a crystalline structure [66—68]. As a consequence, the freezing point decreases as a function of the pore diameter because the fraction of water molecules located next to the pore wall increases. Jahnert et al. observed no melting or freezing peaks in MCM-41 with 2.5 nm pore diameter [69]. The phase diagram for supercooled water confined to cylindrical silica nanopores in terms of pressure, temperature and pore radius was built by Limmer and Chandler [70]. From the third layer until the center of the pore, water molecules crystalize in a mixture of cubic (I_c) and ordinary hexagonal (I_h) forms depending on the degree of water filling [67, 71, 72]. In bulk water, the cubic form of ice is metastable and transforms in Ih when temperature increases. In contrast, cubic ice confined in cylindrical, interconnected cylindrical and interconnected pores of silica is stable up to the melting point [73].

The reduced freezing point of confined water is often exploited to reach *supercooled* water and investigate a second critical point, occurring at ~220 K, separating two liquid phases [74], each with its own properties such as density and compressibility. According to Speedy and Angell [75], such critical point could

explain the anomalous behavior of supercooled water. It must be kept in mind that confined phases differ from bulk phases, owing to the presence of cross interaction between water and substrate as well as to the reduced dimensionality [76], so it could be difficult to interpret supercooled water data gathered upon confinement.

A lowering of the freezing point was also observed for water confined in Multi-Walled Carbon NanoTubes (MWNTs), with the freezing point being higher than water confined in silica glasses (SBA-15) of similar pore diameter [77]. X-ray diffraction revealed that even at room temperature, water molecules confined in hydrophobic nanospaces present an ordered molecular assembly structure [78]. The cylindrical carbon nanotubes wall leads to an ice-like hollow-shell phase of water with a lower mobility than the bulk [79]. This could encourage a liquid-solid transition at higher temperature.

A study conducted by Tombari et al. [80] on the effects of nanoconfinement on thermodynamic properties of water show that, compared to bulk, water confined in Vycor glass of ~4 nm pores experiences an increase in the heat capacity, resulting from the reduction in the density upon nanoconfinement, and a decrease of enthalpy, that is attributed to an average decrease in the temperature of melting.

MD simulations of liquid water confined in a spherical nanocavity predict a significantly smaller dielectric constant compared to bulk water [81]. A nearly 50% decrease is observed when water is confined in a cavity of about 1.2 nm in diameter.

A study based on first principle MD simulations [82] reports a significant decrease of the dipole for water at the interface with graphene sheets or carbon nanotubes compared to bulk water. The same authors did not observe a similar behavior for water close to a hydrophilic surface, in this case, the average dipole moment of interfacial water molecules being close to that of the bulk [83].

Using MD simulation Cao et al. [84] have predicted different mass transfer mechanisms for bulk and confined water that are accountable for differences in the proton transport rate: in the conventional Grotthuss mechanism, occurring in bulk water, proton transfer involves both Eigen ($H_9O_4^+$) and Zundel ($H_5O_2^+$) cations *via* an “Eigen-Zundel-Eigen” mechanism, but when confined in one-dimensional channels, proton transport occurs *via* a “Zundel-Zundel” mechanism with a low barrier, hence more efficiently.

In the present thesis, infrared spectroscopy studies of water confined in silica mesoporous glasses (Vycor), Nafion membrane and Single-Walled Carbon Nanotubes (SWNTs), are presented. Characteristics and properties of those samples are described in the following three Sections.

1—3 POROUS VYCOR® GLASS

For more than half a century, Vycor porous glass has been used as a model mesoporous material. It is a man-made glass, obtained from borosilicate glass through a chemical treatment that removes most of the elements in the glass except silica (SiO_2). Being of a very simple composition and having an extremely low coefficient of expansion and contraction, it has higher heat shock resistance and greater resistance to deformation than commercial glasses. It is then suitable for very precise analytical work.

In this Section we will describe the production process of Vycor glass and this material main property.

1—3.1 PRODUCTION PROCESS

Glasses having the desirable properties of fused quartz, such as low coefficient of expansion and contraction, high heat shock resistance and great resistance to deformation, are known under the trademark Vycor. They are prepared through a unique process discovered by Hood and Nordberg [85]. A relatively soft alkali-borosilicate glass is melted and is then pressed, drawn, or blown according to the standard processes used in glass production. Afterward, it is subject to a heat treatment above the annealing point (T=1020 °C) but below the temperature that would produce deformation (T=1530 °C). During this step, two continuous intermingled glassy phases are produced: one phase is rich in alkali and boric oxide and soluble in acids, the other phase is rich in silica and insoluble. During the next step, the workpiece is immersed into a hot dilute acid solution in order to dissolve the soluble phase and obtain the porous high-silica skeleton. Finally, it is slowly heated to T>1200 °C to consolidate the porous structure and the Vycor glass, with 96% of silica content, is produced.

1—3.2 PROPERTIES OF CORNING VYCOR® 7930 POROUS GLASS

The porous glass used in the experiments presented in this manuscript is a Vycor brand porous glass n°7930, a product of Corning Glass Works. Porous Vycor is an open-cell, porous glass widely used in hydration processes due to its excellent absorbing properties. The bulk of this porous material being mainly composed of silica (96% of SiO_2, as reported in Table 1.3), is a hydrophilic material. The inner surface can nevertheless be easily turned to hydrophobic by silanization.

Table 1.3 – Chemical composition of corning Vycor®7930 (by Corning Incorporated).

Component	Amount (%)
SiO_2	96
B_2O_3	3
Na_2O	0.4
Miscellaneous traces	0.6

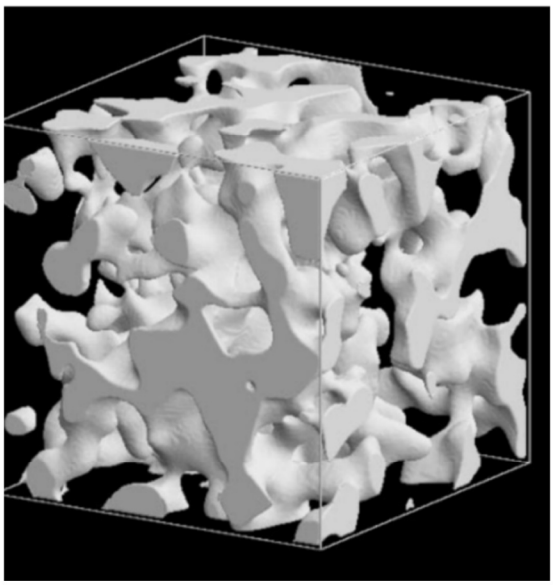

Figure 1.3.1 – Numerical reconstruction of mesoporous silica controlled porous glass. A numerical sample of the cross section of controlled porous glass, also known as Vycor, obtained by using an off-lattice reconstruction method, from [86].

Due to its porosity, this material has a high specific internal surface area of approximately 250 square meters per gram. The schematic structure of mesoporous silica controlled porous glass is shown in Figure 1.3.1 (from [86]).

The silanol groups (Si-O-H), present in large number at the solid-air interface, readily adsorb water molecules. At full hydration, Vycor adsorbs water up to 25% of its dry weight. By considering an average pore section of 50 Å, it was estimated that the fully hydrated Vycor accommodates three to four layers of water in its average pore [87]. An interesting case is observed when Vycor is in equilibrium with a water vapor pressure that would result in 25% of relative humidity (from Eq. 1.2.1). Under such conditions, a monolayer of water, also referred to as interfacial water, is adsorbed.

Some physical properties of Vycor porous glass are listed in Table 1.4.

Table 1.4 – Physical properties of corning Vycor®7930 (by Corning Incorporated).

Density	**1.50 g/cc**
Porosity	28 % of total volume
Specific surface area	250 m^2/g

1—4 NAFION® MEMBRANE

The perfluorosulfonic Nafion® membrane (DuPont™) has been commercially available since more than 40 years. Its applications are manifolds: as acid catalyst in the production of fine chemicals, as membrane in Donnan dialyzers to remove trace amounts of metals from waste streams, in water electrolysis cells to produce oxygen and hydrogen, for gas drying and humidification, *etc*... In particular, the acidic form of Nafion (Nafion-H) has been used since the 1960s as membrane in the proton exchange membrane fuel cells (PEMFCs) developed by General Electric for NASA's Gemini Space Program [88]. The recent interest in fuel cells as efficient clean power source for transportation and portable applications renewed the interest in perfluorosulfonic membranes. Their stability and selective ion transport make them excellent electrolytes in PEMFCs, enabling proton conduction from the anode to the cathode to derive electrical energy directly from a chemical fuel. A general PEMFC is schematized in Figure 1.4.1: chemical energy is generating by continuously feeding hydrogen to the anode and oxygen to the cathode.

PEMFCs performances strongly depend on the proton conductivity of the

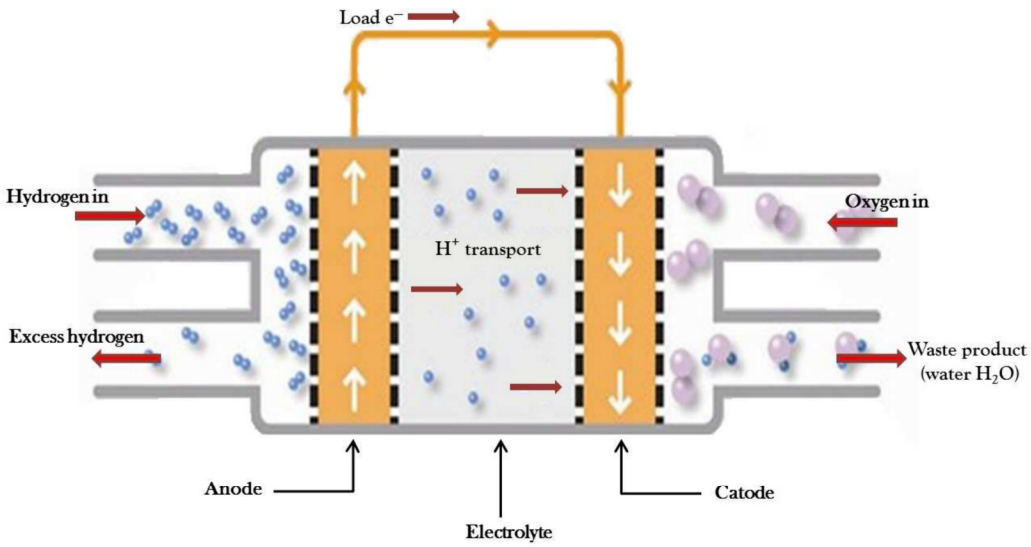

Figure 1.4.1 – Schematic illustration of a general Proton Exchange Membrane Fuel Cell. The electrolyte allows proton conduction from anode to cathode while electrons travel an external circuit.

electrolyte membrane which, in turn, is determined by its morphology and water content. To date, Nafion is the benchmark against which all other membranes are

compared due to its unchallenged proton conductivity at temperatures below 80°C, high mechanical strength, thermal and chemical stability. Despite promising progress in efficiency, there are still several technological and economical barriers that must be overcome before fuel cells can be commercialized at a large scale.

In this Section, we will describe the processing procedures and the properties of the Nafion membrane N211 used to study the ionization process and the protonic species formation occurring in its channels during hydration.

1—4.1 PRODUCTION PROCESS

Nafion® is a copolymer of two monomeric subunits: tetrafluoroethylene, or Teflon®, and perfluoro-4-methyl-3,6-dioxa-7-octene-1-sulfonyl fluoride, or vynil ether. The Teflon serves as a backbone, with fluoride monomers attached at regular intervals along the length of the backbone chain. Thick films, typically thicker than 125 μm, are produced using an established extrusion-cast manufacturing process followed by a conversion from the SO_2F to SO_3K, using an aqueous solution of potassium hydroxide and dimethyl sulfoxide. The ionic functionality is introduced when the pendant groups are converted to sulfonic acid, SO_3H, by means of an acid exchange with nitric acid [89]. The final structure of Nafion is shown in Figure 1.4.2.

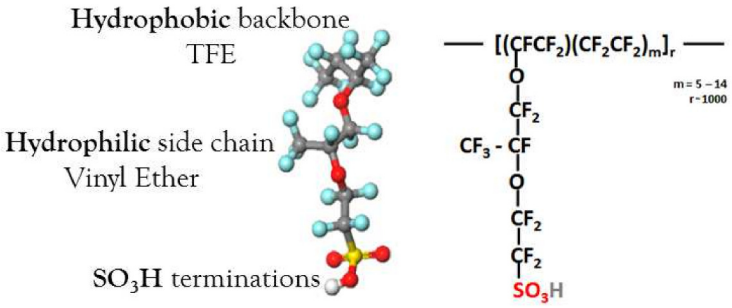

Figure 1.4.2 - Nafion® polymer structure. Nafion structure after conversion to the sulfonic acid form.

Technical advances in fuel cell design and performance have increased demand for thin and low-cost membranes that required the development of a new manufacturing process: the solution-casting process. As reported by Curtin *et al.* [89], the process is taking place in a clean room environment. (i) A backing film is

unwound and measured for thickness. (ii) Polymer dispersion is then applied to the base film and both materials enter a dryer section. (iii) The composite membrane/backing film is measured for total thickness, with the membrane thickness the difference from the initial backing film measurement. (iv) The membrane is inspected for defects and finally protected with a coversheet and wound on a master roll. This process has several advantages: prequalification of large dispersion batches for quality and expected performance, increased overall production rate for H^+ membrane compared to the chemical treatment of polymer extrusion, and improved thickness control and uniformity.

In order to avoid saturation in the infrared spectra measured during hydration, we selected a 25 μm membrane produced with the latter method, the Nafion N211.

1—4.2 PROPERTIES OF NAFION®

Nafion® is not a classical porous material since it swells at the nanometer scale, as mentioned previously. The polymer is formed of a hydrophobic perfluorinated backbone, on which are grafted pendant perfluorinated chains carrying sulfonic acid groups, SO_3H. The amphiphilic character of the polymer causes phase separation between mechanically robust hydrophobic domains and ion-conducting hydrophilic aqueous domains, with sulfonic acid groups located at the interface. Among the many structural models that have been proposed, the fibrillar one developed by Rubatat *et al.* [90] is now well established. It describes Nafion as hydrophobic ribbon-like aggregates embedded in a continuous ionic phase. A common feature to all models is that the hydrophilic phase is made of “ionic clusters/channels” that grow in size from typically 1 to 3 nm and get more interconnected as water is adsorbed to the membrane. In the dry state, the membrane contains isolated, spherical ionic aggregates (with diameters of ~1 nm). Water adsorption causes the aggregate to swell and restructure until an interconnected network of cylindrical channels is formed. Water plays a fundamental role in Nafion (and perfluorosulfonic acid membranes in general): as pore former, pore filler and vehicle for proton transportation. Indeed, the content of water controls the ion conductivity. As an extreme case, without water there is no conductivity and a fuel cell does not operate. Conductivity is also affected by the number of sulfonic acid groups which depends on the extent of the

tetrafluoroethylene branch, represented by the parameter *m* in Figure 1.4.2. The average distance between side chains along the backbone is expressed in term of equivalent weight (*EW*), defined as grams of dry polymer per mole of acid groups. Nafion with equivalent weight of *1100 g/equiv* is by far the most commonly used. It has been suggested that the acid groups in Nafion have a Hammett acidity (-Ho ~ 12) similar to 100% sulfuric acid [91], giving to Nafion a very high acid character.

The dynamic of water is strongly correlated to the efficiency of the proton transfer. Proton transport arises from a complex balance between mass diffusion of hydronium ion, H_3O^+, and Grotthuss-like proton motions occurring through H-bonds formation and breaking in hydrated protonic clusters, schematized in Figure 1.4.3.

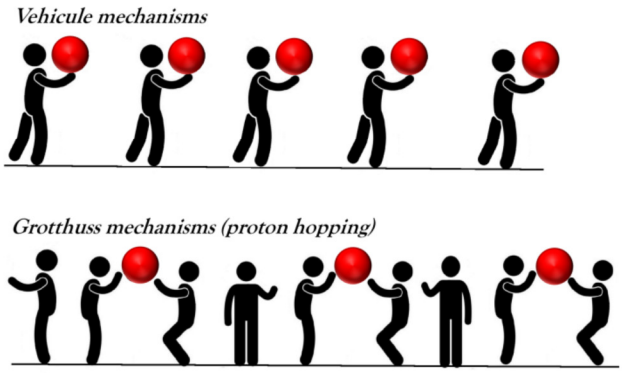

Figure 1.4.3 – Scheme of proton transfer mechanisms. Top: in the vehicle mechanism the proton (in red) takes place with the aid of moving vehicle (H_2O). Bottom: in the Grotthuss mechanism the protons are passed along the hydrogen bond.

The dynamics of water in Nafion slows significantly as the hydration level of the membrane decreases, indicating that the hydrogen-bonding network, and consequently the ability to break and form H-bonds, is strongly perturbed by the confining effects of the interface [92].

The water content of the membrane and the varying sizes of the hydrophilic domains with their complicated topology tremendously affect the dynamics of water and the ion transfer properties.

Some properties of the membrane Nafion 211 provided by DuPont Company are listed in Table 1.5. Measurements were performed with membrane conditioned at 23 °C and 50% of relative humidity.

Table 1.5 – Some properties of Nafion 211 membrane conditioned at 23 °C and 50% of RH.

Typical thickness	25.4 μm
Basic weight	50 g/m^2
Equivalent weight	1100 g/equiv

1—5 SINGLE WALLED CARBON NANOTUBES

Ideal carbon nanotubes (CNTs) are cylindrical-shaped macromolecules whose walls are made up of a hexagonal lattice of carbon atoms like the atomic planes of graphite. Structures comprising only one cylinder are termed Single Walled Carbon Nanotubes (SWNTs), those comprising two or more concentric graphene cylinders are referred to as Multi Walled Carbon Nanotubes (MWNTs). The first discovery of carbon nanotubes is generally attributed to Iijima who reported the preparation of a "new type of finite carbon structure consisting of needle-like tubes" [93]: the MWNTs (shown in Figure 1.5.1).

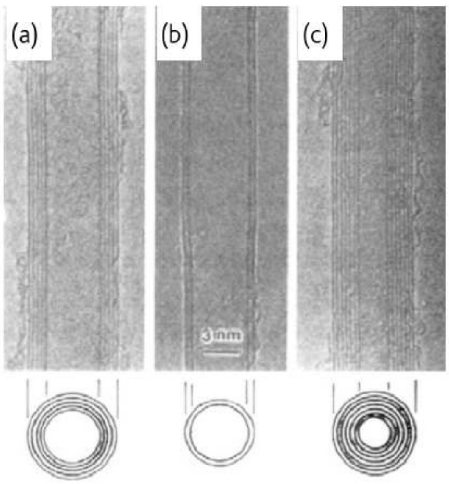

Figure 1.5.1 – Iijima's Multi Walled Carbon Nanotubes. TEM micrographs of three MWNTs consisting of three, five and seven concentric graphene cylinders (adaptation of [93] by [94].

Earlier on, a figure presented in *The Journal of Crystal Growth* in 1976 by Oberlin et al. [95] reported the first viewgraph of what is called nowadays "carbon nanotube". The discovery of Single Walled Carbon Nanotubes (SWNTs) was first reported in the June 17th issue of *Nature* in 1993 by two independent research teams: Iijima and Ichihashi [96], and Bethune *et al*. [97].

There is no doubt, however, that the work on carbon nanotubes was boosted by the report made by Iijima in 1991 where the author detailed the helical arrangement of carbon atoms on seamless coaxial cylinders. Since then, the study of CNTs has become an active field in chemistry, physics and nanotechnology.

In this Section, we report the main properties and the synthesis processes of single walled carbon nanotubes.

1—5.1 PRODUCTION PROCESS

Different techniques have been developed and improved to produce high quality SWNTs, such as carbon arc discharge, laser-ablation technique, electrolysis and chemical vapor deposition (CVD). The latter is the manufacturing method of Nanostructured & Amorphous Materials, Inc. where the sample used in our experiments was purchased (short SWNTs, stock number: 1246YJS). Properties of those nanotubes are listed in Table 1.6 in Section 1—5.2.

As compared to the other methods, CVD is a simple and economic technique for synthesizing carbon nanotubes at low temperature and ambient pressure. Furthermore, because of this method's yield, purity and structure control, CVD is the most popular method to produce CNTs nowadays [98]. In the CVD process (see Figure 1.5.2), a hydrocarbon vapor passes (typically 15-60 min) through a tubular reactor in which a catalyst material is placed at sufficiently high temperature (600-1200 °C) to decompose the hydrocarbon (this is why the technique is also known as thermal CVD or catalytic CVD). To date, no definitive model for the CNTs growth is established, but a widely-accepted general mechanism is reviewed by Kumar and Ando [98].

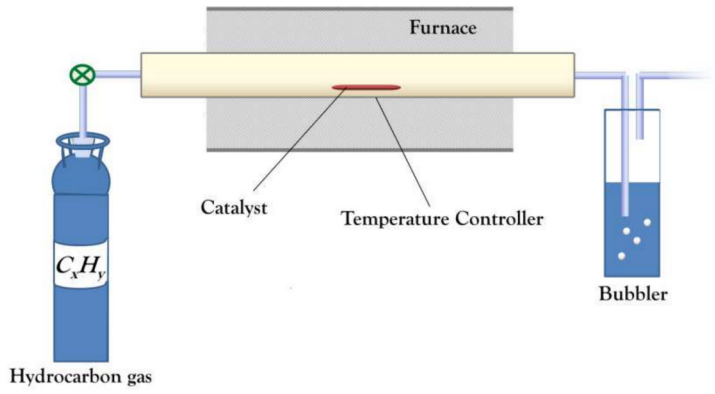

Figure 1.5.2 – Schematic representation of the simplest form of a CVD set-up. The thermal decomposition of a hydrocarbon vapour is achieved in the presence of a hot metal catalyst. Carbon gets dissolved into the metal, hydrogen flies away in the bubbler.

When hydrocarbon vapor comes in contact with the hot metal particles, it decomposes in carbon, which is dissolved into the metal, and free hydrogen molecules. After reaching the carbon-solubility limit in the metal at the given temperature, carbon precipitates out and crystallizes in the form of a cylindrical network having no dangling bonds and hence energetically stable. Hydrocarbon decomposition, being an exothermic process, releases heat to the metal's exposed zone, while carbon crystallization, being an endothermic process, absorbs the heat. The thermal gradient created inside of the metal particle keeps the process on.

In Figure 1.5.3, two models for the growth mechanisms are shown. The tip-growth model illustrates the CNTs synthesis when the catalyst-substrate interaction is weak: hydrocarbon decomposes on the top surface of the metal, carbon atoms diffuse down through the metal and CNT precipitates on the metal bottom pushing the particle off the substrate. Decomposition continues until the metal's top is open. On the contrary, the base-growth model describes the CNTs synthesis when the catalyst-substrate interaction is strong: after hydrocarbon decomposition, CNT precipitation fails to push the metal particle up and is compelled to emerge out of the metal's top. First, carbon crystallizes as a hemispherical dome and then it extends up in a cylindrical form.

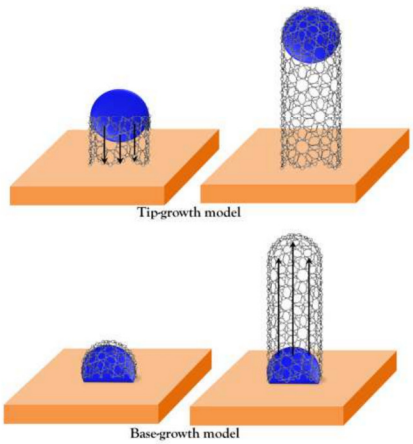

Figure 1.5.3 – Growth mechanisms for CNTs. Top: Tip-growth model for catalyst-substrate weak interaction. Down: Base-growth model for catalyst-substrate strong interaction.

The choice of the hydrocarbon (called precursor), the catalyst and the catalyst support, determine the size and the structure of the carbon nanotubes. SWNTs are generally produced using ethanol as precursor, that is stable at high temperature (900 – 1200 °C), and iron or cobalt as metal catalysts. Their strong adhesion with

the growing CNTs makes them suitable for the production of high-curvature (hence low-diameter) tubes, such as SWNTs.

1—5.2 PROPERTIES OF SWNTS

Ideal single walled carbon nanotubes can be visualized as a rolled-up tubular shell of graphene sheet (graphene is an individual graphite layer) which is made up of benzene type hexagonal rings of carbon atoms. Each atom is joined to three neighbors via a sp^2 bonding. Given the large length-to diameter ratio (aspect ratio) of about 1000, common for SWNTs, they can be considered as nearly one-dimensional structures.

SWNTs are classified according to three possible crystallographic configurations, depending on how the graphene sheet is "rolled-up": zig-zag, armchair, chiral. The structure is specified by the chiral vector *(n,m)* that can be understood with reference to Figure 3.2.4. The integers *n* and *m* correspond to the number of atomic vectors along the two directions in the honeycomb crystal lattice of graphene. In the zig-zag conformation, two opposite C-C bonds of each hexagon are parallel to the tube axis. In the armchair conformation, the C-C bonds are perpendicular to the axis. In other arrangements, the opposite C-C bonds lie at an angle to the tube axis, resulting in a helical nanotube that is chiral.

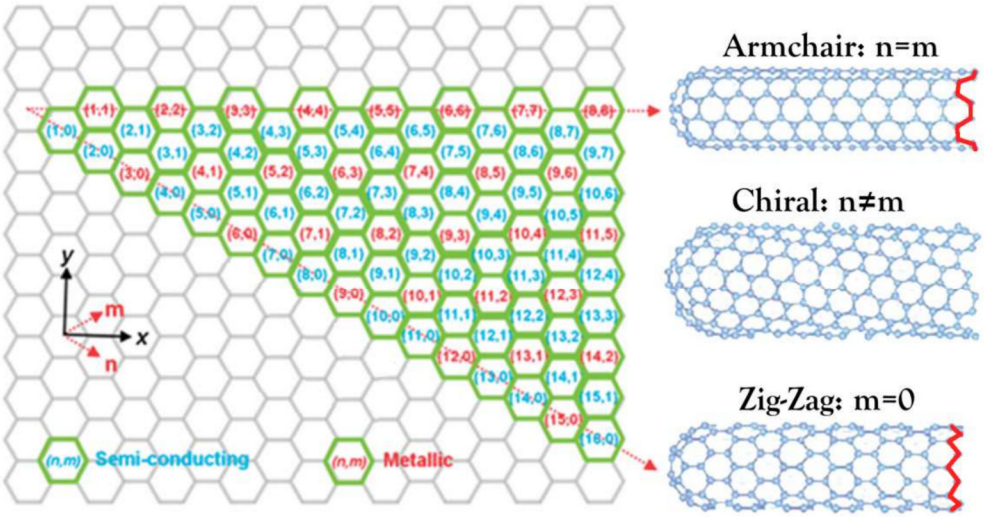

Figure 3.2.4 – Crystallographic configurations of ideal SWNTs. Formation of SWNTs by rolling a graphene sheet along lattice vectors leading to armchair, chiral and zig-zag configurations. Figure adapted from [128].

SWNTs properties are strongly dependent on their structure. As shown in Figure 3.2.4, all armchair and one-third of all zig-zag nanotubes are metallic, while two-third of zig-tag tubes are semiconducting [99]. Thus, some nanotubes have conductivities higher than that of copper, while others behave like silicon. The importance of selectively producing SWNTs with specific characteristics is evident for the development of nanoelectronic devices. However, the available bulk-production methods generally yield mixtures of metallic and semiconducting nanotubes. The research for an efficient production method with uniform structure and properties is still going on.

The strength of the sp^2 carbon-carbon bonds gives to SWNTs amazing mechanical properties. The average breaking strength and the Young' modulus (used to measure a material stiffness and defined as the ratio of the stress, *i.e.* force per unit area, along an axis to the strain, i.e. ratio of deformation over initial length) are 30 GPa and 1002 GPa, respectively [100]. The remarkable strength, coupled with the lightness of nanotubes, has generated a great interest for applications.

It was also demonstrated that, counter of intuition, the hydrophobic SWNTs can have a significant water occupancy [8]. Intrigued by numerical simulations predicting a fast water transport through SWNTs, Holt et al. built an experiment to measure the water transport [101]. They confirmed that a flow enhancement occurs, with a flux of 10 to 40 water molecules nm-2 ns-1, exceeding by more than three orders of magnitude the values calculated from continuum hydrodynamic model. It was then realized that SWNTs can also be suitable as a membrane that allows both high flux and high-sieve selectivity (depending on the tubes diameter).

In our hydration study, we selected short SWNTs with an internal diameter between 0.8 and 1.6 nm. Single walled carbon nanotubes with a narrower diameter distribution arrange themselves in nanotubes bundles (aggregates of metallic and semiconducting nanotubes) preventing the absorbance of the infrared radiation caused by metallic nanotubes. Specifications and components of SWNTs from Nanostructured & Amorphous Materials, Inc. are reported in Table 1.6.

Table 1.6 – Specifications of NanoAmor® short SWNTs (stock number: 1246YJS).

Purity	> 95 vol% (CNTs)
Purity	> 90 vol% (SWNTs)
Outside diameter	1 – 2 nm
Inside diameter	0.8 – 1.6 nm
Length	1 – 3 µm
Specific surface area	> 380 m^2/g
Composition	**C** Bal. **Al** < 0.1 **Cl** < 0.5 **Co** < 3.0 **S** < 0.3

1—6 VIBRATIONAL SPECTROSCOPY

Electromagnetic radiation can be described as wave packets of frequency ν, called photons, whose energy is proportional to the frequency and quantized according to the Plank equation:

$$E = h\nu \tag{1.6.1}$$

The analysis of the infrared electromagnetic radiation (~10^{-3} — ~1 eV) which is absorbed, emitted or scattered upon interaction with matter is the objective of infrared spectroscopy. It permits to get information on matter and physical-chemical processes at the atomic and molecular levels.

In this Section we will introduce the quantum mechanics theory to describe molecular systems. Special attention will be devoted to vibration and rotation motions as their transitions are exploited in infrared spectroscopy to investigate samples structure and dynamics.

1—6.1 DESCRIPTION OF MOLECULAR SYSTEMS

The state of a quantum mechanical system is completely specified by a wave function $\varphi(\vec{r},t)$ that depends on the coordinates of the particles and on time (*postulate 1*). Unlike classical mechanics, that provides information on the behavior of a system over time in terms of its coordinates, quantum mechanics provides only a statistical description of the system by defining

$$\varphi^*(\vec{r},t)\varphi(\vec{r},t)d\vec{r} \tag{1.6.2}$$

as the probability that a particle located in $\vec{r}$ at time t lies in the volume $d\vec{r}$. The evolution of the system over time is given by the time-dependent Schrödinger equation according to the *postulate 5* of the quantum theory:

$$\hat{H}\,\varphi(\vec{r},t) = i\hbar\frac{\partial\varphi}{\partial t} \tag{1.6.3}$$

where $\hat{H}$ is the Hamiltonian operator that correspond to the total energy, accounting for kinetic and potential energy, of the particles forming the system, $\hbar \approx 1.055 \cdot 10^{-34}\ J \cdot s$ is the reduced Planck constant and i the imaginary unit.

If the wave function represents a stationary state, *i.e.* it is independent from time $\varphi(\vec{r}, t) = \varphi(\vec{r})$, the Hamiltonian operator acting on it gives a wave function which is proportional to the stationary state:

$$\hat{H}\,\varphi(\vec{r}) = E\,\varphi(\vec{r}) \tag{1.6.4}$$

Eq. (1.6.4) is called the time-independent Schrödinger equation and the proportionality constant E is the energy of the stationary state $\varphi(\vec{r})$.

Solving the Schrödinger equation for a molecule is extremely complex because the Hamiltonian contains all the interactions between the nuclei and the electrons. However, since the mass of the nuclei is much larger than the electrons, the nuclei can be considered almost stationary with respect to the electrons. As a result, the total wave function can be split into electronic, vibrational and rotational parts according to the **Born-Oppenheimer approximation**. Vibrational $\varphi_{vib}(\vec{R})$ and rotational $\varphi_{rot}(\vec{R})$ wave functions only depend on nuclear coordinates $\vec{R}$ while the electronic wave function $\varphi_{el}\left(\vec{x}, \overrightarrow{R'}\right)$ depends on the coordinates of the electrons $\vec{x}$ and those of the nuclei at equilibrium position $\overrightarrow{R'}$:

$$\varphi(\vec{x}, \vec{R}) = \varphi_{el}\left(\vec{x}, \overrightarrow{R'}\right) \cdot \varphi_{vib}(\vec{R}) \cdot \varphi_{rot}(\vec{R})\,. \tag{1.6.5}$$

1—6.2 VIBRATIONAL TRANSITIONS

Infrared radiation promotes transitions between nuclear states or electronic transitions from a fundamental state to an excited state. Indeed, it is not powerful enough to allow dissociation of molecules or removal of electrons. Molecular effects caused by different radiation energies are schematized in Figure 1.6.1.

The Schrödinger equation for electrons, depending only on the coordinates of the electrons $\vec{x}$ and those of the nuclei at equilibrium position $\overrightarrow{R'}$, is:

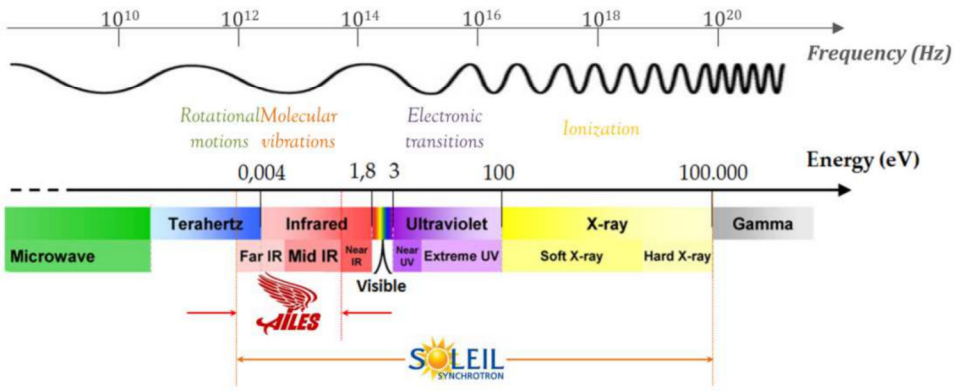

Figure 1.6.1 – Molecular effects triggered by electromagnetic radiation. Energies and frequencies of electromagnetic radiation causing rotational and vibrational motions, electronic transitions and ionization on molecules. Operating energies of synchrotron SOLEIL and AILES beamline are shown.

$$\hat{H}_{el}\varphi_{el}\left(\vec{x},\vec{R'}\right) = E_{el}\left(\vec{R'}\right)\varphi_{el}\left(\vec{x},\vec{R'}\right). \tag{1.6.6}$$

The wave functions $\varphi_{el}\left(\vec{x},\vec{R'}\right)$ that are solutions of (1.6.6) are called orbitals and have a characteristic energy and distribution, as mentioned in Section 1—1.1.

To obtain the nuclear levels of a molecule, we should consider the Hamiltonian for the nuclear motions of the molecule. For the simplest case, a diatomic molecule, the **vibrational motion** can be modeled as a harmonic oscillator oscillating around the center of mass $\mu = \frac{m_1 m_2}{m_1+m_2}$, with m_1 and m_2 the mass of the nuclei of the diatomic molecule. The potential energy of the harmonic oscillator is $V = \frac{1}{2}kq^2$, with k the force constant of the oscillator and q=R-R_0 the coordinate of the vibration motion of the molecule (R_0 is the intermolecular distance of the diatomic molecule at equilibrium). So, the Schrödinger equation for the vibrational motion of the nuclei is:

$$\frac{d^2\varphi(R)}{dR^2} + \frac{8\pi^2\mu}{h^2}\left(E - \frac{1}{2}kq^2\right)\varphi_{vib}(q) = 0 \tag{1.6.7}$$

Such equation has known solutions:

$$\varphi_{vib,v} \propto H_v e^{-\frac{q^2}{2}} \tag{1.6.8}$$

where H_v is the Hermite polynomial. By replacing the wave function (1.6.8) in Eq. (1.6.7) we obtain the quantized vibrational energy:

$$E_{vib} = \left(v + \frac{1}{2}\right)\frac{h}{2\pi}\sqrt{\frac{k}{\mu}} \tag{1.6.9}$$

with v=0,1,2...The vibrational energy of a diatomic molecule can also be express as:

$$E_{vib} = \left(v + \frac{1}{2}\right)h\nu \tag{1.6.10}$$

where ν=$\frac{1}{2\pi}\sqrt{\frac{k}{\mu}}$ is the vibrational frequency for a classical harmonic oscillator. The minimum possible energy, called zero-point, is $E_{vib,0} = (1/2)\cdot h\nu \neq 0$. Here, the probability $|\varphi_v|^2$ to find the oscillator reaches its maximum at the equilibrium position R_0. As v increases, the energy increases, with the energy levels equally spaced by $h\nu$, and their probability distributions change accordingly, as depicted by the dashed orange curves in Figure 1.6.2.

For the firsts vibrational levels, v=0 and 1, the potential energy is well approximated by a harmonic oscillator. However, to take into account the dissociation that occurs when the two atoms move away from each other as well as the repulsion effects when they get too close, the potential energy used in the Hamiltonian departs from the harmonic oscillator and becomes rather a Morse potential:

$$V_{Morse} = D_e\left(1 - e^{-\beta q}\right)^2 \tag{1.6.11}$$

where D_e is the energy dissociation and β = $\sqrt{\frac{k}{2D_e}}$.

The vibrational energy obtained by introducing the Morse potential in Eq. (1.6.7) is:

$$E_{vib} = \left(v + \frac{1}{2}\right)h\nu - \left(v + \frac{1}{2}\right)^2 x_{an}h\nu \tag{1.6.12}$$

where $x_{an} = \frac{h\nu}{4D_e}$ is the anharmonicity constant. By including the anharmonic terms, the spacing between vibrational energy levels decreases as v increases. At high R the spacing approaches zero, see Figure 1.6.2.

The energy gap between vibrational levels is around 10^{-2} – 10^{-1} eV so the transition of the molecule from a vibrational state to another involves absorption or emission of the electromagnetic field in the infrared range.

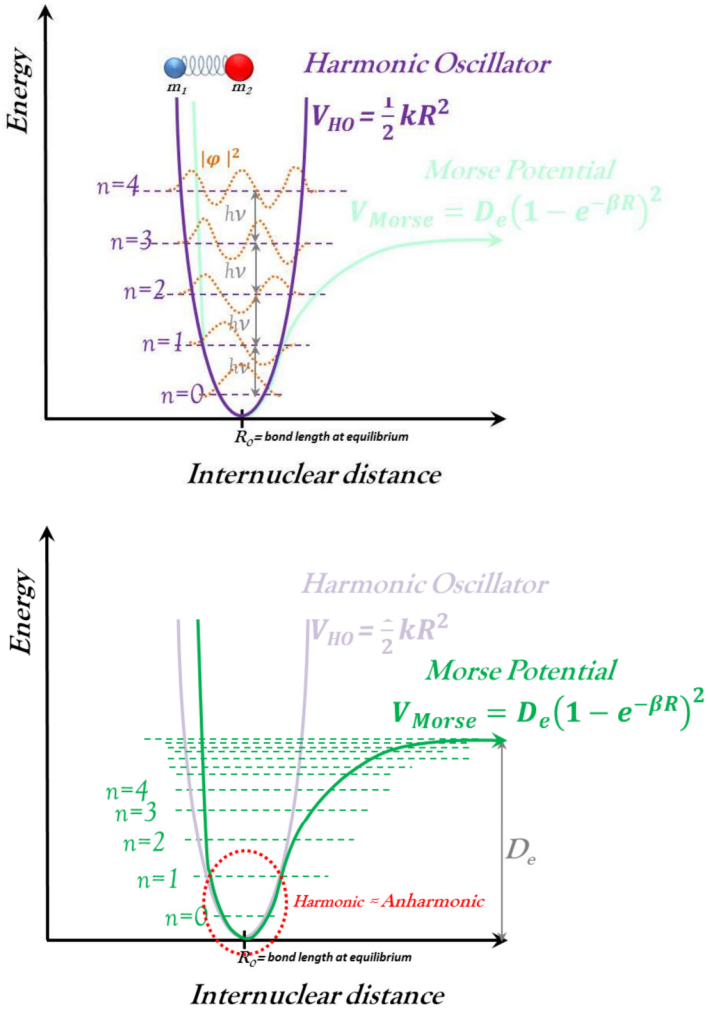

Figure 1.6.2 – Potential energies for a diatomic molecule system. Harmonic oscillator (violet) and Morse (green) potential energies with the respective energy levels. (Top): The harmonic oscillator potential is highlighted and the probability distributions $|\varphi_v|^2$ are shown in orange. (Down): The morse potential is highlighted showing the good accordance for the firsts vibrational levels between the two models.

1—6.3 TRANSITIONS SELECTION RULES

Actually, a transition between two vibrational levels is allowed when two conditions are fulfilled:

a) the radiation energy must be equal to the energy gap between the final and the initial vibrational level involved in the transition $E_f - E_i = h\nu$;
b) the transition moment integral must be non-zero, so that $[\mu]_{if} = \int dq\, \varphi_f^*(q)\, \mu\, \varphi_i(q) \neq 0$, with μ dipole moment operator, $\varphi_f(q)$ and $\varphi_i(q)$ the wave functions of the final and initial state respectively.

The dipole moment μ of the molecule can be expanded in Taylor series using the coordinates of the vibration $q=R-R_0$. If the vibration is of limited amplitude, *i.e.* small q, the Taylor series can be truncated at the second term according to the electrical harmonic approximation:

$$\mu = \mu_0 + \left(\frac{\delta\mu}{\delta q}\right)_{q=0} q \tag{1.6.13}$$

where μ_0 is the dipole moment at equilibrium.

In the harmonic approximation the resulting transition moment integral is:

$$[\mu]_{if} = \int dq\, \varphi_f^*(q)\, \mu\, \varphi_i(q) = \mu_0 \int dq\, \varphi_f^*(q)\, \varphi_i(q) + \left(\frac{\delta\mu}{\delta q}\right)_{q=0} \int dq\, \varphi_f^*(q) q\, \varphi_i(q) \tag{1.6.14}$$

The first term is zero for any vibrational transition because the vibrational wave functions are orthonormal:

$$\int dq\, \varphi_f^*(q)\, \varphi_i(q) = \delta_{fi} \begin{cases} = 1 \text{ if } \varphi_i(q) = \varphi_f(q) \\ = 0 \text{ if } \varphi_i(q) \neq \varphi_f(q) \end{cases} \tag{1.6.15}$$

The integral at second term can be resolved introducing the ladder operators:

$$\hat{Q}^+ = \sqrt{\frac{1}{2}}\left(q - \frac{d}{dq}\right) \text{ and } \hat{Q} = \sqrt{\frac{1}{2}}\left(q + \frac{d}{dq}\right) \tag{1.6.16}$$

with the properties:

$$\text{(i)} \qquad \hat{Q}^+ \varphi_v \rightarrow \varphi_{v+1}\,;$$

$$\text{(ii)} \quad \hat{Q}\,\varphi_v \rightarrow \varphi_{v-1}\,; \qquad \text{(1.6.17)}$$
$$\text{(iii)} \quad \hat{Q}^+ + \hat{Q} = \sqrt{2}q\,.$$

By using (iii), we can express q in term of the ladder operators in the integral at second term of Eq. (1.6.14):

$$\int dq\, \varphi_f^*(q)\, \frac{\hat{Q}^+ + \hat{Q}}{\sqrt{2}} \varphi_i(q) \qquad (1.6.18)$$

and conclude that the integral is not zero only if $\varphi_f = \varphi_{i\pm1}$ according to properties (i) and (ii) of Eq. (1.6.17).

Then, in order for Eq. (1.6.14) to be non-zero, the final and the initial state must be just one level apart, with $\Delta v = \pm 1$, and the vibration must lead to a change in the dipole momentum:

$$\left(\frac{\delta\mu}{\delta q}\right)_{q=0} \neq 0\,. \qquad (1.6.19)$$

When anharmonicity is present, quadratic terms of the dipole moment μ are added, allowing transitions for $\Delta v = \pm 2, \pm 3 \ldots$

1—6.4 THE BOLTZMANN EQUATION

In general the transition occurs from the fundamental vibrational state, however for low energy vibrational states other initial vibrational states may be populated at room temperature. The distribution of particles among energy levels depends on Boltzmann distribution at a given temperature T:

$$\frac{n_e}{n_0} = e^{-\left(\frac{E_e - E_0}{kT}\right)} \qquad (1.6.20)$$

where n_e and n_0 are the number of particles in the excited state and the initial state, E_e and E_0 are their respective energies (with $E_e > E_0$) and $k = 1.38 \cdot 10^{-23}$ J/K is the Boltzmann constant.

From Eq. 1.6.20, it is evident that when $E_e - E_0 >> kT$, the number of particle in the excited state is negligible with respect to the fundamental state. Conversely when $E_e - E_0 << kT$, the number of particles in the excited state is equal to the fundamental one. We can then affirm that at low temperature only the lowest states are

significantly populated, while at high temperature high energy states can be significantly populated, see Figure 1.6.3. At room temperature, transitions between v=0 to v=1 are often observed because the ground state is more populated.

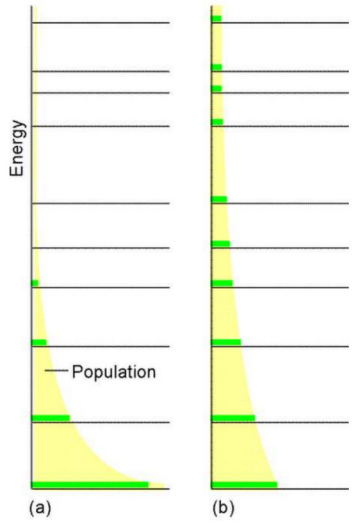

Figure 1.6.3 – Population of energy states according to the Boltzmann equation. (a) At low temperature only the lowest states are significantly populated. (b) At high temperature high energy states are significantly populated too.
Figure from http://staff.um.edu.mt/jgri1/teaching/che2372/notes/06_ST/01/intro_stat_thermo.html)

1—6.5 ROTATIONAL TRANSITIONS

The Schrödinger equation for **rotational motions** is:

$$\hat{H}_{rot}\varphi_{rot}(\vec{R}) = E_{rot}(\vec{R})\varphi_{rot}(\vec{R}) \tag{1.6.21}$$

To solve Eq. (1.6.21) and find the rotational energy levels, E_{rot}, we can approximate a diatomic molecule to a rigid rotor. The potential energy of the system is zero so the Hamiltonian operator is given by the kinetic energy only:

$$\hat{H}_{rot} = \frac{\hat{P}^2}{2I} \tag{1.6.22}$$

$\hat{P}$ is the angular moment operator and I is the momentum of inertia.

The resulting rotational energy is:

$$E_{rot} = \frac{p^2}{2I} = \frac{h^2}{8\pi^2 I} \cdot J(J+1) = B \cdot J(J+1) \tag{1.6.23}$$

where p is the angular moment quantized by J, and $B = \frac{h^2}{8\pi^2 I}$ is the rotational constant.

A better description of the rotational energy levels is obtained by adding a centrifugal distortion term which takes account the bond stretching as the molecule rotates. So the rotational energy is given by:

$$E_{rot} = B \cdot J(J+1) - D \cdot J^2(J+1)^2 \qquad (1.6.24)$$

where D is the centrifugal distortion constant and is several orders of magnitude smaller than B.

Rotational energy levels are separated by ~10^{-4}-10^{-3} eV and a transition from a state to another one involves absorption or emission of the electromagnetic radiation in the microwave and **far infrared** range. Notably, for symmetric rotators the transition is allowed only when ΔJ=+1, while asymmetric rotators allows transitions when ΔJ=0,±1.

Typically in a molecule $\Delta E_{el} \gg \Delta E_{vib} \gg \Delta E_{rot}$, as illustrated in Figure 1.6.4.

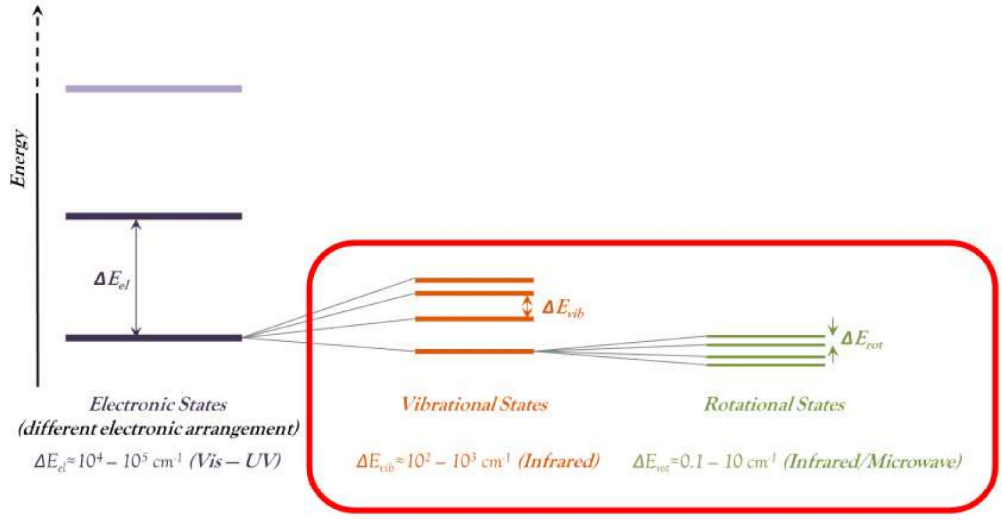

Figure 1.6.4 – Molecular energies. Typical gap energies of electronic, vibrational and rotational states.

Ignoring electronic excitations, the total energy involved in transitions induced by infrared absorption between molecular states results from rovibrational motions and is quantified by the sum of the vibrational and rotational energy:

$$E(n,J) = \left(n+\frac{1}{2}\right)h\nu - \left(n+\frac{1}{2}\right)^2 x_{an}h\nu + B\cdot J(J+1) - D\cdot J^2(J+1)^2. \quad (1.6.25)$$

1—6.6 BEYOND THE DIATOMIC MOLECULE MODEL

Beyond the simple example of diatomic molecules, this theory is still valid but it becomes more complex. Polyatomic molecules undergo vibrations that can be summed or resolved into **normal modes** of vibration.

A non-linear molecule with *N* atoms has *3N* degrees of freedom describing the movement of each atom in the *x*, *y*, and *z* directions. These movements can generate:

- 3 translations of the whole molecule (along x, y, and z);
- 3 rotations (about x, y, and z);
- 3N-6 vibrations (remaining degrees of freedom without 3 translations and 3 rotations already taken into account).

To visualize the kind of vibrations occurring in a polyatomic molecule, we can look at the water molecule, H_2O. It has three atoms so it can vibrate in *3* different ways (the number of vibration is given by 3N-6, since N=3 we obtain $3\cdot3-6=3$) which are depicted in Figure 1.6.5.

Two vibration modes are generated when the two hydrogen-oxygen bonds are

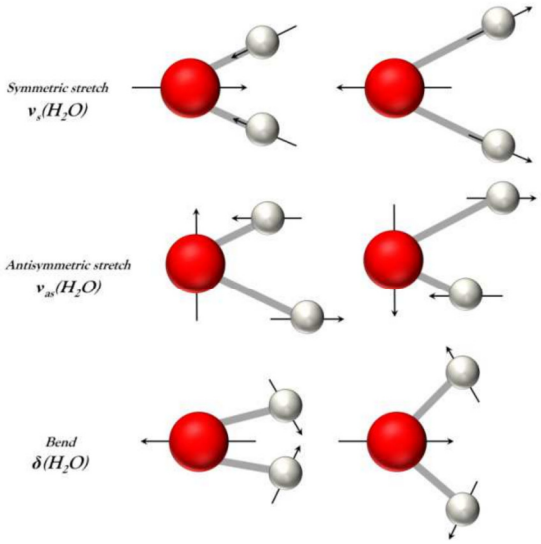

Figure 1.6.5 – Vibrational modes of a water molecule. Movement of oxygen (red) and hydrogen (white) atoms generating symmetric and antisymmetric stretching as well as bending motions.

stretched or compressed: the **symmetric stretching**, ν_1 **or** $\nu_s(H_2O)$, is observed when the two hydrogens move away and towards the oxygen atom at the same time, the **antisymmetric stretching**, ν_3 **or** $\nu_{as}(H_2O)$, corresponds to simultaneous opposite stretching for the two hydrogen atoms. The third vibrational mode, called bending, ν_2 **or** $\delta(H_2O)$, is described as the motion of the two hydrogen atoms which get alternately closer and further apart from each other, changing the angle formed by the three atoms.

As described in Section 1—1.3, hydrogen bonds are established when a water molecule is bond to others. This prevents water molecules to undergo rotations and translations along x, y, and z. The frustrated rotations result in small amplitude oscillations that generate three additional vibrational modes represented in Figure 1.6.6: the **rocking mode**, $r(H_2O)$, arises from the oscillation about *z* axis, the hydrogen atoms go back and forth like a pendulum by keeping the same distance between each other; the **wagging mode**, $\omega(H_2O)$, arises from the oscillation about *x* axis, the two hydrogen atoms move together above and below the plane of the molecule; the **twisting mode**, $\tau(H_2O)$, arises from the oscillation about y axis, the two hydrogen atoms move in a opposite way above and below the plane of the molecule. This latter mode is however infrared inactive since it does not imply a change in the dipole moment.

The oscillation resulting from a frustrated translation can be seen as a stretching

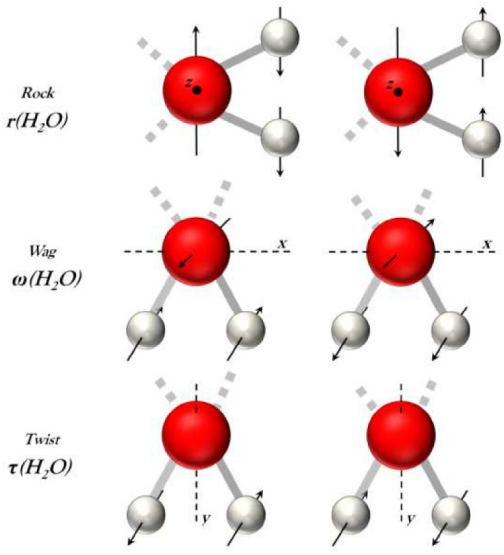

Figure 1.6.6 – Additional vibrational modes in H-bonded water molecules. Oscillations about axis z, x and y giving rocking, wagging and twisting modes respectively.

vibration between molecules (inter-molecular stretching).

It is important to note that each normal mode has its own potential energy and force constant so its own set of energy levels that lie in the far and mid infrared range.

CHAPTER 2

THE EXPERIMENTAL SETUP

The first part of this Chapter is dedicated to the description of the synchrotron radiation and its production in synchrotron facilities. Special focus is then devoted to the synchrotron SOLEIL.

The main elements of AILES, the beamline exploited to the far and mid infrared radiation at SOLEIL, are presented in the second part of the Chapter.

Finally, various setups developed for studying water in different environments are described in an article reported here. The hydration cell, allowing adsorption and desorption measurements *in situ*, is presented in particular.

2—1 SYNCHROTRON RADIATION

Synchrotron spectroscopy plays a key role in fundamental research and technological applications. It is exploited to investigate the structure and the physical and chemical properties of materials deepening the knowledge on physical, chemical, geological and biological sciences.

In this Section, we present the basic principles and the conditions for the production of synchrotron radiation. Characteristics and specificities of synchrotron SOLEIL are reported in more detail.

2—1.1 BASIC PRINCIPLES

Many celestial bodies in the cosmic universe emit synchrotron radiation. However, it has only been one century since researchers were able to reproduce this kind of radiation in electrons accelerator laboratories. The first direct observation of the visible synchrotron radiation (Figure 2.1.1) occurred at the General Electric 70-MeV electron synchrotron in Schenectady, New York, on April 24, 1947 [102].

The concept of **a charged particle emitting energy upon acceleration** has been predicted earlier by Joseph Larmor in 1897 [103]. Following his theory, the total

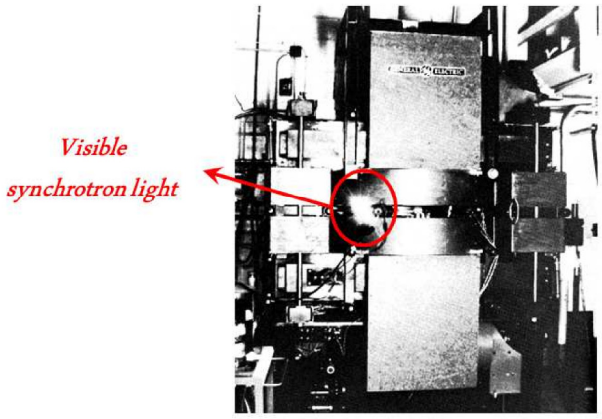

Figure 2.1.1 – First picture of the visible synchrotron light. Observation of the visible sunchrotron radiation at the General electric 70 MeV synchrotron in 1947.

power radiated by an accelerated charged particle is dependent from the electrical charge, q, the acceleration, a, and the speed of light, c:

$$P \propto \frac{q^2 \cdot a^2}{c^3} \tag{2.1.1}$$

At non-relativistic velocity ($v<<c$), when a charged particle decelerates, for instance through passing in a metal cable, it emits an electromagnetic radiation isotropically distributed. This phenomenon is exploited in radio and TV antennae where charges move up and down periodically in the metal at a specific frequency, thus generating the signal.

Larmor's theory was extended to the case of a relativistic particle ($v\sim c$) undergoing centripetal acceleration in a circular trajectory by Alfred-Marie Liénard in 1898 [104]. A charged particle going through a magnetic field experiences a centripetal acceleration forcing the trajectory to curve. As illustrated in Figure 2.1.2, at velocity $v<<c$, the charged particle emits an isotropic electromagnetic radiation, for $v\sim c$ the relativistic charged particle emits the whole radiation along a plate cone with an opening angle of

$$\frac{1}{\gamma} = \frac{m_0 c^2}{E} = \sqrt{1 - \left(\frac{v}{c}\right)^2} \tag{2.1.2}$$

where m_0 and E are the mass and the energy of the particle, respectively.

The energy loss, ΔE, in one tour along the circular trajectory is given by the

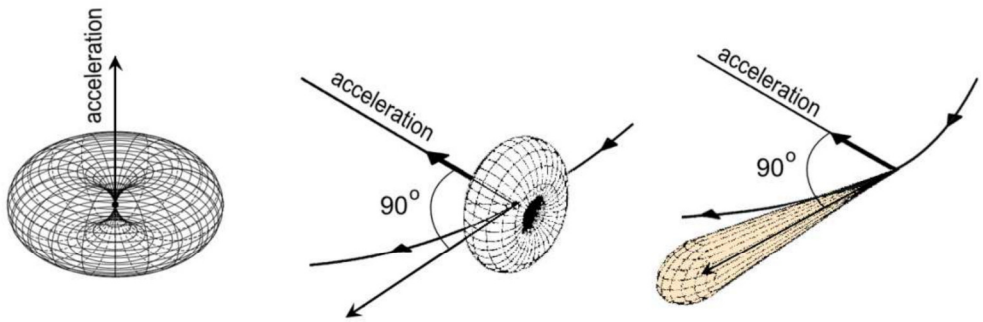

Figure 2.1.2 – Radiation emitted by a charged particle. On the left, non-relativistic electron like radio and TV antenna; in the middle, non –relativistic electron undergoing centripetal acceleration; on the right, relativistic electron undergoing centripetal acceleration.

formula:

$$\Delta E = \frac{4\pi}{3} \cdot \frac{e^2}{R} \gamma^4 \propto \frac{E^4}{{m_0}^4 R} \tag{2.1.3}$$

where R is the curvature angle of the circular trajectory. According to Eq. 2.1.3, ΔE is inversely proportional to the fourth power of the mass particle. Indeed, small particles with small m_0 , like electrons, will emit collimate beam with order of magnitude more power than a heavier mass. This is why the synchrotron facilities are injected with electrons.

Synchrotron radiation was considered a hindrance in the early history of electron accelerators since it causes a significant particle energy loss. Researchers began to investigate on this phenomenon and, eventually, they understood the great potential of synchrotron radiation as a source for spectroscopy. At first, parasites synchrotron radiation studies were carried out at machines built to supply electrons for particle physics studies. Therefore the First-Generation Synchrotrons were experimental laboratories built onto existing facilities. Later in the 1970's-80's dedicated synchrotron facilities were specially constructed to face the great scientific community interest in synchrotron radiation sources. Bending magnets were placed along the storage ring, the cavity in which electrons are spun, in order to force the electron beam to turn by applying a magnetic field. In these new facilities, called Second-Generation Synchrotrons, electrons had higher energies and could produce radiation in a wider range: electrons with energies of the order of hundreds MeV or a few GeV were used to produce radiation in the ultraviolet or X-rays, respectively. From then, synchrotron radiation has become a premier research tool for the study of matter, and synchrotron facilities around the world constantly evolve to provide more powerful and adapted radiation. In the 1990's a further update led to Third-Generation Synchrotrons, which represent the current synchrotron light sources. In the straight sections of the storage ring, specific insertion devices were inserted in order to enhance the emission of specific harmonic modes. The **brightness**, defined as the photon flux per unit area and per unit solid angle at the source, was shown to be significantly higher. The insertion devices, undulators and wigglers, consist of periodic arrangements of alternate dipole magnets generating an alternating static magnetic field which deflects the electron beam sinusoidally. Electrons undergoing such oscillations emit intense

radiation. Along the storage ring, quadrupole and sextupole magnets are used for beam focusing.

A map of synchrotron facilities worldwide is shown in Figure 2.1.3.

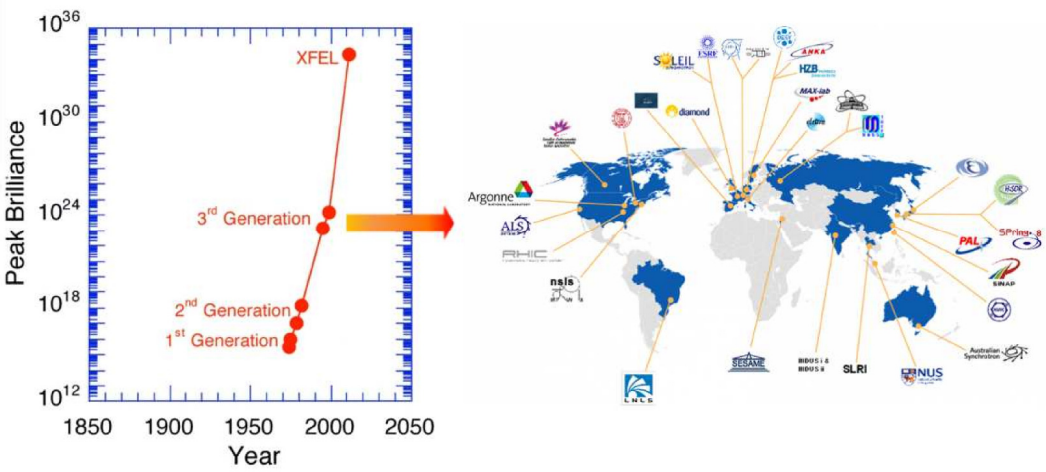

Figure 2.1.3 –Third-generation synchrotron facilities worldwide. Map of synchrotron facilities and comparison between different generations light sources.

Today, laboratories look toward to the Forth-Generation Synchrotron which will be based on the free electron laser (FEL) sources. Its peak brightness in the X-rays range is expected to be many orders of magnitude higher than third-generation synchrotron source.

2—1.2 A THIRD-GENERATION SYNCHROTRON FACILITY: SOLEIL

SOLEIL, the French synchrotron facility, is a third-generation synchrotron radiation source. It is constituted by three particle accelerators (Figure 2.1.4): the linear accelerator (*LINAC*) accelerates the electrons produced by an *electron gun* to 110 MeV and regroups them in bunches. Electrons are then injected into the *Booster,* a circular accelerator of 157 m perimeter, where the energy of the electrons is raised up to 2.75GeV (the nominal energy of synchrotron SOLEIL). The electrons are finally injected into the circular *storage ring* that has a perimeter of 354 m. The relativistic electrons ($v \sim c$) are guided through bending magnets and insertion devices to produce synchrotron radiation in a wide energy range extending **from the infrared to the X-rays**. The photons are exploited in experimental laboratories, called *beamlines,* built around the storage ring.

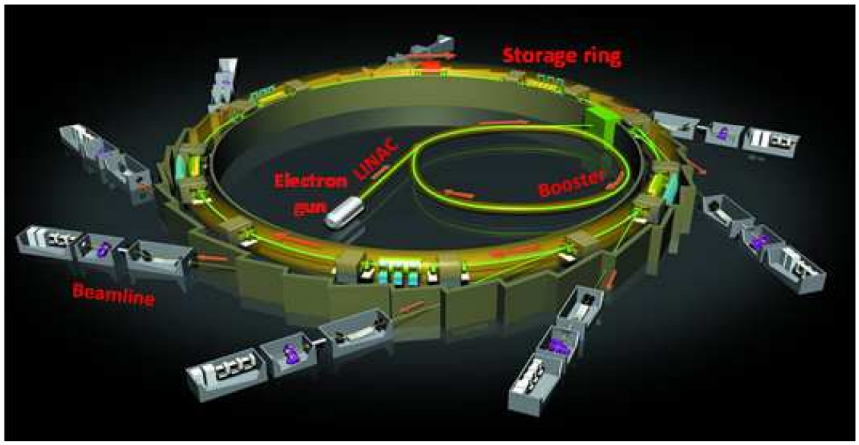

Figure 2.1.4 –Schematic representation of synchrotron SOLEIL. The electron gun produces electrons which are accelerated and packed in the LINAC and the Booster. When electrons reach the energy of 2.75 GeV, they are injected in the storage ring and the produced synchrotron radiation is exploited at the beamlines.

The energy lost by electrons during each revolution is gained back when electrons pass through two radiofrequency cavities where electron bunches are accelerated by an electric field. Nevertheless, the beam has a limited lifetime determined by the scattering with residual gaseous molecules in the storage ring and by intra-bunch electron-electron scattering. To reduce the loss of electrons due to the scattering with residual particles, the storage ring is pumped down to ultra-high vacuum of the order of 10^{-10} mbar. With these expedients, the beam lifetime reaches around twelve hours. The storage ring, however, is opportunely refilled with electrons via the booster so that the electron current in the ring remains approximately constant during the six days of continuous exploitation. Usually one day per week is dedicated to the maintenance and optimization of the accelerators.

Five function modes of the storage ring are available as schematized in table 2.1.

Table 2.1 – Filling functional modes at SOLEIL.

Function mode	Total Current	Periodicity
Multibunch (416 bunches)	500 mA	35 weeks/year
Hybrid (313 bunches)	450 mA	
8 bunches	100 mA	2 weeks/year
1 bunch	15 mA	1 weeks/year
Low α (Hybrid)	16 mA	1 weeks/year

The multibunch mode is characterized by 416 equally spaced electron bunches along the storage ring. Most of the time, however, electrons are injected in the hybrid mode where three quarter of the ring are filled with 312 equally spaced bunches and a single bunch occupies the remaining quarter. In the 8 bunches and 1 bunch functional modes, the storage ring is filled with 8 bunches and a single bunch, respectively. In the low α mode, the 316 bunches provides high flux in the Terahertz region with small sized bunches emitting coherent synchrotron radiation. During each mode, refilling of electron bunches (Top-Up) are provided.

The infrared spectra presented in this manuscript were acquired in the multibunch hybrid mode.

2—2. AILES: ADVANCED INFRARED LINE EXPLOITED FOR SPECTROSCOPY

Synchrotron radiation produced at SOLEIL is a white spectrum extending from the X-rays to the far IR.

Adapted optics and modification of the dipolar chamber allows the **AILES** beamline (Advanced Infrared Line Exploited for Spectroscopy) to cover the spectral range **from the far to the near infrared** (5-10000 cm^{-1}). The photon source of the beamline is constituted by the passage of the electrons bunches through a bending magnet, producing a magnetic field of 1.73 T [105].

In this Section, we present the main elements of the AILES beamline. In particular, we describe the spectroscopic station based on the Michelson interferometer. Acquisition configurations used for measurements in the different infrared ranges are described.

2—2.1 INFRARED SOURCES

Two mechanisms produce radiation in the infrared ranges (Figure 2.2.1). Part of the radiation comes from the relativistic electrons deviated by the constant

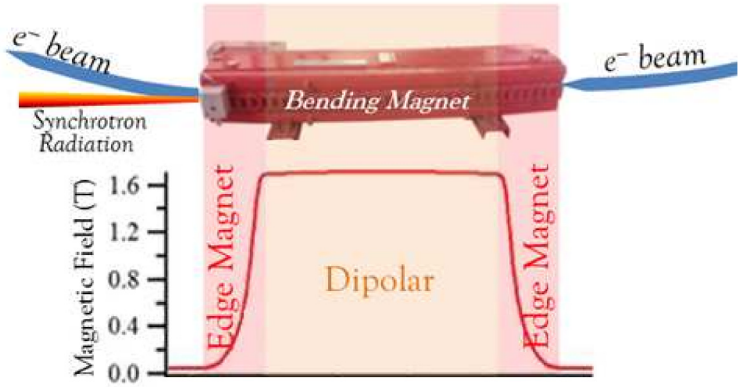

Figure 2.2.1 – Infrared radiation sources in synchrotron facilities. The dipolar source arises from deviated relativistic electrons, while the edge magnet source originates from intermediate no-field/field zones.

magnetic field in the dipolar device. We refer to this kind of radiation as the **dipolar source**. The rest is emitted when electrons go through intermediate zones between no field regions and the maximum field region of the dipole. The emitted radiation is then called the **edge magnet source**.

Figure 2.2.2 shows the spatial distribution of photons along the horizontal direction (the electrons orbital plane) and the vertical direction (out of the electron orbit plane). The distribution of photons was simulated using SRW (Synchrotron radiation Workshop), a software developed with the Igor Pro software. To estimate the radiation collected on the AILES beamline, we consider the extraction on a mirror of 26 mm × 103 mm placed at 1.27 m from the edge of magnet, corresponding to the position of the extraction optics (see Section 2—2.2). The spatial distribution of the incident photons are represented for three photon frequencies in the main working-energy ranges: the simulation at 1000, 100 and 10 cm^{-1} are representative of the photon distribution in the mid infrared (MIR), the far infrared (FIR) and the terahertz region (THz), respectively.

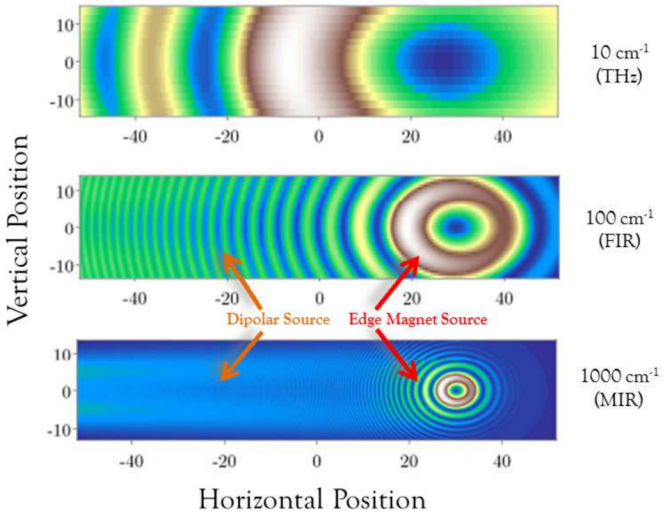

Figure 2.2.2 – Spatial distribution of photons. From top to bottom, photons distributions in terahertz (THz), far (FIR) and mid (MIR) infrared, collected on a mirror of 26 mm × 103 mm placed at 1.27 m from the edge of magnet.

The edge magnet source presents an almost cylindrical symmetry and its angle RMS goes from 6 mrad, in the MIR, to 35 mrad, in the THz. Wider angles are calculated for the dipolar source going from 12 to 45 mrad. Moreover, the emission of the dipolar source can be considered constant in the horizontal plane.

This calculated distribution shows that the long wavelengths require a large extraction angular opening which was granted by an enlarged dipole chamber. This expedient allows the extraction of 20 mrad in the vertical and 78 mrad in the horizontal direction, instead of 8.9 and 33 mrad as in standard dipole chambers.
The photons flux between 2 μm (5000 cm^{-1}) and 1000 μm (10 cm^{-1}) collected at the extraction optics was calculated for AILES and other infrared beamlines in operation. Results are shown in Figure 2.2.3.

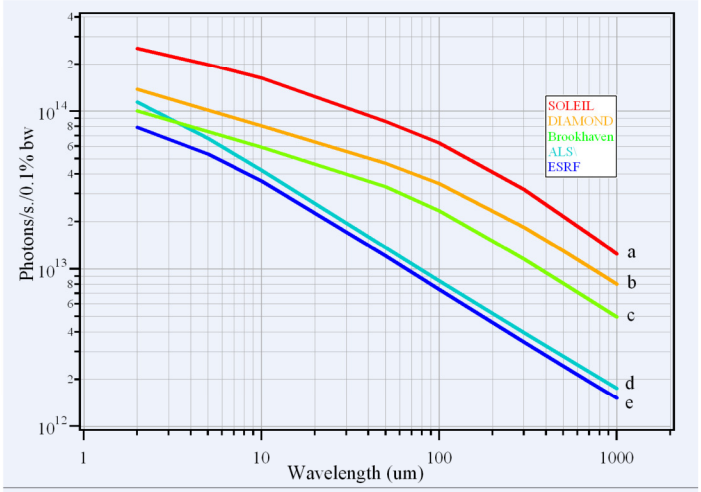

Figure 2.2.3 – Photons flux collected at the extraction optics. A comparison between several infrared beamlines in operation.

Notice that the internal sources equipping the interferometer were also exploited for some of the measurements presented here. In particular, the **internal Globar source** has been used to perform measurements in the mid infrared when the synchrotron source was not available. The Globar, whose name is actually a blend word formed from the words *Glowing* and *Bar,* is a silicon carbide rod electrically heated at 1200K. It emits mid-infrared radiation in the range 300-4500 cm^{-1}. Even though its brightness is several orders of magnitude lower than that of the synchrotron radiation [106], good quality spectra in the mid infrared were obtained for almost all the samples studied during this thesis work.

2—2.2 OPTICS

As illustrated in Figure 2.2.4, an optical system constituted by eleven mirrors is used to convey the synchrotron beam to a Bruker IFS 125 Fourier Transform (FT)-IR spectrometer (SPECTRO 1). Three additional mirrors are needed to transfer the

beam to a second spectrometer employed to perform measurements at high resolution (SPECTRO 2), mainly devoted to gaseous samples. The second spectrometer won't be described further since it was not used to acquire the data presented in this manuscript.

Two mirrors, M1 and M2, are placed in the storage ring wall in order to direct the infrared beam toward the beamline. Higher energy photons are let pass thanks to a slit in the first mirror to prevent damage on the optics as, without the slit, the power incident on the extraction mirror would reach 8000 W. The toroidal mirror M2 focuses the beam within the radiation protected walls where a removable screen and a camera allow to verify that the beam position is adequate. Two plane mirrors M3 and M4 brings the beam at a height compatible with its passage out of the hutch, a radiation shielding made of thick walls of lead and polyethylene. The beam is then intercepted by a toroidal mirror, M5, which redirects it to the toroidal mirror M6. This latter allows a strong focusing between M6 and M7. At this focus point, the reduced size of the image allows the insertion of a natural diamond window, which obviously has limited dimensions (10 mm diameter, 200 µm thick). The natural diamond assures the mechanical resistance needed to isolate the ultra-high vacuum of the ring from the secondary vacuum of the spectrometers and allows the transmission of the beam in the whole infrared and visible ranges. Compared to those produced by Chemical Vapor Deposition (CVD), natural diamonds have the advantages of being more transparent in the complete infrared

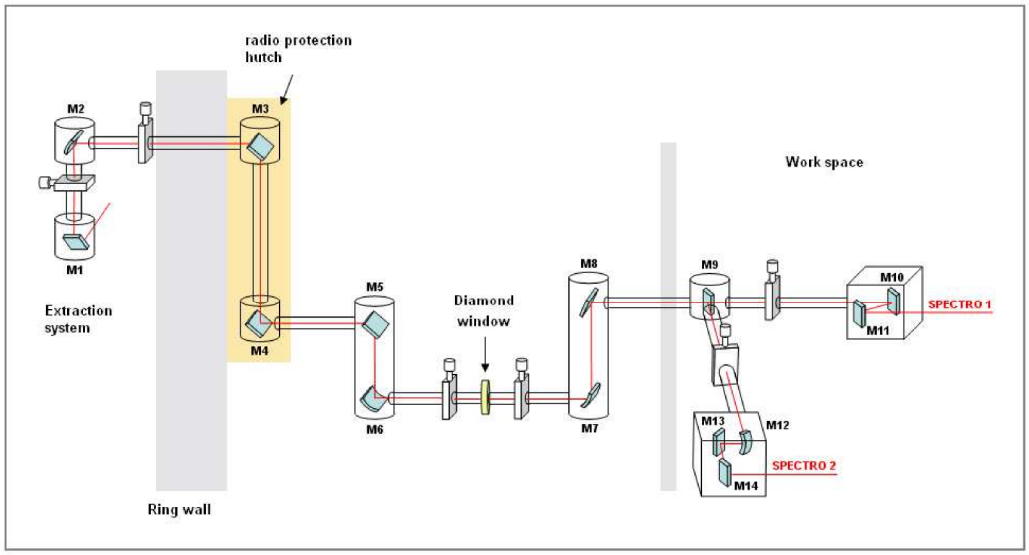

Figure 2.2.4 – Optical system of the AILES beamline. The infrared beam is conveyed from the storage ring to the spectrometer by flats and toroidal mirrors.

range while minimizing phonons structures absorption and degradation of the beam optical quality caused by the scattering of photons. After its passage through the diamond window, the beam is back to is almost parallel configuration and is collected again by two flat mirrors M8 and M9. During this last step, the beam reaches the working height. Notice that a last chamber contains three mirrors allowing for the beam to be optically compatible with the interferometer (focusing at the entrance iris of the interferometer).

2—2.3 THE BRUKER IFS 125 MR SPECTROMETER

A schematic top view of the Bruker IFS 125 MR spectrometer allowing an ultimate resolution of 0.01 cm^{-1} is shown in Figure 2.2.5. It is dedicated to condensed matter studies.

The spectrometer is connected to the beamline to receive the infrared synchrotron radiation but it is also possible to operate with up to three internal sources for far,

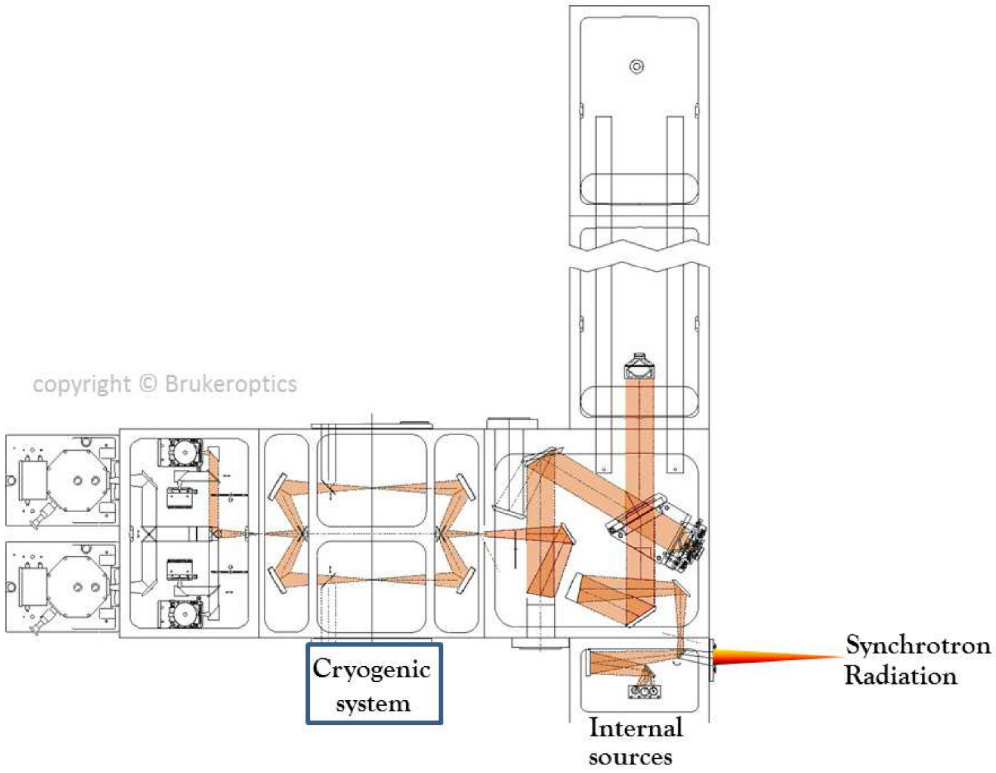

Figure 2.2.5 – Schematic top view of the Bruker IFS 125 MR spectrometer. Synchrotron radiation or internal sources beam are conveyed to the sample and directed to desired detector by a system of mirrors. Two additional mirrors may be placed to convey the beam on a connected chamber for cryogenic measurements.

mid and near infrared. It is based on a Michelson interferometer (see Section 2—2.4) that modulates frequencies and is adapted for allowing measurements over a broad range of frequencies.

In order to reduce absorption due to residual gases, the spectrometer is evacuated using two sets of mechanical and turbo-molecular pumps.

A cryogenic system allows infrared measurements from T=4 K to T=353 K. This helium closed cycle cryostat is placed in a specific chamber, connected to the back compartment of the spectrometer (Figure 2.2.5). The system, represented in Figure 2.2.6, includes a pulse tube cryogenerator provided by Cryomech (PT 405) and its closed loops of helium cools samples down at ~4 K in 1h30. One toroidal mirror focus the beam over the sample and one convey it back to its initial optical configuration. A turbomolecular pump is placed directly under the chamber allowing an efficient evacuation of residual gases around the system.

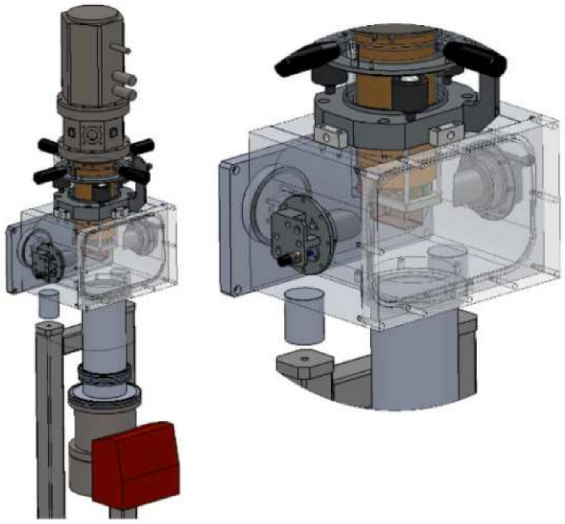

Figure 2.2.6 – Schematic view of the low vibration cryostat. Left: the cryogenic system in the sample chamber (represented as transparent)with the turbomolecular pump. Right: closer view on the sample chamber.

The beam transmitted through the sample is then conveyed to a detector. Up to three detectors can be placed simultaneously on the spectrometer allowing to cover a range from the THz to the NIR: the internal MCT and two external bolometers (described in Section 2—2.5). The combined movement of mirrors redirects the beam toward the selected detector.

Measurements at room temperature are carried out when the vacuum is lower than $1 \cdot 10^{-3}$ mbar. Measurements including cycles in temperature are only performed when the vacuum is under 10^{-5} mbar to prevent condensation on the cold finger of the cryostat or on the window of the cells.

2—2.4 FOURIER TRANSFORM INFRARED SPECTROSCOPY

Fourier Transform (FT)-IR spectrometers are based on a Michelson interferometer which allows to scan all the wavelengths of a polychromatic source simultaneously.

For this purpose, as schematically illustrated in Figure 2.2.7, the photon beam entering in the interferometer is split into two perpendicular beams by a semitransparent mirror, called *beam splitter*. The beam splitter is positioned at a ~45° angle of incidence and, ideally, 50% of the incident light is transmitted while 50% is reflected. The two beams travel separate paths, x_1 and x_2: one beam is transmitted through the beam splitter to a translating mirror while the other beam is reflected at ~90° of its original direction and is conveyed to a fixed mirror. The transmitted beam is then reflected on the beam splitter while the initially reflected beam is then transmitted through the beam splitter. This way both half beams are going through one reflection and one transmission before being recombined in the sample compartment. The optical path difference (OPD) when the beams are recombined is:

$$\delta = 2 \cdot (x_2 - x_1) \qquad (2.2.1)$$

As the path difference is scanned between 0 and a maximum value, the beams interfere successively constructively and destructively.
For photons of wavelength λ_0 and wavenumber $\bar{\nu}_0$, constructive interferences occur when the OPD of the beams is an integral multiple of the wavelength:

$$\delta = n\lambda_0, \quad \text{with n=0,1,2...} \qquad (2.2.2)$$

as the two beams are in phase.

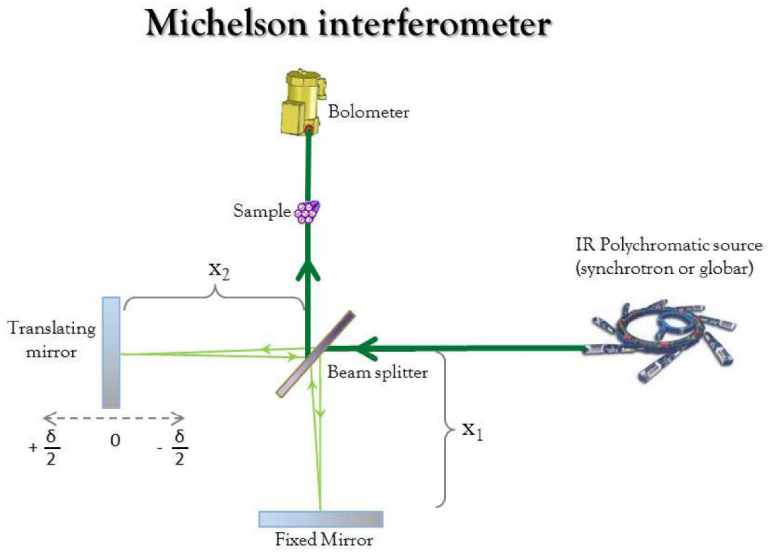

Figure 2.2.7 – Schematic representation of the Michelson interferometer. The infrared source hits the beam splitter that reflects half of the radiation and transmits the other half. The two beams are reflected by a fixed and a translating mirror, respectively, and recombine on the beam splitter after traveling different paths. The beam is then conveyed to the sample and the detector.

On the contrary, destructive interference occurs if the optical paths differ by an odd integral number of half wavelength:

$$\delta = (2n+1)\frac{\lambda_0}{2}, \quad \text{with n=0,1,2...} \tag{2.2.3}$$

In this case, the recombined beams have opposite phases, resulting in the annihilation of the signal.

The translating mirror moves at constant velocity and the intensity of the recombined beams is a sinusoidal signal oscillating from zero (from the destructive interference) to a maximum (constructive interference).

The modulated signal intensity, due to the superposition of the half beams, as a function of the optical path difference, δ, is called **interferogram** $V(\delta)$ (see Figure 2.2.8). For the monochromatic source of wavenumber $\bar{\nu}_0$, the interferogram is:

$$V(\delta) = a(\bar{\nu}_0) \cdot I(\bar{\nu}_0) \cdot [\cos(2\pi\bar{\nu}_0\delta)] \tag{2.2.4}$$

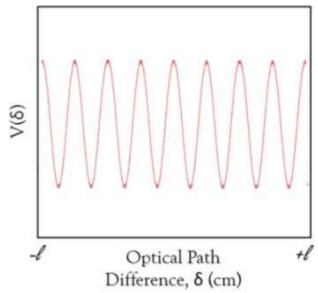

Figure 2.2.8 – Interferogram of a monochromatic source. Interferogram obtained by the modulated signal intensity detected after the beam splitter plotted versus the optical path difference.

where $a(\bar{\nu}_0)$ depends on the transmission and reflection coefficients and $I(\bar{\nu}_0)$ is the **photon intensity** (see Figure 2.2.8)

A **polychromatic source** is usually used in combination to Michelson interferometer. In this case, the interferogram is the sum of all the modulated signals corresponding to each wavelength. Notice that the sum becomes an integral if the source is **continuous**:

$$V(\delta) = \int_{-\infty}^{+\infty} a(\bar{\nu}) \cdot I(\bar{\nu}) \cdot [\cos(2\pi\bar{\nu}\delta)]\, d\bar{\nu} \qquad (2.2.5)$$

As shown in Figure 2.2.9, constructive interference is observed at OPD=0 for all wavelength, giving rise to a large peak centered on $\delta = 0$.

The spectral distribution of a polychromatic source is obtained by Fourier Transform:

$$I(\bar{\nu}) = \frac{1}{a(\bar{\nu})} \int_{-\infty}^{+\infty} V(\delta) \cdot [\cos(2\pi\bar{\nu}\delta)]\, d\delta\,. \qquad (2.2.6)$$

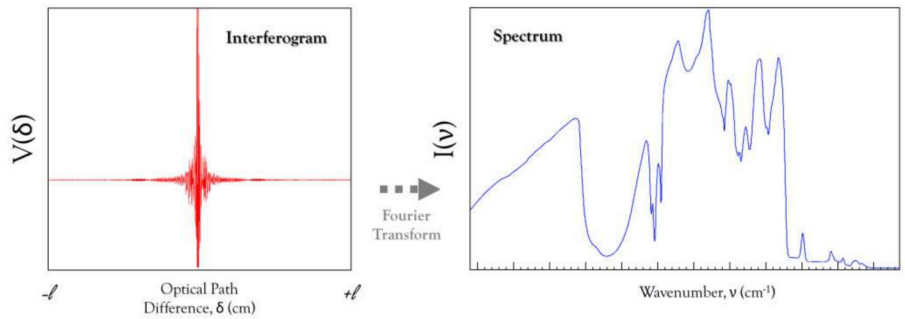

Figure 2.2.9 – Interferogram and spectrum of a polychromatic source. On the left, the interferogram obtained by the modulated signal intensity detected after the beam splitter plotted versus the optical path difference, on the right, the spectrum obtained from the Fourier Transform of the interferogram.

Notice that for real interferometers the OPD is not infinite. In this case, the integral from $-\infty$ to $+\infty$ is then replaced by the sum of points between $\delta = -l$ and $\delta = +l$:

$$I(\bar{\nu}) = \frac{1}{a(\bar{\nu})} \sum_{\delta=-l}^{+l} V(\delta) \cdot \left[\cos(2\pi\bar{\nu}\delta)\right] \tag{2.2.7}$$

After Fourier transform, the spectral distribution is often dominated by the optical elements, namely the beam splitter, the source distribution efficiency, the detector response and all the optical elements transmission. In order to extract the signal coming from the sample itself, one needs to measure a reference, i.e. the light intensity distribution before it interacts with the sample. With such reference (I_0), the transmission (T) or the absorbance (A) can be calculated as:

$$T = \frac{I(v)}{I_0(v)} \tag{2.2.8}$$

$$A = -\log\left[\frac{I(v)}{I_0(v)}\right] \tag{2.2.9}$$

where $I(v)$ and $I_0(v)$ are respectively the sample and the reference spectra, see Figure 2.2.10.

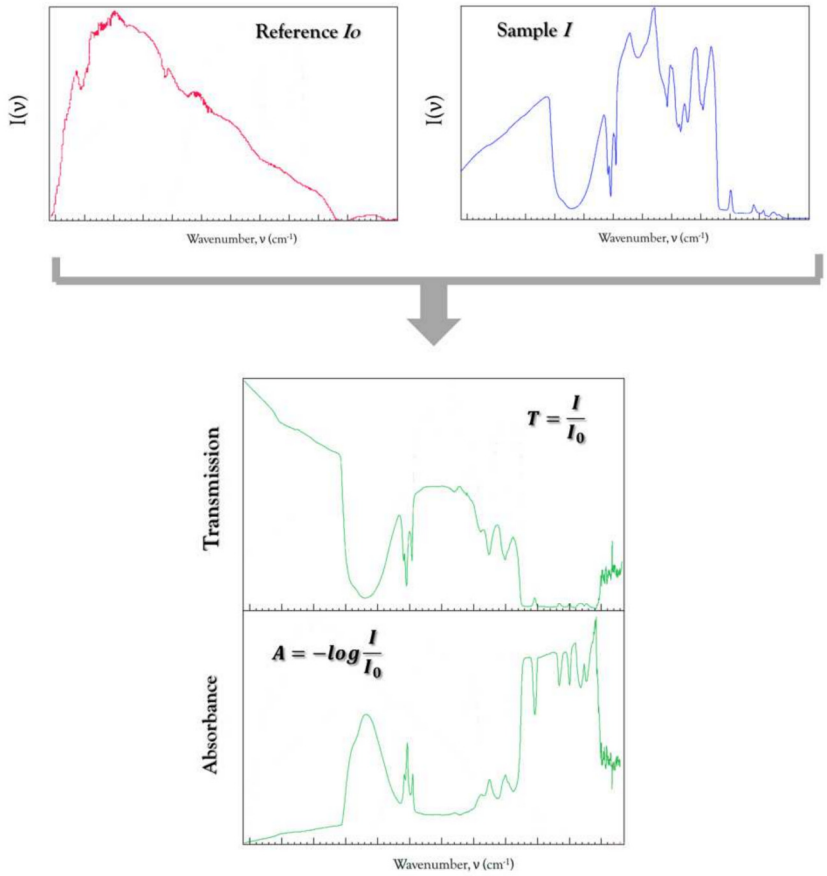

Figure 2.2.10 – Infrared spectra in absorbance and transmission units. Transmission of the sample, I, and a reference, I_0, (on the left) are used to plot infrared spectra in absorbance and transmission units (on the right).

2—2.5 ACQUISITION CONFIGURATIONS

In Section 2—2.4 we have described the Michelson interferometer (Figure 2.2.7) which is constituted by:

- a source,
- a beam splitter,
- a set of two fixed and translating flat mirrors,
- a detector.

Even though the optic conveying the beam from the storage ring to the spectrometer is optimized for the complete infrared range (10-10000 cm^{-1}), the elements of the Michelson interferometer cannot cover this whole range simultaneously. In particular, the beam splitter chemical composition has to grant a splitting of the incident beam (ideally 50% reflected and 50% transmitted) which can only be obtained in a limited range. Therefore, a set of two or three beam splitter are necessary to cover the complete range. The same holds for infrared detectors which differ in sensibility, spectral range, and frequency response. Then, in order to optimize the signal/noise ratio, it is important to use the most appropriate set of beam splitter and detector. Contrariwise, the mirrors are suitable to reflect the incident photons in the whole range. Concerning the source, the synchrotron provides infrared radiation in the whole range but, when synchrotron radiation is not available, the Globar internal source has been used for measurements in the mid and near infrared. The data presented in this manuscript have been acquired in three infrared ranges: the terahertz, the far infrared and the mid infrared. Table 2.2.1 reports the different configurations used for the experiments in these ranges. Synchrotron and Globar sources have been described in Section 2—2.1. The third source is the tungsten lamp, which emits in the near infrared and visible, but it was mainly used as visible source to align the optics inside the spectrometer. In the following, the beam splitters and detectors used for the here presented measurements are described.

The 6 μm Mylar **beam splitter** is a composite of polyethylene terephthalate (Mylar) film of 6 μm, having low far-infrared absorption, and a thin substantially uniformly thick coating of silicon. It operates efficiently in the 20—1000 cm^{-1} range. In the THz range, the 125 μm thickness beam splitter is used to efficiently

Table 2.2.1 – Acquisition configurations in different infrared ranges.

IR range (cm^{-1})		Source	Beam splitter	Detector
THz	20 — 60	Synchrotron	6 μm Mylar	1.6 K Bolometer
FIR	50 — 600	Synchrotron	6 μm Mylar	4.2 K Bolometer
FIR/MIR	200 — 4000	Synchrotron	Ge/KBr	Wide range 4.2 K Bolometer
FIR/MIR	200 — 4000	Globar	Ge/KBr	Wide range 4.2 K Bolometer
MIR	500 — 4000	Synchrotron	Ge/KBr	MCT
MIR	500 — 4000	Globar	Ge/KBr	MCT

split the beam. A potassium bromide (KBr) beam splitter with germanium coating is used in the mid infrared range (400 —4000 cm^{-1}).

Notice that a laser helium-neon at 15798 cm^{-1}, allows a fine control of the translating mirror position from interference fringes detection. For this purpose, a dedicated part of the beam splitters acts as a visible beam splitter and allows transmission of the laser monochromatic light.

Regarding the **detectors**, two different types were exploited (Figure 2.2.11).

Bolometers sensitive to thermal changes are used to measure incident radiation in the microwaves and far IR (2—1000 cm^{-1}). The detector element is an extremely sensitive thermistor. The thermistor is composed of boron-doped silicon and it is placed at the end of a radiation collecting cone assembly. This absorber of heat capacity is thermally connected to a heat reservoir by a resistance. Any thermal radiation that impinges upon the detector causes a temperature change which, in turn, causes a change in resistance. This is then amplified and measured as a voltage difference, as a regulated current is applied to the detector element. The detector is placed under vacuum equipped with a vacuum-sealed wedged window allowing the passage of photon beams. The incident radiation being modulated by the Fourier Transform interferometer, the measurements of AC signal only, allows to minimize contribution from the thermal radiation. In order to limit contribution from the thermal background, the detector is cooled down at liquid helium temperature (4.2 K) for far IR measurements or at pumped liquid helium temperature (1.6K) for THz range where more sensitivity is needed. A wide range

detector, cooled down at 4.2 K, allowed measurements in a wide infrared region,

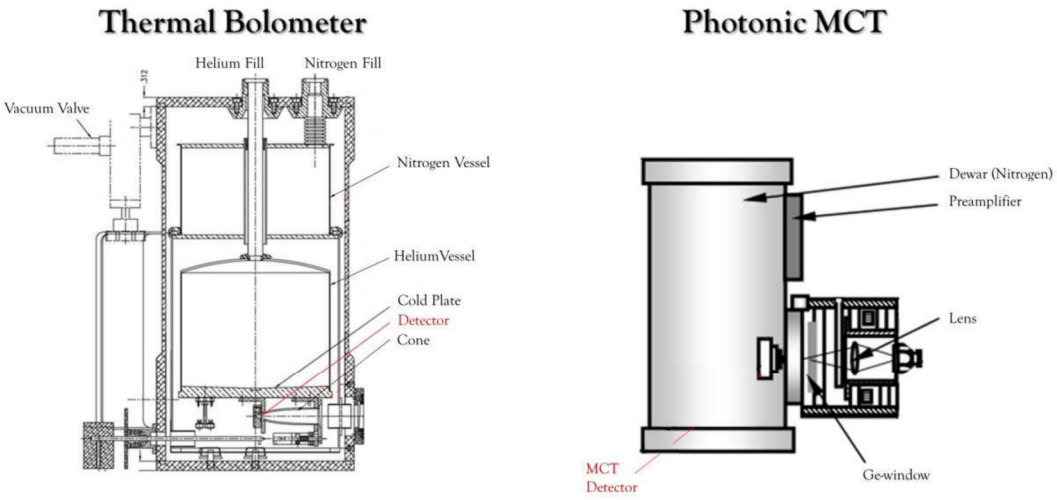

Figure 2.2.11 – Infrared detectors. On the left, the bolometer measuring incident radiation in the range 2-1000 cm^{-1}. On the right, the MCT measuring incident radiation in the range 500-5000 cm^{-1}.

from 200 cm^{-1} to 4000 cm^{-1}). After filling with liquid helium, bolometers are able to efficiently detect the incident infrared radiation during at least eighteen hours.

The other type of detector is the liquid nitrogen cooled mercury-cadmium-tellurium MCT photodetector. It is a ternary semiconductor compound which allows electronic transitions induced by the incident radiation. Photons with energy greater than the semiconductor band-gap excite electrons into the conduction band, thereby increasing the conductivity of the material. Changes in conductivity are directly related to the amount of the incident photons. The MCT used in our measurements is efficient in the mid IR between 500 and 5000 cm^{-1}. After filling with liquid nitrogen, MCT detectors are able to efficiently detect the incident infrared radiation during eight hours.

2—3 THE EXPERIMENTAL SET-UP FOR STUDYING NANOCONFINED WATER

Measurements of water trapped in porous Vycor glass, Nafion membrane and single walled carbon nanotubes were performed using a specific hydration cell, designed to be placed in the supplementary sample compartment of the spectrometer described in Section 2—2.3, so that it can be connected to the cryogenic system (Figure 2.3.1). This setup allows *in situ* adsorption and

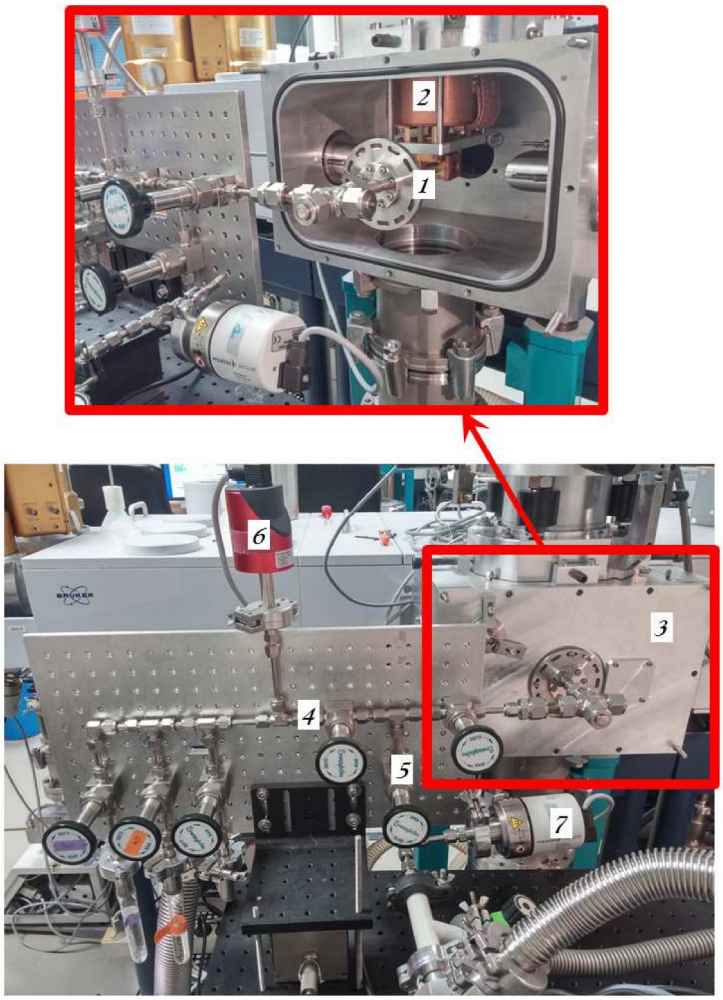

Figure 2.3.1 – Hydration cell set-up installed on Bruker IFS 125 MR spectrometer. The hydration cell (1) connected to the cryostat cold head (2) placed in the sample compartment (3). Pressure in the injection ramp (4) is monitored by a thermostated gauge (6). Pressure in the pumping ramp (5) is monitored by a gauge (7).

desorption of water molecules in nanoporous matrices with a fine control on temperature and water vapor pressure, insuring a precise gas dosage. This ultra-high vacuum cell is equipped with two diamond windows allowing transmission measurements in a wide spectral domain. The high reproducibility of the measurements allows a consistent set of data in the whole infrared range providing a comprehensive molecular picture for rationalizing the complex chemical transformations upon water loading in the matrix, even at very small contents of water.

In the following, we report the performances of the cell through the fir and mid infrared spectra of water adsorbed on pores of a thin Vycor slab (thickness ~80 μm and diameter ~4 mm). Vapor pressure control is monitored through the highly stable infrared spectra of Vycor at equilibrium with a given vapor pressure, from the dry state to 100% of relative humidity (defined in Equation 1.2.1 as $RH=(p/p_0)\cdot 100$, p_0 being the water vapor pressure at experimental condition temperature).

Analyzing the OH stretching band (2550-3450 cm^{-1}) and the connectivity band (50-260 cm^{-1}) of trapped water, we found that the first layer of water molecules interact via strong hydrogen bonds with the hydrophilic surface of the pores. Such strong interaction highly affects water molecules at the interface and weakens their covalent bonds, causing a downshift of the OH stretch frequency. These water molecules poorly interact with each other as a consequence of the high affinity for the wall pores. Only at high level of relative humidity water molecules begin to interact more causing a significant increase of the connectivity band when pores are filled.

New experimental set-ups for studying nanoconfined water on the AILES beamline at Soleil

Dalla Bernardina, S.; Alabarse, F.; Kalinko, A.; Roy, P.; Vita, N.; Hienerwadel, R.; Berthomieu, C.; Judenstein, P.; Zanotti, J. M.; Bantignies, J.L.; Haines, J.; Catafesta, J.; Creff, G.; Manceron, L. and Brubach, J. B. *Vib. Spectrosc*. **75** (2014) 154-161.

ABSTRACT

Three ensembles designed to investigate condensed matter in complex environments have been developed recently on the AILES beamline at Soleil. They have been exploited for studies aiming at understanding the properties of water molecules and their network in various confining systems, namely:

- a hydration and temperature-controlled cell for the study of water confined in nanoporous Vycor,

- a high pressure set-up allowing the study of the evolution of water molecules network trapped in Faujasite through the pressure-induced amorphisation of the matrix material,

- a temperature resolved electrochemical cell used to record FIR difference spectra of metalloproteins interacting with water molecules.

By combining the high infrared flux and collimation of the AILES beamline with these optimized sample environments, it is possible to measure the infrared and THz spectra for minute quantities of samples in precise physical conditions.

2—3.1 INTRODUCTION

The number of synchrotron radiation-based infrared spectroscopy beamlines has increased considerably over the last decade with the advent of dual sources combining edge emission and constant field emission on third generation facilities (ALBA,[1] ALS,[2] ANKA,[3] BESSY II,[4] CLS,[5] DIAMOND,[6]

ELETTRA,[7] LNLS, NSLS II, NSRRC,[8] SESAME,[9] SLS,[10] SLSA,[11] SOLEIL,[12] SPRING 8,[13] etc.). These two emission mechanisms allow for a high flux through the complete infrared range and an extension into the THz domain with a high signal-to-noise ratio. By combining the high infrared flux and collimation of these beamlines with optimized sample environments, it is now possible to measure the infrared and THz spectra for minute quantities of samples in precise physical conditions.

The study of the evolution of the infrared spectra as a function of thermodynamic parameters, such as temperature, time and pressure is a constant requirement for synchrotron radiation (SR) beamlines. It is the aim of this article to give an overview of the possibilities of the AILES facilities and to illustrate them with examples aiming at understanding the properties of water molecules and their network in various confining systems.

2—3.2 EXPERIMENTAL METHODS

A basic introduction to SR-based infrared source will not be reviewed here. The AILES source exploits both the edge emission and a large collection angle of constant field emission.[12] This combination provides significant advantages for measurements requiring either (i) highly focusing optics in the complete infrared range (ii) extension to the THz range (iii) both characteristics. The synchrotron source feeds either one or the other of two spectroscopic stations: a lower resolution interferometer dedicated to the condensed matter studies and a high resolution (0.001 cm^{-1}) interferometer exploited for gas phase experiments.

These interferometers cover the complete infrared range between 4 cm^{-1} and 10,000 cm^{-1} and can be evacuated down to pressure lower than 10^{-5} mbar in order to reduce absorption due to residual gases.[14] Each interferometer is implemented with several beamsplitters (Mylar for far IR, Ge/KBr, TiO_2/Quartz) and detectors (MCT/InSb Sandwich, InSb, 4 K and 1.6 K bolometers).

It is worth noting that a number of studies are based on the high resolution station completed with a rich panel of sample environment.[15] In the following, we will only describe the set-up completing the condensed matter station, namely: (i) a hydration and temperature-controlled cell allowing the study water molecules sorption's in mesoporous systems, (ii) a high pressure set-up

allowing the study of water molecules trapped in Faujasite through the pressure induced amorphisation of the matrix, (iii) an electrochemical cell allowing the studies of metalloproteins and in particular water molecules bound to the active metallic site. An attenuated total reflection set-up is also available and suitable for water studies in various environments and is described in details in a previous study.[16]

2—3.2.1 HYDRATION AND TEMPERATURE-CONTROLLED CELL EXPLOITED FOR THE STUDY OF WATER CONFINED IN NANOPOROUS VYCOR

The properties of confined water in nanoporous materials differ from those of bulk water. Water molecules properties are related to the nature of the nanoscopic environment in which they are confined, hydrophilic or hydrophobic surfaces may generate different changes, but also the system properties can be affected by the amount of absorbed water.

The high sensitivity of infrared spectroscopy for the H_2O vibrational modes can be exploited to study even small amount of water in different environments and under several conditions.

The nature of water in Vycor glass, a hydrophilic porous material, has been investigated by vibrational spectroscopy with a specific setup. Far and mid infrared studies of Vycor during *in situ* absorption and desorption of water molecules were carried out and the connectivity of interfacial water as a monolayer has been investigated.

Vycor glass is a silica-based mesoporous material crossed by a network of cylindrical pores of well-defined diameter.

A thin Vycor slab (thickness ~80 μm, diameter ~4 mm) with pore diameter of about 7 nm is used here.

2—3.2.1.1 TEMPERATURE- AND HYDRATION- CONTROLLED ENSEMBLE

We designed a copper cell allowing: (i) temperature control between 380 K and 40 K; (ii) dosage of the desired amount of adsorbed gas; (iii) pumping down to 10^{-6} mbar for reference measurements free from molecular adsorption. The cell was designed to study the modifications to the infrared spectra following molecular adsorption. The use of a unique cell, in a wide spectral domain, provides complementary information and insures the reproducibility of the adsorption and gas dosage.[17,18]

The cell (Figure 2.3.2) is made in copper in order to allow for good thermal exchange and has a volume of ~1 cm^3 to limit gas absorption at ambient pressure. It is UHV-compatible (leak rate > $1 \cdot 10^{-9}$ mbar·l/s). The cell is connected to a closed-cycle cryostat by a copper braid for cooling and temperature resolved experiments (from 40 K to 380 K). A thermocouple and a resistive heater allow controlling the sample temperature during measurements with a precision of ± 0.1 K. The cell is equipped with two diamond windows (10 mm in diameter, 0.5 mm in thickness at center, 0.5° wedge) allowing to measure the transmission of material from the THz to the mid infrared region with reduced spectral channelling effects. The sample is fixed on a sample holder at precise normal incidence relative to the incident beam. An entry for the gas input/output or the vacuum pump is also present in the body of cell. Gas dosage can be done in static conditions.

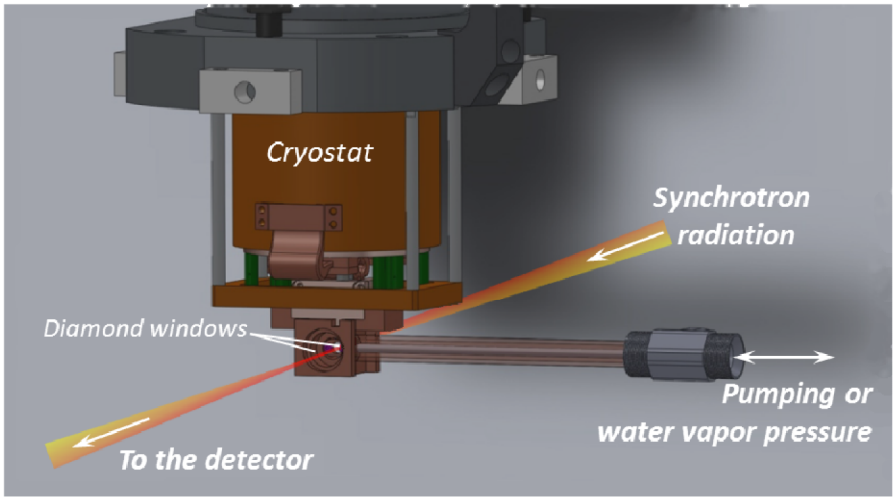

Figure 2.3.2 – Schematic view of the hydration cell designed at AILES beamline. The cell is connected to the cold finger of a closed cycle cryostat and focusing optics allows the modulated beam to pass through the sample in contact with a controlled amount of gas.

In the following, we illustrate the cell performances by presenting the study of Vycor nanoporous absorption of water molecules in both far and mid infrared regions.

During hydration measurements, the system is studied at equilibrium for a given value of relative humidity (defined as the ratio of partial water vapour pressure p and water vapour pressure p_0 (31.7 mbar at 25°C) at a given temperature, $RH=(p/p_0)*100$). A tube containing outgassed deionized liquid water (18.2 M Ω·cm at 25°C) provides the vapour source. The vapour pressure is monitored by a thermostated gauge (0-100 mbar at ±0.02 mbar) and, once at equilibrium, the measurements are performed.

Mid infrared spectra were recorded at 4 cm^{-1} resolution with a Globar source, a Ge/KBr beam splitter and a HgCdTe detector, while far infrared spectra were recorded at 2 cm^{-1} resolution with the synchrotron source, a 6 µm thick Mylar beam splitter and a 4.2 K bolometer. Spectra are presented in absorbance units according to the Lambert-Beer law $A=-log(I/I_0)$, with I the transmission through the sample and I_0 the background.

2—3.2.1.2 H_2O MOLECULES IN NANOPOROUS VYCOR UNDER HYDRATION CONTROL

Figure 2.3.3a shows absorbance spectra from 1500 cm^{-1} to 3900cm^{-1} during adsorption of water at different relative humidity levels (12%, 23%, 36%, 48%, 61%, 73%, 85%, 97% and 100% RH). Dried Vycor obtained by heat treatment up to 313K for 15 hours and under vacuum (~10^{-5} mbar) was used as reference I_o.

Using this procedure, the absorbance spectrum results only from the modifications due to adsorbed water molecules. One can distinguish three vibrational modes:[19] the intramolecular O-H stretching mode, the H-O-H bending mode and the intermolecular $H_2O\cdots H_2O$ connectivity band. Here, positive bands correspond to vibrational modes produced by absorbed water molecules, while negative bands (like the one centered at 3700 cm^{-1} assigned to Si-OH surface modes) result from the disappearance of these surface modes. The broad band centered at 2200 cm^{-1} is a combination of libration (400−1000 cm^{-1}) and bending (1630 cm^{-1}) modes respectively due to the frustrated rotation of water molecules and the deformation in the HOH bond angle.

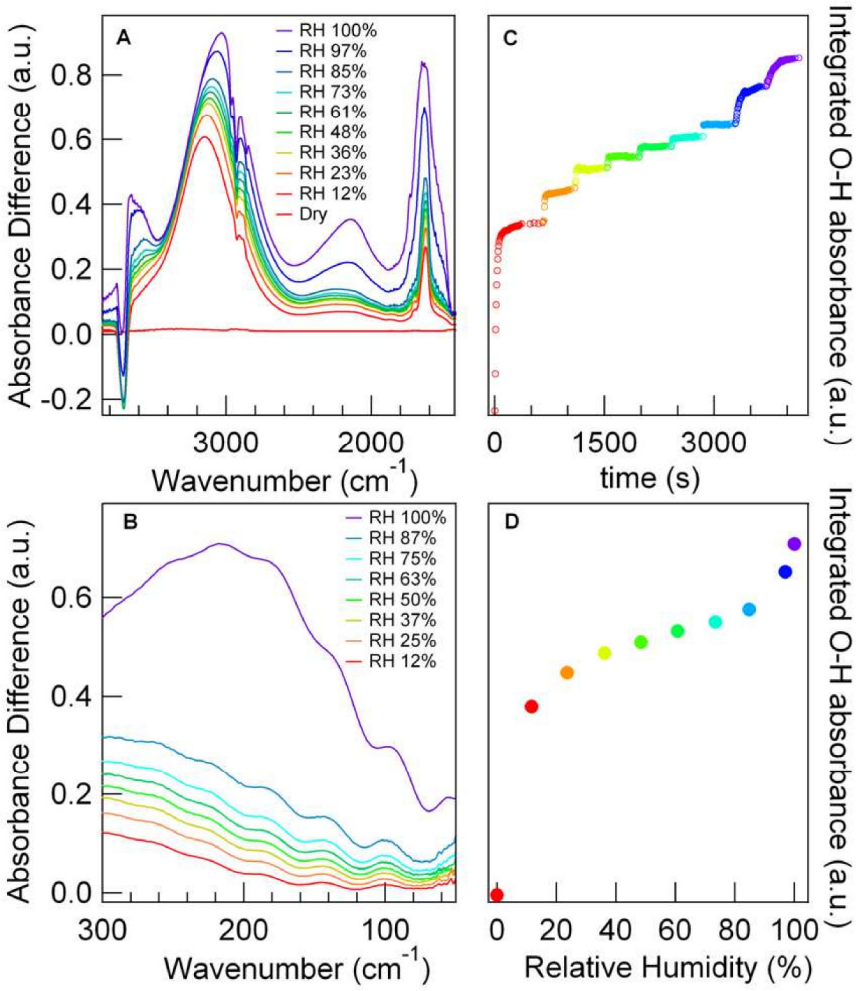

Figure 2.3.3 – IR spectra of water trapped in Vycor at selected RH. (a) Mid infrared spectra during sorption of water at 12%, 23%, 36%, 48%, 61%, 73%, 85%, 97% and 100% RH and (b) the connectivity band in far infrared spectra at 12%, 25% 36%, 50%, 63%, 75%, 87% and 100% of RH. The OH stretching integrated absorbance (between 2550 cm^{-1} and 3450 cm^{-1}) to obtain the time resolved sorption curve as a function of time (c) and relative humidity (d).

In the following, we limit the analysis to the two modes representative of the connectivity of water molecules: the OH stretching and OH···O stretching motions.

The OH band intensity is proportional to the amount of water molecules. In bulk water this band can be considered as a combination of three populations[19] representative of different hydrogen bonding modes. Free, or slightly connected, H_2O molecules absorb around 3600 cm^{-1}, while water molecules with a higher connectivity absorb at lower frequencies. The superposition of these contributions results in an extended band from 3200 to 3600 cm^{-1}.

These vibrational modes of water molecules are affected by the physico-chemical properties of the matrix in which they are confined resulting in a shift of their positions. Other substructures of this broad band may be due to the overlapping asymmetric v_3 and symmetric v_1 H-O-H stretching modes, with a shoulder near 3250 cm^{-1} ascribed to the overtone of the bending $2v_3$ mode.[20,21] During the first step of hydration, the OH stretching modes of water confined in Vycor's pores produce a wide band centered at 3200 cm^{-1} resembling the absorption of H_2O molecules with four established bounds. Proceeding further with hydration steps, band shifts towards lower frequencies.

Figure 2.3.3c presents the integrated absorbance over the stretching band (between 2550cm^{-1} and 3450cm^{-1}) as a function of time during the adsorption process for different hydration levels, from RH=0% to 100%. This evolution shows that for each step, the process kinetics is completed in a few minutes and the OH stretching band does not evolve any further until the next higher water vapour pressure is set. In Figure 2.3.3d, the amount of water molecules at equilibrium as a function of RH is plotted. This sorption curve presents a plateau between 36% and 85% RH, characteristic of a slowing down of the sorption process after the deposition of one monolayer (RH=36%: spectrum in yellow).[22]

Figure 2.3.3b shows the connectivity band between 50 cm^{-1} and 260 cm^{-1} for various RH. Interference fringes due to multiple reflections in the ~80 µm-thick Vycor slab are observed. The hydrogen bond stretching vibration (O-H…O) appears at higher frequency compared to the bulk water value[19] and its weak intensity for low value of RH suggests that water molecules have only established a few H-bonds with the interface. For higher hydration levels (up to 75% RH) the H-bond stretch intensity only slightly increases, when compared to the number of adsorbed water molecules. It is only at the last stage (RH 87%−100%, spectrum in violet) that the connectivity band presents an important increase in intensity and a frequency characteristic of water bulk connectivity. This strong bonding to the Vycor interface allows to explain the evolution of the OH band frequency shift and rejects the suggested highly connected water molecules even at low hydration level.

Therefore, far infrared data provides key information to understand the nature of water in confined environment and at low coverage (hydrophilic environment as the matrix is Vycor): the weak connectivity band proves that there is a modest

association of water molecules through H bonds network while the low frequency of the OH stretching band results from the strong bond to the interface and is not related to the number of established hydrogen bonds.

2—3.2.2 FAR-IR SPECTROSCOPY MEASUREMENT OF CONFINED H2O MOLECULES UNDER HIGH PRESSURE CONDITIONS

To measure samples under well-controlled pressure, diamond anvil cells (DAC) are commonly used.[23] Indeed diamonds offer extreme hardness and are also transparent in the IR and THz ranges, thus well suited for transmission or reflection experiments under high pressure conditions. Nevertheless, such experiments require measuring small samples (of the order of ~hundred microns in dimensions) to reach pressures in the GPa range, since the culet diameter of the anvil is smaller than 1 mm. The infrared synchrotron (IRSR) source is several orders more brilliant than commercial IR sources and thus provides a better signal-to-noise ratio.[15] Therefore, it is ideal to combine DAC and IRSR to allow high pressure measurements in the complete IR range and specifically in the far infrared. For water studies, it allows measuring the connectivity band otherwise impossible to measure with laboratory sources.

Recently, the AILES beamline has been equipped with a set-up allowing to measure rapidly and reproducibly the far IR spectra (30−400 cm^{-1}) of samples under high pressure (see Figures 2.3.5 and 2.3.6). The set-up consists of a vacuum chamber with central dimensions of approxim.ately 45 cm, pumped down to a vacuum of ~10^{-5} mbar. A total of 12 gold coated mirrors direct the IRSR light through a double condenser system (Cassegrain objectives) and a DAC (Figure 2.3.4a).

More precisely, the modulated synchrotron beam enters the high pressure set-up with a diverging beam. This beam is focused using a toroidal mirror (focus 76 mm). A flat mirror directs the beam toward a 25 mm collimator allowing to enter with a 5 mm parallel beam the highly focusing Cassegrain optics (magnification X15, N.A. 0.28, working distance 25.4 mm). Thanks to the Cassegrain, the beam is focused on the center of the DAC allowing for a maximum transmission (focusing spot: ~300 µm). After this passage, an equivalent sequence: second Cassegrain, collimator, flat and toroidal mirrors

allows the beam to reenter the sample compartment of the interferometer where it is directed toward one of the detectors (see interferometer description).

Both Cassegrain objectives are adjustable following two angles through motorized stages and the DAC position is controlled via a xyz-motorized stages. This computer-controlled optics permits tuning the alignment of these components under vacuum.

2—3.2.2.1 HIGH PRESSURE SET-UP

Typical gasket thickness and hole diameter required for the HP experiments in the far-IR region are about 30-60 μm and ~300 μm, respectively. This hole size limits the lower frequency to ~30 cm^{-1} and the maximum pressure to ~20 GPa. To improve the spectral quality, Type IIa diamond was selected for IR studies. Nevertheless, a strong two-phonon absorption band at approximately 1900−2300 cm^{-1} range remains.[24] The alternative Type Ia diamonds have nitrogen impurities, resulting in an additional undesired strong absorption below 1200 cm^{-1}.

The list of pressure transmitting medium used in DAC experiments includes inert gases as He and Ar, liquids such as glycerin, Daphne oil, methanol-ethanol mixtures or even solid powders as KBr and KCl. For the far-IR, we commonly use polyethylene, since it is transparent at low frequencies (4−700 cm^{-1}). The pressure is determined through the measurement of the shift of fluorescence bands R1 and R2 of ruby.[25] This fluorescence measurement is carried out by sliding the DAC from the IRSR position (Figure 2.3.4a) to the fluorescence system position (Figure 2.3.4b) using a motorized rail. After applying the desired pressure, the DAC is moved back to the IRSR light position with 3 μm accuracy. Both positions can be controlled via a visible camera image of the sample hole. The ability of measuring both IR spectra and ruby fluorescence without breaking the vacuum, allows reaching the exact same position for both the sample and the ruby when changing pressure and results in high pressure experiments in a wide pressure range in few hours at AILES beamline.

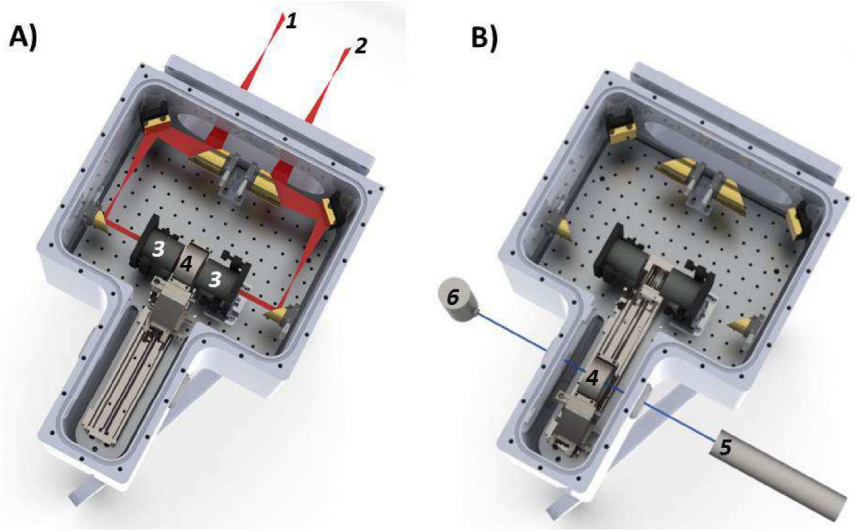

Figure 2.3.4 – Schematic view of the far-IR high pressure set up. (a) Synchrotron infrared light position. The modulated beam from the interferometer (1) enters the set-up while the transmitted beam (2) is sent to one of the interferometer detectors. The Cassegrain objectives (3); and diamond anvil cell (4) are fed with a collimated beam. (b) Fluorescence position. The DAC is moved by a long range translation allowing to be placed in front of an ruby fluorescence measurement set-up (5) and a visible light source (6) in order to measure the pressure without opening the vacuum chamber.

2—3.2.2.2 H_2O MOLECULES IN NANOPOROUS FAUJASITE UNDER PRESSURE

This example of high-pressure measurements using synchrotron sources concerns confined H_2O molecules in nanoporous Faujasite NaX.[26] Faujasite is a hydrated sodium aluminosilicate zeolite with a cubic structure built up of sodalite cages linked by double six-membered rings (D6MR) of TO_4 (T=Si, Al) tetrahedral.[27]

In particular, water molecules have been shown to act as local probes for the pressure-induced amorphisation (PIA) of this material. Faujasite undergoes a PIA around 2 GPa.[28—31]

In the 2−4 GPa pressure range , a polyamorphism phenomenon is observed, linked to local depressurization due to the significant volume change during the low-density amorphous (LDA) to a high-density amorphous (HDA) form transformation.[30—32] In this example, we report how the hydrogen-bond between

confined water molecules located inside the porous network of the solid structure can be used as a local probe to follow the structural changes occurring during pressure induced amorphisation and the LDA-HDA transformation of this material.

Figure 2.3.5 presents the study of water molecules confined in Faujasite NaX at high pressure using mid- and far-IR spectroscopy. The framework modes of the Faujasite, appearing in the MIR correspond to the antisymmetric and symmetric O-*T*-O stretching modes (ν_{as}(O*T*) and (ν_{s}(O*T*)), symmetric T-O-T stretching modes (ν_{s}(*T*O)), and the D6MR modes. Their frequency dependence does not provide clear information about the structure transformation during the pressure increase.[26]

In contrast, in the OH stretching region (Figures 2.3.5 and 2.3.6) three hydroxyl stretching components (ν(OH)) between 3200 and 3600 cm^{-1} show softening between 0.7 and 2 GPa, supporting a strengthening of H-bonds and the weakening of the internal O-H bonds. In the range 2−7 GPa, these three modes shift to higher wavenumbers and reach values similar to those observed at 0.1 MPa providing clear evidence of local depressurization. Finally, above 7 GPa these bands begin to decrease in wavenumber and broaden with new features appearing at lower wavenumbers, indicating a wider distribution of hydrogen bonding environments for the confined water molecules.[28,33,34]

In the far-IR region (50−300 cm^{-1}), intermolecular modes due to H-bonding (νHB) are directly probed (Figures 2.3.5 and 2.3.6). At ambient pressure, 0.1 MPa, two well defined H bonding (νHB) vibrational features are observed at ~180 and 118 cm^{-1}. In dehydrated NaX, sharp modes of Na+ cations are observed at 189 and 110 cm^{-1}, respectively. In hydrated NaX, coupling could be expected to occur between the translations of the hydrated Na+ cations and stretching of the H bonds. Then in the hydrated material, the bands in this region are much broader and the relative intensity of the lower frequency band with respect to the higher frequency band is significantly higher.
This assignment is described in detail in Ref. 26.[26] With pressure increase up to 2 GPa, a progressive shift toward higher frequency and broadening of the external features νHB is observed, demonstrating a strengthening of the hydrogen bonds. Above 2 GPa, the higher frequency component νHB (180 cm^{-1}), corresponding to the stronger H-bonds, start decreasing in frequency as a

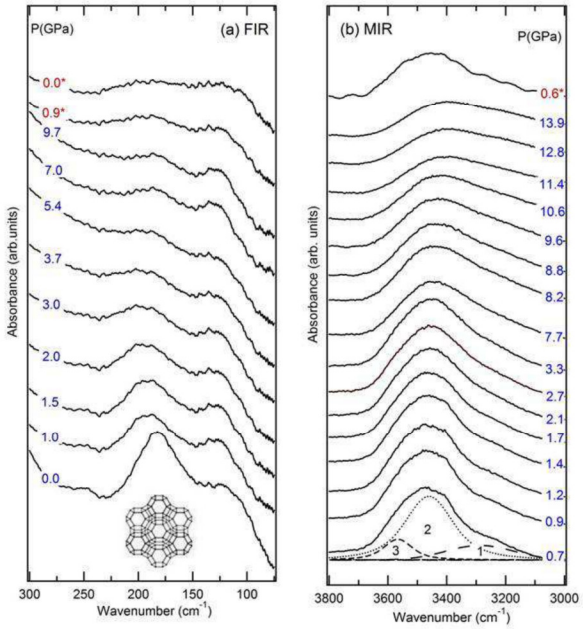

Figure 2.3.5 – IR spectra of Faujasite at selected pressures. (a) Far and (b) mid (OH stretching region) IR spectra of Faujasite at selected pressures on compression and on decompression (*) with sequence displayed from bottom to top. Inset: representation of the structure of Faujasite showing the *T*-atom framework. Figure adapted from Catafesta et al.[26]

function of pressure, showing again the weakening of the hydrogen-bonding. Between 3.5 and 7 GPa, this band returns to its ambient pressure position. This shows clear evidence for local depressurization during the LDA-HDA transformation. At higher pressures, a broad band is present corresponding to a large distribution of H bonding in agreement with the *v*(OH) behavior.

With the collapse of the Faujasite structure, producing the HDA form, the intermolecular H-bonding modes decrease and display a broad distribution of H-bonds. Releasing the pressure, the H-bonding features (internal modes *v*OH and external modes *v*HB) broaden, but *v*OH is always found at lower frequencies with respect to those obtained upon compression suggesting a larger distribution of hydrogen bonds.

The present infrared results show that H_2O molecules act as local probes for the local depressurization occurring during the amorphisation process and the strong volume decrease occurring at the formation of the HDA form in Faujasite. Spectroscopic methods are extremely powerful to probe changes at local level especially when following the behavior of molecules confined in the cages and channels of the porous structure. This method complements X-ray diffraction

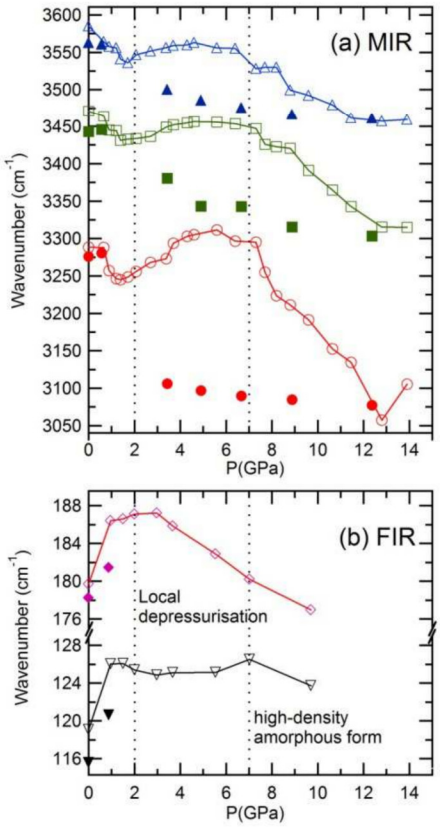

Figure 2.3.6 – Pressure dependence of the IR bands (OH and H-bond stretching regions) of Faujasite. Open and solid symbols correspond to points obtained on compression and decompression, respectively. Figure adapted from Catafesta et al.[26]

studies information about phase transitions, for which losses of signal, resulting from the disappearance of long-range order upon PIA.[29—32]

2—3.2.3 A TEMPERATURE-CONTROLLED ELECTROCHEMICAL CELL FOR PROBING THE HYDROGEN BONDS IN METALLOPROTEINS

Vibrational analysis of proteins or biological molecules provides new information on biomolecular structures, dynamics and properties of intra- and intermolecular hydrogen bonds. Bending vibrational modes of amino acids as well as metal-ligand vibrations also absorb in the far-IR and terahertz domain (600−3 cm^{-1} or 18−0.1 THz), which is particularly appealing for probing metal active sites in metalloproteins.[14,35—37]

Far-IR absorption spectra of proteins in aqueous solution are dominated by the strong absorption of water. The brilliance and stability of the far-IR beamline AILES,[12,14,19] enable far IR measurements, capable of detailing molecular properties of metal sites or metal redox states of proteins. Due to the weakness of the signals to probe, typically of the order of 10^{-5}–10^{-3} absorbance unit, difference spectroscopy is needed to identify modes associated with active sites.

2—3.2.3.1 ELECTROCHEMICAL CELL FOR DIFFERENCE SPECTROSCOPY

In order to combine electrochemical experiments with infrared data collection, we developed a vacuum-tight electrochemical cell, on the basis of that described by Moss[38] with modifications to access the far-IR domain.[14,39]

The electrochemical cell presented in Figure 2.3.7 includes two 1° wedged CVD diamond windows (Φ= 10 mm, 300 µm thickness at center). The cell chamber is sealed by squeezing the two faces of a thermostated copper holder. The working electrode is a chemically modified gold grid (4−6 µm-thick) deposited on one of the windows.

The counter electrode is a thin platinum foil deposited at the window periphery, and the reference electrode consists in a silver (Ag) wire covered by AgCl and immersed in a 3 M KCl solution. The electrode is screwed in the epoxy body

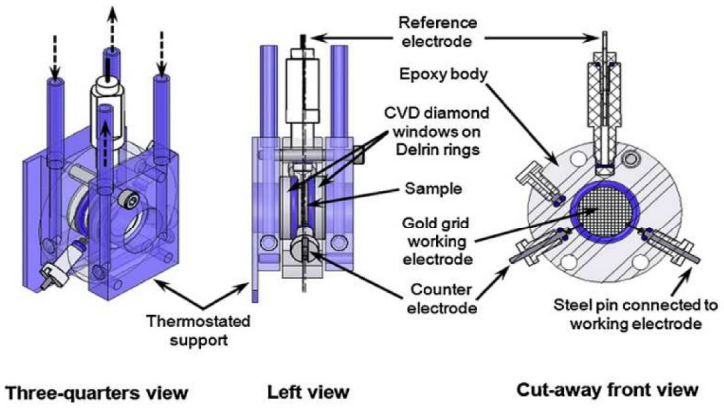

Figure 2.3.7 – Technical drawings of the spectroelectrochemical cell. This electrochemical cell is derived from the Moss et al.[38] transmission conventional 3 electrode set-up. All the modifications have been done to make the cell airtight. The dashed arrows indicate the water circulation flow in the thermostated support.

and its electrical contact with the cell chamber is obtained via a cotton linter. The working and counter electrodes are connected to steel nails plugged in nylon screws via platinum (Pt) wires passing through the epoxy body. All connections are tightened using silicone sealants and/or O-rings.

Electrochemically induced FT-IR difference spectroscopy experiments were performed with 10 mM Cu−azurin in 50 mM Tris−HCl 100 mM KCl pH 8.5. An amount of 15 µL of sample was then deposited between the two CVD windows and the cell path length was adjusted manually until the IR absorption of the sample at 1643 cm^{-1} (δ(O−H)H2O contribution) was less than 0.9 absorbance units (AU). The electrochemical cell was thermostatted at 2, 8, or 36 °C within 0.1 °C with a water circulation system using a PT100 sensor connected to a controller (Huber cc 805). A potentiostat (EG&G 362, Princeton Applied Research or Microstat, Sycopel Scientific Ltd.) triggered by the FT-IR spectrometer was used to apply the oxidizing (560 mV vs NHE) and reducing (−40 mV vs NHE) potentials to the electrochemical cell. After the change in redox potential, a 5 min delay was awaited prior to the spectral measurements, for ensuring complete oxidation or reduction of Cu−azurin (Em =293 mV vs NHE at pH 836).

FT-IR spectra in the 450−50 cm^{-1} range were measured at 2 cm^{-1} resolution using the evacuated (10^{-5} mbar) Bruker IFS125 spectrometer of the far-IR terahertz beamline AILES connected to the synchrotron source SOLEIL. Each single Spectrum resulted from the averaging of 500 scans recorded at 40 kHz. Each sample results from 10 to 20 successive independent redox cycles averaged.

2—3.2.3.2 PROBING HYDROGEN BONDING IN METALLOPROTEINS BY FAR-IR DIFFERENCE SPECTROSCOPY

Using this cell, we recorded reduced-minus-oxidized infrared difference spectra of the model protein Cu-azurin in the 450−50 cm^{-1} domain. In vivo, azurin is involved in electron transfer reactions. The redox Cu forms strong interactions with two histidine (His) imidazole and the thiolate of one cysteine (Cys), and two weak interactions with a methionine thioether and the carbonyl of a glycine.

Only vibrations of chemical groups selectively perturbed by the Cu redox switch contribute in electrochemically induced difference spectra.

Indeed, in Figure 2.3.8, well-defined and reproducible bands are observed for the Cu(II) state (pointing downwards) and for the Cu(I) state (pointing upwards). Averaging of spectra (typically of 300 scans were recorded for each single beam spectrum) recorded for 10−20 electrochemical cycles allowed us to obtain difference spectra with high signal to noise ratio (less than 2.5×10^{-5}). The signal to noise was slightly better below 300 cm^{-1} because of the higher emission of the synchrotron IR source at these frequencies. Vibrations involving Cu-ligand interactions as well as ligand bending modes or deformation modes of the protein are expected to contribute in whole region. In addition, contributions from vibrational bands due to intra- and intermolecular *ν*(H···O) or *ν*(H···N) hydrogen bonds and contributions from the water solvent are expected to contribute below 300 cm^{-1}.[19,41,42]

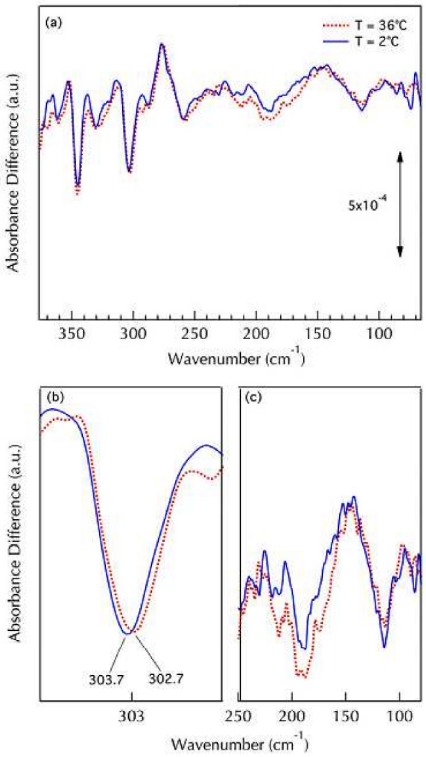

Figure 2.3.8 – Temperature dependence of the FTIR difference spectra. Superimposition of reduced-minus-oxidized FTIR difference spectra recorded at 36 °C (red-dots) and 2 °C (blue) on Cu-azurin samples at 2 cm^{-1} resolution. The main temperature effects are zoomed in (b) and (c). Potentials of 560 mV and −40 mV vs NHE were applied to the electrochemical cell to record spectra corresponding to oxidized and reduced Cu–azurin, respectively. After the change in redox potential, a 5 min delay was awaited prior to the spectral measurements.

To identify IR modes involving Cu-ligand vibrations, we compared spectra ^{63}Cu- and ^{65}Cu-azurin with resonance Raman spectroscopy. This last technique is restricted to the oxidized Cu(II) state, which gives rise to a characteristic absorption band at 627 nm in the visible range, while the Cu(I) state presents no absorption in this spectral domain.[43,44]

The band at 407.3 cm^{-1} was assigned to the *v*(Cu-SCys) mode, strongly coupled with deformation modes of amino acids, and the band at 303 cm^{-1} to the ν_{as}(Cu-$(NHis)_2$) IR mode, coupled with bending modes of the Cu ligands.

The properties of hydrogen-bonds in proteins, and notably those involving the water solvent, are highly sensitive to the temperature. In particular, a weakening of hydrogen bonds formed with the solvent is expected with increasing temperatures.[45] Therefore, we used the thermal dependence of the FIR FTIR difference spectra recorded with Cu-azurin to identify modes contributed by hydrogen-bonds to solvent molecules.

Figure 2.3.8 shows reduced-minus-oxidized difference spectra recorded at 2 °C and 36°C of Cu-azurin in H_2O. The spectra are highly similar except for a greater amplitude of the negative broad band at 225−150 cm^{-1} at 36 °C and a downshift of the 303.7 cm^{-1} band to 302.7 cm^{-1} switching from 2° C to 36 °C.

The band at 225−150 cm^{-1} corresponds to intermolecular H-bond stretching, arising from the longitudinal motion of the hydrogen atom along the hydrogen bond axis. The band at 303 cm^{-1} contains significant contribution from *v*(Cu-$(NHis)_2$) vibration. Interestingly, in the crystallographic structure of Cu-azurin, one of the histidine Cu ligands is hydrogen-bonded to a water solvent molecule. A weakening of this hydrogen bond at 36 °C may explain the temperature dependence of the 303 cm^{-1} band frequency. The frequency downshift observed upon temperature increase is in line with a decreased electronegativity of the imidazole ligand due to a weakening of the imidazole $NH\cdots OH_2$ intermolecular bond.

In short, the improved resolution spectra obtained using synchrotron sources and the coupling of far-IR difference spectroscopy with temperature changes has allowed the description of the vibrational modes of the metal active site of Cu-azurin and the detection of hydrogen-bonding between this active site and water solvent molecules, selectively relevant to the protein function.

2—3. 3 CONCLUSION

The AILES infrared beamline at synchrotron SOLEIL has been designed to provide a source covering the complete infrared range with an extension to the THz domain. The beamline performances: stability, brilliance and extension to the THz domain are suitable for a wide class of condensed matter studies. A set of sample environment completes the beamline and allows for exploiting its exceptional characteristics. This combination of a highly stable and intense IR/THz beam with well controlled sample environments is particularly adapted for the study of water in various confining systems. Future set-ups currently under development include ensembles for measurements under low temperature and high pressure simultaneously, cryostat at sub kelvin temperatures, high pressure optical set-ups for the reflectivity measurements and near field optical ensemble with a spatial resolution in the nanometre range.

REFERENCES

(1) The MIRAS Proposal can be found here:

www.miras2.es/PDF/MIRAS_4_ALBA_PUBLIC_Sep09.pdf

(2) J. M. Byrd, W. P. Leemans, A. Loftsdottir, B. Marcelis, M. C. Martin, W. R. McKinney, F. Sannibale, T. Scarvie, C. Steier, Phys.Rev. Lett. 89 224801 (**2002**).

(3) Y.-L. Mathis, B. Gasharova, D. Moss, J. Biol. Phys. 29 (**2003**), 313.

(4) W.B. Peatman, and U. Schade, Rev. Sci. Instr. 72 (**2001**) pp. 1620-1624.

(5) B.E. Billinghurst, J.C. Bergstrom, L. Dallin, M. de Jong, T.E. May, J. M. Vogt, W.A. Wurtz, Phys. Rev. ST Accel. Beams 16(**2013**), 060702.

(6) G. Cinque, M. Frogley, R. Bartolini, "Far-IR/THz spectral characterization of the coherent synchrotron radiation emission at diamond IR beamline B22" Rend. Fis. Acc. Lincei, 22(1) (**2011**) 33-47.

(7) A. Nucara, S. Lupi, and P. Calvani, Rev. Sci. Instr. 74, 3934 (2003).

(8) L.-F. Chiu, P.-Y. Huang, W.-F. Chiang, T.-Y. Wong, S.-H. Lin, Y.-C. Lee*, D.-B. Shieh*, Anal. Bioanal. Chem. 405 (**2013**), 1995.

(9) I. Yousef, S. Lefrançois, T. Moreno, J.-P. Daguerre, H. Hoorani, F. Makahleh, A. Nadji, and P. Dumas. Nuclear Instruments and Methods A, 2012, 673(1) (**2012**) 73–81.

(10) Erika Levenson a, Philippe Lerch b, Michael C. Martin, Infrared Physics & Technology 51 (**2008**) 413–416.

(11) M. Tobin, L. Puskar, R. Barber, E. Harvey, P. Heraud, B. Wood, K. Bambery, C. Dillon, K. Munroe, Vib. Spec. 53 (**2010**), 34-38.

(12) P. Roy, M. Rouzieres, Z.M. Qi, O. Chubar, Infrared Physics & Technology, 49 (**2006**), 139-146.

(13) Y. Ikemoto, M. Ishikawa, S. Nakashima, H. Okamura, Y. Haruyama, S. Matsui, T. Moriwaki and T. Kinoshita, Opt. Communications 285 (**2012**) 2212.

(14) N. Vita, J-B. Brubach, R. Hienerwadel, N. Bremond, D. Berthomieu, P. Roy, C. Berthomieu, Analytical Chemistry, 85 (**2013**), 2891.

(15) J. B. Brubach, L. Manceron, M. Rouzière, O. Pirali, D. Balcon, F. Kwabia Tchana, V. Boudon, M. Tudorie, T. Huet, A. Cuisset, P. Roy, AIP Conference Proceedings, (**2010**), 1214: 81-84.

(16) S. Le Caer, S. Pin, S. Esnouf, Q. Raffy, J. Ph. Renault, J.-B. Brubach, G. Creff, P. Roy, Phys. Chem. Chem. Phys., 13 (**2011**), 17658–17666.

(17) Garrone, E; Bonelli, B; Lamberti, C; et al. Journal of Chemical Physics Volume: 117 Issue: 22 (**2002**), 10274-10282,.

(18) Lamberti, C; Prestipino, C; Bordiga, S; et al. Nuclear Instruments & Methods in Physics Research B- Volume: 200, (**2003**) 196-201.

(19) J-B. Brubach, A. Mermet, A. Filabozzi, A. Gerschel, P. Roy, J. Chem. Phys., 122 (**2005**), 184509.

(20) J. Madejovà, M. Janek, P. Komadei, H-J. Herbert, H.C. Moog, Appl. Clay Sci., 20 (**2002**), 255-271.

(21) J-L. Bishop, C.M. Pieters, J.O. Edwards, Clays Clay Miner., 42 (**1994**), 702-716.

(22) J.M. Zanotti, M.C. Bellissent-Funel, S.H. Chen, Europhysics Letters, 71 (**2005**), 91-97.

(23) M. I. Eremets: High Pressure Experimental Methods (Oxford University Press, Oxford, **1996**).

(24) H.Okamura, M.Matsunami, R.Kitamura, S.Ishida, A.Ochiai, T. Nanba, J. Phys. Conf. Ser., 125 (**2010**), 012051.

(25) H. K. Mao, J. Xu, P. M. Bell, J Geophys Res-Solid, 91 (1986), 4673-4676.

(26) J. Catafesta, F. Alabarse, C. Levelut, A. Isambert, P. Hébert, S. Kohara, D. Maurin, J-L. Bantignies, O. Cambon, G. Creff, P. Roy, J-B. Brubach, T. Hammouda, D. Andrault, J. Haines, Phys. Chem. Chem.I Phys., 16 (**2014**), 12202-12208.

(27) N. Greaves, F. Meneau, J Phys-Condens Mat, 16 (**2004**), S3459-S3472.

(28) F. Busch, N. Jaeger, G. SchulzEkloff, R. Schnell, H. Klein, H. Fuess, Zeolites, 17 (**1996**), 244-249.

(29) M. Colligan, P. M. Forster, A. K. Cheetham, Y. Lee, T. Vogt, J. A. Hriljac, J Am Chem Soc, 126 (**2004**), 12015-12022.

(30) H. J. Liu, R. A. Secco and Y. N. Huang, Physchemcomm, 4 (**2001**), 37-39.

(31) G. N. Greaves, F. Meneau, A. Sapelkin, L. M. Colyer, I. A. Gwynn, S. Wade, G. Sankar, Nat Mater, 2 (**2003**), 622-629.

(32) A. Isambert, E. Angot, P. Hebert, J. Haines, C. Levelut, R. Le Parc, Y. Ohishi, S. Kohara, D. A. Keen, J Mater Chem, 18 (**2008**), 5746-5752.

(33) D. D. Klug, E. Whalley, Rev Sci Instrum, 54 (**1983**), 1205-1208.

(34) M. Ceppatelli, M. Santoro, R. Bini, V. Schettino, J. Chem. Phys., 113 (**2000**), 5991-6000.

(35) L. Marboutin, A. Desbois, C. Berthomieu, J. Phys. Chem. B, 113 (**2009**), 4492−4499.

(36) L. Marboutin, H. Petitjean, B. Xerri, N. Vita, F. Dupeyrat, J.P. Flament, D. Berthomieu, C. Berthomieu, Angew. Chem. Int., 50 (**2011**), 8062-8066.

(37) Y. El Khoury, P. Hellwig, ChemPhysChem 12 (**2011**), 2669 – 2674.

(38) D. Moss, E. Nabedryk, J. Breton, W. Mantele, Eur. J. Biochem., 187 (**1990**), 565−572.

(39) C. Berthomieu, L. Marboutin, F. Dupeyrat, P. Bouyer, Biopolymers, 82 (**2006**), 363−367.

(40) H. Nar, A. Messerschmidt, R. Huber, M. van de Kamp, G.W. Canters, J. Mol. Biol. 221 (**1991**), 765−772.

(41) H.R. Zelsmann,J. Mol. Struct., 350 (**1995**), 95−114.

(42) N. Miura, H. Yamada, A. Moon, Spectrochim. Acta, Part A, 77 (**2010**), 1048−1053.

(43) Solomon, E. I. Inorg Chem (**2006**), 45, 8012-8025.

(44) Blair, F. G.; Campbell, G. W.; Cho, W. K.; English, A. M.; Fry, H. A.; Lum, V.; Norton, K. A.; Schoonover, J. R.; Chan, S. I. J. Am. Chem. SOC. (**1985**), 107, 5755-5766.

(45) S.H. Brewer, Y.F. Tang, D.M. Vu, S. Gnanakaran, D.P. Raeigh, R.B. Dyer, Biochemistry 51 (**2012**), 5293−5299.

CHAPTER 3

BULK WATER

Vibrational spectroscopies are used to understand the structure and dynamics of water in different phases since rotational and vibrational modes are sensitive to the local environment of molecules.

In order to understand the effects of confining media on water molecules, we carried out a preliminary study on bulk water in gaseous, liquid and ambient pressure solid states.

3—1 WATER VAPOR

Absorption spectra acquired during hydration measurements at controlled water vapor pressure include, evidently, a contribution of the vibrational and rotational modes of the water vapor molecules, which are present in the hydration cell, described in Section 2—3, and lie in the optical path of the beam. Such contribution is negligible for low vapor pressure but becomes more important as the relative humidity increases.

Water molecules in the gaseous phase, that are in equilibrium with the sample under investigation, poorly interact with each other and do not develop an extended hydrogen bond network, while those that are adsorbed in the porous matrix are condensed in liquid-like or solid-like state. The vapor and condensed spectral signatures in the infrared spectra can be distinguished allowing the contribution of the water vapor to be removed. For this purpose, spectra of gaseous water have been acquired for a few vapor pressures for each experiment and were readily subtracted to the spectra acquired during hydration measurements.

In this Section we report and describe the spectrum of outgassed deionized water vapor at 25 mbar in the far and mid infrared (~20 — ~4100 cm^{-1}).

3—1.1 WATER VAPOR ABSORPTION SPECTRA

Water vapor at room temperature and 25 mbar was introduced in the hydration cell, described in Section 2—3. Its spectra have been recorded using the acquisition parameters, detailed in Table 2.2.1, in the far (with the 6 μm Mylar beam splitter, 4.6 K bolometer detector and 2 cm^{-1} resolution) and mid infrared (with the KBr beam splitter, MCT detector and 4 cm^{-1} resolution) regions. Spectra were then combined together, as shown in Figure 3.1.1.

The whole spectrum appears as narrow bands. Pure rotational modes produced by transitions between quantized rotational states of the molecules give rise to highly dense and intense absorption lines in the whole far infrared region, namely below 600 cm^{-1}.

Vibrational-rotational contributions, resulting from transitions from the several populated rotational levels of the ground vibrational state to rotational levels of excited vibrational state, are observed in the mid infrared region, above 600 cm^{-1}. For asymmetric rotators, transitions between rotational states occur if they involve a decrease in rotational quantum number, ΔJ=-1 (P branch transitions), an increase in rotational quantum number, ΔJ=+1(R branch transitions) and for constant rotational quantum number in the ground and excited state, $\Delta J=0$ (Q branch transitions), according to the selection rule $\Delta J=0,\pm1$ mentioned in Section 1—6.5.

Absorption lines appearing around 1595 cm^{-1} are associated to vibrational-rotational transitions of the bending states, ν_2 or $\delta(H_2O)$. The presence of the rotational fine structure is accountable for the breadth of this band. Lines in the range 3000-4000 cm^{-1} are associated to vibrational-rotational transitions of symmetric stretching states, ν_1 or $\nu_s(H_2O)$, centered at ~3655 cm^{-1}, asymmetric stretching states, ν_3 or $\nu_a(H_2O)$, centered at 3756 cm^{-1} and to the overtone of bending states transitions, $2\nu_2$, at 3154 cm^{-1} [107].

A small amount of gaseous CO_2 is observed between 2600 and 2900 cm^{-1}.

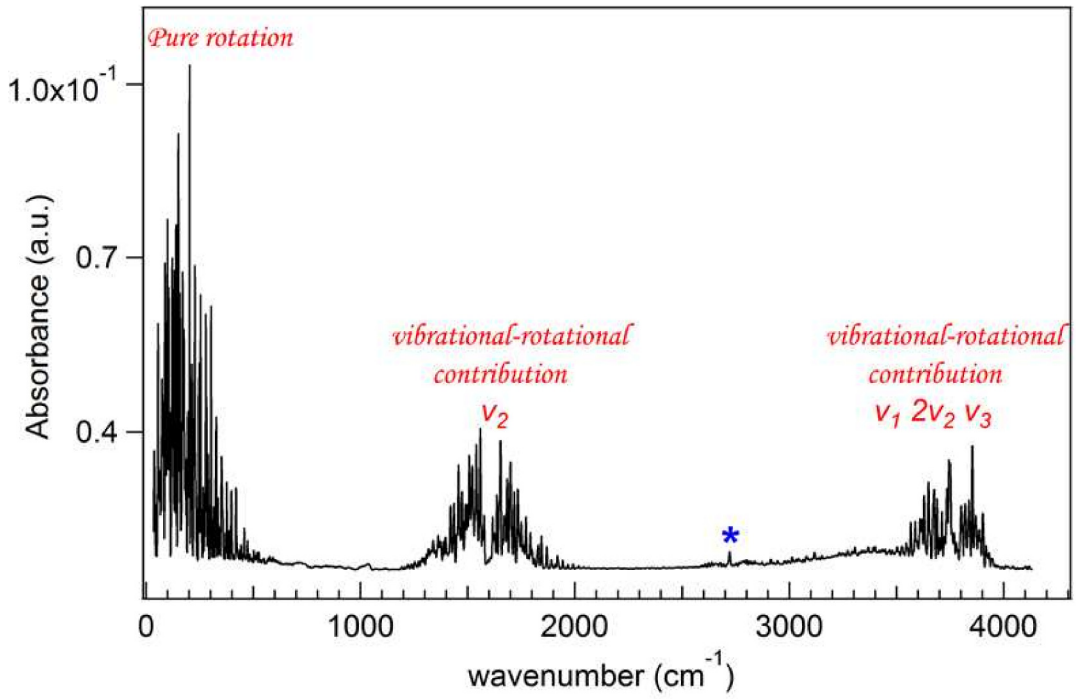

Figure 3.1.1 - FIR and MIR spectra of water vapor. Far and mid infrared (0-4000 cm^{-1}) spectra of vapor water at 25 mbar. Absorption lines below 600 cm^{-1} are accountable for pure rotational modes, while vibrational-rotational modes lie in the mid infrared. The symbol * shows the presence of CO_2.

3—2 CONDENSED WATER

When water is in its liquid or solid state, pure molecules rotations are hindered by the establishment of hydrogen bonds, and the fine structure is replaced by broader and unresolved vibrational bands in both the far and mid infrared spectra. The degree of connectivity and the structure assumed by water molecules depend on temperature and pressure, as shown in the complex phase diagram in Figure 3.2.1.

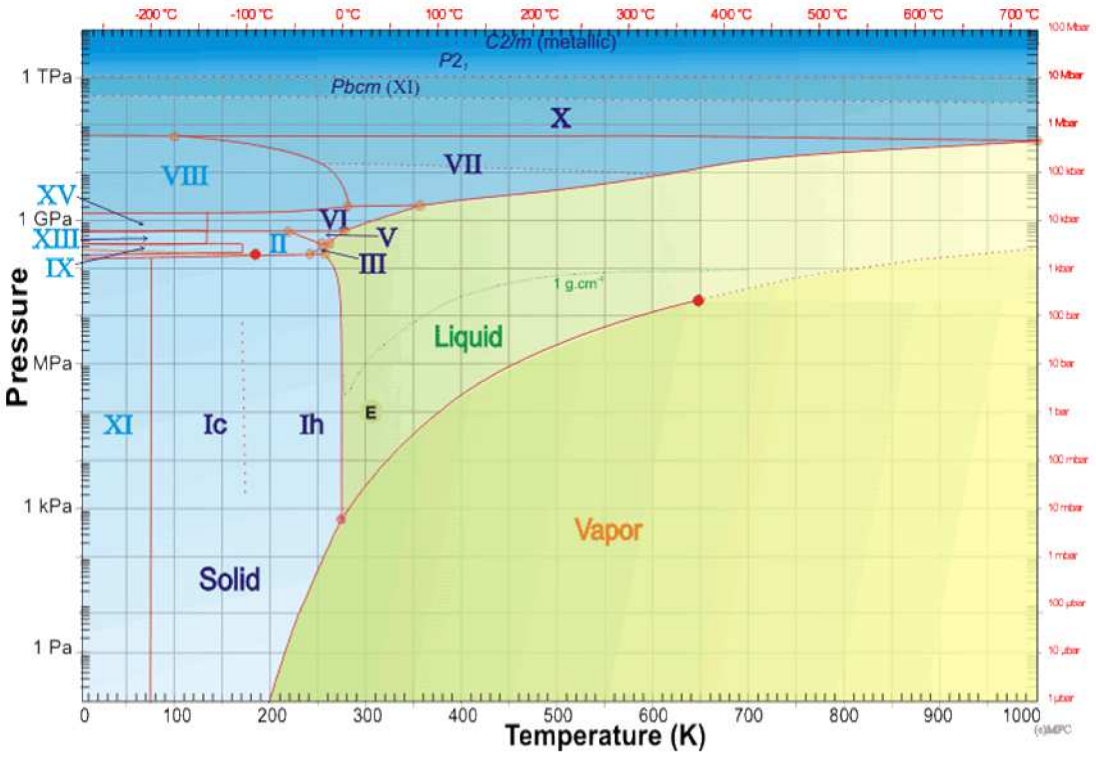

Figure 3.2.1 – Phase diagram of water. Vapor, liquid and several solid structures are shown. Dark blue and light blue structures refer to proton-disordered and proton-ordered phases, respectively. The mean surface conditions on Earth are indicated by the letter E.
From: http://www1.lsbu.ac.uk/water/water_phase_diagram.html

More than fourteen crystalline phases (labelled with roman numerals) and amorphous phases are known. The crystalline ice structures that share boundaries with the liquid phase have the oxygen atoms arranged in a regular lattice, while intramolecular structures are disordered resulting from the disordered hydrogen bonding. The disorder in the protons positions is accountable for the residual

entropy of those ice structures [108]. At lower temperatures, order is further improved when protons are arranged in a regular way. There exist pairs of ice structures which differ only in proton ordering, such as I_h/*XI*, *V*/*XIII* or *VI*/*XV*.

We measured the water absorption at ambient pressure in the far and mid infrared for liquid, three crystalline structures (I_h, I_c and *XI*) and amorphous ice. Since water experiences a large change of dipole moment through the various transitions, its absorption is particularly strong. This makes infrared spectroscopy a highly sensitive technique for the study of water, and aqueous systems in general, but the quantity of water under investigation can not exceed the thickness of a few microns in order to avoid bands saturation.

Firstly, the infrared spectra of each condensed phase will be presented and described separately. It will be followed by a comparison between the spectra aimed at analyzing similarities and differences.

3—2.1 LIQUID PHASE

A cell containing a thin film of liquid sample, designed as liquid cell, was used to acquire the infrared spectra of liquid water at 23 °C. A few microliters of deionized water (18.2 M Ω·cm at 25°C) were placed between two flat diamond windows and held in a copper cell body, which is also connected to the closed cycle helium cryostat (described in Section 2—2.3) to allow measurements at well controlled temperature between T=6 to 355 K at ±0.05 K.

As shown in Figure 3.2.2, four main bands are observed in the spectrum of liquid water.

The two bands below 1000 cm^{-1} correspond to intermolecular modes resulting from the H-bond network established between water molecules. The broad and asymmetric libration band, at ~680 cm^{-1}, arises from rotational transitions of molecules restrained by hydrogen bonds. This frustrated rotation is the origin of ruptures and rearrangements in the H-bond network [5]. The connectivity band emerges out of the low frequency tail of the libration band at 185 cm^{-1} [5, 109]. It arises from the longitudinal motion of the hydrogen atom along the H-bond axis. The shape and the position of these two intermolecular bands are highly affected by the strength and structure of the hydrogen bond network.

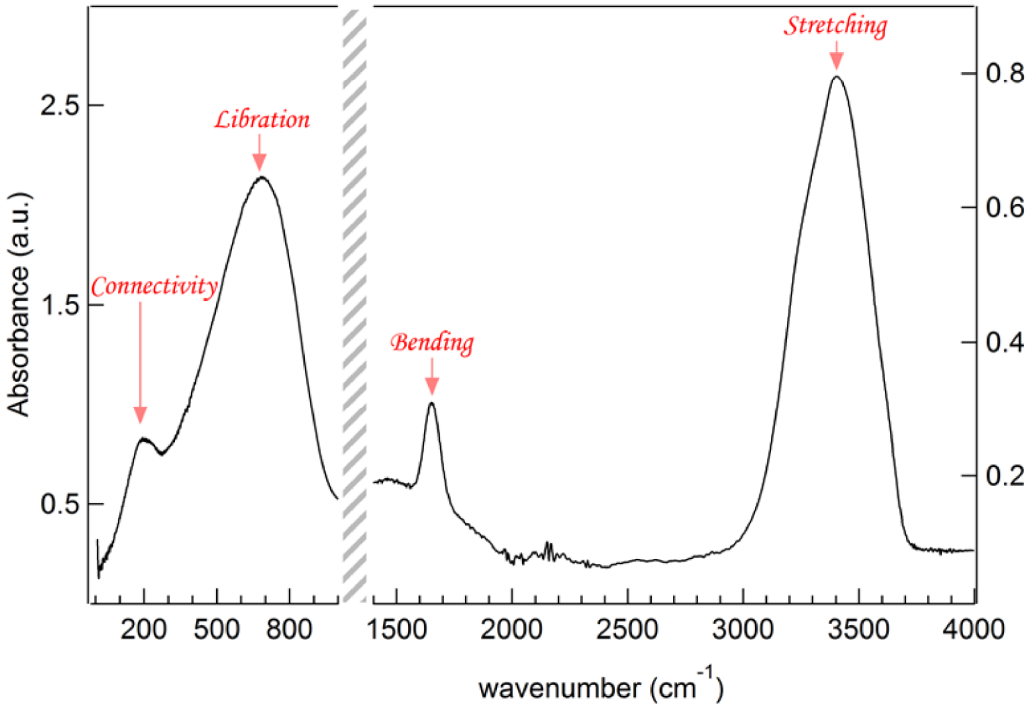

Figure 3.2.2 – FIR and MIR spectra of liquid water. Far and mid infrared (0-4000 cm^{-1}) spectra of liquid water at 298 K. The connectivity and libration bands (at 185 and ~700 cm^{-1} respectively) are plotted on a different ordinate axis with respect to the bending and stretching bands (at 1650 and ~3400 cm^{-1} respectively) whose intensities are greater.

At higher frequency, two intramolecular modes are observed at 1650 cm^{-1} and ~3400 cm^{-1}, corresponding to the HOH bending and OH stretching band, respectively. The OH stretching mode is formed by several substructures and many attempts have been made over the last decades to attribute each component to a specific mode. There is not a general agreement even in the number of subcomponents. Most of the authors explain the OH stretch band in terms of three Gaussians but some interpretation also involves four, five or six Gaussians.

Some authors, like Venyaminov at al. [110], found three subcomponents. They attributed the first component at 3250 cm^{-1} to the overtone of the bending, $2\nu_2$, enhanced by Fermi resonance, the second component at 3450 cm^{-1} to the symmetric stretching, ν_1, and the last component at 3600 cm^{-1} to the asymmetric stretching, ν_3.

Other authors consider the intramolecular OH bond sensitivity to the strength of the hydrogen bonding. Under such assumption, Brubach et al. [5] explain the three

subcomponents as different populations of water molecules involved in different levels of hydrogen bonding. The more H-bonds a given molecule establishes with its neighbors, the weaker its OH oscillator strength is, and the more downshifted the corresponding OH stretch frequency is. In particular, the lowest frequency component, 3295 cm^{-1}, is assigned to molecules having H-bond coordination number close to four, the intermediate component, 3460 cm^{-1}, is assigned to molecules with an intermediate degree of connections, and the higher component, 3590 cm^{-1}, is assigned to poorly connected water molecules.

Evidences on the amount of established H-bonds can not be obtained from the other intramolecular mode, the HOH bending band at 1650 cm^{-1}. Indeed, its single Gaussian shape makes difficult to distinguish different contributions coming from water molecules with specifics degrees of hydrogen bonding. Its intensity may bring however some information. As the change in the dipole momentum (Eq. 1.6.19) associated to the bending vibration decreases with the increase of the HOH angle [111], we can assert that the contribution to the bending band of a given molecule decreases as the number of established H-bonds increases since it causes the opening of the HOH angle (as mentioned in Section 1—1.3).

3—2.2 HEXAGONAL ICE (I_h)

Hexagonal ice, I_h, is the thermodynamically stable crystalline structure of water at ambient pressure below the freezing point (the *I* stands for the first named phase and *h* for hexagonal). The oxygen atoms form a hexagonal lattice and the hydrogens (protons) give rise to an orientationally disordered tetrahedral network, as described by the Pauling ice-rules [108]:

(i) In ice, each oxygen atom has two hydrogen atoms adjacent to it;

(ii) Each water molecule is oriented so that its two hydrogen atoms are directed approximately toward two of the four oxygen atoms which surround it tetrahedrally, forming hydrogen bonds;

(iii) The orientations of adjacent water molecules are such that only one hydrogen atom lies approximately along

each oxygen-oxygen axis (*i.e.* there is only one hydrogen per bond);

(iv) Under ordinary conditions the interaction of non-adjacent molecules is not such as to appreciably stabilize any one of the many configurations satisfying the preceding conditions with reference to the others.

Several network configurations may satisfy these rules so that a multiplicity of local molecular environments is possible [112]. Pauling's finding demonstrated that hexagonal ice shows residual entropy even at T=0 K accountable to the proton disorder.

To measure the far and mid infrared spectra of hexagonal ice, we used the cell for liquid samples described in Section 3—2.1. Initially, a thin film of liquid water was placed between the two diamond windows and then temperature was decreased to 12 K. Once this temperature was reached, we heated the sample up to T=300 K, by steps of 10 K , waiting for the stabilization of the temperature (with a precision of ±0.05 K) before the spectrum acquisition at each step.

The spectrum presented in Figure 3.2.3 corresponds to that of ice at T=190 K.

Compared to liquid water (Figure 3.2.2), the I_h spectrum has narrower and more structured bands as a consequence of a better defined environment experienced by the molecules in this crystalline phase. The OH stretching is centered at ~3230 cm^{-1}, about 180 cm^{-1} lower in frequency than in liquid water, correlated to the increase of the hydrogen bonds strength, and is significantly narrower. The bending band experiences a strong reduction of its intensity after crystallization. Indeed, water molecules establish a maximum number of hydrogen bonds in ice, leading to a loss of induced transition dipole moment through the bending motion [111]. Moreover, the bending vibration become more rigid when temperature decreases, causing a shift of this band towards higher frequency compared to bulk [5]. The libration band is displaced to higher frequency (~850 cm^{-1}) and is now completely separated from the connectivity band. This latter evolves strongly from a shoulder in the liquid phase to a thin and intense structure in hexagonal ice. This change witnesses the passage from a disordered phase to a crystalline one. Indeed, the connectivity band appears as a doublet constituted by a sharp band centered at 223 cm^{-1} and a broader band at 163 cm^{-1}.

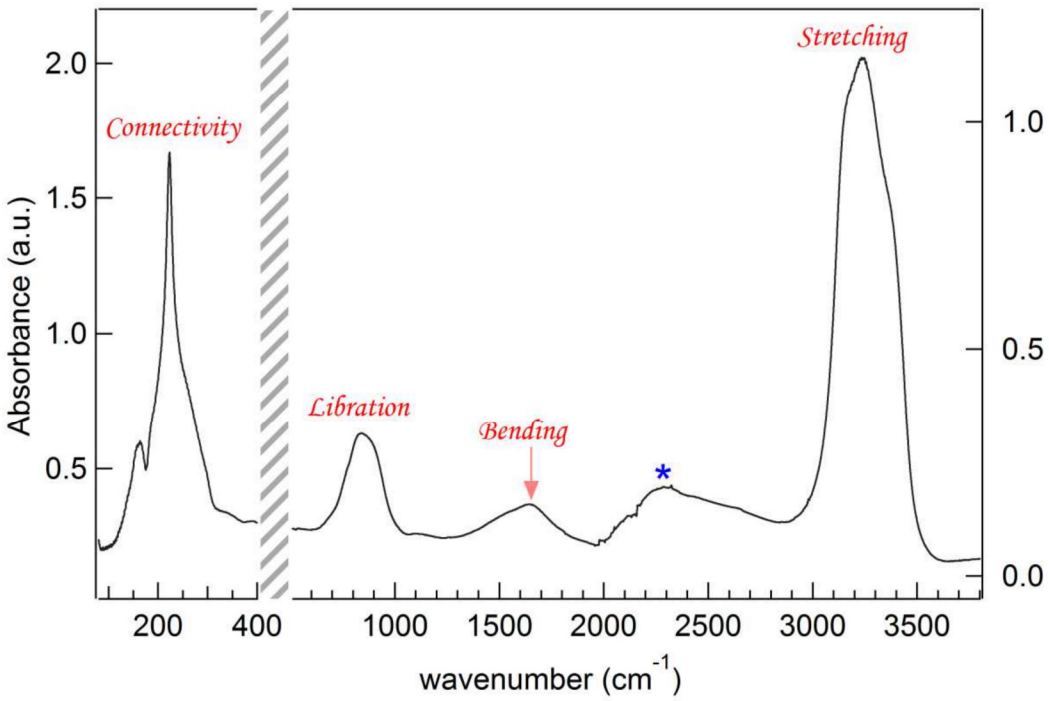

Figure 3.2.3 – FIR and MIR spectra of Ice I_h. Far and mid infrared (0-4000 cm^{-1}) spectra of ordinary ice I_h at 190 K. The two spectral regions are plotted on a different ordinate axis. The symbol * indicates a band most likely due to the combination of the modes ν_1- ν_{lib}.

A broad band around ~2300 cm^{-1} originates most likely from the combination of the stretching and libration modes, with $\nu_1 - \nu_{lib} = 3200 - 900 = 2300$.

Figure 3.2.4 shows the spectra of hexagonal ice measured at T=12 K, 60 K, 120 K, 160 K, 220 K and 270 K (from blue to red). At low temperature, the components of all vibrational bands sharpen up, intermolecular modes (connectivity and libration bands) shift toward higher frequency while the intramolecular OH stretch shift toward lower frequency. This trend is an evidence for further strengthening of the H-bonds as the temperature decreases. Although the phase diagram (Figure 3.2.1) shows that at low temperatures (below T=70 K) the ice is in the proton ordered phase, *XI*, it is clear that our sample is always in its hexagonal form since the transition time from ice I_h to *XI* is of the order of 10^4 years [113, 114] without a catalyst, such as KOH.

At T=12 K, the stretching band is formed by three subcomponents centered at 3135, 3213 and 3350 cm^{-1}. In this case, all the water molecules have a coordination number close to four and the attribution of each component remains uncertain. In the libration band, two components are observed at ~850 and ~915 cm^{-1}. The

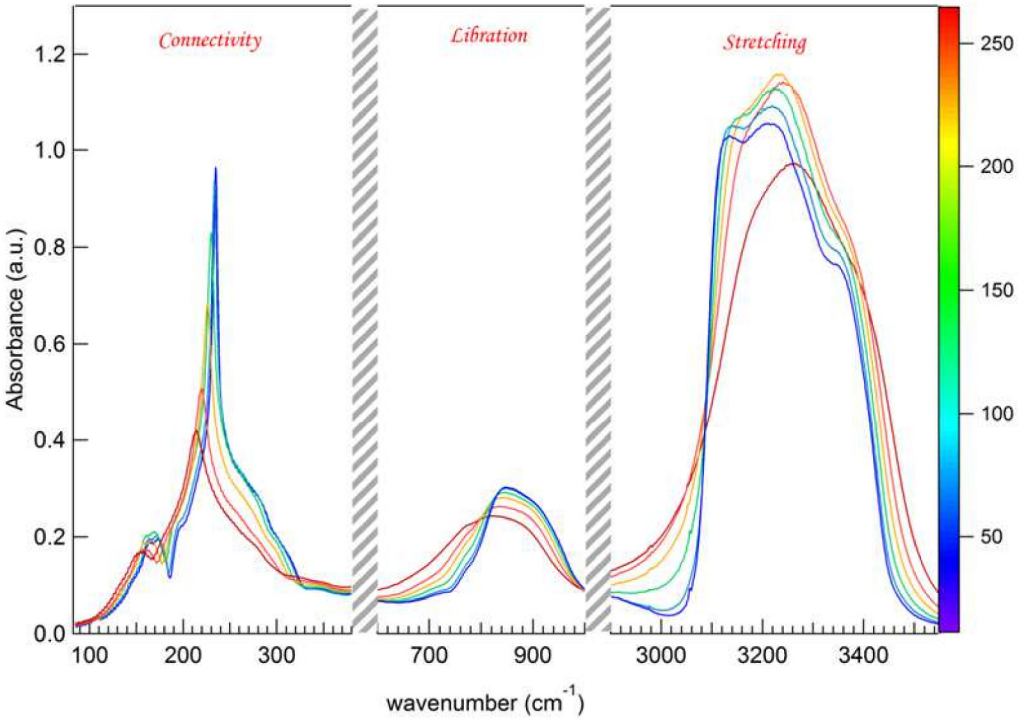

Figure 3.2.4 – Spectra of hexagonal ice. Connectivity (100 —350 cm^{-1}), libration (600 —1000 cm^{-1}) and stretching (3000 —3500 cm^{-1}) bands of hexagonal ice at 12 K, 60 K, 120 K, 160 K, 220 K and 270 K. Colours code on the right axis.

connectivity band (100—330 cm^{-1}) is associated to the translational lattice vibrations. According to Bertie and Whalley [115], in-phase (LA) and out-of-phase (LO) stretching mode of hydrogen bonds within a bilayer form a band at 164 cm^{-1} (that become a doublet at 164 and 174 cm^{-1} at low temperature, namely below T=160 K) and a band at 197 cm^{-1}. The stretching of hydrogen bonds between bilayers (TO) is responsible for the narrow and intense peak at 234 cm^{-1}. This latter band emerges out of the broad structure (from ~234 to ~350 cm^{-1}) originating from LO-TO splitting [112].

3—2.3 ORTHORHOMBIC ICE (*XI*)

Ice *XI* (ice eleven) is the proton-ordered form of hexagonal ice forming orthorhombic crystals. It has an ordered array of protons and all hydrogen bonds parallel to the c-axis are oriented in the same direction [31]. Thus, ice XI is ferroelectric [116]. It was experimentally observed for the first time by Tajima et al. [117] in a calorimetric experiment in which they showed a first-order phase

transition, taking place in KOH doped ice crystals, together with a reduction of the residual entropy of the ice crystal. Indeed, the lattice defects introduced by doping the ice crystals accelerate the rate of rearrangement of proton configurations by catalyzing proton migration.

In order to acquire our spectra of ice *XI*, we placed an aqueous solution of KOH (0.1 M) in the liquid cell. We cooled down the sample to T=65 K and kept it at this temperature for 48 hours. Then, we further decreased the temperature and kept the sample at T=13 K for about one hour. After that, we heated the sample up by steps of 10 K, waiting for the stabilization of the temperature (with a precision of ±0.05 K as for the ice I_h).

In Figure 3.2.5, we show the spectrum at T=13 K.

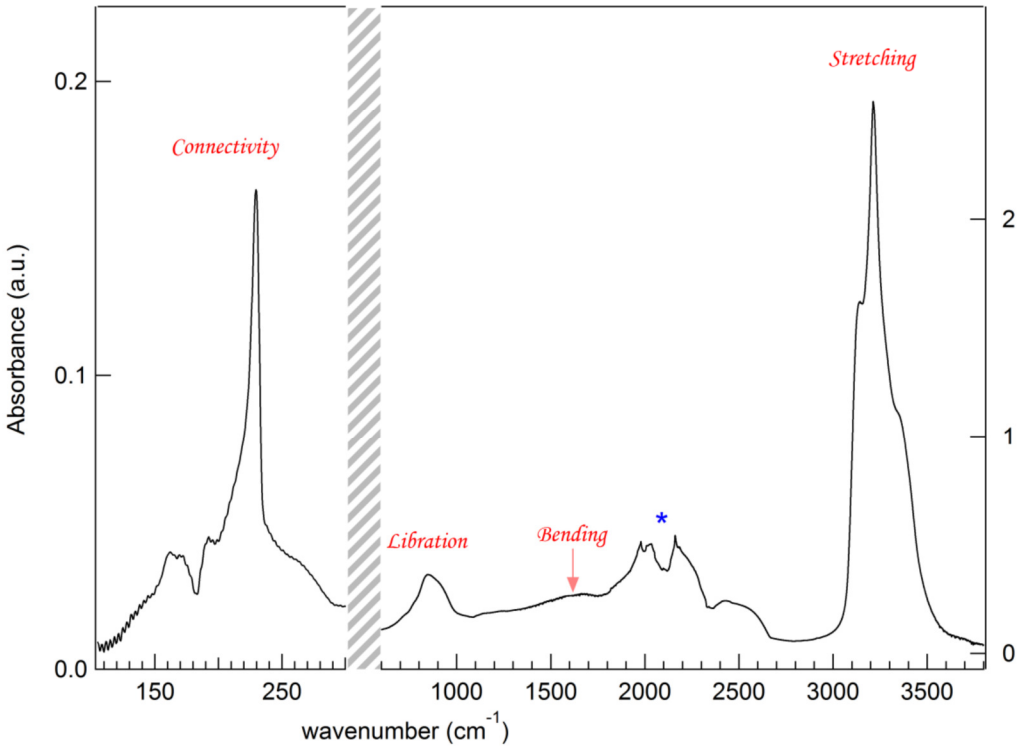

Figure 3.2.5 - FIR and MIR spectra of Ice *XI* at T=13 K. Far and mid infrared (0-4000 cm^{-1}) spectra of ferroelectric ice *XI*. The two spectral regions are plotted on a different ordinate axis. The symbol * indicates the vibrational modes of the cell's diamond window.

The stretching band is formed by three well resolved components at 3141, 3213 and 3350 cm^{-1}. These components appear at the same positions of those observed in the ice I_h at T=12 K (Figure 3.2.4) but their shapes and relative intensities are

different, notably for the intense sharp component at 3213 cm^{-1}. Going down in frequency, we observe the contribution of the CVD diamond window of the liquid cell and the bending band, almost vanished as for all crystalline forms. The shape and position of the libration band are similar to those of hexagonal ice, with the two components at ~850 and ~920 cm^{-1}. However, in the ice I_h at 12K, the intensity of the libration is four times smaller than the intensity of the stretching band at 3213 cm^{-1}, while in ice *XI* the intensity of the libration is almost ten times smaller than that of the stretching band.

In the connectivity band we find several bands slightly redshifted compared to hexagonal ice: the doublet at 162 and 172 cm^{-1} and the band at 191 cm^{-1} attributed to in-phase and out-of-phase stretching modes of hydrogen bonds within a bilayer, as well as the intense sharp peak at 229 cm^{-1}, associated to the hydrogen bonds stretching between layers. It is noteworthy that the broad structure from ~234 to ~350 cm^{-1}, originating from LO-TO splitting, is less intense in the proton-ordered phase.

3—2.4 CUBIC ICE (I_c)

Cubic ice (I_c) is a metastable form of ice as it transforms spontaneously into hexagonal ice (I_h) for temperature above T~240 K. In both configurations, water molecules form layers consisting of six-membered puckered rings. As highlighted in Figure 3.2.6, the difference between ice I_h and ice I_c lies in the stacking of these layers: in ice I_h, each layer is a mirror image of the previous layer, resulting in an overall hexagonal symmetry; in ice I_c, each successive layer is shifted a distance equal to half the diameter of a six-membered ring so that the oxygen atoms are arranged in the same way as carbon atoms in the cubic lattice of diamond [118].

Cubic ice is produced by heating amorphous ice up to T=160 K [119]. We firstly injected deionized water vapor inside the hydration cell, previously cooled down to T=50 K. Amorphous ice is formed upon condensation of the vapor on the cold diamond windows. We then heated the cell up to T=160 K to crystallize the amorphous ice and obtain cubic ice. Once the cubic ice was formed, we cooled the sample down to T=50 K in order to acquire spectra of ice I_c from 50 K to 150 K by steps of 10 K. The spectrum of ice I_c, shown in Figure 3.2.7, was measured at T= 50 K.

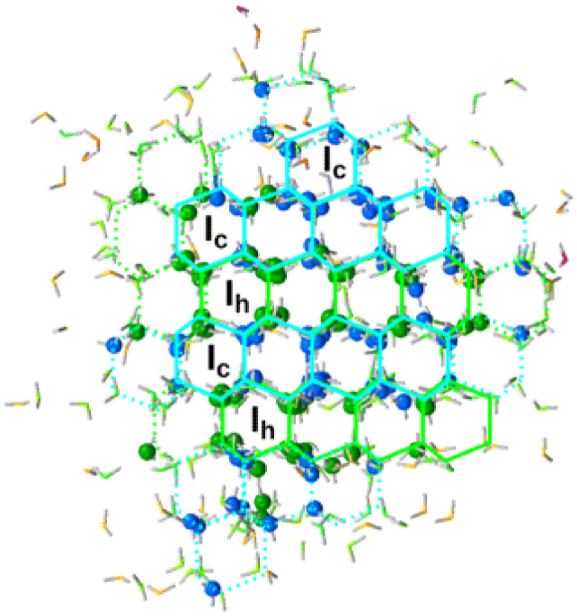

Figure 3.2.6 – Cubic and hexagonal stacking in ice. The snapshot of ice crystal structure at T=220 K, observed in Monte Carlo molecular simulations shows the oxygen atoms in the ice I_h environment in green and those in the ice I_c configuration in blue. Molecules involved in the crystalline structure are shown as spheres, those not involved in the crystalline structure are shown with sticks. Figure from [118].

Unexpectedly, the mid infrared spectrum (800—3600 cm^{-1}) resembles more to ferroelectric ice *XI* (Figure 3.2.5) than hexagonal ice I_h (Figure 3.2.4). Indeed, the stretching band presents three subcomponents at 3138, 3211 and 3344 cm^{-1}, with the second component extremely sharp and intense, not observed in ice I_h. Moreover, the intensity of this component is fourteen times larger than that of the libration band, a value closer to that observed in ferroelectric ice than in hexagonal ice. It is tempting to associate the spectrum in Figure 3.2.7 to the proton-ordered counterpart of cubic ice but, as mentioned in Section 3—2.2, phase transition of proton-disordered ice to proton-ordered ice requires an extremely long time without an expedient, such as the presence of KOH in the water sample [120] or the use of electron beam irradiation [114]. One can not rule out the presence of some impurity that may have caused the transition nevertheless.

The connectivity band presents some differences. The doublet at low frequency is replaced by a single peak at 161 cm^{-1}, the peak at 195 cm^{-1} is less resolved and looks like a shoulder at the low frequency tail of the intense peak at 228 cm^{-1}.

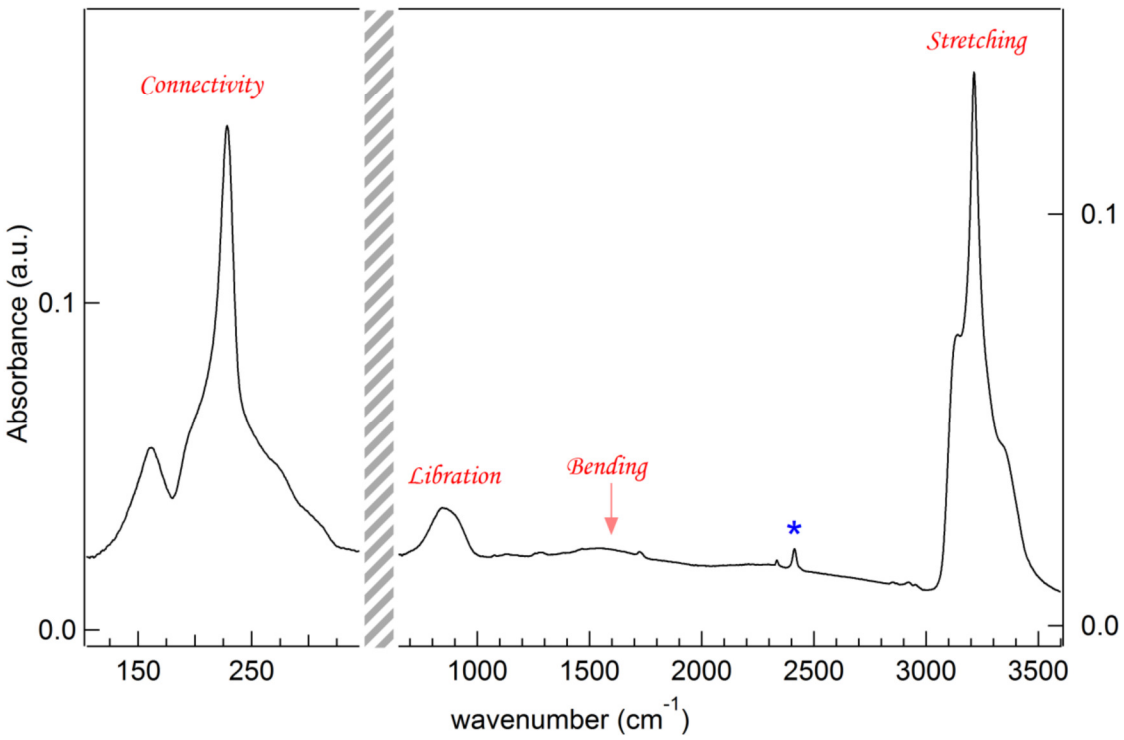

Figure 3.2.7 - FIR and MIR spectra of Ice *Ic*. Far and mid infrared (0-4000 cm^{-1}) spectra of the metastable cubic ice at 50 K. The two spectral regions are plotted on a different ordinate axis. The symbol * indicates the presence of a small amount of CO2 in the water vapor injected on the hydration cell to produce cubic ice.

3—2.5 AMORPHOUS ICE

Amorphous ice was obtained upon condensation of water vapor on the diamond windows of the hydration cell at T=50 K, as described in Section 3—2.4. Its far and mid infrared spectra are shown in Figure 3.2.8.

The thin bands associated to crystalline structures are absent in the amorphous ice and the whole spectrum resembles that of liquid water (Figure 3.2.2) since both liquid and amorphous ice are unordered phases. Moreover, the bending band, not observed in the spectra of other crystalline forms, is present and assumes an asymmetric shape. Its presence in the amorphous ice spectrum may confirm that this mode reflects water molecules that do not lie in a symmetric tetrahedral environment [5]. Moreover its position is the same as liquid water, 1650 cm^{-1}, while all the other bands are shifted as a result of fully established network (~4 hydrogen bonds per molecule) not achieved in liquid water: the intramolecular OH stretch is redshifted at 3295 cm^{-1}, the intermolecular modes of connectivity and libration are blueshifted at 213 cm^{-1} and 770 cm^{-1}, respectively.

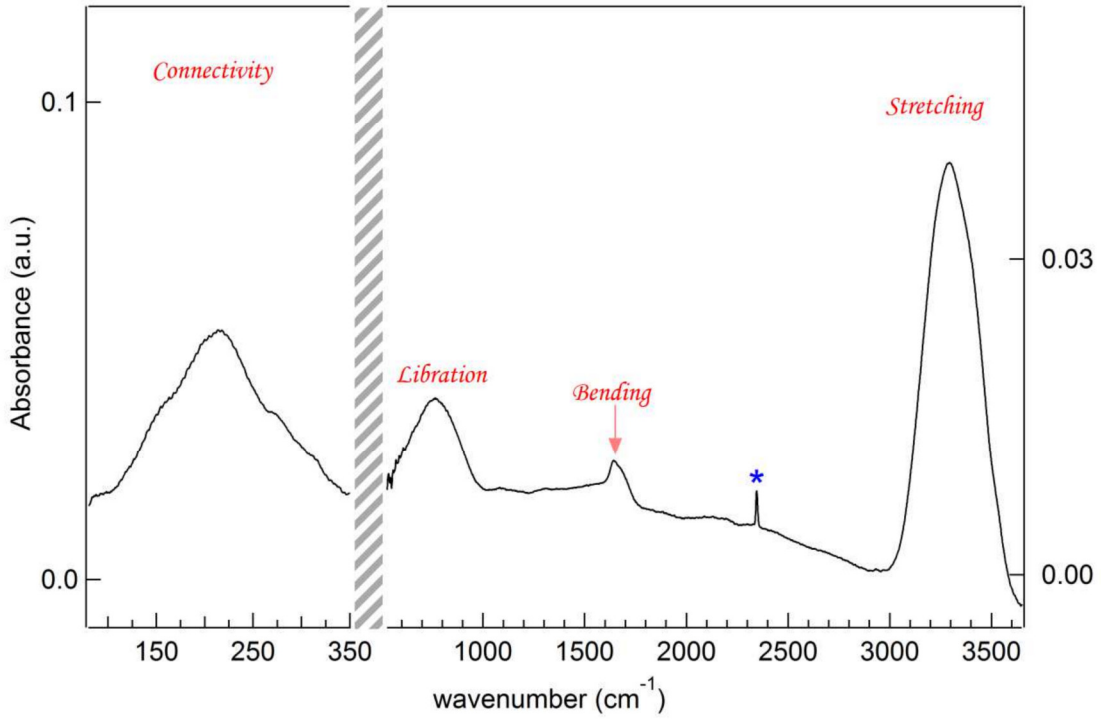

Figure 3.2.8 – FIR and MIR spectra amorphous Ice. Far and mid infrared (0-4000 cm^{-1}) spectra of and amorphous ice at 50 K. The two spectral regions are plotted on a different ordinate axis. The symbol * indicates the presence of a small amount of CO2 in the water vapor injected on the hydration cell to produce cubic ice.

3—2.6 A COMPARISON BETWEEN ICE PHASES

In order to emphasize the differences and the similarities observed in the infrared spectra of crystalline (I_h, I_{XI} and I_c) and amorphous ice, described previously, we compare the spectra in three regions showing the superimposition of the connectivity bands (between 110—340 cm^{-1}, in Figure 3.2.9), the libration bands (between 540—1150 cm^{-1}, in Figure 3.2.10) and the stretching bands (between 3000—3680 cm^{-1}, in Figure 3.2.11). Bending bands are not shown due to their low intensity in crystalline structures. It is worth to remember that each sample was prepared independently and differs in thickness, hence, the incident beam probes a different number of water molecules.

All spectra displayed here are acquired at T=70 K and the absorbance values are normalized to make more evident a parallel between the subcomponents of each band.

It is clear from Figure 3.2.9 that the connectivity band presents narrow bands only when the ice lattice is ordered. While the peak at ~162 cm^{-1} is common for the three crystalline structures, two bands at ~172 and ~192 cm^{-1} are observed only in the spectra of I_h and I_{XI}. We then associate these two bands to oxygen atoms order. A shoulder at low frequency (~140 cm^{-1}) is observed only in I_{XI} spectrum and can be accountable for the proton order. From Figure 3.2.9, it is also evident that all bands in the connectivity region are shifted towards higher frequency in hexagonal ice spectrum.

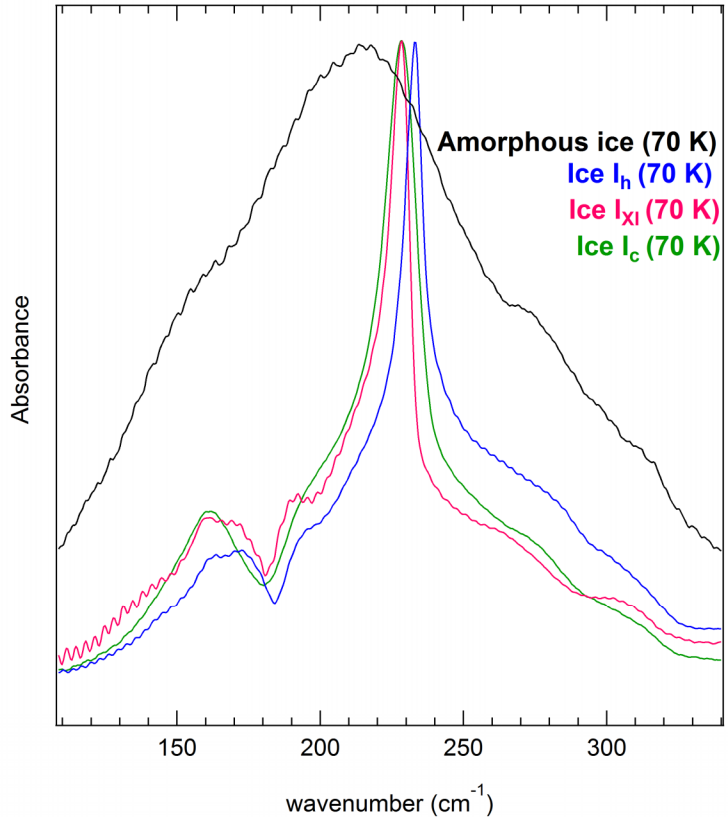

Figure 3.2.9 – Comparison between connectivity bands. Far infrared spectra (110—340 cm^{-1}) of amorphous ice (black), hexagonal ice (blue), ferroelectric ice (pink) and cubic ice (green) at T=70 K.

In the spectrum of amorphous ice, we can observe a weak band at ~160 cm^{-1} emerging out of a broader band centered at ~213 cm^{-1}. This latter band reveals the disorder arrangement of water molecules. Also, its position suggests that the hydrogen bond is stronger in crystalline forms in which an intense and narrow peak is observed at higher frequency (~228 cm^{-1} in cubic and ferroelectric ice, 234 cm^{-1} in hexagonal ice). This peak is slightly broader in the cubic form than in ice I_{XI} but its width do not depend from the proton order since the peaks in ferroelectric

and hexagonal forms have the same width. On the contrary, the band from 250 to 320 cm^{-1} is larger in the hexagonal ice revealing most likely a proton disorder effect.

Finally, it is noteworthy that two weak bands at ~275 and ~305 cm^{-1} are common for the four spectra.

According to Arakawa et al. [121] and Geiger at al. [120], the decrease of the librational width is attributable to the ordering arrangements of hydrogen atoms in ice. Indeed, the librational vibration of the water molecule is a motion of the two hydrogen atoms which is consequently sensitive to the hydrogen ordering. Under such assumption, the proton ordering of ice I_h [121] and ice I_c [120] was monitored through variation of the libration band width.

In Figure 3.2.10, we show the libration band region of the four ice forms at T=70 K (baseline differs since the spectra are acquired under different experimental conditions). In amorphous ice, the broad full width at half maximum (FWHM~245 cm^{-1}) and its position (~770 cm^{-1}) can be easily associated to the water molecules disorder. All crystalline forms are shifted at higher frequency and present a maximum at ~850 cm^{-1}, while the component at ~920 cm^{-1} is slightly less intense in proton-ordered ice I_{XI}. In the study of Arakawa et al. [121], the libration band FWHM undergoes a decrease of ~40 cm^{-1} upon proton ordering (from 220 cm^{-1} in hexagonal ice to 180 cm^{-1} in ferroelectric ice). A smaller effect is observed by Geiger at al. [120], where a decrease of only 10 cm^{-1} was observed on a ~200 cm^{-1} band width.

Our FWHM values are significantly lower for both ordered- and disordered-proton phases. However, as observed in Figure 3.2.11, we find that the width of ice I_{XI} (pink) is always narrower than hexagonal ice (blue), while the FWHM of cubic ice (green) and hexagonal ice are comparable. We can also observe a gradual decrease of the libration width during transition from amorphous (black) to cubic ice.

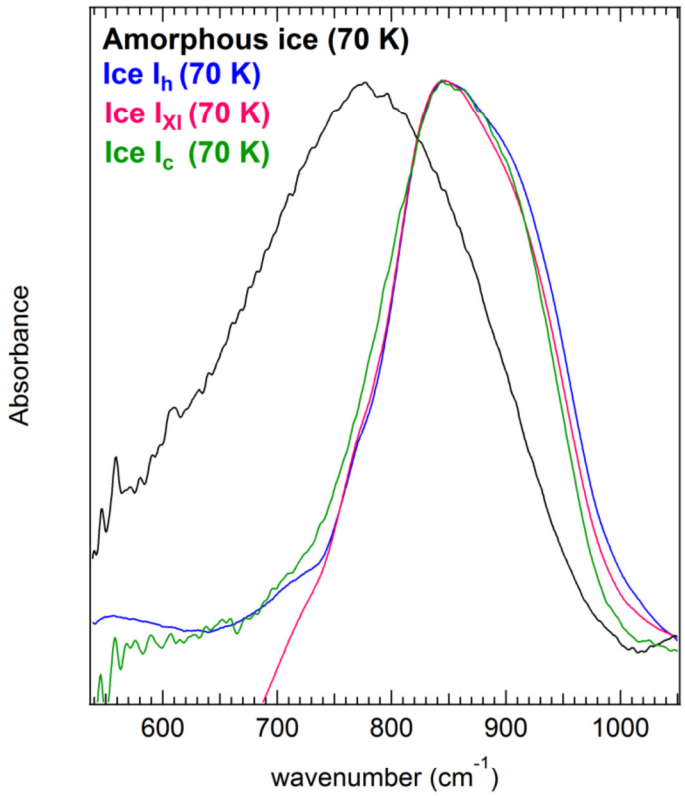

Figure 3.2.10 – Comparison between libration bands. Mid infrared spectra (540—1050 cm^{-1}) of amorphous ice (black), hexagonal ice (blue), ferroelectric ice (pink) and cubic ice (green) at T=70 K.

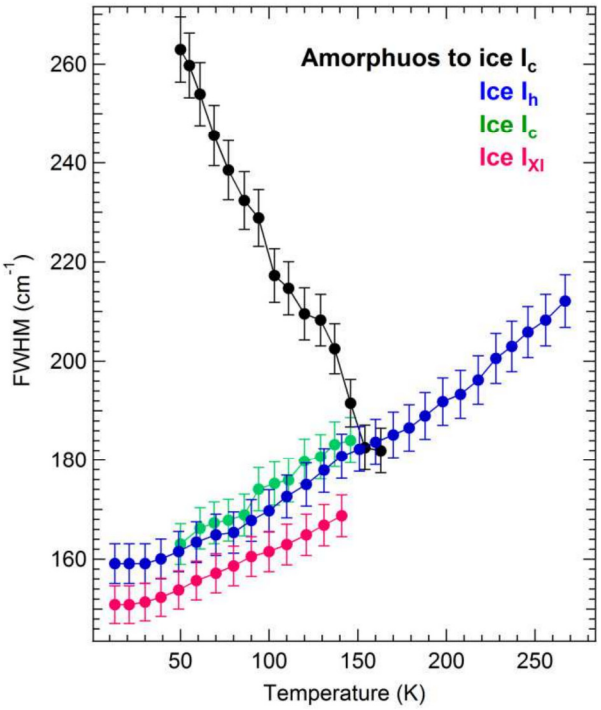

Figure 3.2.11 – Libration bands FWHM of ice phases. Full width at half maximum of amorphous ice (black) from 50 to 163 K, hexagonal ice (blue) from 13 to 267 K, cubic ice (green) from 50 to 146 K and ferroelectric ice (pink) from 13 to 141 K.

Major differences between crystalline structures are observed in the stretching band, as shown in Figure 3.2.12. Three subcomponents are observed at approximately the same positions (~3141, ~3213 and ~3350 cm^{-1}) but their relative intensity varies significantly. In ice I_{XI} and I_c, the intermediary peak is narrower and more intense suggesting that a larger number of molecules experience the same environment with respect to the hexagonal form.

Once again, amorphous ice presents a less resolved stretching band as a consequence of the molecular disorder.

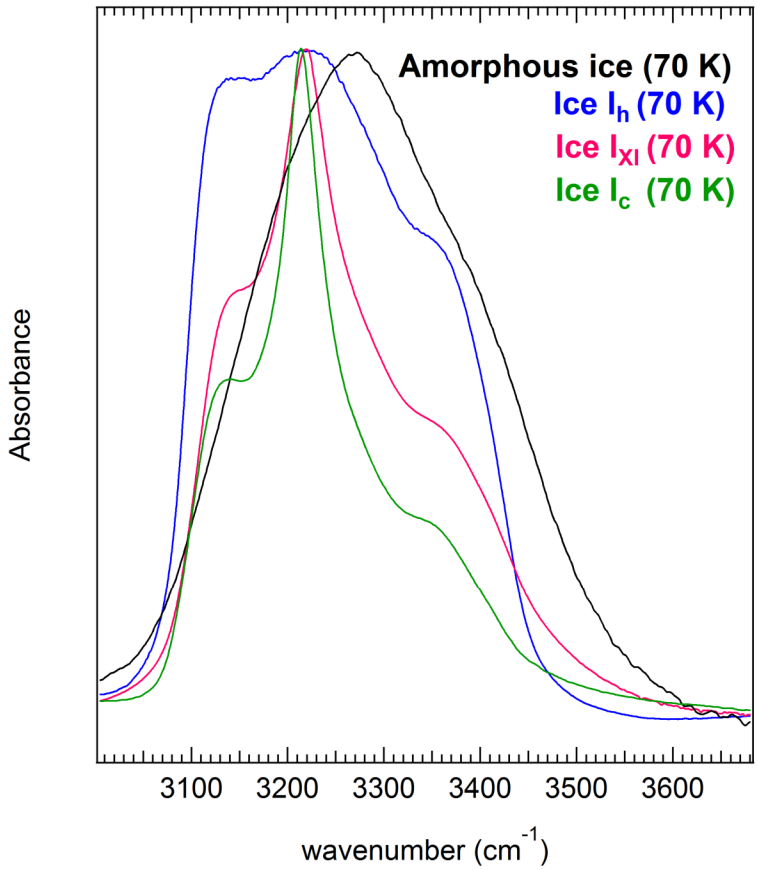

Figure 3.2.12 – Comparison between stretching bands. Mid infrared spectra (3000—3680 cm^{-1}) of amorphous ice (black), hexagonal ice (blue), ferroelectric ice (pink) and cubic ice (green) at T=70 K.

3—2.7 CONCLUSIONS

This Chapter provides experimental evidence to the sensitivity of the infrared spectroscopy to the local environment of water molecules. General trends are observed upon crystallization: more resolved bands appear, intermolecular and intramolecular modes shift towards higher and lower frequency, respectively, as hydrogen bonding strengthens. Moreover, we have shown that crystalline phases spectra of ice I_h, I_{XI} and I_c differ from each other, mainly in the connectivity and the stretching bands. Oxygen atoms arrangement in hexagonal or cubic lattices promote slight differences in the connectivity band, between 130 and 180 cm^{-1}, and the intermediary peak of the stretching band (at ~3213 cm^{-1}) which is more intense in cubic ice form. Proton ordering causes mainly a slight decrease of the FWHM of the libration band and promotes an enhancement of the intermediary peak of the stretching band at the expense of the two side bands in comparison with the proton-disordered counterpart.

It would be interesting to perform an X-ray diffraction study on equivalent systems, i.e. upon equivalent experimental conditions, in order to obtain definitive information on their crystal structure.

CHAPTER 4

LOW-DIMENSIONAL WATER NETWORK IN POROUS VYCOR

The reduced freezing point of water confined in narrow pores is often exploited as expedient to reach *supercooled* water to probe the liquid phase between the homogeneous nucleation temperature (T=235 K) and the crystallization temperature of glassy forms of water (T=150 K).

However, we show here the not negligible effect of the surface contribution proving that interfacial water, represented by the two-dimensional network interacting with the hydrophilic Vycor's pores (chemically and dynamically inert), exhibits transitions in this range of temperature, due to specific surface interactions.

4—1 COMPETING COEXISTING PHASES IN 2D WATER

The effect of a hydrophilic surface on the structure, density and dynamics of water molecules at the interface has been investigated using partially hydrated Vycor, described in Section 1—3. In order to adsorb one monolayer of water molecules on the pores' surface, the 80 μm thick Vycor was placed in the hydration cell (Section 2—3) and a water vapor pressure of 9.1 mbar, corresponding to ~30% of relative humidity (see Eq. 1.2.1), was applied to the sample. At such water vapor pressure, all accessible silanol groups (Si-O-H) on the pore walls establish a hydrogen bond with an adsorbed water molecule. Indeed, as it is observed in the infrared spectra, the OH oscillators of the silanol groups produce a specific band at 3695 cm^{-1} when Vycor is dry that disappears upon hydration until RH~30% (as shown in Figure 4.1.1).

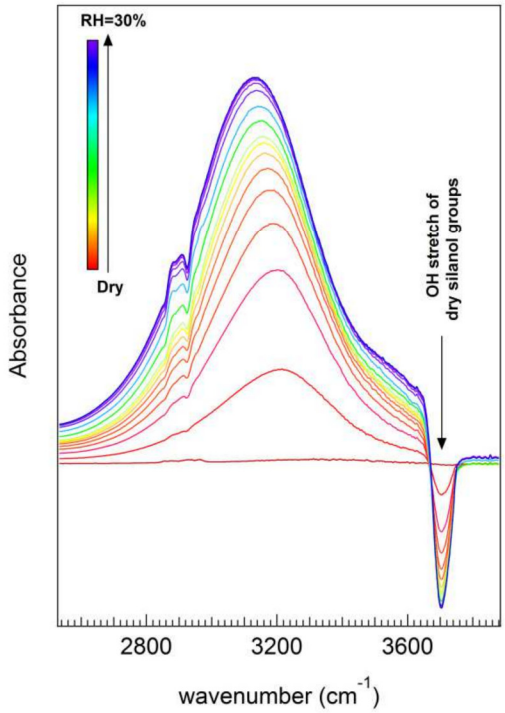

Figure 4.1.1 – OH stretching band of Vycor during hydration (from dry to RH=30%). Spectra of difference during hydration, from the dry sample (red) to RH=30% (blue). Vycor dry is taken as reference. The OH stretch band of the silanol groups disappear as water is adsorbed in Vycor's pores.

To highlight the contribution of interfacial water, we show absorbance spectra (Eq. 2.2.9) using the dry Vycor spectra as reference $I_0(v)$.

The hydrogen bond strength was monitored through the connectivity band (100—250 cm^{-1}) and the OH stretching band (2700—3600 cm^{-1}) between T=70 K and T=300 K. Comparing the spectra with those of amorphous and crystalline ice, presented in Chapter 3, we could affirm that interfacial water at low temperature is not crystalline but it establishes a strong hydrogen bond with the hydrophilic surface.

A change in the connectivity band and a shift of the stretching band, both occurring at T~160 K, evidence a modification in the H-bond network. At higher temperature, no more information can be obtained from the connectivity band, which is hidden by the libration band. However, further shifts of the OH stretching band show two additional modifications in the water network at T~220 K and T~250 K.

Changes in the hydrogen bond network at these temperatures are observed with other experimental techniques (specific heat measurements, solid-state quadrupolar NMR, quasi-elastic neutron scattering) so that a percolation model on the connectivity of the H-bond network has been proposed: by increasing temperature, *(i)* liquid 4-HBonded molecules patches appear among amorphous interfacial ice water at T~160 K, *(ii)* these domains then percolate at T~220 K and (iii) cover the surface at T~240 K.

This study shows that the effect of the hydrophilic surface on interfacial water is not negligible. Hence, transitions observed in supercooled water trapped in narrow pores cannot be only considered as a direct evidence of the low temperature critical point that is supposed to separate two liquid phase at T~220 K.

Competing coexisting phases in 2D water

Zanotti, J.-M.; Judeinstein, P.; Dalla Bernardina, S.; Greff, G.;
Brubach, J.-B.; Roy, P.; Bonetti, M.; Ollievier, J.; Sakellariou, D.;
Bellissent-Funel, M.-C. *Nature Comm.*, submitted.

ABSTRACT

The surprising properties of bulk water come from an unusual delicate balance of interactions on length scales encompassing several orders of magnitudes: i) the Hydrogen Bond (HBond) at the molecular scale and ii)the extension of this HBond network up to the macroscopic level. Here, we address the physics of water in the case where the three dimensional extension of the HBond network is frustrated so that the molecules are forced to organize in only two dimensions. We show that this 2D-water is characterized by the coexistence of low and high-density transient clusters. We elucidate the surprising structural, dynamical and thermodynamical properties of this system. These findings shed light on central and critical aspects of the fundamental debate about the existence of a low temperature critical point in water. They also have a high relevance in all the fields where interfacial water is at play: from cement technology to biology.

4—1.1 INTRODUCTION

In bulk water, local energetics and long range connectivity come along with a very specific local three-dimensional (3D) tetrahedral organization of the hydrogen bond (HBond) network (Figure 4.1.2a). Altogether these properties drive the numerous so-called “water anomalies”.[1,2]

Transport of water molecules in Carbon NanoTubes (CNT), can be cited as an emblematic example[3] of how the frustration of the natural 3D tetrahedral organization of the hydrogen bond network profoundly modifies the water physical properties: when trapped inside CNT, water is found to flow-up three orders of magnitude faster than predicted by the continuum hydrodynamics picture.

This is the consequence of the peculiar organization of the water hydrogen bond network imposed by the restricted radial volume of the tube. In a 1.4 nm diameter CNT, as no interaction with the graphenic CNT internal structure is possible,[4] the water form a 1D central chain surrounded by a corona of water molecules. The chain-water molecules, experiencing only two HBonds (instead of on average 3 to 4 in bulk), they lay in a very metastable state showing an extremely high mobility: they can adopt a liquid-like behavior at temperatures as low[5] as 150 K.

In this paper, we go deeper in the behavior of the HBond network under reduced dimensionality and focus on the physics of water in two dimensions (2D). This topology can be, for example, obtained by water vapour adsorption as a monolayer onto the surface of Vycor®[6], a hydrophilic porous silica glass (Figure 4.1.2b). As the Vycor surface is uniformly covered with silanol (Si-OH) groups, water molecules interact with the neighbouring water molecules, but

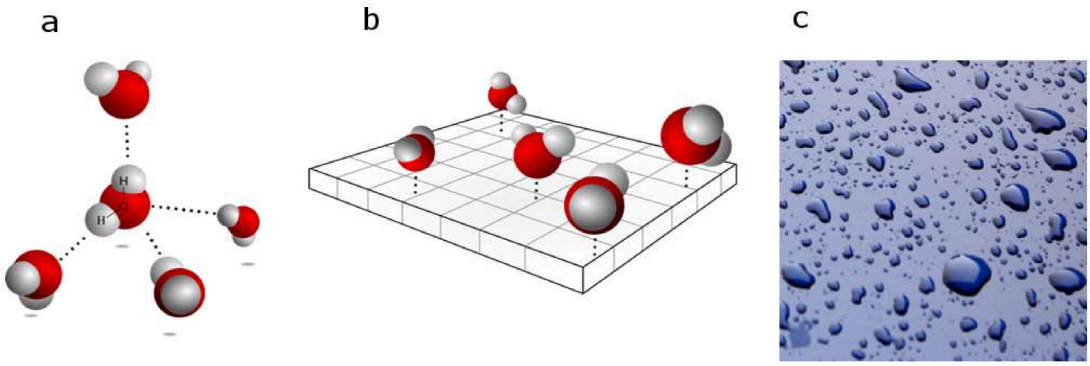

Figure 4.1.2 – Illustrations of three-dimensional and two-dimensional water. a) In bulk liquid water, a molecule is connected by HBonds (dotted lines) to an average of slightly less than four molecules. We represent here the perfect tetrahedral geometry found in hexagonal ice (After Wikipedia commons). b) In this paper, water is adsorbed as a monolayer (6 wt%) onto the surface of Vycor, a porous hydrophilic silica glass whose surface is uniformly covered with silanol (Si-OH) groups. Vycor surface presents 18 silanol groups by square nanometer. This sketch is a realistic graphical representation of the microscopic structure of the 2D-water we consider: the water molecules form a single monolayer. In this topology, the ideal tetrahedral arrangement shown in (a) is lost and each water molecules interact with the neighboring molecules with distorted HBonds (not shown). All the water molecules are nevertheless always HBonded (dotted lines) to a surface silanol. For clarity, these groups are not explicitly represented, but each basal square on the sketch stands for the specific surface of a single silanol. c) Artist view of the structure of interfacial water at the mesoscopic scale this paper concludes to: interfacial water is a heterogeneous structure where high density monolayer patches (dark blue) coexist with low density ones (light blues). The temperature dependence of this structure on the whole investigated temperature range is shown on Figure 4.1.7.

also with the surface, only through HBonds. This is indeed a key condition to probe the sole influence of the dimensionality on the HBond energetics and connectivity, and discard any other specific interaction with the surface.

We combine specific heat measurements, Far and Mid Infra-Red (FIR & MIR) spectroscopy, Magic-Angle Spinning Solid-State Quadrupolar NMR (SS-NMR) and Quasi-Elastic Neutron Scattering (QENS) to experimentally investigate the physical behaviour of this Interfacial Water (IW) over a broad temperature range (100-300 K).

Instead of addressing an *average* water dynamics, we gain considerable physical insight by considering separately the rotational and translational modes to the water molecules overall dynamics[10]: while QENS probes both the rotational and the translational contributions, SS-NMR focuses on the sole rotational contribution and also allows identifying strong dynamical heterogeneities.

At this point, we consider the extension of the hydrogen bond network that, as they probe the system at the local scale (few angstroms), the spectroscopic techniques above are not sensitive to. The usual way to address its mesoscopic structuration is through molecular dynamics simulations, but in this work, we describe this network using a simple and purely analytical mean-field percolation model that focuses on the temperature dependence of the statistics of the four HBonds coordinated water molecules.

We reach the conclusion that, over a wide temperature range, 2D water is a heterogeneous system that can be described as the coexistence of two transient phases (Figure 4.1.2c) of different densities, and that the fraction of each density species is strongly controlled by the temperature.

4—1.2 RESULTS

4—1.2.1 COMPARED TO ICE, INTERFACIAL WATER SHOWS A LARGE SPECIFIC HEAT SUGGESTING SPECIFIC DYNAMICAL MODES AT LOW TEMPERATURE

Nanometric confinement of molecular fluids is a classical route to stabilize metastable states by achieving the frustration of the bulk natural fluctuations

and/or phase transitions. Figure 4.1.3 illustrates how confinement can lead to a dramatic downshift of the water phase diagram: the clear endothermic signal with onset at 250 K in fully hydrated Vycor (25wt% i.e. the 50 Å characteristic size Vycor pores are filled with water) is the signature of ice melting. Next to this 23 K depression of the melting point compared to the bulk situation (the so called Gibbs-Thomson effect[7,8]), it is noteworthy how larger is the specific heat (C_p) of water as a monolayer in Vycor compared to bulk ice or fully hydrated Vycor. This heat capacity excess is a strong evidence of the large mobility of interfacial water compared to that of ice (in bulk or confined within Vycor). Also, according to the statistical physical approach, this large C_p values suggest large entropy fluctuations ($C_p \sim \langle \delta S^2 \rangle$.

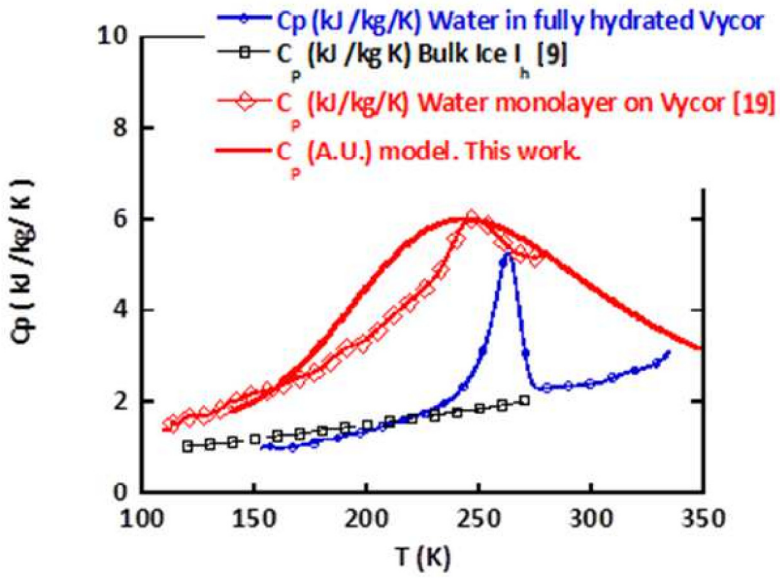

Figure 4.1.3 – Specific heat of bulk and confined water. Specific heat (C_p) measurement of water confined in fully hydrated (25wt%) and monolayer hydrated (6wt%) Vycor (the dry Vycor contribution has been subtracted). Specific heat of bulk hexagonal ice[9] is given for reference. The very significant specific heat excess of 2D water compared to bulk ice of Vycor confined ice indicates a large mobility of interfacial water compared to ice (bulk or confined within Vycor). The C_p derived from the percolation model presented here is shown as a full red line.

The dynamics of interfacial water has already been analysed in details by neutron diffraction and quasi-elastic neutron scattering. In QENS, in a way similar to the Debye-Waller effect, the Q dependent Gaussian intensity loss $e^{-Q^2 \cdot \langle u^2 \rangle}$ can be related to the spatial extension (<u^2>) of atoms around their equilibrium position (also referred as Mean-Square Displacement, MSD).

Furthermore, the exact Q dependence of the neutron intensity loss enables to assess, $\langle u^2 \rangle_{Rot}$ and $\langle u^2 \rangle_{Trans}$, the MSD due to respectively the rotational and translational modes of the water molecules.[10]

QENS data as a function of temperature indicate[11] (see Figure 4.1.8), that on a 1 nanosecond timescale:

(i) Below 155 K, interfacial water is a Low Density Amorphous (LDA) ice (with $Q_0=Q_0^{LDA}=1.71$ Å^{-1} the first peak in *S(Q)* structure factor) showing no long range translational dynamics ($\langle u^2 \rangle_{Trans} \approx 0$). Above 160 K, no change is observed in water density but translational dynamics becomes possible on a 1 nanosecond timescale, as shown by the $\langle u^2 \rangle_{Trans}$ non null value. This is a clear signature of a glass transition.

(ii) On increasing the temperature, $\langle u^2 \rangle_{Trans}$ and $\langle u^2 \rangle_{Rot}$ increases linearly as the related correlations times decrease. At 220 K, however, the correlation times associated to $\langle u^2 \rangle_{Rot}$ becomes suddenly more temperature dependent.

(iii) At 250 K, this Low Density Liquid (LDL) experiences a transition to Higher Density Liquid HDL ($Q_0=1.86$ Å^{-1}) and rotational and translational correlation times related to $\langle u^2 \rangle_{Trans}$ and $\langle u^2 \rangle_{Rot}$ significantly decrease and become shorter than the accessible time window of the spectrometer (1 ns).

4—1.2.2 INFRA-RED SPECTRA EVIDENCE PHASES AND/OR DYNAMICAL TRANSITIONS IN THE 160, 220 AND 250 K REGIONS

The temperature dependence of MIR and FIR absorbance spectra of interfacial water from 70 to 300 K are shown on Figure 4.1.4. In each case, the reference used for calculating the absorbance is the dry sample, before hydration and at the same temperature.

The MIR and FIR data show a common trend: depending on the temperature, the spectra of 2D-water resemble the one of the LDA amorphous ice or liquid water but are very different from the one of hexagonal ice. While indirect, this is nevertheless evidence that the structure of interfacial water is not crystalline.

The intermolecular OH stretching band (also referred as the connectivity band[12]) in the 100-350 cm^{-1} region is shown on Figure 4.1.4a. This mode is a

combination of intermolecular hydrogen bond O-H···O stretching and bending related to clusters of water molecules. Since this mode only involves small protons displacements, this excitation is poorly detected in inelastic incoherent neutron scattering so that this FIR derived information is a real asset in the scope of the present paper.

In order to follow the changes of intensity of this connectivity band, the region between 106 cm^{-1} and 236 cm^{-1} was integrated and a background corresponding to the contribution of the libration band, starting at 250 cm^{-1}, was subtracted. The result of this subtraction and the related difference-band integration are presented Figure 4.1.4c. It shows that the connectivity intensity experiences only few changes between 70 K and the 150 K region, but that it strongly decreases above 150-160 K. This indicates a modification of the connectivity of the HBond network around 160 K. This mode is not detected anymore above 175 K.

MIR spectra of 2D water (Figure 4.1.4b) can be decomposed in three distinct intramolecular bands: 1911-2508 cm^{-1} related to a mixing of bending and libration modes, and 2912-3149 cm^{-1} and 3183-3356 cm^{-1} two bands related to the OH stretching mode. A monolayer of water molecules on Vycor produces an OH stretching mode at 3230 cm^{-1}. The peak position reveals that the HBonds at play in the system are significantly stronger than in bulk liquid water. A numerical estimation of the enthalpy of these HBonds will be given below.

Measurements as a function of temperature between 75 and 300 K show that the frequency of the stretching band maximum shifts from lower to higher frequencies as the temperature increases. This is perfectly in line with previous deep inelastic neutron scattering measurements[13]. As shown by IR study of ice VII under pressure[14], a shift of the intra-molecular stretching OH towards higher energy is correlated with a decrease of the average H-Bond strength**.** As shown in Figure 4.1.4d, two transitions at 160 K and 250 K suggest noticeable changes of the HBond strength at these temperatures.The MIR spectra also carry critical information about the sample characterization and in particular its temperature stability: the silanol groups (Si-O-H) of the Vycor matrix appear at 3695 cm-1 as a negative band. This shows that the number of free silanol groups of the dry Vycor significantly decrease upon water adsorption. The fact that the band remains stable shows that for all temperatures, the water molecules remain

bonded to the surface and no sublimation or lyophilisation occurs at any temperature.

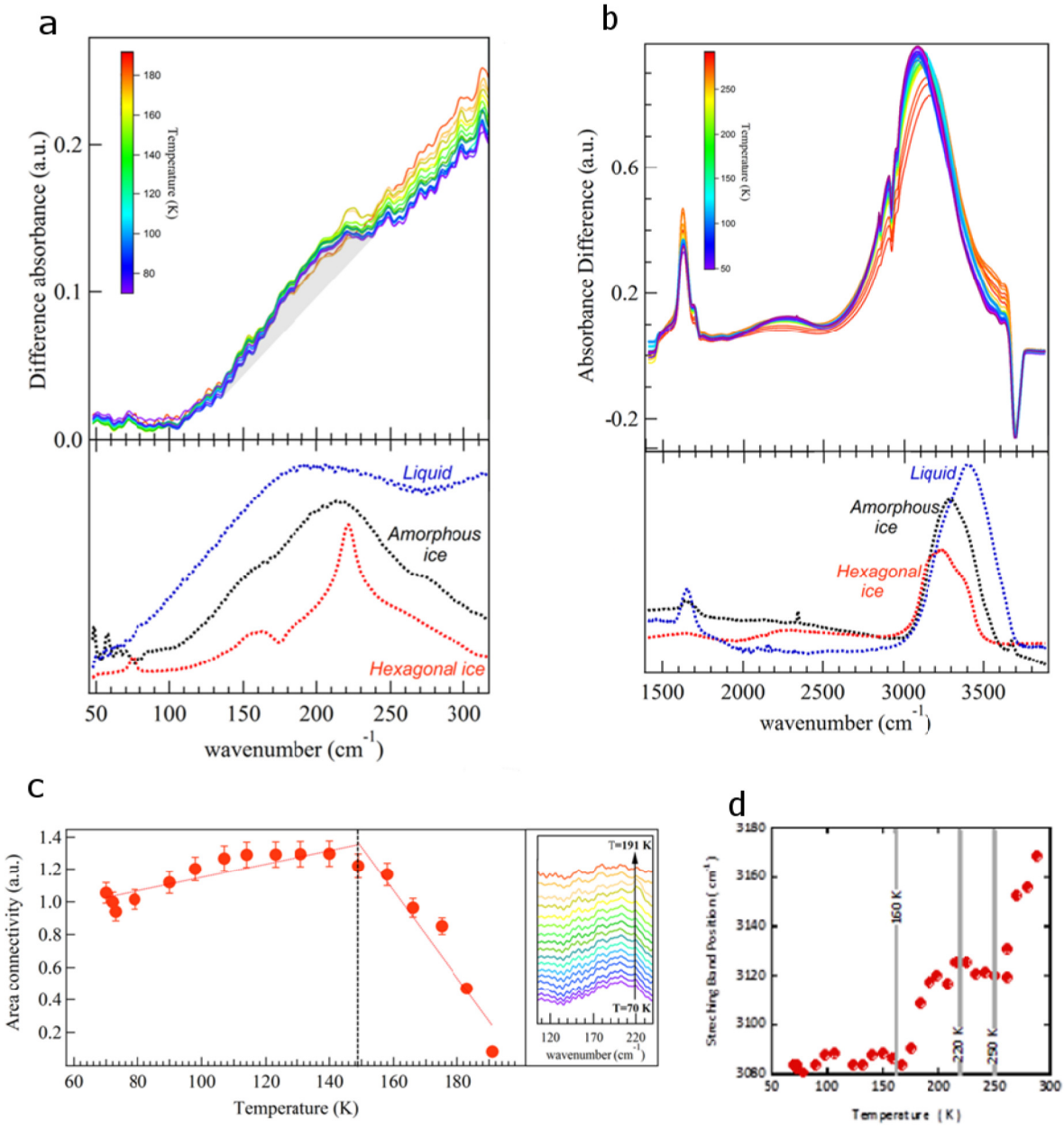

Figure 4.1.4 –Temperature dependence of FIR (a) and MIR (b) spectra of interfacial water from 70 to 300 K. In each case, the signal of hexagonal or amorphous ice (LDA) and liquid water are shown for comparison. The weak and broad band around 210 cm^{-1} shown in a) is the connectivity band. It is superimposed on the libration band starting at 250 cm^{-1}. c) Integrated intensity of the spectra shown in the inset on the right. These are the difference spectra (grey area shown in a)) of the FIR connectivity band and a linear background accounting for the libration band. d) Position of the maximum of the MIR stretching band as a function of temperature.

4—1.2.3 SOLID STATE QUADRIPOLAR NMR REVEALS A STRONG DYNAMICAL HETEROGENEITY AND THE TEMPERATURE DEPENDENCE OF A LIQUID-LIKE AND A SOLID-LIKE PHASE

Since both neutron scattering and IR spectroscopy probe the ensemble average of the water molecules dynamics, no information is available about any possible dynamical heterogeneity. ^{2}H SS-NMR spectra of water as a monolayer in Vycor have been recorded over a large temperature range (Figure 4.1.5). At the lowest temperatures, all these NMR spectra show two very distinct contributions: a broad *Pake* patterned doublet (≈240 kHz broad) and a narrower signal (≈20 kHz FWHM). The first signal demonstrates the presence of immobilized water molecules (*solid-like*), while the second one, assigned to water molecules experiencing a significant degree of mobility, evidences a *liquid-like* water fraction, *f*, within the sample. In addition, quadrupolar NMR can be used to directly separate translational and reorientational dynamics.

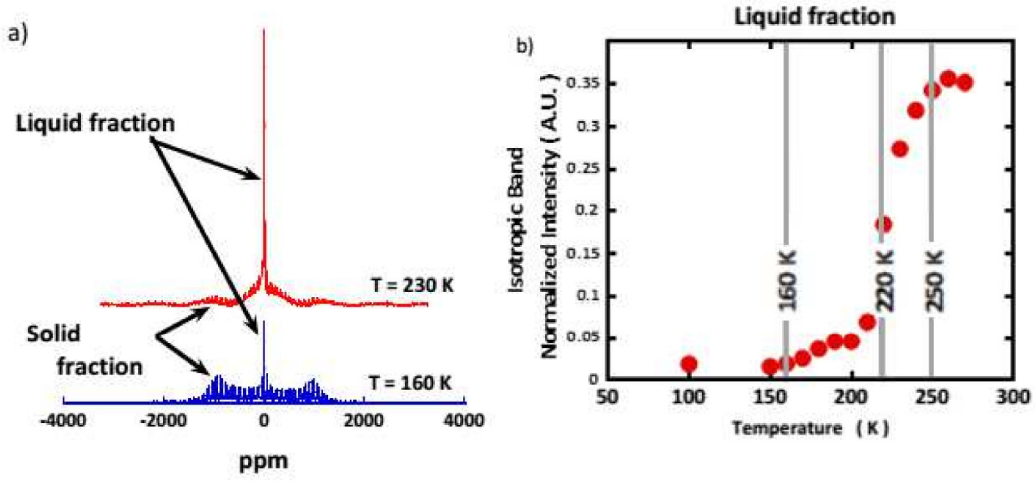

Figure 4.1.5 – Fraction of liquid water in Vycor pores revealed by ^{2}H SS-NMR. a) SS-NMR spectra of water D_2O monolayer in Vycor at 160 and 230 K. The broad *Pake* pattern at c.a. 1000 ppm is to be inferred to a fraction of molecules with no mobility (solid-like), while the central narrow band at 0 ppm is due to a fraction of molecules experiencing rapid reorientational dynamics (liquid-like). b) Evolution as a function of temperature, of the fraction of mobile (liquid-like) water molecules, *f*, estimated from the relative intensity of the central isotropic line as a function of temperature.

At all the investigated temperatures, from 100 to 270 K, the central line is well accounted for by a Lorentzian line and *f* can be simply evaluated by considering the relative integrated intensity of this Lorentzian (Figure 4.1.5b). The onset of

the rotational motion is clearly detected around 160 K and is followed by a sigmoidal increase with a characteristic temperature around 220 K. These two temperatures correspond to the onset of dynamical rotational events detected by neutron scattering.[11] Nevertheless, the NMR results bring into play important new information: the fraction of population experiencing the rotational dynamics is strongly temperature dependent *i.e.* the dynamics is highly heterogeneous.

4—1.2.4 A MEAN-FIELD PERCOLATION MODEL TO ACCOUNT FOR THE CONNECTIVITY OF THE HYDROGEN BOND NETWORK

Hydrogen bond rules the properties of water on two very different length scales: at the local scale, a pure energetic term defines if the bond is formed or not. In bulk, a water molecule can be engaged in 0, 1, 2, 3 or 4 HBonds with its neighboring molecules. The directionality of the O-H···O vector and the O O distance are there the key parameters. At a significantly larger scale, encompassing tens of water molecules, the relevant parameter is not energetics but the connectivity of the hydrogen bond network. Stanley and Teixeira[16] have derived a random-bond percolation model to interpret the unusual properties of bulk water.

Let's consider *p* as the probability, to form a hydrogen bond. Symmetrically, *(1-p)* is the probability that a possible Hbond, chosen at random, is broken. In bulk, the water molecules can then be classified in 5 groups f_i (i=0, 1…4), where i defines the number of intact Hbonds engaged by a given molecule. This statistics is strongly affected by the temperature (below 273 K, the probability to have 4 stable HBonds is close to 1).

In this paper, water molecules have a strong interaction with the Vycor surface. Hbonds between the interfacial water molecules and the numerous silanol groups at the surface of Vycor can therefore be considered as rather stable. Then by respect to the bulk situation, in the interfacial situation, the statistics is modified[15]: f_0=0 (a molecule has always a Hbond engaged with a Vycor surface silanol group). The statistics of the f_i classes simply follows the binomial distribution of the remaining three possible HBonds:

$$f_i = \binom{3}{i} p^i (1-p)^{3-i} \qquad (4.1.1)$$

Let's give a numerical example by considering *i)* a central water molecule, *ii)* its four immediate neighbours and *iii)* that the probability to form HBond is *p*=0.5. If nothing is known about the connectivity of the neighbours, the probability that this central molecules is HBonded to her neighbours is $p^4 = 0.5^4 \approx 0.06$. But now, if we know that each of the four neighbouring molecules are themselves engaged in four HBonds with their own neighbours, then, the probability that the central molecule is herself engaged in four HBonds is 1. In other words, if each of the four neighbours of a given water molecules have all four intact HBonds, this class also belong to the f_4 class.[16]

Now, if each of the four neighbours of a given water molecules have all four intact Hbonds (i.e. belong to the class f_4), this molecule also belongs to the f_4 class.[15] In that sense, the model is a correlated-site percolation model and this explains a striking result: the molecules belonging to the different classes are not randomly distributed but instead form "patches" (represented as dark blue zones on Fig1.c), where all the water molecules form 4 hydrogen bonds. In bulk, the sharp increase in the fraction of four-coordinated molecules in supercooled liquid water explains its anomalous thermodynamics and also controls the rate and mechanisms of ice formation.[16]

As the HBond is a transient interaction (typically a few ps at room temperature), an assembly of water molecules experiences constant density, hence entropy, fluctuations.

The weight fraction of molecules part of an s-site network of four Hbonded molecules writes:

$$W^*(s,p) = sA_3(s)p^{2s+1}(1-p)^{s+2} \qquad (4.1.2)$$

where $A_3(s) = \frac{3(2s)!}{s!(s+2)!}$.

The total number of patches, *G*(p)* and their average size *S*(p)* are:

$$G^*(p) = \sum_{s\geq 1} s^{-1} W^*(s,p) \qquad (4.1.3)$$

$$S^*(p) = \sum_{s\geq 1} s\, W^*(s,p) \qquad (4.1.4)$$

Compared to the overall HBond global network, the high connectivity within these domains induces a local lower density (ice floats on liquid water!) and entropy. As the temperature is lowered, the probability of forming Hbonds

increases. The size and the number of the f_4 patches increase accordingly and hence the entropy fluctuations.

4—1.2.5 THE SELF-DIFFUSION COEFFICIENT AS MEASURED BY QENS CAN BE USED TO TUNE THE TEMPERATURE DEPENDENCE OF *P*, THE PROBABILITY TO FORM A HYDROGEN BOND

To tune the temperature dependence of p, we use the temperature dependence of the self-diffusion coefficient (Figure 4.1.6a) of IW as measured at the local scale by incoherent QENS.

If one considers that diffusional motion is only possible for molecules with zero or a single intact HBond the fraction of immobile molecules is $F_{Im}=f_2+f_3+f_4$, we calculate:

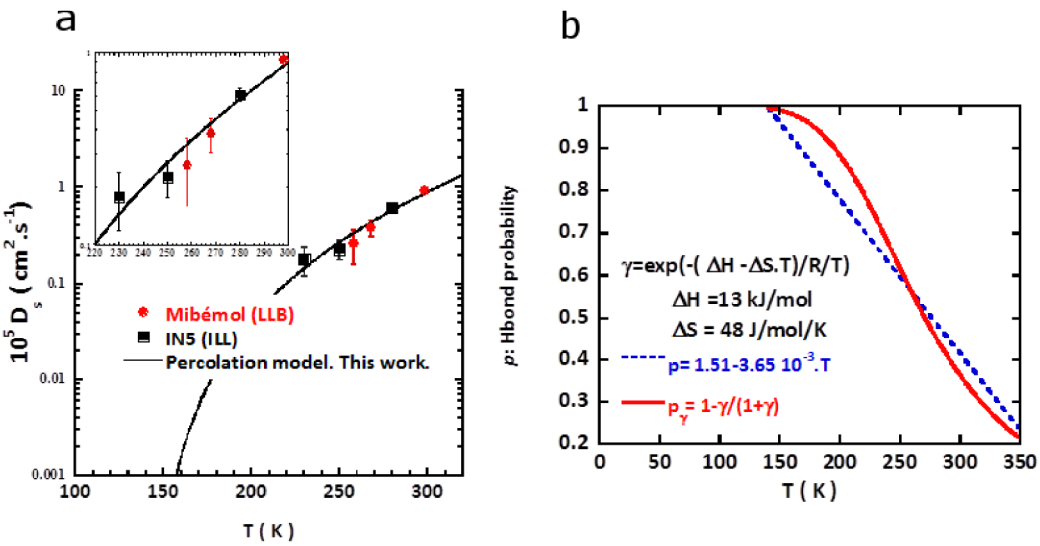

Figure 4.1.6 – Estimate of the temperature dependence on the probability to form H bonds. a) To tune p, the probability to form a HBond, we use the temperature dependence of the self-diffusion coefficient (Eq.4.1.6) as measured by QENS (Spectrometers Mibémol at LLB, Saclay and IN5 at ILL, Grenoble). A good agreement (a zoom is shown in inset) is reached for a first-order approximation: p =1.51-3.65 10^{-3}*T. b) Considering the Hbond network structure as resulting from the dynamical equilibrium between broken and intact Hbonds, one can estimate the Enthalpy and Entropy associated to the formation of a HBond. In this case p_γ, the probability for a HBond to be formed is not linear (Eq. 4.1.9) and an estimate of the temperature dependence of the interfacial water specific heat can be computed (Eq. 4.1.10). The calculated C_p temperature dependence is shown on Figure 4.1.2.

$$F_{Im} = \sum_{i=2}^{4} \binom{3}{i} p^2 (1-p)^{3-i} = 3p - 3p^2 + p^3 \quad (4.1.5)$$

The self-diffusion coefficient then writes:

$$D_s = C \ln(F_{Im}) \quad (4.1.6)$$

where C is a constant.

The D_s data Figure 4.1.6a are fairly well described (Figure 4.1.6b) with a simple temperature dependence $p(T) = \alpha - \beta * T$ with $\alpha = 1.51$ and $\beta = 3.65\ 10^{-3} K^{-1}$. Using $p(T)$ as an input, the temperature dependence of S^* and G^* can be determined: S^*, the size of the patches of 4 HBonded molecules reaches a maximum at 220 K, while G^* the number of these high density patches is maximum at 240-250 K (Figure 4.1.7). These two predicted temperature crossovers are perfectly in tune with the transitions experimentally detected in NMR and QENS.

4—1.2.6 ESTIMATE OF THERMODYNAMICAL QUANTITIES: HBOND ENTHALPY AND ENTROPY OF 2D WATER

While it is able to reproduce the temperature of dynamical changes experimentally observed, at this stage, key information when it comes to phase transitions are still missing, in particular thermodynamics quantities like entropy and enthalpy.

These quantities can be introduced if one considers the water connectivity as the result of the dynamical equilibrium between broken and intact Hbonds[17]:

$$\mathrm{HBond}_{intact} \leftrightharpoons \mathrm{HBond}_{broken} \quad (4.1.7)$$

The equilibrium constant writes:

$$\gamma = e^{\left(-\frac{\Delta H - T \cdot \Delta S}{RT}\right)} \quad (4.1.8)$$

where ΔH and ΔS are the enthalpy and entropy of an HBond and R=8.31 J/K/mol.

The fraction of broken bond is:

$$p_\gamma = 1 - \frac{\gamma}{1+\gamma} \quad (4.1.9)$$

Values ΔH=13 kJ/mol and ΔS= 48 J/mol/K (Fig.5b) account for the linear temperature dependence of the fraction of intact interfacial HBonds estimated from the self-diffusion coefficient. Compared to bulk water (ΔH_{Bulk}=9.80 kJ/mol and ΔS_{Bulk}= 21.6 J/mol/K), this clearly shows the excess of entropy, and hence the increased disorder induced by the low dimension of the 2D topology. The interpretation of the enthalpy value is more subtle: a single HBond with a silanol surface group of an interfacial water molecule on Vycor is stronger (larger enthalpy i.e. the system is hygroscopic, see above) than a HBond in bulk, but the probability to deal with an intact bond being smaller, after thermal average, the average HBond strength is smaller than in bulk. We point-out that such a softer HBond strength in interfacial water is consistent with the experimental observation that interfacial water remains liquid above 160 K (Figure 4.1.5b). This conclusion is also in line with the conclusion derived from the MIR data (Figure 4.1.4d) that the HBond becomes “softer” when temperature increases above 160 K.

4—1.2.7 ROBUSTNESS OF THE MODEL: TEMPERATURE DEPENDENCE OF INTERFACIAL WATER SPECIFIC HEAT

In bulk, the large specific heat of water, allows its good heat transfer property, is a direct consequence of the energy needed to break HBonds. In the framework of the present model of interfacial water, the temperature dependence of the interfacial specific heat can be directly estimated as the temperature derivative of the probability to have an intact bond:

$$C_p \approx \frac{dp_\gamma}{dT} \tag{4.1.9}$$

As shown on Figure 4.1.2, the model presented here provides a qualitative agreement with the experimental C_p measurement.[18] In particular it reproduces well the experimental increase of the C_p values above 160 K. This C_p increase is indeed due to the increased dynamics in the system (Figure 4.1.5b and Figure 4.1.8).

4—1.3 DISCUSSION

We consider the two key interactions at play when it comes to water *i)* the hydrogen bond at the local level and *ii)* the extension of the HBond network at the mesoscopic scale. The essence of the approach developed here is to point-out that the local density around a given water molecule is ruled by the number of short-lived HBonds this molecule experiences. Two extreme situations can be described: the presence of a molecule engaged in four HBond induces a local low *ice-like* density, while the density is maximum if the molecule is not bound to any neighbouring molecule.

Compared to bulk water, where such a zero-HBond situation is possible, the specificity of the 2D situation is to consider that a water molecule is permanently engaged in at least one HBond: the one between the “tagged” water molecule and the hydrophilic surface.

As the HBond is a transient interaction (typically a few ps at room temperature), an assembly of water molecules experiences constant density, hence entropy, fluctuations.

We account for the fluctuating HBond network with a simple and purely analytical mean-field percolation model: from experimental self-diffusion coefficients data, we estimate the temperature dependence of the probability for a Hbond to be formed. We then focus on the statistics of the four coordinated water molecules.

We are able to derive the average entropy and enthalpy of interfacial water. The entropy (ΔS= 48 J/mol/K) is found to be twice the one of bulk water. Our interpretation is that the two dimension topology frustrates the optimal perfect tetrahedral geometry easily reached in bulk (hexagonal ice). As a consequence, even at temperatures as low as 160 K, the thermal energy is sufficient to break a few HBonds. Even if the correlation time is very long (slow glassy-like dynamics), the molecules can then reorient and find the conformation of minimal energy i.e. form 4 HBonds.

In the framework of the percolation view of the HBond network, the fraction of water molecules engaged in 4 HBonds are not distributed at random but form patches (Figure 4.1.2c). At 160 K, once a few molecules experience 4HBond (even imperfect on a geometrical point of view) they tend to clamp together.

The model presented here provides then a sound and clear interpretation of the different events experimentally (neutron, NMR and infra-red spectroscopy) detected in interfacial water at 160, 220 and 250 K. Starting from an amorphous state of water at low temperature, these transitions are respectively interpreted as the onset of appearance of transient patches of 4-HBonded molecules at 160 K. By increasing the temperature, these *nuclei* of 4Hbonds *molecules* become more likely (G* increase, Figure 4.1.7) and grow in size (S* increase, Figure 4.1.7). At 220 K, these domains percolate and finally totally cover the surface at 240 K. This picture provides a qualitative explanation for the, so far unexplained, broad transition at 160 K detected in the specific heat of interfacial water, but also for the significantly shift of the C_p to a larger value compared to the bulk water (i.e. ice below 273 K).

As the most recent developments on the physics of water are mostly based on molecular dynamics (MD) results, we think that the simple and physical appealing model proposed here, shows a noticeable originality. We nevertheless note that MD results would be particularly adapted for estimating the precise contributions of the two or three HBonds “patches” neglected here.

4—1.3.1 RELEVANCE TO THE DEBATE ON THE EXISTENCE OF A LOW TEMPERATURE CRITICAL POINT IN WATER

At first sight, the intense activity around about the physics of water can appear as quite surprising. This interest is sustained by the hypothesized[1] existence of a Low Temperature Critical Point of water (LTCP) at $T_s \approx 228$ K and $P_s \approx 100$ MPa. If proven true, this LTCP would lead to a revolutionary re-interpretation of the physical properties of water, and in particular its numerous so-called *anomalies*. The properties of the bulk liquid water in the thermodynamic conditions of the LTCP have been so far unreachable to experiments: the LTCP

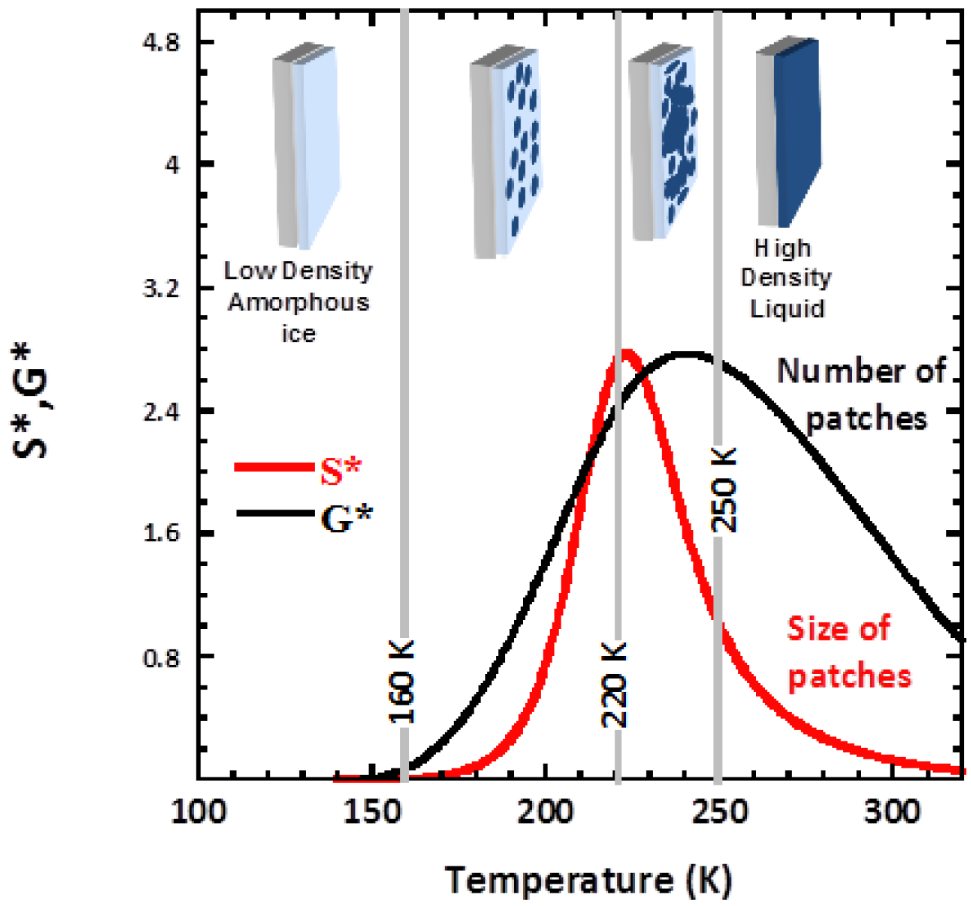

Figure 4.1.7 – Size and number of 4-HBonded patches as a function of temperature. By injecting the temperature dependence of p, the probability to form a HBond (Figure 4.1.6b), in Eqs. 4.1.3 and 4.1.4, we estimate the temperature dependence of S* and G*, respectively the size and the number of patches of water molecules all engaged in 4 HBonds (these patches show a low density). Within the 2D percolation model, we focus on the patches of 4 HBonded molecules (one Hbond engaged with the surface and three with neighbouring water molecules) and propose a global interpretation of the three dynamical crossovers experimentally observed, in terms of water molecules connectivity: i) at 160 K, the thermal energy of the system is large enough to induce the breaking of few HBonds. The system experiences a glass transition temperature and dynamical, although rare and associated with long correlation times, events become possible ii) at 220 K a percolation of the high density patches occurs while iii) at 250 K their number and hence the density fluctuations are maximum, inducing a liquid-liquid transition. The four sketches shown on top of the figure provide snapshots view (in reality, the structure is a dynamical equilibrium) of the different mesoscopic structures of the water monolayer. The Vycor substrate is represented in grey, the light blue area stands for low density and the dark blue for the high density liquid fraction.

temperature lays in-between the homogenous nucleation temperature (235 K) and the crystallization temperature of glassy forms of water (150 K).

Since it is a notorious way to avoid nucleation, nanometric confinement of water is currently intensively used to probe the liquid phase in this 150 to 235 K "No man's land".[19] The idea is to exalt the Gibbs-Thomson effect (i.e. the depression of the melting point[6]) by confinement of water in porous structure with extremely narrow pores (as low as 1.4 nm).

A strong *caveat* is nevertheless hiding there: the more the pore size decreases, the more the surface contribution increases.

We have evidenced that due to specific surface interactions, interfacial water exhibits dynamical transitions around 220 K, where the LTCP signature is expected to show-up. Therefore in our view, despite its interest and technical difficulties, the 220 K Fragile to Strong Transition (FST) of water confined in the narrow pores (1.4 nm in diameter) of MCM41 cannot be considered as an evidence of the existence of the LTCP.[20]

4—1.3.2 RELEVANCE TO BIOPHYSICS

We have shown that interfacial water at the surface of Vycor, a hydrophilic inert (chemically and dynamically) material, experiences different dynamical crossovers. As far as rotational motion of water is concerned, transitions are detected at 160 and 220 K.

It turns out that, a strong transition is also detected at 150 K in the specific heat of hydrated lysozyme crystals.[21] This is an evidence for a direct change in entropy fluctuations of the protein-water system at this temperature. Nevertheless, by calorimetry alone, it is not possible to discriminate wether the transition is due to the protein, to hydration water or both.

Neutron scattering data have shown a strong parallel[22] evolution at 150-160 and 220 K between the mean-square displacements related *i)* to interfacial water rotational dynamics and *ii)* to protons dynamics of a hydrated protein. This connection is made at the local scale (few Angstroems) and in the timescale of nanoseconds. Neutron scattering data suggests that both the hydration water and the protein are experiencing a transition. We interpret these observations

as evidences that interfacial water rotational dynamics is the real source of entropy driving protein dynamics[22]. We propose that the 220 K dynamical crossover could then be associated to a large scale structural change in HBond connectivity. All together, we reach a view of the protein-hydration water interaction and how this interaction can drive the protein function: the protein external side-chains short time motions, induced by fast water reorientational motion, propagate in a hierarchical way,[23] along the protein structure from the side-chains residue down to the protein core to induce the longer timescale protein backbone motion necessary for its function.

On a more general and technical point-of-view, the two dimensional water is of a high relevance in all the fields where interfacial water is at play: cement technology,[24] nuclear waste management,[25] geology[26] and biology.[27]

4—1.4 MATERIAL AND METHODS

4—1.4.1 SAMPLE PREPARATION

Vycor®[28] is made of a SiO_2 open porous network with a characteristic size of 50 Å and an interface of 130 m^2/g specific surface area.[29,30] The numerous silanol (Si-OH) groups covering its surface make the Vycor a very hydrophilic material. It can for example easily absorb water up to 25% of its dry mass. This is fully (100%) hydrated Vycor. Partially hydrated samples can also be prepared by absorption of water in the vapour phase. In this paper, we specifically consider two extreme samples: (i) fully hydrated Vycor (corresponding to the mass ratio $x_m=m_{water}/m_{dry\ Vycor}=0.25$) and (ii) low hydrated sample ($x_m=0.06$ also referred as 25% hydration). In the later, water realizes monolayer coverage of the Vycor surface and will be referred to, hereafter, as interfacial water (IW). Vycor has been hydrated with D_2O and H_2O for SS-NMR and quasi-elastic neutron scattering experiments respectively.

4—1.4.2 INFRA RED SPECTROSCOPY

Interfacial water IR were measured on the Ailes spectrometer. Sample was hydrated by H_2O. Measurements were performed at the AILES beamline[31] with a Bruker IFS125 FT-IR spectrometer using synchrotron far and mid infrared

radiation emitted at SOLEIL facility[32] (Saint-Aubin, France). Spectra from 20 cm^{-1} to 5000 cm^{-1} were obtained by averaging 200 scans. In the far infrared region (FIR: 20 cm^{-1} to 600 cm^{-1}) spectra were recorded using a 6 µm thick Mylar beam splitter and a bolometer with a resolution of 2 cm^{-1}, while in the mid infrared region (MIR: 600 cm^{-1} to 5000 cm^{-1}) they were recorded using a KBr beam splitter and a MCT detector with a resolution of 4 cm^{-1}.

A specific homemade cell[33] was used to measure hydration/dehydration processes *in situ.* This cell is equipped with two diamond windows to allow absorbance measurements (leak rate $<10^{-9}$ mbars·l/s). Vycor sample (thickness of ~80 µm) was placed inside the cell, perpendicularly to the incident beam with both surfaces exposed to the humidified air/pumping allowing the hydration/dehydration processes. As described elsewhere,[33] sample temperature is controlled by a cryostat (precision 0.2 K) while sample hydration is monitored by a thermostated gauge (0-100 mbar with a precision of 0.02 mbar). The gauge provides control of the water vapor pressure (*p)* in the cell. The relative humidity (RH) to which Vycor is exposed can be precisely set to the value $(p/p_0)*100$, p_0 being the water vapor pressure equal to 28.1 mbar at 23°C. By setting the pressure at 9.1 mbar we were able to prepare Vycor equilibrated at 32.4% RH. Firstly, spectra of the dried sample from T=70 K to T=298 K were acquired to be used as a reference. Then, spectra of the sample in equilibrium with 9 mbar of water vapor pressure were recorded at the same temperatures. Difference spectra are displayed in absorbance units as $-log(I/I_0)$, where I and I_o are respectively the hydrated sample and dried sample transmissions at the same temperature.

4—1.4.3 NMR

Soild state Magic Angle Spinning NMR (SS-NMR) experiments were performed on a Bruker AVANCE II spectrometer operating at 11.74 T. Spectra were recorded at 76.8 MHz and spinning rate of the rotor was ajusted to 4 kHz. The Vycor sample was hydrated by D_2O and packed inside a 7 mm outer diameter Bruker rotor. A liquid nitrogen dewar was used to provide gas for bearing and drive and the temperature of the sample was set by the Bruker temperature control unit. Special care was put to avoid freezing the bore of the magnet, and users should be extremely careful.

4—1.4.4 SPECIFIC HEAT MEASUREMENTS

Specific heat measurements were performed using quasi-adiabatic AC calorimetry where the sample is heated periodically at f_0=10 mHz and the corresponding temperature oscillation is measured at $2f_0$ around the mean temperature of the reservoir. Slices of Vycor 2 mm thick and 12 mm in diameter soaked with water were housed in a leak-proof small silver cell enclosed in cryostat cooled by liquid nitrogen. Specific heat measurements were performed by heating the cell at rate of ≈1mK/s in the temperature range -160°C to 70°C after cooling the sample at a rate between 1 and 2 K/min.

Supplementary Figure

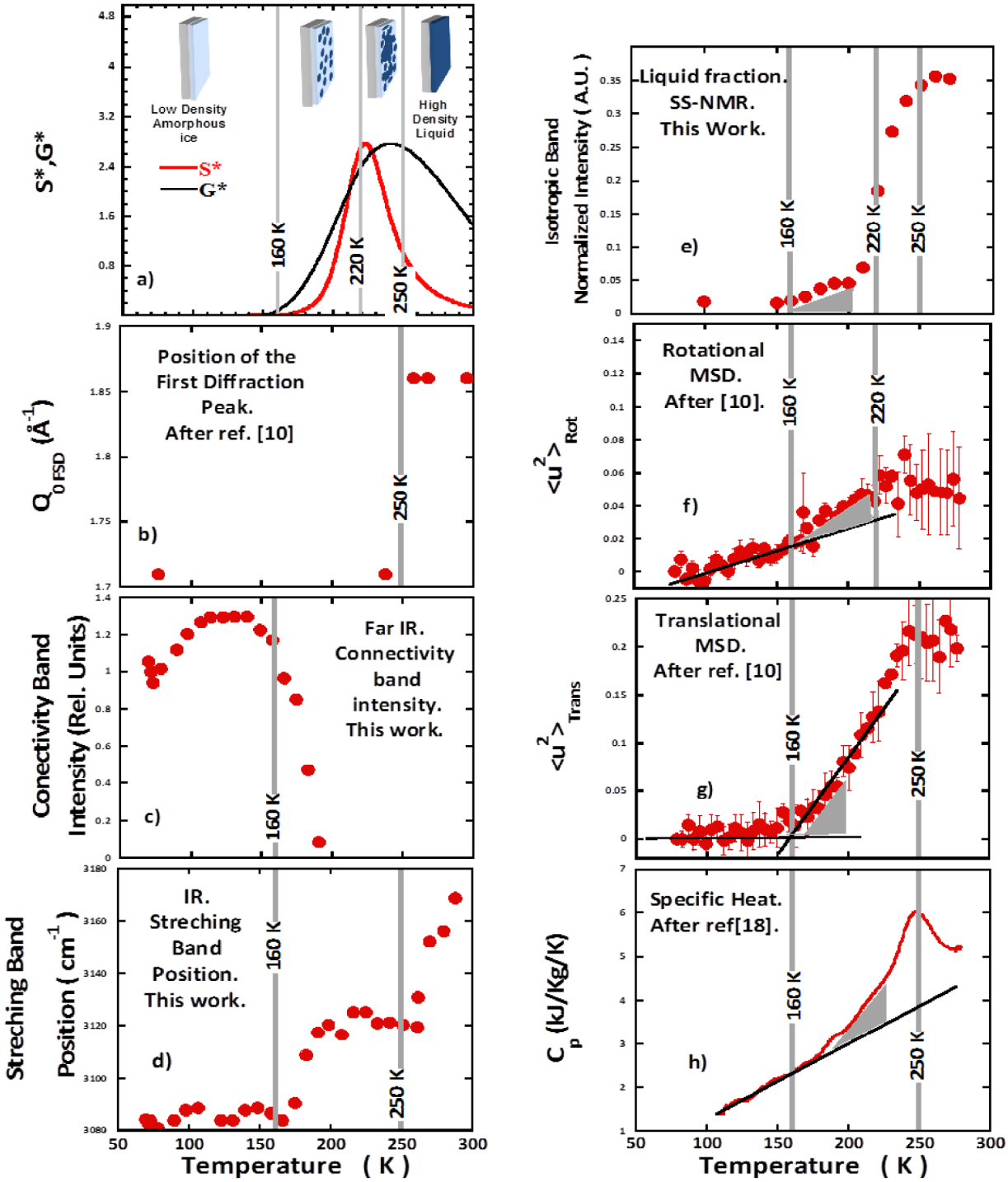

Figure 4.1.8 – Synoptic view of the temperature dependence of available experimental quantities of 2D water as a function of temperature.

For the sake of comparison the top Figure 4.1.8a reproduces the Figure 4.1.7 to show along with the experimental data the size (S*) and the number (G*) of the high density liquid patches derived from the percolation model.

The specific heat of a material is the integration of the number of dynamical modes. The grey area colored on Figure 4.1.8 e) f) g) and h) highlight the concomitance of dynamical modes related quantities (MSD and fraction of liquid) of interfacial water molecules as measured by SS-NMR and neutron scattering, with the onset of specific heat excess above 160 K. The sudden change in the FIR connectivity band (Figure 4.1.8c) intensity at this temperature indicates a change in the intermolecular collective dynamics of clusters of water molecules. This change has an incidence on the MIR intramolecular stretching mode (Figure 4.1.8d). Our interpretation is that at 160 K, the thermal energy is sufficient to break few distorted HBonds so that few molecules can experience enough dynamics to collapse in few small patches of mobile high density liquid patches. We assign the 160 K events to a glass transition of interfacial water.

At 220 K the sudden increase of the fraction of liquid-like water as detected by SS-NMR (Figure 4.1.8e) comes along with a saturation (due to instrumental limitation see reference[10]) of the MSD due to the water rotational modes (Figure 4.1.8f). Our interpretation is that, at this temperature, the high density liquid patches formed above 160 K have increased in both number and size (Figure 4.1.8a) so that when they percolate the surface accessible to the molecules suddenly significantly increases hence their MSD.

At 250 K, the high density liquid patches have grown up and multiplied so much (Figure 4.1.8a) that the high density liquid totally invades the surface: both the fraction of liquid (Figure 4.1.8e) and its translational MSD (Figure 4.1.8f) are at their maximum. The water density, as inferred for the position of the neutron diffraction first sharp diffraction peak (Figure 4.1.8b) and MIR stretching mode tend to recover the values of water, but somehow supercooled. This is a real thermodynamical event (we interprete as liquid-liquid transition) well detected in calorimetry (Figure 4.1.8h).

This plot shows a global trend: the reality of the experimental transitions we describe at 160, 220 and 250 K and their coherence with our interpretation within the surface percolation model we propose in this paper.

REFERENCES

(1) Stanley H. E., Mysteries of water in Hydration process in Biology, M.C. Bellissent-Funel (Ed.), Nato Science Series – Serie A, vol 305, IOS Press (**1999**).

(2) Debenedetti P.G. and Stanley H.E., *Physics Today* 56, 6, 40 (**2003**).

(3) Whitby M., Cagnon L., Thanou M. and Quirke N., Enhanced Fluid Flow through Nanoscale Carbon Pipes, *Nano Lett*. 8, 2632-2637 (**2008**).

(4) Falk K., Sedlmeier F., Joly L., Netz R.R. and Bocquet L, Molecular Origin of Fast Water Transport in Carbon Nanotube Membranes: Superlubricity versus Curvature Dependent Friction, *Nano Lett.* 10, 4067-4073 (**2010**).

(5) Kolesnikov A.I., Zanotti J.-M., Loong C.K., Thiyagarajan P., Moravsky A.P., Loutfy R.O. and Burnham C.J., Anomalously soft dynamics of water in a nanotube: A revelation of nanoscale confinement, *Physical Review Letters* 93, 35503 (**2004**).

(6) The Gibbs-Thomson effect is directly related to *i)* the significant contribution of a term related to the solid-liquid interface in the Gibbs-Duhem chemical equilibrium relation (in bulk this interfacial contribution is neglected) and *ii)* to the existence of a surface curvature imposed by the confining geometry. This is formalized by the expression: $\Delta T_m = (4.\ \sigma_{sl} / \Delta H_f / v).T_m/d$, where ΔH_f is the bulk enthalpy of fusion, v is the molar volume of the solid fraction, σ_{sl} the surface energy of the solid-liquid interface, T_m the bulk melting point and d the pore diameter. It clearly appears that, ΔT_m, the downshift of the melting temperature is inversely proportional to the characteristic size of the porous structure.

(7) Alcoutlabi M. and McKenna G. B., Effects of confinement on material behaviour at the nanometre size scale. *Journal of Physics-Condensed Matter*, 17,R461–R524 (**2005**).

(8) Leaist D.G., Murray J.J., Post M.L. and Davidson D.W., Enthalpies of decomposition and heat-capacities of ethylene-oxide and tetrahydrofuran hydrates, *J. Phys. Chem*. 86, 4175–4178 (**1982**).

(9) In bulk liquid water, a molecule is hydrogen bonded to on average slightly less than four neighboring molecules. If due to thermal energy, a hydrogen bond (HBond) O---H-O moves apart from linearity by more than 25°, the bond breaks. When several H-bonds engaged by a molecule are simultaneously broken, the molecule is free to experience a rotational diffusive motion until several hydrogen bonds are formed again leading to the formation of a transient localization “site”. Indeed, instead of addressing an *average* water dynamics, considerable insight is obtained by individually considering the rotational and translational modes to the overall dynamics.

(10) Zanotti J.-M., Bellissent-Funel M.-C. and Chen S.H., Experimental evidence of a liquid-liquid transition in supercooled water*. Europhys. Lett*., 71, 91–77 (**2005**).

(11) Brubach J.-B., Mermet A, Filabozzi A, Gerschel A. and Roy P. Signatures of the hydrogen bonding in the infrared bands of water**,** *J. Chem. Phys*., 122, 184509 (**2005**).

(12) Zanotti J.-M., Bellissent-Funel M.- C., Chen S.-H. and Kolesnikov A.I. Further evidence of a liquid–liquid transition in interfacial water, *J. Phys.: Condens. Matter,* 18, S22299–S2304 (**2006**).

(13) Klug D. D. and Whalley E. The uncoupled O–H stretch in ice VII. The infrared frequency and integrated intensity up to 189 kBar, *J. Chem. Phys*., 81,1220 (**1984**).

(14) Teixeira J., Zanotti J. M., Bellissent-Funel M. C. and Chen S. H., Water in confined geometries. *Physica B* 234, 370–374 (**1997**).

(15) Stanley H. E. and Teixeira J., Interpretation of the unusual behavior of H2O and D2O at low-temperatures - tests of a percolation model*. J. Chem. Phys.* 73, 3404–3422 (**1980**).

(16) Moore E. B. and Molinero V., Structural transformation in supercooled water controls the crystallization rate of ice, *Nature* 479, 506-509 (**2011**).

(17) Muller N., Search for a realistic view of hydrophobic effects. *Accounts of Chemical Research* 23, 23–28, (**1990**).

(18) Tombari E., Ferrari C., Salvetti G., and Johari G. P., Dynamic and apparent specific heats during transformation of water in partly filled nanopores during slow cooling to 110 k and heating, *Thermochimica Acta* 492, 37–44 (**2009**).

(19) Debenedetti P. G. and Stanley H. E., *Phys. Today* 56, 6, 40-46 (**2003**).

(20) Liu L., Chen S.H., Faraone A., Yen C.W. and C.Y. Mou. Pressure dependence of fragile-to-strong transition and a possible second critical point in supercooled confined water. *Physical Review Letters,* 95, 117802 (**2005**).

(21) Miyazaki Y., Matsuo T., and Suga H. Low-temperature heat capacity and glassy behavior of lysozyme crystal. *Journal of Physical Chemistry B* 104, 8044–8052 (**2000**).

(22) Zanotti J. M., Gibrat G., and Bellissent-Funel M.-C., Hydration water rotational motion as a source of configurational entropy driving protein dynamics. crossovers at 150 and 220 k. *PCCP* 10, 4865-4870 (**2008**).

(23) Zanotti J.-M., Bellissent-Funel M.-C. and Parello J., Dynamics of a globular protein as studied by neutron scattering and solid-state NMR, *PHYSICA B*, 234, 228-230 (**1997**).

(24) Abdolhosseini Qomi M.J., Krakowiak K.J., Bauchy M. et al., Combinatorial molecular optimization of cement hydrates, *Nature Communications*, 494, 5:4960 (**2014**).

(25) Cailleteau C., Angeli F., Devreux F., et al., *Nature Materials* 7, 978 (**2008**).

(26) Malikova N., Longeville S., Zanotti et al., *Phys. Rev. Lett.* 101, 265901 (**2008**).

(27) G. Schiro, Y. Fichou, F.-X. Gallat, K. Wood et al., Translational diffusion of hydration water correlates with functional motions in folded and intrinsically disordered proteins, *Nature*, 6, 6490 (**2015**).

(28) Vycor brand porous glass n° 7930 is a product of Corning Glass Works.

(29) Levitz P., Ehret G., Sinha S.K., Drake J.M., Porous vycor glass: The microstructure as probed by electron microscopy, direct energy transfer, small-angle scattering, and molecular adsorption, *J. Chem. Phys.* 95**,** 6151-6161 (**1991**).

(30) Pellenq R., J. M., Rousseau B. and Levitz P. E., A grand canonical Monte-Carlo study of argon adsorption/condensation in mesoporous silica glasses. *Physical Chemistry Chemical Physics*, 3, 1207–1212 (**2001**).

(31) Brubach, J. B.; Manceron, L.; Rouziére, M.; Pirali, O.; Balcon, D.; Kwabia Tchana, F.; Boudon, V.; Tudorie, M.; Huet, T.; Cuisset, A.; Roy, P. *AIP Conference Proceedings*, 1214, 81-84 (**2010**).

(32) Roy, P.; Rouzieres, M.; Qi, Z. M.; Chubar, O. *Infrared Physics & Technology 49*, 139-146 (**2006**).

(33) Dalla Bernardina, S.; Alabarse, F.; Kalinko, A.; Roy, P.; Vita, N.; Hienerwadel, R.; Berthomieu, C.; Judenstein, P.; Zanotti, J. M.; Bantignies, J.L.; Haines, J.; Catafesta, J.; Creff, G.; Manceron, L.; Brubach, J. B. *Vib. Spectrosc., 75* : 154–161 (**2014**).

CHAPTER 5

HYDRATION PROCESSES IN PROTON CONDUCTING NANOSTRUCTURED IONOMERS

Hydrated acidic polymers are extensively studied for their potential use in fuel cells, electrolysers, ionic separation and water purification. The properties of such hydrogen-bonded nanomaterials are largely controlled by nanoconfinement and water-ions interactions. Indeed, these materials possess outstanding proton conducting properties due to the interconnected H-bond network that forms inside hydrophilic channels upon water loading. We report here an article reporting an infrared kinetics study of the hydration mechanism in benchmark perfluorinated sulfonic acid (PFSA) membranes, e.g. Nafion™.

5—1 MECHANISM OF IONIZATION, HYDRATION, AND INTERMOLECULAR H-BONDING IN PROTON CONDUCTING NANOSTRUCTURED IONOMERS

A 25 μm thick Nafion N211 membrane, described in Section 1—4, has been exploited to investigate on the hydration process of perfluorinated sulfonic acid membranes. In particular, the ionization process, hydronium ion formation, protonic species formation, and molecular interactions have been highlighted by a complete set of infrared spectra recorded both in the FIR [20-500 cm^{-1}] and MIR [500-4000 cm^{-1}]. This study was accomplished with the hydration cell described in Section 2—3, with which we controlled the initial dry state of the polymer and proceeded to sequences of hydration.

The spectral signatures obtained *in situ* in the FIR region, leads to unprecedented clues regarding the intermolecular arrangement between ionic groups, proton species and water molecules in the ultra-low water content state.

The molecular picture that emerges from this study is a three-step hydration process (Figure 5.1.1).

In the initial dry polymer state, sulfonic groups are linked through hydrogen bonding, thus suggesting a locally bridged ionic structure in the absence of water. Such situation, which was already hypothesized on the basis of MIR results, is herein assessed from the intermolecular spectral modes probed in the FIR range.

A first threshold of hydration is reached as several bands show simultaneous and drastic increase until reaching a maximum, while other bands present opposite evolution until disappearing. They are the signatures of the gradual dissociation of SO_3H leading to the formation of the hydronium ion until one water molecule per ionic group (λ=1) is adsorbed. Monitoring specific bands characteristic of hydronium ions (250 and 2700 cm^{-1}), SO_3H (912 cm^{-1}) and SO_3^- (1064 cm^{-1}) in the

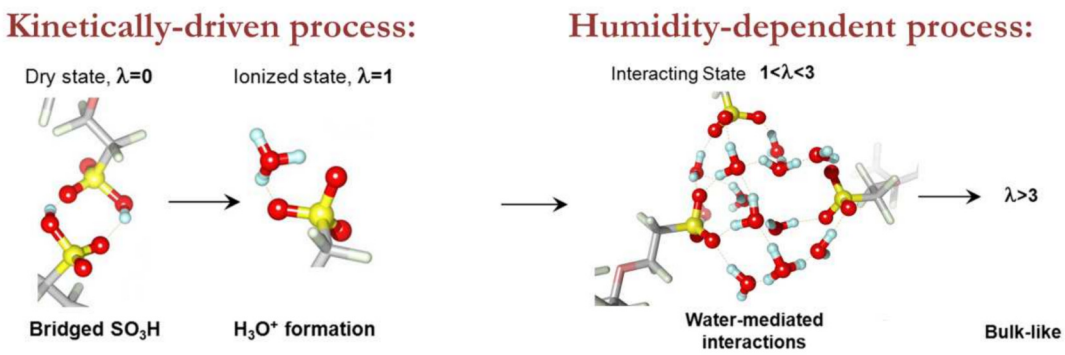

Figure 5.1.1 – Schematic view of Nafion hydration process. Schematic view of water interacting with SO3H groups of Nafion membrane. In the dry state (λ=0) sulfonic groups are linked through H bonding. At λ=1 $SO_3^-\cdots H_3O^+$ species are formed via a kinetically-driven process;. Further steps depend on the water vapor pressure applied to the membrane: for 1<λ<3 hydrated protonic complexes are formed, for λ>3 an extended H-bond network is established.

FIR and MIR regions for several hydration sequences, we could state that ionization is a kinetically-driven process, leading to the formation of $SO_3^-\cdots H_3O^+$ species. The first step of water sorption is then independent from the set vapor pressure.

The second threshold found at λ=3 corresponds to the intercalation of water molecules between $H_3O^+\cdots SO_3^-$ groups. Water preferentially hydrates the SO_3^- functions, and H_3O^+ species do not directly interact with SO_3^-. Hydrated protonic Zundel and Eigen complexes are then formed and allow the fast transfer of charge carriers in a dense H-bond network.

Combining FIR and MIR allowed us to propose an alternative attribution of controversial MIR features and to identify hydronium ion signatures in both regions (250 cm^{-1} and 2700 cm^{-1}).

Mechanism of ionization, hydration, and intermolecular h-bonding in proton conducting nanostructured ionomers

Dalla Bernardina, S.; Brubach, J.-B.; Berrod, Q.; Guillermo, A.; Judeinstein, P.; Roy P. and Lyonnard, S. *J. Phys. Chem. C* **118** (2014) 25468-25479.

ABSTRACT

Water-ions interactions and spatial confinement largely determine the properties of hydrogen-bonded nanomaterials. Hydrated acidic polymers possess outstanding proton-conducting properties due to the interconnected H-bond network that forms inside hydrophilic channels upon water loading. We report here the first far infrared (FIR) coupled to mid infrared (MIR) kinetics study of the hydration mechanism in benchmark perfluorinated sulfonic acid (PFSA) membranes, e.g. Nafion. The hydration process was followed in situ, starting from a well-prepared dry state, within unprecedented continuous control of the relative humidity. A step-by-step mechanism involving two hydration thresholds, at respectively λ=1 and λ=3 water molecules per ionic group, is assessed. The molecular environment of water molecules, protonic species and polar groups are thoroughly described along the various states of the polymer membrane, *i.e.* dry ($\lambda \approx 0$), fully ionized ($\lambda = 1$), interacting ($\lambda = 1$—3), and H-bonded ($\lambda > 3$).

This unique extended set of IR data provides a comprehensive picture of the complex chemical transformations upon loading water into proton-conducting membranes, giving insights into the state of confined water in charged nanochannels and its role in driving key functional properties as ionic conduction.

5—1.1 INTRODUCTION

Understanding the mechanism of water sorption in hydrophilic or hydrophobic nanostructures is a key issue in food science, geology, biology, environmental and energy science. The fluid confinement is accounted for huge deviations

from bulk behavior. Water-ions and water-host interactions create distorted H-bonded networks inducing peculiar hydration and transport mechanisms. In turn, the functional properties of the host materials, *e.g.* macromolecules, proteins, hydrogels, clays, porous materials, polymers, highly depend on their hydration level. Some ionic polymers, *e.g.* ionomers, exhibit a phase-separation at nanoscale between mechanically robust hydrophobic domains and ion-conducting aqueous hydrophilic domains. They are extensively studied for their potential use in fuel cells, electrolyzers, red-flow batteries, transducer, ionic separation and water purification.[1,2] The proton conducting membranes based on perfluorosulfonic acid (PFSA) ionomers are benchmark electrolytes owing to their high proton conductivities when hydrated.[3] PFSA ionomers, as Nafion, are constituted of Teflon-like main chains bearing pendant chains terminated by sulfonic acid functions. A molecular-level description of the effect of water content on protonic species formation and properties is needed to unveil the outstanding behavior of these materials and establish the interplay between spatial confinement, wetting behavior and complex host-fluid interactions. The proton transport arises from a complex balance between mass diffusion of hydronium ions and Grotthuss-like proton motions occurring through H-bonds formation and breaking in hydrated protonic clusters.[4] For several decades, tremendous efforts have been devoted to characterize the role of water molecules in structuring the ionomer, in dissociating the polar groups situated at the hydrophobic/hydrophilic interface and in mediating proton transfer.[5] Nevertheless, none of them provided the full sequence of chemical events occurring when a dry ionomer is exposed to low water vapor pressures.

The sorption, proton transfer mechanisms and water properties in PFSA materials were scrutinized by a variety of experimental and numerical means including sorption measurements,[6—10] X-rays and neutron scattering,[11—15] infrared spectroscopy,[16—22] nuclear magnetic resonance (NMR),[2,6,23—26] dielectric spectroscopy,[27] differential scanning calorimetry (DSC)[28,29] as well as numerical simulations (*ab initio* simulations,[30—32] molecular dynamics simulations,[33—39] and Empirical Valence Bond models[40—42]). Vibrational spectroscopy techniques were extensively employed since the 1980's and in particular infrared (IR) spectroscopy. This technique has provided invaluable information on (i) the confined water molecules bonds, (ii) the perfluorinated main and side-chains, (iii) side-chains ether groups, and (iv) the SO_3 species. The attribution of several Nafion bands is nevertheless a subject of intense

debates in the literature. Since the pioneering studies of Falk[16] and Ostrowska,[17] the efforts have been focused on attributing backbone, side-chains and water modes. With the same aim, further infrared studies of Nafion under controlled water vapor pressure performed by Di Noto,[21,22] Iwamoto,[20] and Laporta.[19] Buzzoni[18] also reported a comparison of Nafion membrane with acids of similar strength. More scarce studies were devoted to elucidate the kinetics of charge dissociation and hydronium formation processes,[10,43] at low-water content states. A general finding is that most experimental studies failed to provide quantified molecular information for hydration level under three water molecules per ionic group, the water content being quantified as the number of water molecules per ionic group.[6] Moreover, no vibrational study of the intermolecular water modes was reported to date. These far infra-red (FIR) bands, appearing below 600 cm^{-1}, provide direct information on the extent of the H-bonds which clearly control the proton conduction efficiency.

Thus, this void regarding both the characterization of the ionization process and the formation of protonic species at low hydration motivated the present study of the hydration process in the early stages of water loading, starting from a true dry state.

We herein report on the first investigation of a PFSA ionomer membrane in the FIR region by means of advanced IR synchrotron spectroscopy. The hydration was investigated *in situ* starting from a well-prepared and carefully characterized dry state ($\lambda \approx 0$). Through monitoring the various chemical species, SO_3H, SO_3^-, ($H^+ \cdots H_2O$), upon hydration, we were able to identify the major steps of membrane evolution at molecular level as water is absorbed. These steps occur as follow: full ionization, creation of hydrated species, and further water molecules penetration into ionic domains. This set of IR data provides an unprecedented comprehensive molecular picture for rationalizing the complex chemical transformations upon water loading at very small contents. Our results highlight the role of ionic interactions and confinement, which are differently balanced upon increasing hydration, thus bringing insights into the properties of a polar fluid embedded at nanoscale inside charged cavities.

5—1.2 EXPERIMENTAL SECTION

5—1.2.1 MATERIALS

Trifluoromethanesulfonic (triflic) acid (CF_3SO_3H, Sigma-Aldrich, 99% purity) was used without further purification. Nafion (Nafion^{TM} 211) membrane (nominal thickness: 25 µm; equivalent weight: 1100 g/equiv) was provided by DuPont Company. The as-received Nafion membrane was immersed in 1M HNO_3 solution for 3 h at 50 °C to insure full acidification and then rinsed several times with deionized water (Nafion-H). The Na-exchanged Nafion membrane (Nafion-Na) was obtained by immersing part of the as-received sample in a 1M NaOH solution at 50 °C for 1 h and then washed several times with deionized water. Three different temperatures 60, 80 and 120 °C have been set to establish the treatment needed to obtain a dehydrated acidic membrane. Two 8 mm × 15 mm pieces of Nafion were cut from the acidified sample. The first sample was heated 15 h at 60 °C and after a hydration cycle was dehydrated again 15 h at 80 °C under a vacuum (10^{-5} mbar). This sample was used for all subsequent hydration/dehydration studies. The second sample was kept under a vacuum (10^{-5} mbar) 4 days at 120 °C to check the efficiency of the drying process for removing all water molecules from the polymer matrix. The Na-exchanged dry membrane was dried at 80 °C for 12 h under a vacuum (10^{-5} mbar).

5—1.2.2 INSTRUMENTS AND METHODS

Measurements were performed at the AILES beamline[44] with a Bruker IFS125 FT-IR spectrometer using synchrotron far and mid infrared radiation emitted at SOLEIL facility.[45] Spectra from 20 cm^{-1} to 5000 cm^{-1} were obtained by averaging 200 scans. In the far infrared region (FIR: 20 cm^{-1} to 600 cm^{-1}) spectra were recorded using a 6 µm thick Mylar beam splitter and a bolometer with a resolution of 2 cm^{-1}, at 4 cm/s mirror speed, while in the mid infrared region (MIR: 600 cm^{-1} to 5000 cm^{-1}) they were recorded using a KBr beam splitter and a MCT detector with a resolution of 4 cm^{-1} at 2 cm/s mirror speed. All measurements were done at 23 °C.

A specific homemade cell[46] was used to measure hydration/dehydration processes *in situ*. This cell is equipped with two diamond windows to allow absorbance measurements (leak rate <10^{-9} mbars·l/s). Nafion membrane

sample (8 mm × 15 mm) was placed inside the cell, perpendicularly to the incident beam with both surfaces exposed to the humidified air/pumping allowing the hydration/dehydration processes. As described elsewhere,[46] sample temperature is controlled by a cryostat (precision 0.05 K), while sample hydration is monitored by a thermostated gauge (0—100 mbar with a precision of 0.02 mbar). The gauge provides control of the water vapor pressure (*p)* in the cell. The relative humidity (RH) to which Nafion is exposed can be precisely set to the value $(p/p_0) \times 100$, p_0 being the water vapor pressure equal to 28.1 mbar at 23 °C. By setting the pressure at 0.2 mbar, 0.5 mbar, 1 mbar, 1.9 mbar, 3.4 mbar, 5.0 mbar, 6.9 mbar, 9.1 mbar, 13.4 mbar, 18.8 mbar, 21.5 mbar, 25.2 mbar and 28.1 mbar, we were able to prepare Nafion equilibrated at respectively 0.7%, 1.8%, 3.5%, 6.8%, 12.1%, 17.8%, 24.5%, 32.4%, 47.7%, 66.9%, 76.5%, 89.7%, and 100% RH.

Two types of kinetics sequences were performed. For ultra-low hydration measurements (RH ≤ 3.5%), the sample was first dried *in situ* and the water vapor pressure was set to $p_{ultralow}$ ≤1 mbar. This was repeated three times to evaluate the effect of the final set ultralow RH on the kinetics (values of set vapor pressure: 0.2, 0.5, and 1 mbar). Higher hydration kinetics sequences were then successively applied starting from $p_{ultralow}$ to p_1=1.9 mbar, p_1 to p_2=3.4 mbar, until the final hydration step p_9 to p_{10}=28.1 mbar. To accurately follow the abrupt spectral changes occurring in the first minutes at each hydration step, fast acquisitions were programmed with a repetition rate of 7 seconds, corresponding to 20 scans per spectra. Then, the time sampling rate was increased to further follow the hydration until equilibrium (no more change in IR spectra). This protocol was repeated for each hydration step and applied in the same way for both FIR and MIR spectral ranges. As a tool for identifying structure in FIR spectra, absorbance of highly concentrated solution of triflic acid ($CF_3SO_3H/H_2O \approx 1$) was measured by placing a liquid film between two diamond windows.

All spectra are displayed in absorbance units as $-log(I/I_0)$, where I and I_o are respectively the sample and empty cell transmissions.

Schematic drawings were created with the freewares Avogadro[47] and Chimera.[48]

5—1.3 RESULTS

The FIR and MIR spectra of acidic Nafion-H were recorded in the various dried states and along different hydration/dehydration sequences. The MIR region has been already highly documented in Nafion and other PFSA membranes[10,16—22,43] but the FIR spectra were never reported in the literature. 3D plots of a typical hydration sequence from dry to 100%RH are shown on Figure 5.1.2. The extended spectral region has been divided into three zones: FIR [20-500 cm^{-1}] (A), MIR [600-1100 cm^{-1}] (B) and MIR [1400-4000 cm^{-1}] (C).

The 3D plots evidence several distinct mechanisms identified through the appearance or disappearance of characteristic bands in both the FIR and MIR. Two hydration thresholds are identified, as will be discussed in details later. The first one corresponds to the total disappearance of the well-known 912 cm^{-1} band due to stretching SO of SO_3H (Figure 5.1.2B). Therefore, it denotes the full dissociation of all sulfonic groups. The second threshold, found at RH~30%, is commensurate to the appearance of the typical 3450 cm^{-1} bulk water signature (Figure 5.1.2C). In the following we proceed to a 3-steps data analysis: 1) dry state; 2) kinetics of hydration up to full ionic dissociation (first threshold); 3) low water content ionized state (first to second threshold) and higher water contents up to saturation.

In order to quantitatively describe the hydration process, the main vibrational modes have to be assigned. We compare Nafion-H to Nafion-Na and Nafion-H to triflic acid solution in order to identify specific H-bonds[49] as well as perfluorinated and sulfonic acid features[18,22] [Table 5.1]. More specifically, the membrane evolution upon water loading will be followed through the appearance/disappearance of some characteristic FIR bands *i)* $SO_3H…HO_3S$; *ii)* $SO_3^-…H_3O^+$; *iii)* $H_3O^+…H_2O$; iv) $SO_3^-…H_2O$; v) $H_2O…H_2O$ and MIR bonds *i)* O-H; *ii)* S-O; *iii)* H-O-H bending.

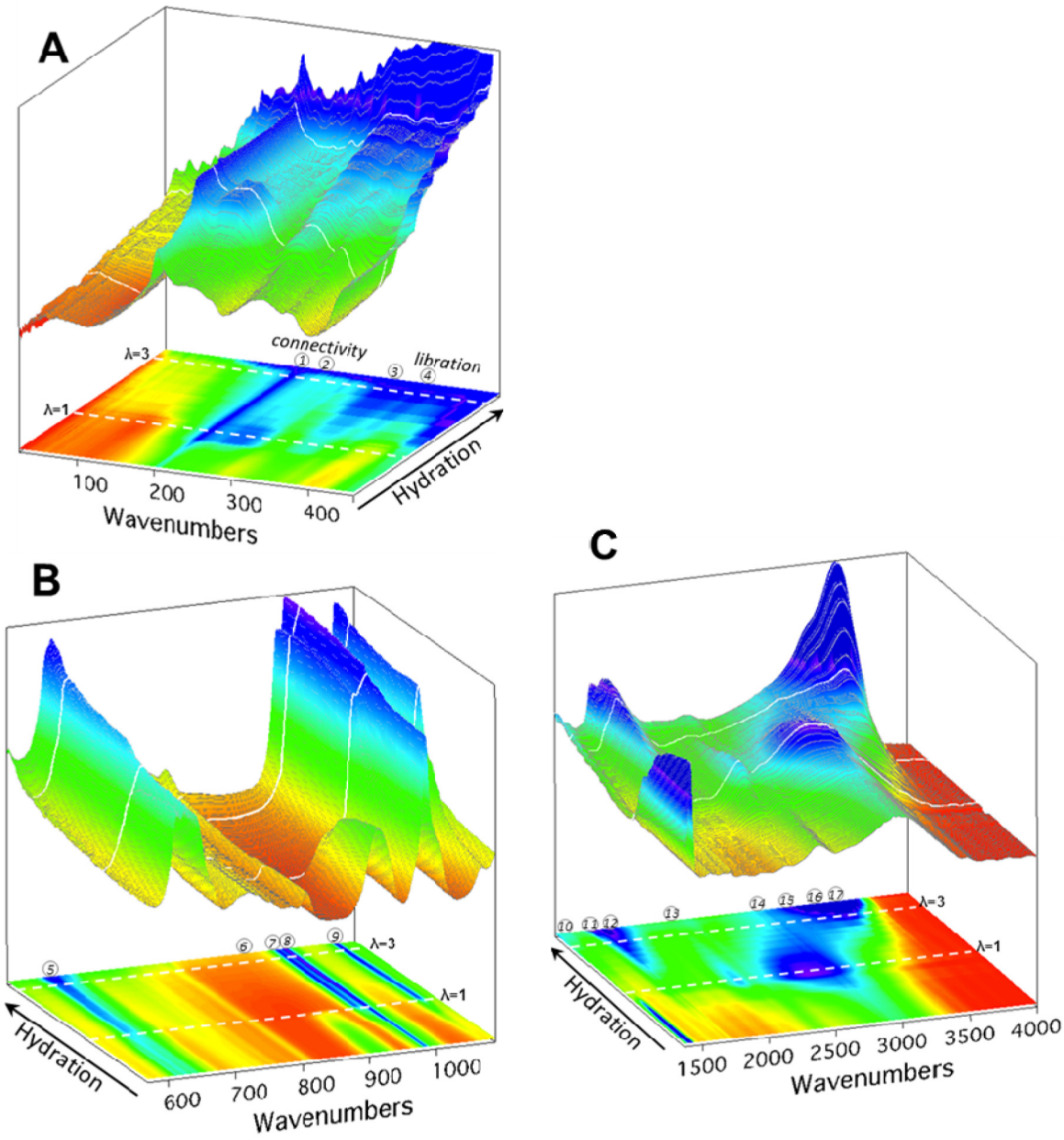

Figure 5.1.2 – Nafion hydration sequences. Nafion-H absorbance evolution with hydration levels in the FIR (A) 50 cm^{-1} to 500 cm^{-1} and MIR (B) 600 cm^{-1} to 1100 cm^{-1} and (C) 1400 cm^{-1} to 4000 cm^{-1}. Intensity grows from red to blue. Bottom: Projection of the evolution (same color code). The λ=1 and λ=3 states are highlighted (white dashed lines). The assignment of the main labeled bands (1 to 17) is reported in Table 1. The H-bond between the sulfonic groups and H_3O^+ (Band 2: ~250 cm^{-1}) presents a maximum for λ=1. At λ=1 the ionization process is completed, resulting in a full disappearance of SO_3H band (band 6: 912 cm^{-1}) and the appearance of SO_3^- bands (band 9: 1062 cm^{-1}). The C-spectra show four bands associated to OH stretching in H_2O (band 17 ~3450 cm^{-1}) and in H_3O^+ (band 14 ~2700 cm^{-1}), HOH bending in H_2O (band 11 ~1634 cm^{-1}) and H_3O^+ (band 12 ~1730 cm^{-1}). The maximum for H_3O^+ bending is observed for λ=1.

Table 5.1 – Assignement and position (in cm^{-1}) of vibrational bands observed in the FIR and MIR regions [50-4000 cm^{-1}].

	Assignment	Dry state	λ=1	λ>3	Ref.
	FIR				
	Structure ?	165			
	H···O H-bond in H_2O			190	49
	H-matrix ($SO_3H\cdots HO_3S$ *in dry state*) H-ion ($SO_3^-\cdots H_3O^+$ *for λ=1*)	200	200		
1	CF_2 rocking	204	204	204	51
	H_2O libration			>240	49
2	H-matrix ($SO_3H\cdots HO_3S$ *in dry state*) H-ion ($SO_3^-\cdots H_3O^+$ *for λ=1*)	250	250		
	CSO bending	322	322	322	72
3	H-matrix ($SO_3H\cdots HO_3S$ *in dry state*) H-ion ($SO_3^-\cdots H_3O^+$ *for λ=1*)	335	335		
	SCF_3 wagging	345	345	345	73
4	H-matrix ($SO_3H\cdots HO_3S$ *in dry state*) H-ion ($SO_3^-\cdots H_3O^+$ *for λ=1*)	375	375		
	CF_3 bending	377	377	377	51
	MIR				
	SO_3H wagging	495			73
	CF_2 bending	503	503	503	74
	OSO bending in SO_3^-		515	515	19
	CF_2 bending	555	555	555	51
	OSO bending in SO_3 H	614			73
	CF_2 wagging	626, 639	626, 639	626, 639	74
5	OSO bending in SO_3^-		640	640	17
	CS stretching	805	805	805	74
6	S-OH symmetric stretching in SO_3H	912			18
7	?		969	971	
8	COC symmetric stretching	983	983	983	56
	?	1003	992	992	
9	SO stretching (in $SO_3^-\cdots H_3O^+$ *for λ=1*; in ($SO_3^-\cdots H_2O$ *for λ>3*)		1064	1057	17—19
10	S-O_2 stretching in SO_3H	1415			18
11	HOH bending in H_2O			1634	49
12	HOH bending (in H_3O^+ *for λ=1*; in $H^+\cdot n(H_2O)$ *for λ>3*)		1650, 1787	1730	52,59
13	OH stretching in H_3O^+		2210		
	CF_2 overtone	2370	2370	2370	18
14	OH stretching in H_3O^+		2700		
15	OH stretching in SO_3H	2980			17
16	OH symmetric stretching in H_2O			3230	49
17	OH asymmetric stretching in H_2O			3450	49

5—1.4.1 DRY STATE: SO3H…HO3S INTERACTIONS

A prerequisite to any quantitative study of hydration states is to characterize the fully dehydrated membrane. MIR spectra of Nafion-H and Nafion-Na dehydrated *in situ* by heating under vacuum are shown in Figure 5.1.3 and Figure 5.1.4. The S-O stretching modes have been well documented in the literature.[17-19] The S-O bands are accordingly observed in Nafion-H at 912 cm^{-1} and 1415 cm^{-1} for undissociated SO_3H, while at 1064 cm^{-1} for the SO_3^- groups. Only the latter is present in Nafion-Na spectrum since SO_3^- groups are involved in ionic bonds with Na^+ cations (Figure 5.1.3A). Nafion-H dehydration must go along with the appearance of SO_3H and disappearance of SO_3^- modes. Indeed, for a fully dried membrane, i.e. λ=0, the IR spectrum should not present 1064 cm^{-1} band but maximal 912 cm^{-1} and 1415 cm^{-1} features.

Figure 5.1.3B shows that it is not the case in Nafion-H dehydrated at 60°C, as both dissociated and undissociated forms coexist. In contrast, little or no SO_3^- is evidenced for Nafion-H dehydrated at higher temperatures. The severe heating at 120°C should more efficiently dry the sample and remove residual water, as claimed by several authors.[50] However, the S-O features do not give evidence of such behavior, as the 912 cm^{-1} peak appears to be slightly more intense at 80°C than 120°C.

Analysis of the MIR and FIR regions provide additional insights into drying above 60°C. As shown in Figure 5.1.4, a structure at 2370 cm^{-1} is observed in both Nafion-H and Nafion-Na samples.

Nafion-H, wide structures are centered respectively at 2700 cm^{-1} for the 60°C and 2980 cm^{-1} for both 80°C and 120°C membranes. These bands are clearly not due to bulk water, absorbing around 3400 cm^{-1},[49] but must originate from O-H stretching in sulfonic species or hydronium ions. Notice that the present 60°C dried measurement is in agreement with literature data for dried Nafion-H.[17-19] For the drier samples, a more unique O-H configuration can be inferred from the frequency shift and the narrow bandwidth. Hence, these observations suggest one contribution due to SO_3H for the T≥80°C dried samples (2980 cm^{-1}) [18] and a mix of SO_3H and H_3O^+ (2980 cm^{-1} and 2700 cm^{-1}) for the 60°C membrane resulting from the ionization process:

$$-SO_3H + H_2O \leftrightarrow -SO_3^- + H_3O^+$$

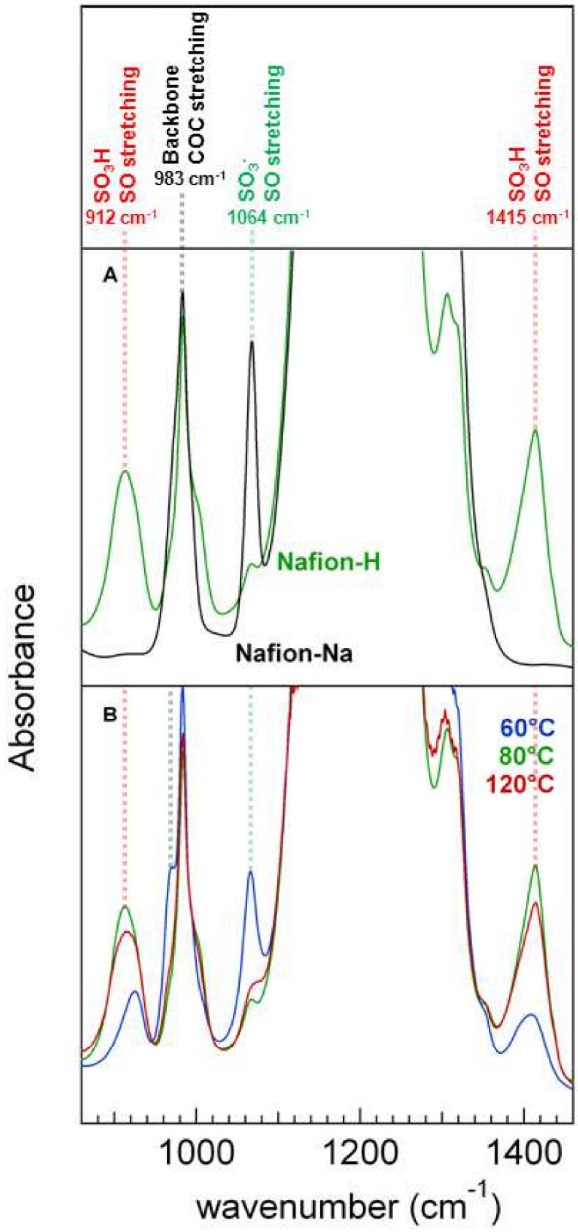

FIGURE 5.1.3 – MIR [600-1500 cm^{-1}] spectra of dehydrated Nafion-H and Nafion-Na. A) Mid infrared spectra [600-1500 cm^{-1}] of Nafion-H dried at 80°C (green) and Nafion-Na (black) dried at 80°C. B) In the same spectral range, spectra of Nafion-H dried at 60°C (blue), 80°C (green) and 120°C (red) are compared.

Drying at 120°C leads to a decrease of the OH stretching band with respect to the 80°C. Two smaller bands, at lower frequencies, are observed only for the 60°C sample. The band at 1665 cm^{-1} is most likely due to the bending of H_3O^+, and is lacking in the T≥80°C membranes. The band at 2210 cm^{-1} may also be related to H_3O^+. Both O-H stretching and bending modes thus show that drying

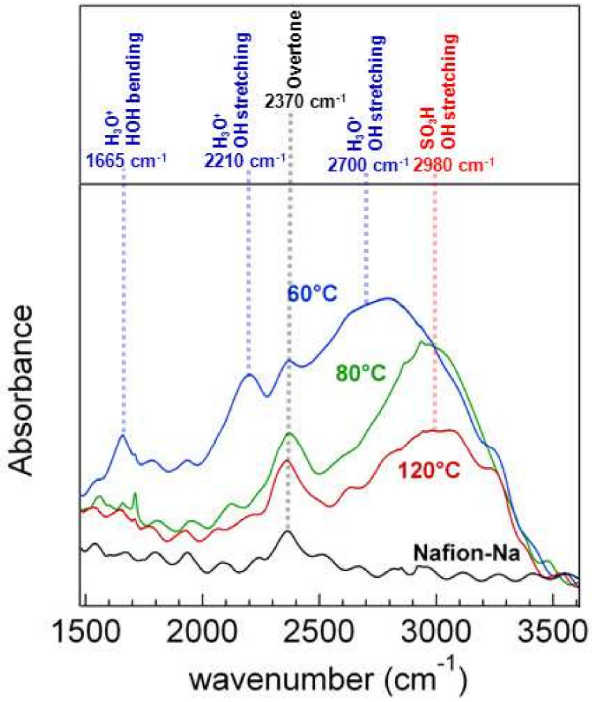

FIGURE 5.1.4 – MIR [1500-3500 cm^{-1}] spectra of dehydrated Nafion-H and Nafion-Na. Mid infrared spectra [1500-3500 cm^{-1}] of Nafion-H dried at 60°C (blue), 80°C (green) and 120°C (red), and Nafion-Na (black) dried at 80°C.

at 80°C the Nafion-H removes most H_3O^+ while restoring the SO_3H groups, as discussed above (Figure 5.1.3). At this stage, it is worth completing this analysis with FIR data. The region 100-400 cm^{-1} is dominated by *i)* the rocking in CF_2 at 204 cm^{-1},[51] appearing as a strong and narrow band in all samples and *ii)* H-bond stretching[49] (Figure 5.1.5A). The spectra of Nafion-Na and the driest Nafion-H also show a shoulder around 165 cm^{-1} which disappears with partial hydration and is possibly related to Nafion structure. The most prominent difference between Nafion-H and Nafion-Na membranes stems from a large vibration mode around 250 cm^{-1} only present in Nafion-H, whose intensity decreases upon drying temperature, and two other bands almost insensitive to the drying temperature at 335 cm^{-1} and 375 cm^{-1} (Figure 5.1.5A).

These three features are observed even in the most dried acid Nafion. Therefore, we can hypothesize that they arise from H-bonds established between two neighboring sulfonic groups (referred here as H-matrix interaction) in T≥80°C dried membranes, as represented in Figure 5.1.6.

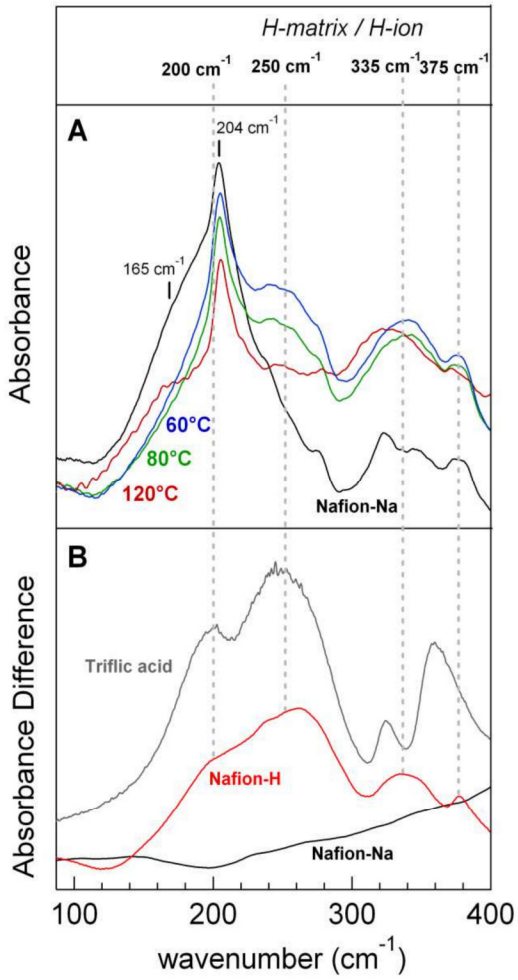

FIGURE 5.1.5 – FIR [100-400 cm^{-1}] spectra of dehydrated Nafion-H and Nafion-Na. (A) Far infrared spectra [100-400 cm^{-1}] of Nafion-H dried at 60°C (blue), 80°C (green) and 120°C (red), and Nafion-Na (black) dried at 80°C. (B) FIR absorption spectra of highly concentrated triflic acid solution ($\lambda=H_2O/SO_3H$ ~ 1) in gray; difference spectra of Nafion-H (red) and Nafion-Na (black) obtained by subtracting the absorbance spectrum of dry membrane from that of the membrane at λ=1. These difference spectra show the spectral signature from hydronium ions in Nafion-H channels (red) and water molecules in Nafion-Na (black).

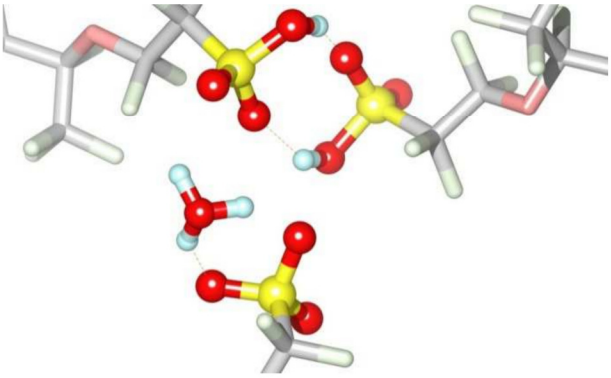

FIGURE 5.1.6 – Representation of H-matrix and H-ion. Schematic view of H-matrix [$SO_3H\ldots HSO_3$] (top) and H-ion [$SO_3\ldots.H_3O^+$] (bottom) for $0<\lambda<1$. Dashed lines show H-bonds. Color code: Oxygen (red), Sulfur (yellow), Hydrogen (light blue), Carbon (light grey) and Fluorine (light green).

In the 60°C dried samples, some sulfonic acid groups are found to be dissociated (as shown by MIR results), and one might expect to have an additional signature due to the intermolecular interaction between sulfonate ions and hydronium ions (labeled H-ion, Figure 5.1.6).

To further characterize H-ion interactions, we removed the signature of the matrix by subtracting the absorbance spectrum of dehydrated Nafion-H and Nafion-Na from these of the corresponding partially hydrated membranes (λ=1 as defined in the next section). The difference spectra are shown in Figure 5.1.5B together with the hydrated triflic acid (λ=1) spectrum used as a reference for sulfonate-hydronium interactions. Between 100 cm^{-1} and 400 cm^{-1}, the spectrum of the resulting Nafion-H subtracted curve remarkably resembles that of concentrated triflic acid solution. Actually, four bands are present in both systems: ~200 cm^{-1}, 250 cm^{-1}, 335 cm^{-1} and 375 cm^{-1}. They are not found in Nafion-Na (Figure 5.1.5B), and flagrantly originate from H-bonding. The similarity with triflic acid spectrum supports the predominance of H-ion interaction in λ=1 Nafion membrane. Such assignment is consistent with previous work on the H-bond of hydronium ion clusters[52] observed by IR^2MS^2 in the 260-1000 cm^{-1}. Three bands (~279 cm^{-1}, 358 cm^{-1} and 373 cm^{-1}) were assigned to the H-bond stretch involving a hydronium ion. In the present study, these bands are observed in Nafion-H but slightly shifted to lower frequencies. The observed shift may result from different H-bond strength between SO_3^- and H_3O^+ with respect to H_3O^+ …H_2O. From Figure 4A and B, we finally conclude that H-matrix and H-ion interactions absorb at similar frequencies, suggesting bondings with similar strength.

To summarize, the MIR data show that the Nafion-H membrane heated at 60°C contains a residual amount of H_3O^+ ($0<\lambda<1$) together with dissociated SO_3^-. Heating the Nafion-H membrane at 80°C results in a significant decrease of hydration towards an undissociated and hydronium-free state, labeled λ~0. No further recovery of SO_3H functions is found when increasing the drying temperature to 120°C, and only limited further drying is gained. As high temperature exposure may cause polymer reorganization affecting the membrane sorption properties,[53] we pursued the hydration studies using 80°C dried sample. The cation exchange allowed us to discern the bands associated to O...H bonds in the FIR spectra (Table 5.1). In the fully dehydrated state (λ~0), the FIR data show the presence of H-bonds between neighboring side chains

undissociated terminations (H-matrix), as was hypothesized in the recent work of Di Noto *et al*.[22] When a few water molecules are present in the membrane (λ<1), additional H-bonding between SO_3^- groups and hydronium ions is evidenced (H-ion).

5—1.4.2 HYDRATION UP TO λ=1: SULFONIC ACID DISSOCIATION AND HYDRONIUM ION FORMATION

Hydration of Nafion-H was investigated in FIR and MIR regions. As observed in Figure 5.1.2 and detailed in Figure 5.1.7, a first threshold of hydration is reached as several bands, 200 cm^{-1}, 250 cm^{-1}, 335 cm^{-1}, 375 cm^{-1}, 1064 cm^{-1}, 2210 cm^{-1} and 2700 cm^{-1} show simultaneous and drastic increase until reaching a maximum while bands at 912 cm^{-1} and 1412 cm^{-1} present opposite evolution until disappearing. They are the signatures of the gradual dissociation of SO_3H leading to the formation of the hydronium ion.

This ionization process of the sulfonic acid groups in the early stage of hydration was investigated by setting the membrane initially dry (80°C), under constant static pressures. Three sequences were set: dry to 0.2 mbar (RH=0.7 %), dry to 0.5 mbar (RH=1.8%) and dry to 1 mbar (RH=3.5%). The IR spectra were recorded until the equilibrium was reached, *i.e.* IR spectra did not evolve further on. Figure 5.1.7 displays the time- dependence of the intensity of specific bands characteristic of hydronium ions (250 cm^{-1} and 2700 cm^{-1}), SO_3H (912 cm^{-1}) and SO_3^- (1064 cm^{-1}) in the FIR and MIR regions (Figure 5.1.7A, B, C). The continuous increase of the 250 cm^{-1} band upon hydration (Figure 5.1.7A), confirms its assignment to intermolecular hydrogen bonding $H_3O^+ \ldots SO_3^-$ (H-ion), and thus constitutes a fingerprint of the increasing number of ionic species. The maximum of the intensity of the 250 cm^{-1} band corresponds to a fully established H-bond between H_3O^+ and SO_3^-, *i.e.* to a fully ionized λ=1 state. This state is reached after 20 minutes in the 1 mbar sequence, as seen from the net maximum visible on Figure 5.1.7A. Three hours are needed in the 0.5 mbar sequence. The subsequent decrease of the intensity for λ>1 (Figure 5.1.2A) evidences the diminution of the H-bonded $H_3O^+ \ldots SO_3^-$, as it will be discussed in details in the next section. In the 0.2 mbar sequence, the intensity reaches the λ=1 threshold in ~15 hours showing that, in this case, the ionization process is markedly slowed down.

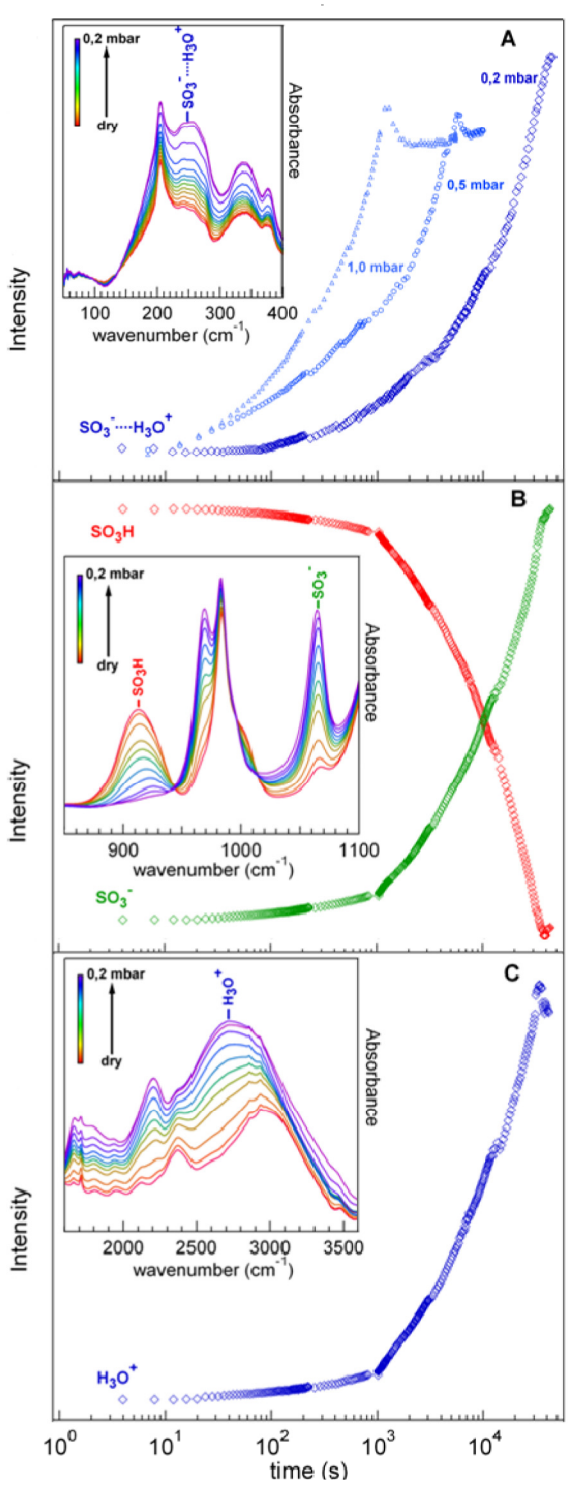

FIGURE 5.1.7 – First threshold of hydration. Insets: Evolution of the Nafion spectra during hydration, from dry (red spectrum) to 0.2 mbar of water vapor pressure (violet). The time-dependence of normalized band surfaces during hydration (A): kinetics of H_30^+ appearance from the band at 250 cm^{-1} for the 0.2, 0.5 and 1.0 mbar hydration sequences; (B): Ionization process: kinetics of SO_3^- formation obtained from the band at 1064 cm^{-1} (green) and SO_3H dissociation obtained from the band at 912 cm^{-1} (violet); (C) kinetics of H_3O^+ appearance from the band at 2700 cm^{-1}.

From these FIR kinetics data, we can conclude that, independently from the set vapor pressure, the first step of water sorption by a Nafion-H membrane lasts until all sulfonic groups are dissociated. We show that the λ=1 state can be reached for water vapor pressure lower than these generally used in sorption measurements.[7] That is due to the fact that the energy of the sulfonic acid solvation is greater than the deformation energy of the matrix.[8]

However, the water absorption from λ~0 to λ=1 is a kinetically-limited process depending on the flow rate of water molecules. A straightforward consequence is that in order to be relevant, sorption experiments at ultra-low relative humidity (below 1%) need to be performed on a dried sample during a day-long exposure to water vapor. The pressure dependence of the sorption kinetics is satisfactorily described by logarithmic time dependence. The logarithm of the time necessary to reach the complete ionization (λ =1) decreases linearly with the water vapor pressure. The *log(t)* dependence of water sorption kinetics in Nafion membranes was recently reported.[54] It was hypothesized that such behavior could originate from water penetration restrictions due to slow polymer relaxations.

The ionization scenario assessed by the FIR spectra variations is confirmed by the behavior of the MIR bands. Figure 5.1.7B shows the ionic dissociation monitored through the total disappearance of SO_3H band at 912 cm^{-1} (the same effect is observed on the 1415 cm^{-1} band) and the simultaneous appearance of SO_3^- species revealed by the increasing of the 1064 cm^{-1} mode. The equilibrium state reached at 0.2 mbar after 15 hours is characterized by $[SO_3H]=0$ and $[SO_3^-]=1$, corresponding to a full ionization of the SO_3H groups and, accordingly to the FIR data, to λ=1. Additionally, we observe interesting features in the region [2000-3000 cm^{-1}]. The time-dependence variation of the intensity of the 2210 cm^{-1} and 2700 cm^{-1} bands (Figure 5.1.7C) is highly correlated to the evolution of both the SO_3^- (1064 cm^{-1}) and $H_3O^+ \ldots SO_3^-$ (250 cm^{-1}) curves (Figure 5.1.7B and 5.1.7A). As for the H-bond stretch of H_3O^+ at 250 cm^{-1}, the 2210 cm^{-1} and 2700 cm^{-1} bands reach a maximum for λ=1 (Figure 5.1.2C). Moreover, they are not observed in Nafion-Na where no H_3O^+ species are present (not represented here). The 2210 cm^{-1} and 2700 cm^{-1} modes are then attributed to the O-H stretching of the H_3O^+ species and we exclude an assignment to SO_3H groups[17,20,43] or to a Fermi resonance.[18] Instead, they constitute the MIR signature of hydronium ions formation when a water

molecule interacts with one sulfonic group. Clearly, correlating FIR and MIR data provides a unique appealing opportunity to consistently ascribe vibrational modes of the hydronium ions and their interaction with the Nafion-H sulfonate groups for 0<λ<1.

Other spectral features of the MIR show interesting evolution upon water uptake. The band at 969 cm^{-1} evolves upon hydration. Several authors have assigned this band to the COC stretching of the side chains[18,19,55] or to CF_3 vibration.[56] From its similar evolution to the SO stretching of SO_3^- (1064 cm^{-1}) as a function of water vapor pressure, we alternatively suggest that it may be related to a SO_3^- species. The band at 983 cm^{-1} is unaffected by the hydration process supporting previous assignment[56] to the stretching of the ether groups inside the side chains to the backbone or the –CF stretching in the CF_2CFCF_3 group as previously suggested.[57] A shoulder at higher frequency is sensitive to the hydration level as it shifts from 1003 cm^{-1}, when the membrane is dry, to 992 cm^{-1} for λ=1. The attribution of this band is still controversial.[22]

5—1.4.3 LOW WATER CONTENT IONIZED STATE, λ=1 TO 3: HYDRONIUM-WATER-SULFONIC CHARGES INTERACTIONS, AND HIGH WATER CONTENT λ=3 TO 14

After completion of the ionization process, stepwise hydration was performed by gradually increasing the pressure in the range 1.0 mbar to 28.1 mbar (RH=3.5% to 100%). Several major effects are witnessed for λ>1: *i)* a modification of the chemical environment of SO_3^- species (640 cm^{-1} and 1064 cm^{-1}, Figure 5.1.2B) *ii)* the disappearance of the stretching bands associated to the H_3O^+ species (2210 and 2700 cm^{-1}, Figure 5.1.2C) and *iii)* the gradual disappearance of H-ion associated to $SO_3^-\ldots H_3O^+$ (250 cm^{-1}) (Figure 5.1.2A). The evolution of spectra in these regions are detailed in Figure 5.1.8A and B with the bottom curves corresponding to the λ=1 to 3 hydration, and the top curves to the λ=3 to 14 hydration. These dramatic evolutions are monitored through *i)* the variations of SO_3^- frequency and the intensity variations of *ii)* specific MIR bands (ν(O-H) H_3O^+) and *iii)* FIR bands (H-ion, water H-bond), reported in Figure 5.1.8C and D.

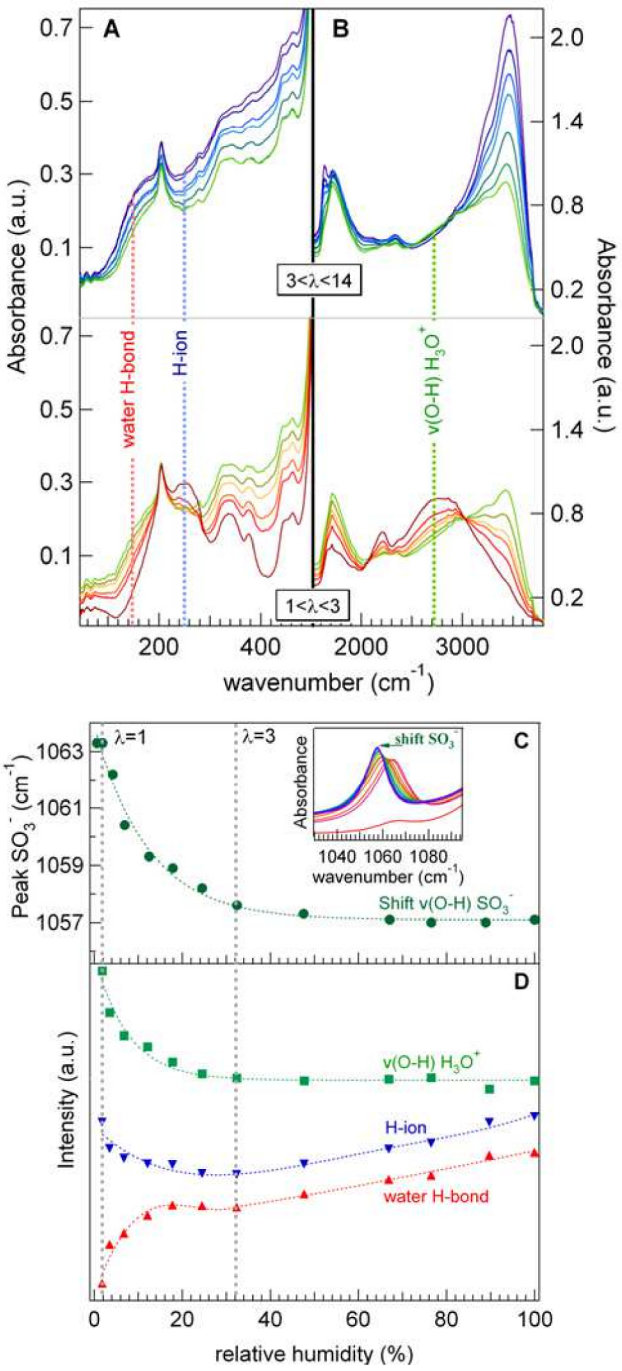

FIGURE 5.1.8 – High water content Nafion. (A) FIR spectra [50-500 cm^{-1}] of Nafion-H at different humidity levels for 1>λ>3 (bottom, spectra from red to green) and 3>λ>14 (top, spectra from green to violet). (B) MIR spectra [1500-3800 cm^{-1}] of Nafion-H at different humidity levels for 1>λ>3 (bottom, spectra from red to green) and 3>λ>14 (top, spectra from green to violet). Bands used to follow both the water and the hydronium ion evolutions in the FIR and MIR regions are highlighted (red, blue, green). (C)Frequency shift of the stretching SO in SO_3^- and (D) evolution of selected bands in the FIR region (water H-bond 145 cm^{-1}, H-ion 250 cm^{-1}) and the MIR region (v(O-H) H_3O^+ 2710 cm^{-1}) as a function of relative humidity for λ>1, evidencing the λ=3 threshold. The lines are guide for the eyes. Inset: Shift of the band associated to the stretching SO in SO_3^- from ~1064 cm^{-1} to ~1057 cm^{-1}.

In all cases, major modifications are observed up to a value of ~30% RH, (yielding an hydration level λ=3)[58] that concomitantly corresponds to the growing of bulk like water spectral features such as connectivity band ~200cm^{-1} and libration band ~350 cm^{-1} (Figure 5.1.8A), HOH bending and O-H stretching bands at 1634 cm^{-1} and ~3400 cm^{-1} (Figure 5.1.8B).

We thus evidence a second hydration threshold that separates the so-called low water content regime starting at 3.5% and ending at ~30% (1<λ<3), and the high water content regime for λ>3.

Let us describe more specifically the low water content regime, for 1<λ<3. Upon hydration the 1064 cm^{-1} band associated to the SO_3^- stretching mode shifts continuously towards lower wavenumbers (1064 cm^{-1} to ~1057 cm^{-1}) until reaching the ~30% RH threshold (Figure 5.1.8C). This frequency shift suggests an increase of the number of H-Bond between water molecules and the sulfonic head. Furthermore, the disappearance of a direct H_3O^+…SO_3^- interaction, is visualized through the decreasing of the 250 cm^{-1} intensity observed when 1<λ<3 (Figure 5.1.8A and 5.1.8D). Simultaneously the appearance of a shoulder at ~150 cm^{-1} and the growing of the band at ~350 cm^{-1} indicate the presence of H-bonded water molecules to the sulfonic group H_2O...SO_3^- (Figure 5.1.8A).

Figures 5.1.8B and D show the intensity evolution of the 2700 cm^{-1} band attributed to OH stretching in the H_3O^+ species when bonded to SO_3^-. It is clearly correlated to the 250 cm^{-1} band (Figure 5.1.8A), and indicates the disappearance of these bonded hydronium ions. This is further corroborated by the similar decreasing of the 2210 cm^{-1} band and the increasing of the 1730 cm^{-1} associated to the hydrated proton bending (Figure 5.1.8B).

All these spectral evolutions probe the progressive replacing of H_3O^+ by H_2O in the SO_3^- environment. One can notice the presence at 3032 cm^{-1} of an isobestic-like point in Figure 5.1.8B suggesting an equilibrium as such:

$$-SO_3^-\ldots H_3O^+ + H_2O \leftrightarrow -SO_3^- + H_2O + H_3O^+$$

At this stage for λ>1 we have characterized the progressive removal of hydronium ion from the vicinity of SO_3^-, yet the question about the H^+ environment remains. At λ=3, all protons are likely surrounded only by water

molecules and develop the so-called Zundel ($H_5O_2^+$) or Eigen ($H_9O_4^+$) cations as represented in Figure 5.1.9. According to the literature, Zundel ion bands are predicted[52,59] in the 3000-3160cm^{-1}, and the Eigen ion should give rise to a very broad band around 2000-3000 cm^{-1}.[60] The bending modes are all predicted

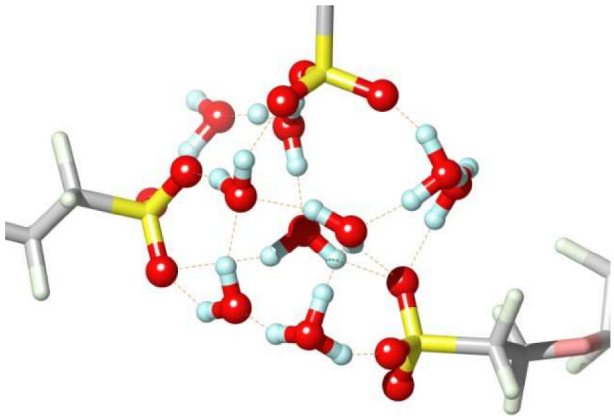

FIGURE 5.1.9 – Representation of hydrated Nafion. Schematic view of hydrated Nafion-H for λ=3. Dashed lines show H-bonds. Color code: Oxygen (red), Sulfur (yellow), Hydrogen (light blue), Carbon (light grey) and Fluorine (light green).

around 1730 cm^{-1} and therefore cannot be used to discriminate the H^+ environment.

As seen in Figure 5.1.8B for λ~3, a broad feature is indeed present at 2000-3000 cm^{-1} in addition to the intense contribution of the water molecules at higher frequency. Moreover an unresolved contribution can also be observed at 3100 cm^{-1}. These data cannot point out at a progressive replacing of Zundel into Eigen form but instead suggest a coexistence of both ions even at highest water content.

Figure 5.1.8A and 5.1.8B (top curves) present the evolution of the spectra for higher hydrations, λ>3. The strong increase of the bending at 1634 cm^{-1} and stretching at 3230 cm^{-1} and 3450 cm^{-1} is clearly the signature of bulk-like water molecules although their frequencies are slightly shifted compared to pure bulk water.[49] Such frequency shifts are likely caused by the presence of ions as well as spatial confinement inside ionic channels. These bands as well as the connectivity (Figure 5.1.8A) and libration broad features[61] show a continuous increase up to RH=100%, i.e. λ=14. The sorption process continues without noticeable changes in bands evolution until saturation of the membrane.

As soon as λ=3, we thus observe an increased number of water molecules interacting together showing the establishment of a bulk-like H-bond network inside ionic channels.

5—1.5 DISCUSSION

The Nafion FIR bands are reported in Table 5.1 with new attributions underlined in color. Selected MIR features are also summarized in Table 5.1, highlighting some new assignments provided here on the basis of the FIR-MIR combination. A schematic evolution of molecular environments upon hydration is depicted in Figure 5.1.6 for 0<λ<1 and Figure 5.1.9 for λ=3. Protons, hydronium ions and water molecules are shown together with sulfonic acid groups. H-bonds established among the various chemical species are represented by dashed lines. The effects that we observe upon *in situ* calibrated hydration provide a comprehensive picture of a three-step molecular-level sorption mechanism. FIR and MIR spectral features evolve upon water loading in a complementary correlated way. By carefully inspecting the absorbance spectra starting from a highly dehydrated initial state (dry membrane at 80°C, λ~0) along the whole spectral range [50-3500 cm^{-1}], we were able to assess the existence of two well-defined hydration threshold, respectively at λ=1 and λ=3. These thresholds are precisely determined through abrupt and unambiguous IR bands disappearance or appearance, which reveal a homogeneous behavior of the whole membrane at local scale upon hydration. The existence of characteristic thresholds associated to different proton transfer mechanisms has been widely discussed in the literature, in regards of the functional properties of the ionomer membrane, the morphological reorganizations of polymer matrix upon swelling, the molecular properties of the ionic species and the overall proton transport efficiency. However, the abundant literature on the subject remains somehow controversial, and mostly focused on λ>3 investigations. An important output of the present study is thus to shed new light on the role of water molecules in, first, dissociating protons, and, second, mediating the proton-SO_3^- interactions.

Previous IR studies showed that the first molecular process when hydrating a PFSA membrane is the ionization of terminal headgroups, *i.e.* breaking of the covalent bond between the hydrogen and the sulfonate. Yet, the values of the full sulfonic acid dissociation are quite scattered in the literature, ranging from

λ=1-2[22,62] to 6. A thermodynamical analysis of the sorption isotherm leads to a threshold at λ=2.[6] It has to be stressed that IR and sorption results are dependent on the presence or not of residual water in the initial dry state, thus inducing discrepancies in the definition of the reference "zero" value. The dissociation process was studied also by *ab initio* molecular simulations.[30—32] H_3O^+-SO_3^- ion-pairing was reported for λ<3. The threshold for the formation of hydronium ions separated from the sulfonates was found at typically λ~3 for various PFSA membranes. The most favorable configurations were found to occur when the polymer chains are distorted, thus inducing side-chains terminations to be bridged through proton complexes.

After ionization is completed, the low water content until λ=3 appears as a critical regime for establishing the conditions towards fast proton diffusion inside ionic domains. Kreuer *et al* reported that, below the λ=3 threshold, the values of the self-diffusion coefficient of water, D_s, determined by PFG-NMR and the proton diffusion coefficient, D_σ, extracted through the Nernst-Einstein equation from conductivity measurements, merge.[2] This finding was interpreted as the predominance of a mass diffusion mechanism of hydroniums at low hydration. Below λ=3, the H-bond network is too poorly developed to allow ultra-fast structural diffusion of protons through H-bonds breaking and forming in hydrated protonic clusters, as confirmed by molecular dynamics simulations.[33] The structural diffusion appears at λ>3 and then predominates at high water content, leading to efficient proton transfer. Additional insights into proton and water motions were gained at a molecular level by Quasi Elastic Neutron Scattering (QENS) experiments performed on Nafion membranes hydrated from λ= 1.5 to 18.[63] It was shown that, at the experimental time scale shorter than ~1 ns, the threshold for detecting proton diffusive motions is λ~3. Below this value, a slow hopping process was evidenced and attributed to hydronium localized motions restricted in the vicinity of the ionic groups. The "slow protons" form an interfacial layer located at the hydrophobic/hydrophilic interface, in strong interaction with ionic headgroups. In contrast, above λ=3 the QENS data showed the appearance of confined translational diffusion in small water droplets accompanied by long-range Fickian diffusion at nanoscale. Both diffusive and jump processes are accelerated upon hydration, with steep variations of H_3O^+ and H_2O diffusion coefficients observed as soon as λ=3. Our IR results are in good agreement with these studies. The present IR data suggest that the limiting factor at low water content is likely to be the strength of

hydronium and sulfonate ions interactions. Below the□□=3 threshold, sulfonate ions act as proton traps inhibiting hydronium diffusion (H-ion interaction). Such inhibiting effect was postulated by all-atoms Molecular Dynamics Simulations[34—37] and Empirical Valence Bond models.[38—40] Proton mobility was also found to be hindered at λ<3 by the presence of ionic cages (H_3O^+ interacting with several SO_3^-)[41] and bridging Zundel ions ($SO_3…H_2O_5^+…SO_3$).[30,35—37,42]

The high water content behavior of the membrane is more documented in the literature (most simulation studies start at λ>3 in the as-designed fully ionized situation). Several thresholds were hypothesized in the region 4<λ<10 depending on the method employed to investigate either the polymer morphology, the water properties or the proton behavior. Time-resolved IR studies revealed a significant reduction of bounded water molecules at λ=5[64—66] interpreted as a rearrangement of the interfacial region leading to a decreasing number of water molecules bridging neighboring sulfonate groups. The dielectric constant of Nafion was also showed to suddenly increase at λ=6.[27] All-atoms MD simulations[34—37] predicted that most H_2O and H_3O^+ are bounded to SO_3^- up to λ=7, the number of H_2O water molecules around one SO_3^- increases rapidly until λ=5 and then saturates above λ=9. The QENS data[14,67] show a bulk-like behavior of protons at λ=10, when the dynamical size of confining droplets reaches that of a hydrated Eigen ion. Several recent studies reported also a significant modification of the nanostructure at λ=5-6. A threshold for proton conduction due to a change in ionic domains topology, shape and size was found at λ~4 in coarse-grained simulations.[68] Similarly, the percolation of connected ionic domains was determined at λ=5 by all atoms simulations.[37] In the same spirit, NMR relaxometry experiments showed that protons are confined in anisotropic lamellar-like channels for λ<5.[25] At λ=5, a 2D-to-3D morphological transition was deduced from the NMR relaxation profiles, and interpreted as the building of an isotropic network of non-wetting interconnected channels characterized by almost no proton-sulfonate interactions, thus promoting enhanced ionic mobility.

Overall, the existence of a “transition” originating from morphological modifications or different proton motion mechanisms, or both, is not clearly established in the region λ>3. In the present study, we observed no subsequent threshold above λ=3 but the evolution of IR spectra towards bulk-like properties,

as evidenced by the huge increase in connectivity, libration, bending and stretching modes of water. The sorption process is clearly continuous and can be rationalized by the additional penetration of water molecules inside the ionic hydrated channels without significant impact on the chemical environment of ionic species.

The first hydration phase up to λ=3 corresponds to the solvation of polar groups and the formation of disconnected aqueous clusters centered on the ionic functions. Once H-ion interactions are screened by water molecules intercalated in between hydronium and sulfonate ions, we observe the densification of the continuous H-bond network. The proton transfer efficiency depends on the balance between local interactions with charges, spatial confinement inside ionic domains and nanoscale connectivity. On the basis of the present IR study, we can draw the conclusion that in the early stages of hydration the functional behavior of the Nafion membrane is governed by the ionic interactions. The super acidity of the terminal sulfonic functions and high hydrophobicity of the perfluorinated polymer backbone insure a full ionic dissociation at λ=1 and the absence of detrimental proton-polymer interactions. The initial bridged configurations observed in dry membranes (H-matrix interactions) favor the intercalation of protonic species between neighboring ionic species, as predicted by simulations.[30] Few conduction pathways could appear as soon as λ>1 along the charged hydrophobic/hydrophilic interface,[33,69,70] allowing protons to be transferred across membrane thickness via slow hops, before structural diffusion can more efficiently occur at higher hydrations. The observation of thresholds among well-defined sequenced processes, namely ionization, water clustering and creation of dense network, is a characteristic diagnosis of the peculiarity of Nafion membrane with respect to other proton conducting membranes such as polyaromatic ones.[71]

5—1.6 CONCLUSIONS

The ionization process, hydronium ion formation, protonic species formation, and molecular interactions in a Nafion membrane have been highlighted by a complete set of infrared spectra recorded both in the FIR and MIR regions by exploiting the AILES beamline of synchrotron SOLEIL. Using a specially designed cell, we carefully controlled the initial dry state of the polymer and

proceeded to sequences of hydration allowing a quantitative description of the various processes at stake. For the first time, the spectral signatures were obtained *in situ* in the FIR region, leading to unprecedented clues regarding the intermolecular arrangement between ionic groups, proton species and water molecules in the ultra-low water content state. Combining FIR and MIR allowed us also to propose an alternative attribution of controversial MIR features. The molecular picture that emerges from this study is a three-step hydration process. In the initial dry polymer state, sulfonic groups are linked through hydrogen bonding, thus suggesting a locally bridged ionic structure in the absence of water. Such situation, which was already hypothesized on the basis of MIR results,[22] is herein assessed from the intermolecular spectral modes probed in the FIR range. Next, two thresholds are found, firstly, a water content corresponding to 1 water molecule per ionic group, and secondly, 3 water molecules per ionic group. The former is related to the kinetically-driven ionization process leading to the formation of SO_3^-…H_3O^+ species. The latter governed by water vapor pressure corresponds to the intercalation of water molecules between these species. At λ=3 we find that water preferentially hydrate the SO_3^- functions, and H_3O^+ species are not likely to directly interact with SO_3^-. Hydrated protonic Zundel and Eigen complexes are then formed and the fast transfer of charge carriers can develop in the denser H-bond network. This study opens the path to the investigation of other H-bonded electrolytes developed for advanced electrochemical devices, such as fuel cells, electrolysers, red flow batteries. Polymer membranes alternative to Nafion could be invaluably investigated to deepen the knowledge on proton formation and hydration as a function of relevant parameters as the chemical architecture, the side chain length and the density of ionic charges. The FIR synchrotron spectroscopy is an elegant tool to unravel the complex nature of intermolecular interactions in protonic conductors. Cross-fertilized by complementary inputs from molecular-level studies (simulations, QENS, NMR), it provides a detailed understanding of the protonic species environment and hydration mechanisms, enabling to progress towards the design of efficient nanostructured polymers with controlled and optimized hydration-driven functional properties. This is a critical issue in energy-related applications, filtration, ionic separation and bioinspired nanodevices.

REFERENCES

(1) Elabd, Y. A.; Hickner M. A. *Macromolecules,* 44, 1–11 (**2011**).

(2) Duncan A. J.; Leo D. J.; Long T. E. *Macromolecules*, 41 (21), 7764-7775 (**2008**).

(3) Mauritz, K. A.; Moore, R. B. *Chemical Reviews*, 104, 4535-4585 (**2004**).

(4) Kreuer, K. D.; Paddison, S. J.; Spohr, E.; Schuster, M. *Chemical Reviews*, 104, 4637-4678 (**2004**).

(5) Li, N.; Guiver, M. D. *Macromolecules*, 47, 2175-2198 (**2014**).

(6) Zawodzinski, T.A.; Spinger, T. E.; Davey, J.; Jeste, R.; Lopez, C.; Valerio, J.; Gottesfeld, S. *J. Electrochem. Soc.*, 140, 1981-1985 (**1993**).

(7) Jalani, N. H.; Choi, P.; Datta, R. *J. Memb. Sci.*, 254, 31-38 (**2005**) .

(8) Satterfield, M. B.; Benziger, J. B. *J. Phys. Chem. B*, 112, 3693-3704 (**2008**).

(9) Monroe, C. W.; Romero, T.; Merida, W.; Eikerling, M. *J. Memb. Sci.*, 324, 1-6 (**2008**).

(10) Hallinan, D. T.; De Angelis, M. G.; Baschetti, M. G.; Sarti, G. C.; Elabd, Y. A. *Macromolecules*, 43, 4667-4678 (**2010**).

(11) Gierke, T. D.; Munn, G. E.; Wilson, F. C. *J. Polym. Sci.*, 19, 1687-1704 (**1981**).

(12) Gebel, G. *Polymer*, 41, 5829-5838 (**2000**).

(13) Rubatat, L.; Rollet, A. L.; Gebel, G.; Diat, O. *Macromolecules*, 35, 4050-4055 (**2002**).

(14) Perrin, J. C.; Lyonnard, S.; Volino, F. *J. Phys. Chem. C*, 111, 3393-3404 (**2007**).

(15) Kusoglu, A.; Modestino, M. A.; Hexemer, A.; Segalman, R. A.; Weber, A. Z. *ACS Macro Letters*, 1, 33-36 (**2012**).

(16) Falk, M. *Can. J. Chem.*, 58, 1495-1501 (**1980**).

(17) Ostrowska, J.; Narebska, A. *Colloid Polym. Sci.*, 261, 93-98 (**1983**).

(18) Buzzoni, R.; Bordiga, S.; Ricchiardi, G.; Spoto, G.; Zecchina, A. *J. Phys. Chem.*, 99, 11937-11951 (**1995**).

(19) Laporta, M.; Pegoraro, M.; Zanderighi, L. *Phys. Chem. Chem. Phys.*, 1, 4619-4628 (**1999**).

(20) Iwamoto, R.; Oguro, K.; Sato, M.; Iseki, Y. *J. Phys. Chem. B*, 106, 6973-6979 (**2002**).

(21) Hofmann, D. W. M.; Kuleshova, L.; D'Aguanno, B.; Di Noto, V.; Negro, E.; Conti, F.; Vittadello, M. *J. Phys. Chem. B*, 113, 632-639 (**2009**).

(22) Negro, E.; Vittadello, M.; Vezzù, K.; Paddison, S.; Di noto, V. *Solild State Ionics*, 252, 84-92 (**2013**).

(23) MacMillan, B.; Sharp, A. R.; Armstrong, R. L. *Polymer*, 40, 2471-2480 (**1999**).

(24) Ye, G.; Janzen, N.; Goward, G. R. *Macromolecules*, 39, 3283-3290 (**2006**).

(25) Perrin, J. C.; Lyonnard, S.; Guillermo, A.; Levitz, P. *J. Phys. Chem. B* , 110, 5439-5444 (**2006**).

(26) Guillermo, A.; Gebel, G.; Mendil-Jakani, H.; Pinton, E. *J. Phys. Chem. B*, 113, 6710-6717 (**2009**).

(27) Lu, Z. J. Polizos, G.; Macdonald, D. D.; Manias, E. *J. Electrochem. Soc.*, 155, B163-B171 (**2008**).

(28) Yoshida, H.; Miura, Y. *J. Memb. Sci.*, 68, 1-10 (**1992**).

(29) Kalapos, T.L.; Decker, B.; Every, H.A.; Ghassemi, H.; Zawodzinski, T.A. *J. Power Sources*, 172, 14-19 (**2007**).

(30) Paddison, S.J.; Elliot, J.A. *J. Phys. Chem. A*, 109, 7583-7593 (**2005**).

(31) Paddison, S.J.; Elliot, J.A. *Phys. Chem. Chem. Phys.*, 8, 2193-2203 (**2006**).

(32) Paddison, S.J.; Elliot, J.A. *Solid State Ionics*, 177, 2385-2390 (**2007**).

(33) Paddison, S.J.; Paul, R. *Phys. Chem. Chem. Phys.*, 4, 1158-1163 (**2002**).

(34) Venkatnathan, A.; Devanathan, R.; Dupuis, M. *J. Phys. Chem. B*, 111, 7234-7244 (**2007**).

(35) Devanathan, R.; Venkatnathan, A.; Dupuis, M. *J. Phys. Chem. B*, 111, 13006-13013 (**2007**).

(36) Devanathan, R.; Venkatnathan, A.; Dupuis, M. *J. Phys. Chem. B*, 111, 8069-8079 (**2007**).

(37) Devanathan, R.; Venkatnathan, A.; Rousseau, R. ; Dupuis, M.; Frigato, T.; Gu, W.; Helms, V. *J. Phys. Chem. B*, 114, 13681-13690 (**2010**).

(38) Spohr, E. *Molecular Simulation*, 30, 107-115 (**2004**).

(39) Petersen, M. K.; Voth, G. A. *J. Phys. Chem. B*, 110, 18594-18600 (**2006**).

(40) Kornyshev, A. A.; Kuznetsov, A. M.; Spohr, E.; Ulstrup, J. *J. Phys. Chem. B*, 107, 3351-3366 (**2003**).

(41) Hristov, I. H.; Paddison, S. J.; Paul, R. *J. Phys. Chem. B*, 112, 2937-2949 (**2008**).

(42) Elliott, J. A.; Paddison, S. J. *Phys. Chem. Chem. Phys.*, 9, 2602-2618 (**2007**).

(43) Hallinan, D. T.; Elabd, Y.A. *J.Phys.Chem. B*, 113, 4257-4266 (**2009**).

(44) Brubach, J. B.; Manceron, L.; Rouziére, M.; Pirali, O.; Balcon, D.; Kwabia Tchana, F.; Boudon, V.; Tudorie, M.; Huet, T.; Cuisset, A.; Roy, P. *AIP Conference Proceedings*, 1214, 81-84 (**2010**).

(45) Roy, P.; Rouzieres, M.; Qi, Z. M.; Chubar, O. *Infrared Physics & Technology*, 49, 139-146 (**2006**).

(46) Dalla Bernardina, S.; Alabarse, F.; Kalinko, A.; Roy, P.; Vita, N.; Hienerwadel, R.; Berthomieu, C.; Judenstein, P.; Zanotti, J. M.; Bantignies, J.L.; Haines, J.; Catafesta, J.; Creff, G.; Manceron, L.; Brubach, J. B. *Vib. Spectrosc.*, 75, 154–161 (**2014**).

(47) Hanwell, M. D.; Curtis, D. E.; Lonie, D. C.; Vandermeersch, T.; Zurek, E.; Hutchison, G. R . *J. of Cheminformatics* , 4, 17 (**2012**).

(48) Pettersen, E. F.; Goddard, T. D.; Huang, C. C.; Couch, G. S.; Greenblatt, D. M.; Meng, E. C.; Ferrin, T. E. *J. Comput. Chem.*, 25, 1605-1612 (**2004**).

(49) Brubach, J. B.; Mermet, A.; Filabozzi, A.; Gerschel, A.; Roy, P. *J. Phys. Chem.*, 122, 184509 (**2005**).

(50) DeAngelis, M. G.; Lodge, S.; Giacinti Baschetti, M.; Sarti, G. C.; Sanguineti, A.; Fossati, P. *Desalination*, 193, 398-404 (**2006**).

(51) Liang, C.Y.; Krimm, S. *J. Chem. Phys.*, 25, 563-571 (**1955**).

(52) Heine, N.; Fagiani, M. R.; Rossi, M.; Wende, T.; Berden, G.; Blum, V.; Asmis K. R. *J. Am. Chem. Soc.*, 135, 8266-8273 (**2013**).

(53) Maldonado, L.; Perrin, J.C.; Dillet, J.; Lottin, O. *J. Memb. Sci.*, 389, 43-56 (**2012**).

(54) Gebel, G.; Lyonnard, S.; Mendil-Jakani, H.; Morin, A. *J. Phys.: Condens Matter,* 23*,* 234107 (**2011**).

(55) Korzeniewski, C.; Snow, D. E.; Basnayake, R. *Applied Spectroscopy*, , 60, 599-604 (**2006**).

(56) Danilczuk, M.; Lin, L.; Schlick, S.; Hamrock, S.; Schaberg, M. *J. Power Sources*, 196, 8216-8224 (**2011**).

(57) Ferrari, M. C.; Catalano, J.; Baschetti, M. G.; De Angelis, M. G.; Sarti, G. C. *Macromolecules*, 45, 1901-1912 (**2012**).

(58) Peron, J.; Mani, A.; Zhao, XS.; Edwards, D.; Adachi, M.; Soboleva, T.; Shi, ZQ.; Xie, Z.; Navessin, T.; Holdcroft, S. *J. Membr. Sci.*, 356, 44 (**2010**).

(59) Haedrick, J. M.; Diken, E. G.; Walters, R. S.; Hammer, N. I.; Christie, R. A.; Cui, J.; Myshakin, E. M.; Duncan, M. A.; Johnson, M. A.; Jordan, K. D. *Science*, 308, 1765-1769 (**2005**).

(60) Kulig, W.; Agmon, N. *Nat. Chem.*, 5, 29-35 (**2013**).

(61) Miura, N.; Yamada, H.; Moon, A. *Spectrochim. Acta, Part A*, 77, 1048-1053 (**2010**).

(62) Giffin, G. A.; Haugen, G. M.; Hamrock, S. J.; Di Noto V. *J. Am. Chem. Soc.*, 135, 822-834 (**2012**).

(63) Perrin, J. C.; Lyonnard, S.; Volino, F. *J. Phys. Chem. C*, 111, 3393-3404 (**2007**).

(64) Spry, D. B.; Goun, A.; Glusac, K.; Moilanen, D. E.; Fayer, M. D. *J. Am. Chem. Soc.*, 129, 8122-8130 (**2007**).

(65) Moilanen, D. E.; Piletic, I. R.; Fayer, M. D. *J. Phys. Chem. C*, 111, 8884-8891 (**2007**).

(66) Moilanen, D. E.; Spry, D. B.; Fayer, M. D. *Langmuir*, 24, 3690-3698 (**2008**).

(67) Pivovar, A. A.; Pivovar, B. S. *J. Phys. Chem. B*, 109, 785-793 (**2005**).

(68) Malek, K.; Eikerling, M.; Wang, Q.P.; Liu, Z.S.; Otsuka, S.; Akizuki, K.; Abe, M. *J. Chem. Phys.*, 129, 204702 (**2008**).

(69) Roudgar, A.; Narasimachary, S. P.; Eikerling, M. *J. Phys. Chem. B*, 110, 20469-20477 (**2006**).

(70) Eikerling, M.; Kornyshev, A.A. *J. Electroanal. Chem.*, 502, 1-14 (**2001**).

(71) Maréchal, Y. *J. Mol. Struct.*, 700, 217-236 (**2004**).

(72) Givan, A.; Loewenschuss, A.; Nielsen, C.J. *J. Mol. Struct.*, 748, 77-90 (**2005**).

(73) Varetti, E.L. *Spectrochim Acta*, 44A, 733 (**1988**).

(74) Gruger, A.; Regis, A.; Schmatko, T.; Colomban,P. *Vib. Spectrosc.*, 26, 215-225 (**2001**).

CHAPTER 6

QUASI 1-D CONFINEMENT: WATER IN SWNTs

Water filling of hydrophobic carbon nanotubes having size of a few molecular diameters is a surprising evidence, firstly predicted by numerical simulations [122]. Water molecules, undergoing such an extreme confinement, arrange themselves establishing distorted hydrogen bonds networks. We report here the terahertz and mid infrared study of the hydration process of SWNTs having a diameter distribution of 1.4±0.5 nm. An anomalous arrangement of water molecules is observed. This manuscript is submitted to Nano Letters.

6—1 WATER IN CARBON NANOTUBES: THE PECULIAR HYDROGEN BOND NETWORK REVEALED BY INFRARED SPECTROSCOPY

The hydration process of single walled carbon nanotubes (SWNTs) and the water molecule arrangement have been revealed by a set of data from the terahertz to the mid infrared (25—4000 cm^{-1}). In this range, carbon nanotubes have an extremely high absorbance coefficient, hence, the use of the bright synchrotron source, coupled with the use of the hydration setup described in Section 2—3, allowed us to measure the weak infrared signal coming from trapped water molecules.

The noise in the spectra makes the interpretation of some bands difficult, in particular the connectivity band (~200 cm^{-1}) could not be observed. Other bands, such as the OH stretching (3000—3700 cm^{-1}), the libration (400—900 cm^{-1}) and a unassigned low frequency band (30—50 cm^{-1}), appears clearly and evolves as water is adsorbed into the sample.

A quantitative analysis of the OH stretching band, allowed us to determine the water network arrangement inside the carbon nanotubes as a function of the applied water vapor pressure. Data are interpreted upon the assumption that the OH oscillator strength depends on the number of established hydrogen bonds [5] so that each subcomponent of the OH stretching band originates from water molecules involved in different levels of H bonding, as mentioned in Section 3—2.1.

At low hydration, RH=9%, isolated or poorly connected water lie in the nanotubes. The infrared signature of dangling OH bonds facing the hydrophobic walls of the carbon nanotubes has been identified in the high frequency subcomponents at 3560 and 3640 cm^{-1}.

An ordered organization of water molecules was found at higher hydration, RH=30%, when a low frequency components appear at 3215 and 3340 cm^{-1}. This result is the experimental evidence of what has been predicted in some numerical

simulations studies [123—125]: an ice-like arrangement of water in small pores (~1.2 nm) nanotubes occurs at room temperature.

At fully hydration, larger nanotubes are filled and water molecules establish a more disordered network.

The evolution of the low-frequency band at ~40 cm^{-1} as a function of the relative humidity, shown in Figure 6.1.1, is likely associated to the progressive development of the hydrogen bond network of water confined in SWNTs. This evolution supports the hypothesis that smaller tubes fill up first giving rise to an organized (ice-like) network at RH=30%, while larger tubes fill at higher relative humidity developing an unordered liquid-like network.

During the whole hydration process a significant amount of dangling bonds facing carbon walls are present, revealing that the adsorbed water molecule weakly interact with the internal walls of carbon nanotubes. Such result is the experimental evidence of the little friction between water and hydrophobic walls, enabling the surprisingly enhanced water flow through SWNTs.

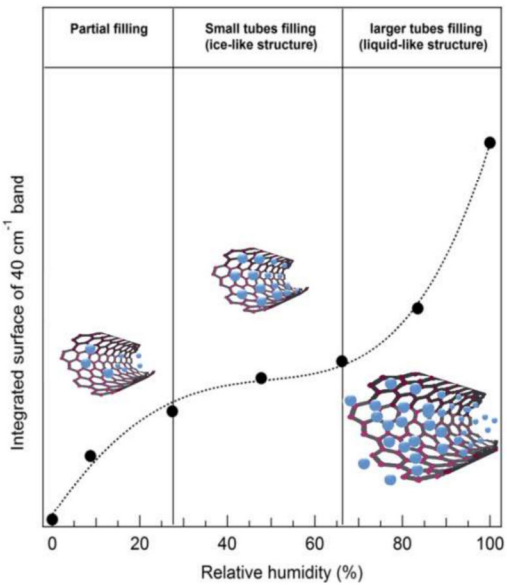

Figure 6.1.1 – Integrated surface area of 40 cm^{-1} band vs relative humidity. The three steps correspond to (i) partial filling of tubes with dangling OH facing carbon walls, (ii) full filling of small tubes developing organized ice-like structure, and (iii) full filling of larger tubes with unordered liquid-like structure. The insets are schematics view of water molecules inside the small and large CNT.

Water in carbon nanotubes: the peculiar hydrogen bond network revealed by infrared spectroscopy

Dalla Bernardina, S.; Paineau, E.; Brubach, J.-B.; Judeinstein, P.;
Rouzière, S.; Launois, P.; Roy, P. *Nano Letters*, submitted.

ABSTRACT

Carbon nanotubes are used as models to highlight the properties of water upon nanometric confinement at the origin of exceptional behavior, such as enhanced water flow and a variety of new water ice phases not observed in bulk. These specificities are generally considered to be related to the particular hydrogen bonding network of water in carbon nanotubes. Infrared spectroscopy is a privilege technique to follow modification of such network through the inter- and intra-molecular bonds of water molecules. Here we report the first room temperature infrared study of water uptake at controlled vapor pressure in single walled carbon nanotubes (SWNTs). The measurements as a function of hydration level reveal the critical role of the tube size in the organization of water under extreme conditions of confinement. In particular, this analysis provides experimental evidence for OH dangling bonds at the origin of the structure of confined water in nanotubes. For small diameter nanotubes (0.8 nm) the dominating dangling bond signature suggests a 1D structure. For medium diameter nanotubes (1.1-1.2 nm) such dangling bond features accompanied by ice-like features support an organized water network. As for larger diameter nanotubes (≥1.4 nm) the signature of an external layer with “free” OH bonds comes with broad features indicative of unorganized water. These findings support theoretical models suggesting in particular the dominating role of dangling bonds responsible for the ultra-low friction of water through SWCNTs.

6—1.1 RESULTS AND DISCUSSION

A groundbreaking discovery in the emerging field of nanofluidics was the demonstration of the tremendously enhanced water permeability of carbon nanotubes[1,2], which makes carbon nanotube membranes serious candidates for

water treatment[3,4]. The original behavior of water at the nanoscale is also of concern to biology, where the extreme permeability to water of aquaporins, those membrane proteins that form nanopores, is crucial for many physiological processes[5], as well as with respect to the unimpeded permeation of water through graphene-based membranes[6]. Numerical calculations point towards the central role of hydrogen bonding network modifications to explain ultra-low friction properties of water in carbon nanotubes[7,8,9,10]. Infrared spectroscopy is a technique of choice to study the hydrogen bond network[11,12]. Here, we report the first room temperature infrared study, at controlled vapor pressures, of the water dynamics in single walled carbon nanotubes with diameters ranging from 0.7 to 2.1 nm. The specific thermodynamic and transport properties of water in such nanotubes are benchmarked against these new experimental results. Infrared (IR) absorption spectra were realized on Single Walled Carbon Nanotubes (SWCNTs – see SI for structural characterization) deposited on a gold grid and hydrated in-situ under different water vapor pressures between 9% and 100% of relative humidity (RH). In order to highlight the differences occurring as the system passes from the dry state to a fully hydrated one, we subtracted absorbance of the dry sample and the water vapor contribution from the equivalent hydrated measurements. Difference spectra of the hydration sequence were performed in the THz (20-50 cm^{-1}), FIR (50-500 cm^{-1}) and MIR (500-4000 cm^{-1}) regions; the observed absorption bands are displayed in Figure 1 from the dry state (bottom) to 100% of relative humidity. Spectra are presented in absorbance, defined as $-log\left(\frac{I}{I_0}\right)$, where I and I_0 are respectively the transmission of the nanotubes with a given value of relative humidity and the transmission of nanotubes in the dry state. As the dry state is used as a reference, positive absorbance results from water molecules sorption. One can observe the OH stretching band between 3100 and 3700 cm^{-1} (Figure 1D), the water bending mode around 1625 cm^{-1} (Figure 1C), its libration mode around 560 cm^{-1} (Figure 1B), as well as a low frequency mode at 40 cm^{-1} (Figure 1A). These results can be compared with those in ref. 11, where Martí and Gordillo calculated the IR spectrum of water confined inside SWCNTs with diameters ranging from 0.8 to 1.6 nm. Like experimental spectra in Fig. 1, calculated spectra exhibit clear stretching, bending and libration modes. Moreover, Martí and Gordillo predict a red shift for the bending motion compared to bulk water that has indeed been observed in our experiments: the mode around 1625 cm^{-1} (Figure 1C) is red shifted by ~25 cm^{-1} with respect to that in bulk water[13]. The

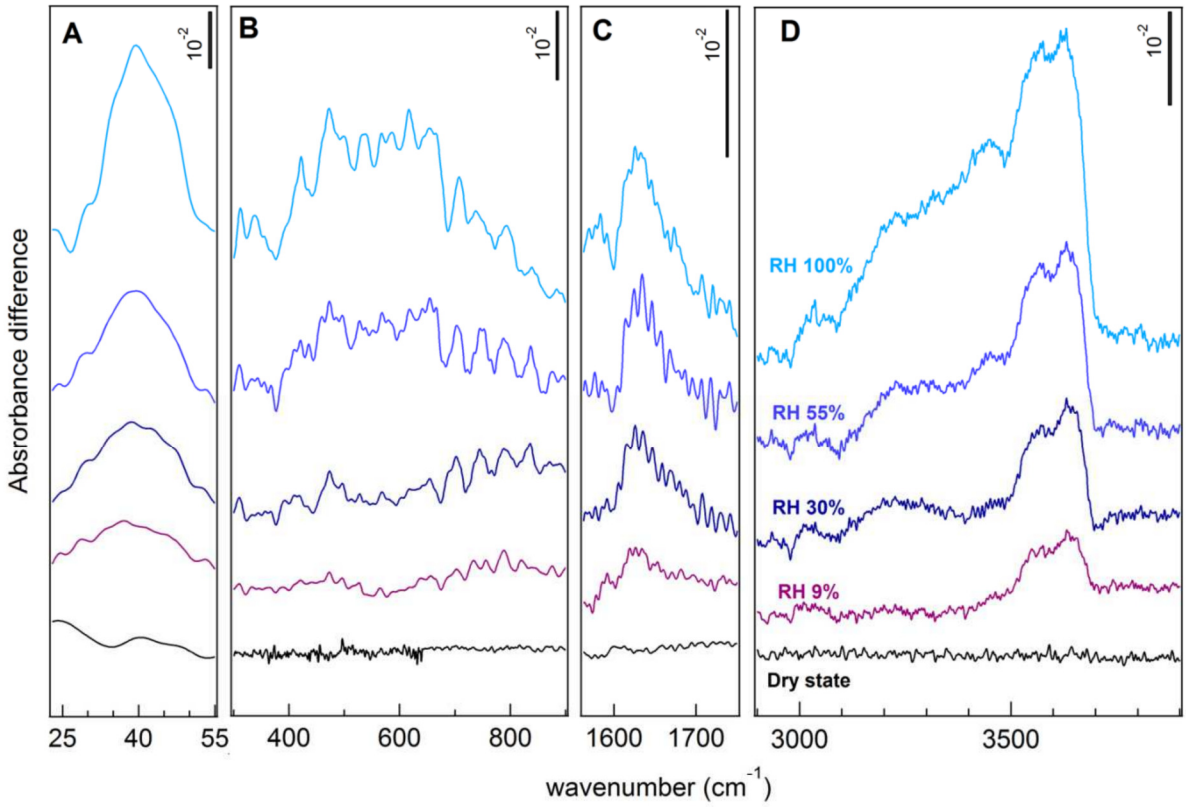

Figure 1 – Spectra of water in SWCNTs for various hydration steps. Absorbance of water inside SWCNTs from dry state to 9%, 30%, 55%, and 100% of relative humidity. Water content increases from bottom to top. Different spectral ranges are shown to highlight vibrational modes of adsorbed water during hydration: (A) around 40 cm^{-1}; (B) around 560 cm^{-1} (C) around 1625 cm^{-1}; (D) between 3100 and 3700 cm^{-1}. Spectra are translated vertically for the sake of clarity.

assignment of the mode at 40 cm^{-1} is less straightforward since there is no agreement about its existence nor about its interpretation even in bulk water[11]. Whatever the assignment of this mode, its intensity, like those of the libration, bending and stretching modes, gradually increases upon water sorption in Figure 1, confirming that all these modes should be attributed to water progressively encapsulated inside SWCNTs with increasing vapor water pressure[9,14]. Major modifications in the shape distribution of the stretching band are also evidenced, as discussed in details in the following.

The OH stretching band of water provides detailed information about its networking: the oscillator strengths and thus associated vibrational frequencies decreasing when coordination number increases. Stretching bands of bulk liquid and ice are reported in Fig. 2. Both are well fitted with three Gaussian functions. For liquid water (Figure 2B down), the high energy Gaussian is assigned to poorly connected water molecules (two, one or zero H bonds), the lowest

energy is representative of highly connected water (four H-bonds) and the intermediate energy component is representative of water with a coordination number close to three[13,15]. For ice water I_h (Figure 2A down), a shift towards low frequency is observed as the result of the establishment of the rigid tetrahedral network.

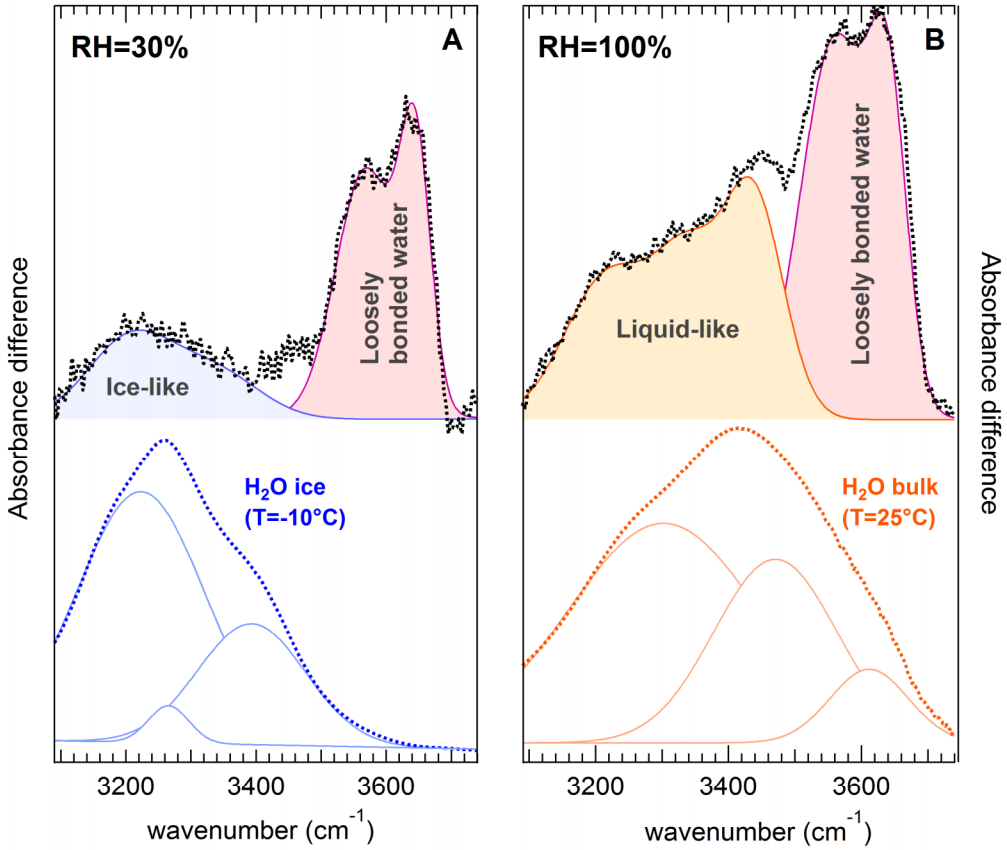

Figure 2 – Comparison of O-H stretching bands. (A) the OH stretching band (3100-3740 cm^{-1}) of water adsorbed in SWCNTs at RH=30% (top) and the spectrum of the bulk ice water (bottom) in the same range of frequencies. The ice-like contribution of confined water at low frequencies is highlighted in blue. (B) the OH stretching band of water adsorbed in SWCNTs at RH=100% (top) and bulk liquid water (bottom). The liquid-like contribution of the adsorbed water at low frequencies is highlighted in orange. The contributions of loosely bonded water inside SWCNTs are highlighted in pink.

Between 3100 and 3500 cm^{-1}, similarities between bulk ice I_h and water in SWCNTs at RH=30% and between bulk water and water in SWCNTs at RH=100% are evidenced. Pascal and co-workers[16] discussed different stabilization mechanisms for water inside SWCNTs, depending on the nanotube diameter. In particular, an enthalpy stabilized, ice-like phase is predicted at

room temperature for nanotube diameters of 1.1-1.2 nm and a liquid-like phase, stabilized by the increase of translational entropy, is predicted for nanotubes diameters above 1.4 nm. Assuming, in agreement with experimental and calculation results[9,17], that smaller diameter nanotubes start trapping water first, the ice-like component visible at RH=30% in Fig. 2A is attributed to this peculiar ice-like nanoconfined water, corroborating the X-ray diffraction results of Kyakuno et al.[18] At higher water pressure, the filling of larger nanotubes dominates[9,14]. Accordingly, the proportion of liquid-like confined water increases as demonstrated by the appearance of a liquid-like contribution in the IR spectrum in Fig. 2B.

The major difference between water confined in SWCNTs and bulk water is the presence of an intense high frequency component at 3500-3700 cm^{-1}. This observation is truly original with respect to all experimental results on the dynamics of water inside SWCNTs in the literature[9,19,20,21]. Indeed, ref. 19 focuses on large amplitude motions of H in SWCNTs while ref. 21 is concerned with nanoconfined ice at low temperature. The IR spectra in ref. 9 are unfortunately dominated by vapor pressure signatures while, surprisingly, room temperature IR study in ref. 20 does not show any specific confined water signature. To ascertain our result, we studied SWCNTs in equilibrium with a D_2O vapor pressure. The O-D stretching band rightly presents an intense high-frequency component with the expected isotopic shift[22] (see fig. SI1). It should be underlined here that, according to numerical simulations, the main difference between bulk water and water confined in SWCNTs is its reduced number of H bonds[7,8,23,24,25,26]. Accordingly, high frequency components are predicted for water confined in SWCNTs[11,27]. The high frequency component of the stretching mode at 3500-3700 cm^{-1} thus characterizes loosely bonded water in SWCNTs.

A semi-quantitative analysis of the evolution of the stretching band with vapor water pressure is proposed, based on its deconvolution with five Gaussian functions G1, G2, G3, G4 and G5 centered at 3215, 3340, 3435, 3560 and 3640 cm^{-1}, respectively (Figure 3). The relative areas of each subcomponent are used to quantify the evolution of the H-bond network during the filling of SWCNTs. In the first step of filling (RH=9%), the stretching band is mainly constituted (85%) by the high frequency components G4 and G5, Figure 3A. It could be attributed to water with coordination number smaller or equal to two, forming one-dimensional (1D) chains in narrowest nanotubes with diameter

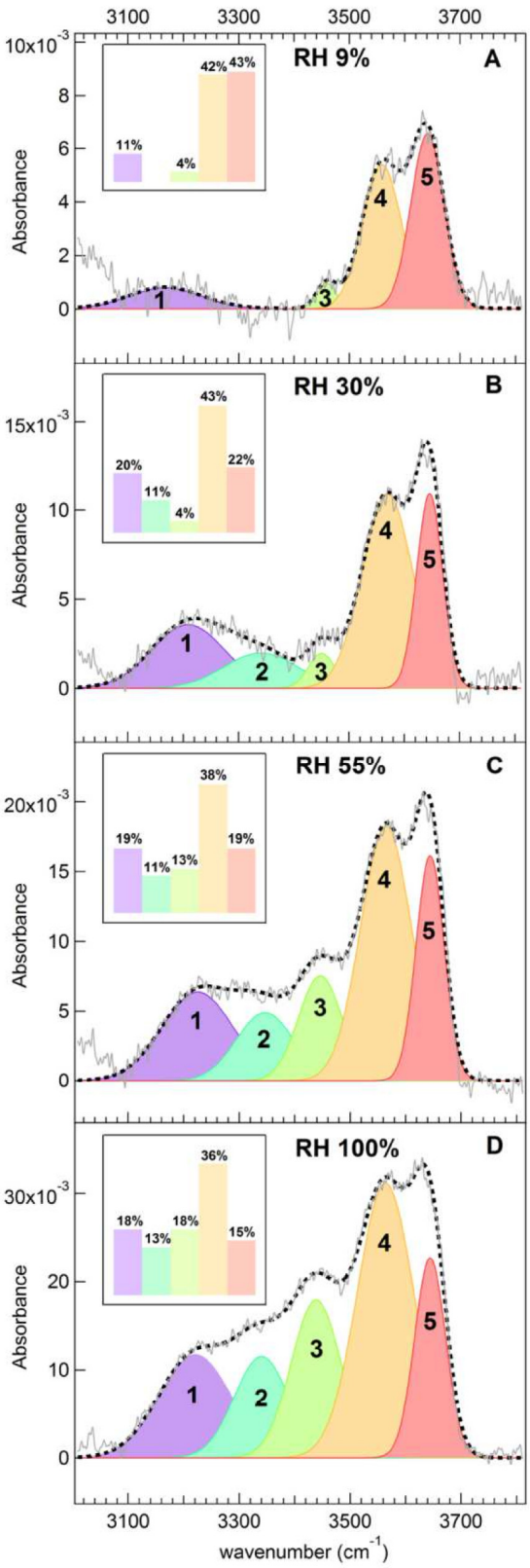

Figure 3 – Deconvolution of O-H stretching band for each hydration level. Deconvolution of the O-H stretching band with five Gaussians at 9% (A), 30% (B), 55% (C), and 100% (D) of relative humidity. Inset: proportion (in percent) of each subcomponent.

around 0.8 nm[7,11] or forming very local clusters[26]. Meanwhile, the low energy contribution G1 is also observed, which corresponds to ice-like n-gonal configurations in nanotubes with diameters of 1.1-1.2 nm[16,26]. While water relative humidity increases (RH=30%), the amount of strongly bonded water molecules increases, as demonstrated by the increase of the two low frequency components G1 and G2, Figure 3B.

For RH≥50%, in Figure 3C,D, an intermediate component, G3, appears with a significant intensity at 3435 cm^{-1}. The spectral distribution of OH stretching band between 3100 and 3500 cm^{-1} then resembles to its bulk liquid counterpart (see Figure 2B) supporting an H-bond network similar to bulk water. Accordingly, G3 appearance is concomitant with that of the libration band (Fig. 1B). A progressive structuration of water in layers was however observed by X-ray scattering during 1.4 nm diameter nanotubes filling[28] and such structuration is also expected to occur in nanotubes with diameters above 1.4 nm[23,24,25]. A non-negligible part of the high frequency signature (G4 and G5) for RH≥50% should thus be attributed to the molecules in the external layer, with “free” OH bonds pointing towards the nanotube wall.

6—1.3 CONCLUSIONS

In a context where our knowledge of water structure inside SWCNTs is based on numerical approaches, this analysis provides experimental evidence for (i) the 1D structure of confined water in small diameter (0.8 nm) nanotubes, (ii) its ice-like structure in medium diameter (1.1-1.2 nm) nanotubes and (iii) the presence of an external layer with “free” OH bonds for liquid water in larger diameter (≥1.4 nm) nanotubes. Our experimental results show that the water network is strongly affected by confinement and that more than half of the intensity of the stretching band comes from loosely bonded water molecules inside SWCNTs, even for fully hydrated nanotubes. The observation of ice-like water corroborates the theoretical approach developed to explain the spontaneous filling of hydrophobic carbon nanotubes[16], a counterintuitive phenomenon. Our results also support theoretical studies about the ultra-low friction of water through SWCNTs. Indeed, besides geometrical effects[29], it was claimed that the 1D structure of water inside the smaller diameter nanotubes or the peculiar hydrogen bonding at the interface in larger ones significantly eases

the flow rates[7,8]. Finally, one should underline that simulations of nanoconfined water properties are mainly based on phenomenological models, each designed to explain specific bulk water properties[25], with model-dependent results[10]. The present experimental data provide a solid reference for the elaboration of an energetic model accounting for the properties of water in hydrophobic nanochannels. This should also be relevant for biological channels like aquaporines[5]. On another issue, let us mention graphene-like membranes which were shown to be highly permeable to water, a property attributed to low friction flow of a monolayer of water between closely spaced graphene sheets[6]. Strong modifications of the H bonds networks and of the corresponding IR spectrum are predicted[12]. The experimental approach developed here should apply successfully to study water confined between graphene sheets.

6—1.4 METHODS

Measurements have been performed at AILES beamline of synchrotron SOLEIL. A Bruker IFS125 FT-IR spectrometer was equipped with a 6 µm Mylar beam splitter and a 1.6 K bolometer for terahertz (THz: 20-60 cm^{-1} at 2 cm^{-1} resolution), the same beam splitter and a 4.2 K bolometer for far infrared (FIR : 50-500 cm^{-1} at 2 cm^{-1} resolution), and a KBr beam splitter combined with a wide range 4.2K bolometer from Irlabs for mid infrared (MIR: 500-4000 cm^{-1} at 4 cm^{-1} resolution). A hydration cell especially designed for *in situ* infrared measurements during hydration and dehydration[27] has been used to finely control the water vapor pressure applied to a layer of SWNTs, initially dried at 310 K with a pressure of 10^{-6} mbar. The cell is equipped with two diamond windows (10 mm in diameter, 0.5 mm in thickness at center, 0.5° wedge) allowing to measure the transmission of material from the THz to the mid infrared region with reduced spectral channeling effects. The sample is fixed on a sample holder at precise normal incidence relative to the incident beam. An entry for the gas input/output or the vacuum pump is also present in the body of cell. Gas dosage can be done in static conditions. Different values of water vapor pressure *p* were set, in order to study the hydration of the sample in equilibrium at 9%, 30%, 55% and 100% of relative humidity $RH = \left(\frac{p}{p_0}\right) \times 100$, p_0 being the water vapor pressure equal to 31.7 mbar at 298 K. Additional spectra in the THz range have been acquired, at 66% and 83% of RH. Although the

equilibrium was reached in less than one hour for all water pressures, measurements presented here were performed after several hours (typically eight hours) at a well-controlled pressure.

Supplementary information

Sample characterization

Short Single Walled Carbon Nanotubes (>95 vol% CNT; >90 vol% SWNT) were bought from Nanostructured & Amorphous Materials, Inc. (NanoAmor) were used without any further purification. We verified that they were exempt from impurities (no COC and C=O bands were detected at 1100 and 1710 cm^{-1}, respectively[31]).The length of the tubes is between 1 and 3 μm and their diameter between 1 and 2 nm. Raman measurements confirmed the size distribution as centered on 14±5 Å.

Raman spectroscopy (see Figure SI1) has been used to reveal the structure and the electronic and phonon properties of the sample.[32] The radial breathing mode (RBM) corresponds to the coherent vibration of the C atoms in the radial direction. For SWNTs with diameters in the range 0.7 - 2 nm the RBM modes occur between 120 – 350 cm^{-1}. The G-band involves an optical phonon mode between two dissimilar atoms in the unit cell. It is composed of several peaks due to the phonon wave vector confinement along the circumferential direction and to the symmetry breaking effects associated with SWNTs curvature. From the G-band lineshape we can conclude that our sample is constituted by semiconducting SWNTs.[32]

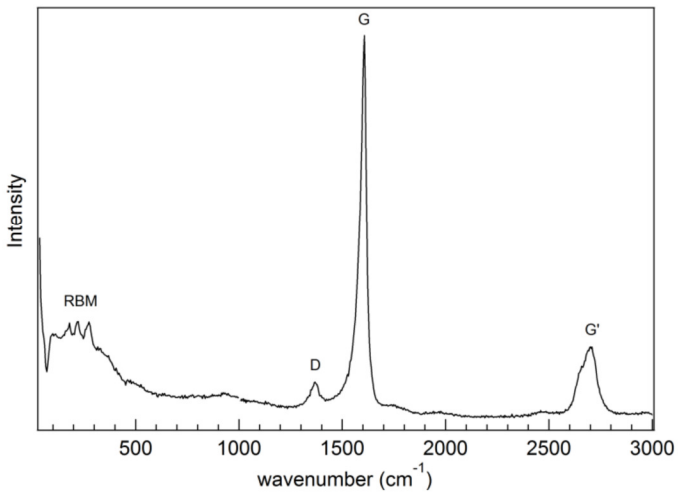

Figure SI1 – Raman spectrum of NanoAmor SWNTs. The spectrum show the RBM band, the D-band, the G-band and the G' band.

Hydration with D_2O

Measurements of adsorption of heavy water, D_2O, within the SWNTs have been performed to complete and verify our results obtained during the hydration with H_2O. Figure SI2 shows the spectrum of SWNTs in equilibrium with a D_2O vapor pressure corresponding to 60% of RH as well as the spectrum of bulk heavy water. Indeed D_2O presents the same band profile as H_2O displaced by the isotopic shift with an intense component in the higher frequency region of the band (2600-2750 cm^{-1}).

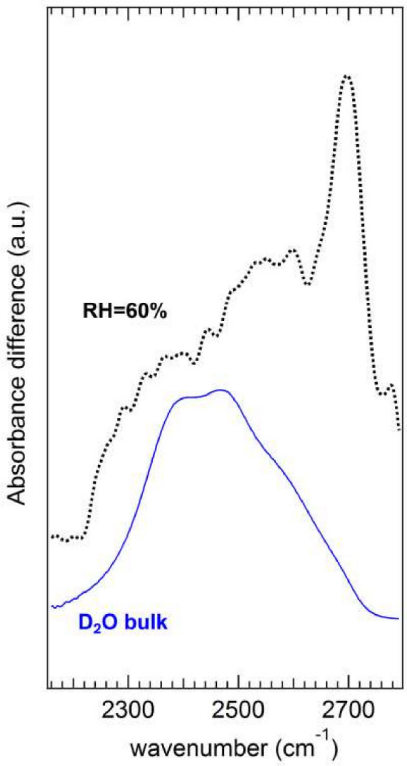

Figure SI2 – Comparison between the OD stretching bands. Spectra of D_2O adsorbed in SWNTs at RH=60% (top) and D_2O bulk (bottom) between 2150 and 2800 cm^{-1}.

REFERENCES

(1) Majumder *et al.* Nanoscale hydrodynamics: enhanced flow in carbon nanotubes, *Nature* 438, 44 (**2005**).

(2) Holt, J. K *et al.* Fast mass transport through sub-2-nanometer carbon nanotubes, *Science* 312, 1034-1037 (**2006**).

(3) Yang H. Y. *et al.* Carbon nanotube membranes with ultrahigh specific adsorption capacity for water desalination and purification. *Nature Comm.* 4:2220 (**2013**).

(4) Lee B. *et al.* A carbon nanotube wall membrane for water treatment, *Nature Comm*. 6:7109 (**2015**).

(5) Sui H. *et al*. Structural basis of water specific transport through the AQP1 water channel, *Nature* 414, 872 (**2001**).

(6) Nair R. R. *et al.* Unimpeded permeation of water through helium-leak-tight graphene-based membranes, *Science* 335, 442 (**2012**).

(7) Hummer, G. *et al.* Water conduction through the hydrophobic channel of a carbon nanotube, *Nature* 414, 188-190 (**2001**).

(8) Joseph S. and Aluru N. R. Why are carbon nanotubes fast transporters of water? *Nano Lett*. 8, 452 (**2008**).

(9) Ohba, T. *et al.*Rapid water transportation through narrow one-dimensional channels by restricted hydrogen bonds, *Langmuir* 29, 1077-1082 (**2013**).

(10) Liu L. and Patey G. N. Simulations of water transport through carbon nanotubes: how different water models influence the conduction rate, *J. Chem. Phys.* 141, 18C518 (**2014**).

(11) Martí, J. and Gordillo, M. C. Effects of confinement on the vibrational spectra of liquid water adsorbed in carbon nanotubes. *Phys. Rev. B* 63, 165430 (**2001**).

(12) Sharma, M. *et al*. Probing properties of water under confinement: Infrared spectra, *Nano Lett.* 8, 2959-2962 (**2008**).

(13) Brubach, J. B. *et al.* Signatures of the hydrogen bonding in the infrared bands of water. *J. Chem. Phys.* 122, 184509 (**2005**).

(14) Kim P. *et al.* Adsorption equilibrium and kinetics of water vapor in carbon nanotubes and its comparison with activated carbon. Ind. Eng. Chem. Res. 47, 3170 (**2008**).

(15) Bergonzi, I. *et al.* Gibbs free energy of liquid water derived from infrared measurements. *Phys. Chem. Chem. Phys.* 16, 24830-24840 (**2014**).

(16) Pascal T. A. *et al*. Entropy and the Driving Force for the Filling of Carbon Nanotubes with Water, *PNAS*, 108, 11794-11798 (**2011**).

(17) Striolo, A. *et al.* Water in carbon nanotubes: Adsorption isotherms and thermodynamic properties from molecular simulation, *J. Chem. Phys.* 122, 234712 (**2005**).

(18) Kyakuno H. *et al.* Confined water inside single-walled carbon nanotubes: global phase diagrams and effect of finite length, *J. Chem. Phys.* 134, 244501 (**2011**).

(19) Kolesnikov, A. I. *et al.* Anomalously soft dynamics of water in a nanotube: A revelation of nanoscale confinement, *Phys. Rev. Lett.* 93, 035503 (**2004**).

(20) Ellison M. D. *et al*. Interaction of Water with Single-Walled Carbon Nanotubes: Reaction and Adsorption, *J. Phys. Chem. B*, 109, 10640-10646 (**2005**).

(21) Byl, O. *et al*. Unusual hydrogen bonding in water-filled carbon nanotubes, *J. Am. Chem. Soc.* 128, 12090-7 (**2006**).

(22) Cicero, G. *et al.* Water confined in nanotubes and between graphene sheets: A first principle study, *J. Am. Chem. Soc*. 130, 1871-1878 (**2008**).

(23) Gordillo M. C. and Martí J. Hydrogen bond structure of liquid water confined in nanotubes. *Chem. Phys. Lett.* 329, 341 (**2000**).

(24) Hanasaki I. and Nakatani A. Hydrogen bond dynamics and microscopic structure of confined water inside carbon nanotubes, *J. Chem. Phys.* 124, 174714 (**2006**).

(25) Alexiadis A.and Kassinos S. Molecular Simulation of Water in Carbon Nanotubes, *Chem. Rev*., 108, 5014-5034 (**2008**).

(26) Sadeghi, M. and Parsafar, G. A. Density-induced molecular arrangements of water inside carbon nanotubes. *Phys. Chem. Chem. Phys.* 15, 7379 (**2013**).

(27) Mann, D. J. and Halls, M. D. Water alignment and proton conduction inside carbon nanotubes, *Phys. Rev. Lett*. 90, 195503 (**2003**).

(28) Paineau, E. *et al.* X-ray scattering determination of the structure of water during carbon nanotube filling, *Nano Lett.* 4, 1751-1756 (**2013**).

(29) Falk K. *et al.* Molecular origin of fast water transport in carbon nanotube membranes: superlubricity versus curvature dependent friction, *Nano Lett*. 10, 4067 (**2010**).

(30) Dalla Bernardina, S. *et al*. New experimental set-ups for studying nanoconfined water on the AILES beamline at SOLEIL. *Vib. Spectrosc.* 75, 154-161 (**2014**).

(31) Dresselhaus, M. S. *et al*. Raman spectroscopy of carbon nanotubes, *Physics Reports* 409, 47-99 (**2005**).

(32) Kim, U. J. *et al*. Infrared-active vibrational modes of single-walled carbon nanotubes, *Phys. Rev. Lett.* 95, 157402 (**2005**).

CONCLUSIONS

This thesis aims at highlighting the effect of nanoconfinement on water molecules by vibrational spectroscopy. The influence of water on the chemical and physical status of a specific confining system was also investigated. Changes in the hydrogen bond network, water structure and dynamics were monitored mainly through the evolution of four bands during adsorption and desorption of water molecules: two intermolecular bands in the far infrared (FIR) region, the connectivity and the libration bands, below 1000 cm^{-1}, and two intramolecular bands in the mid infrared (MIR) region, the bending and stretching, between 1600 and 4000 cm^{-1}. Indeed, if compared to bulk, these bands appear altered in the spectra of trapped water.

In order to perform this study, a specific setup allowing hydration and dehydration *in situ* measurements was developed. It is compatible with the spectrometer available at the AILES beamline that is adapted to the infrared synchrotron source produced at the synchrotron SOLEIL. This specific setup, was first used to prepare dried samples and from there to follow the hydration processes taking place in several porous materials, namely Vycor glass, Nafion membrane and SWNTs, from a very small amount of water (RH<1%) to a full hydration (RH=100%). These samples were selected, among many other porous materials, since their diversity allowed us to investigate how various factors (such as temperature, walls nature, pores size and shape) affect the confined molecules network.

We found that when interfacial water interacts with a hydrophilic surface establishing strong hydrogen bonds the intramolecular covalent OH bonds of water is weaken. Following the evolution of trapped water spectra at several temperatures, we evidenced that such interactions promote changes in the hydrogen bond network at specific temperatures (T=160, 220, 240 K). The resulting OH stretching band of confined water is downshifted compared to liquid bulk originating a band at ~3230 cm^{-1}. Such frequency is comparable with that of the OH stretching band of four H-bonded hexagonal ice.

An opposite behavior is observed for water confined in narrow hydrophobic carbon nanotubes. In this system, water molecules are constrained into cylindrical carbon walls but do not directly interact with them. Dangling OH groups of water molecules facing the pore's walls give rise to specific OH stretching band at high frequencies, 3560 and 3640 cm^{-1}, never observed in bulk or in water trapped in hydrophilic systems. Surprisingly, low frequencies subcomponents of the OH stretching band appear at low hydration level. This has been interpreted as the experimental evidence of an anomalous ordered arrangement of water molecules in narrow carbon nanotubes at room temperature. Indeed, water molecules being unable to interact with the surface, give rise to an ordered network in the narrow volume of the pores, most probably forming stacked hydrogen bonded ring as it was predicted by numerical simulations studies [123—125].

As for water adsorbed into Nafion membrane, it reveals a more "bulk-like" behavior. Indeed, Nafion chemical structure consists in a hydrophobic/hydrophilic nanophase separation of the membranes, where hydrophobic domains warp upon water uptake promoting the channels swelling. As a result, water molecules can arrange themselves in a slightly distorted three-dimensional network where protons, formed from the interaction between water and the sulfonic acid groups, may diffuse.

A common behavior is observed in the bending band of confined water. As it has been already proposed [5], such band seems to be unaffected by the number of hydrogen bonds established by the molecule. We have observed that a downshift always occurs in spectra of confined water, in either hydrophilic or hydrophobic systems. Both in hydrophilic Vycor pores and hydrophobic SWNTs, the bending band of adsorbed water appears at 1625 cm^{-1}, as compared to 1650 cm^{-1} in bulk water. When confined in larger pores as a consequence of the swelling, the bending band of water adsorbed in Nafion membrane, is less affected by confinement and is only downshifted to 1634 cm^{-1}. It was also observed that the intensity of the bending band of water becomes larger as a result of the confinement. Most probably, the distorted arrangement adopted by trapped water molecules causes an enhancement in the change of dipole moment associated to this mode.

Concerning the intermolecular modes, major information was provided by the connectivity band. In contrast, the libration band was often outshined by the strong absorbance of the matrix, as in Vycor or Nafion, or made ambiguous by the

noise signal, as in SWNTs. The main information provided by intermolecular modes can be resumed as follow.

Through the analysis of the connectivity band observed for the interfacial water in Vycor pores, we evidenced that amorphous ice is formed at low temperature and no crystalline form is observed. Once again, the effect of the surface causes a strong modification on the water structure.

The connectivity band of water trapped in SWNTs is too weak to be detected with our setup. However, a low frequency mode at ~40 cm^{-1}, associated to the hydrogen bond network, suggests that hydrogen bonding is enhanced at high levels of relative humidity, corresponding to the filling of the larger tubes under investigation (diameter between ~1.5 and ~2.0 nm).

The interaction of water with the sulfonic acid groups of the dried Nafion membrane was monitored as the first water molecules were adsorbed into the membrane. The signature of the resulting hydronium ion, H_3O^+, hydrogen bonded with the sulfonic group, SO_3^-, has been identified. It was also found that the hydrogen bond strength between the two species is comparable with that of the hydrogen bond established between two SO_3H groups. By coupling far and mid infrared data, we could also find the signature of the hydronium ion OH stretching, at 2210 and 2700 cm^{-1}, and we prove that the ionization occurs via a kinetically-driven process not depending on the water vapor pressure.

Additional studies of the herein investigated samples are still needed to get further information on these systems and the interactions taking place therein. Actually, the benchmark Nafion membrane produced by Dupont has been challenged in the last few years by new PFSA membranes prepared with shorter side chains, namely the Aquivion from Solvay-Solexis and the 3M membranes produced by 3M Company. The latter caught the interest of researchers since improved stabilities at higher temperatures and overall enhanced fuel cell performances have been reported [126, 127]. A study can be performed with our setup in order to compare the data acquired in our experiments on Nafion with those of short-side chain Aquivion and medium-side chain 3M membranes. Both the variation of the side chains length and their distribution, *i.e.* ion exchange capacity variation, will be the relevant properties to *(i)* quantify the proportion of sulfonic acid clusters in the dry state, *(ii)* to disclose the contributions of matrix H-bonds (SO_3H—SO_3H) and

ionic H-bonds (SO_3^-—H_3O^+) in the broad 250-300 cm^{-1} band of the FIR spectra and *(iii)* to quantify the global kinetics of the acid dissociation (water absorption plus dissociation) in order to find the origin of the *log(t)* dependence evidenced in Figure 5.1.7.

Also, hydration measurements on selected single walled nanotubes having narrower diameter distributions could be very useful to discriminate the hydration processes and the hydrogen bond structure in the carbon nanotubes according to their size. This implies, however, a clarification on the contribution of the metallic and semiconducting tubes.

A Quartz balance may also be implemented in the hydration setup in order to quantify the amount of water molecules adsorbed in the system as a function of the relative humidity, allowing the description of adsorption isotherms. The quartz balance should be placed in an ultra-high vacuum compatible case and should be connected to both the water vapor injection and the pumping ramps, so that the sample under investigation and that on the microbalance undergo the same treatment

In summary, we designed a new hydration setup to study the adsorption of water in two model systems, chemically and dynamically inert, such as Vycor and SWNTs, and to analyze the hydration process taking place in a more complex system, the Nafion membrane. We have shown that coupling FIR and MIR data can be used to explain tangled processes. Despite the experimental difficulties, linked to insuring a fine control of the hydration setup and for exploiting fully the high brightness of the infrared synchrotron source, the resulting infrared spectra of confined water could be interpreted. Clearly, this study does not pretend to provide an exhaustive picture of the countless interactions experienced by water molecules when trapped in chemical, biological or geophysical systems. Nevertheless, it brings new experimental evidences improving the understanding of confined water, also exploitable for technological applications. The present study paves the way for future studies of more complex systems, such as biological systems in which the interaction with a well-controlled degree of humidity is vital.

ANNEX

RÉSUMÉ

Le réseau de molécules d'eau

La plupart des propriétés uniques de l'eau résultent du réseau de liaison hydrogène tridimensionnelle étendu qui s'établit entre les molécules d'eau. La structure de ce réseau, étant perturbée lorsque les molécules sont piégées dans des milieux confinés ou liées à une interface, ces perturbations peuvent favoriser des transitions de phase et de nouvelles propriétés dynamiques peuvent se développer.

L'eau confinée et en interface joue un des rôles clé dans nombreuses réactions. L'eau est nécessaire au pliage des protéines, et est cruciale dans l'état *in vivo* pour l'hydratation des membranes et des biomolécules. L'eau est généralement en contact avec des interfaces solides au cours des réactions catalytiques et durant le transport des ions et lorsqu'elle agit en tant que solvant polaire. Son adsorption dans des formations rocheuses poreuses ou dans des polymères conducteurs est exploitée pour plusieurs applications, telles que la purification des eaux ou la production d'énergie propre. De toute évidence, comprendre les mécanismes d'absorption de l'eau, ainsi que l'arrangement moléculaire adopté lors du confinement à l'échelle nanométrique, se révèle crucial.

La spectroscopie d'absorption infrarouge et térahertz

Le domaine des infrarouges est la portion du spectre électromagnétique de fréquences comprises entre 30 et 5000 cm^{-1}. Cet intervalle de fréquences s'insère entre la région du visible et celle des microondes et inclut à plus basse énergie le domaine térahertz (THz) s'étendant entre 3 et 300 cm^{-1}.

La spectroscopie d'absorption infrarouge exploite le fait que les molécules possèdent des fréquences spécifiques pour lesquelles elles peuvent absorber des quanta d'énergie correspondant à l'excitation de modes vibratoires. Ces fréquences de résonance sont déterminées par la forme des surfaces d'énergie potentielle, les masses atomiques et par le couplage vibronique associé et peuvent être dans une

première approche liées à la force de la liaison entre atomes, et aux masses atomiques de cette liaison. Ainsi, les fréquences des vibrations dans l'infrarouge moyen (entre 600 et 4000 cm^{-1}) peuvent exciter des liaisons chimiques telles que la liaison O-H centrée sur 3000 cm^{-1} environ. Les photons de l'infrarouges lointain (ou du domaine THz) quant à eux peuvent exciter des liaisons plus faibles telles que les liaisons de Van der Waals ou les liaisons hydrogène qui lient entre elles les molécules d'eau par exemple. Ainsi pour appréhender l'ensemble des propriétés d'un système moléculaire liquide, la mesure de l'absorption s'étendant de l'infrarouge moyen à l'infrarouge lointain permettra de sonder à la fois l'état des molécules du système via les liaisons intramoléculaires et les forces physiques qui lient entre elles ces molécules via leurs liaisons intermoléculaires sondées à plus basses fréquences.

En pratique, la détermination des "signatures" spectrales d'espèces à étudier est faite en faisant passer dans une enceinte (de composition, de pression et de températures connues), un faisceau de photons dont l'absorption sera analysée à l'aide d'un ensemble spectrométrique adapté. La spectroscopie par transformée de Fourier est l'un des outils les plus adéquats pour ce type d'étude car elle permet en un temps réduit de connaître la position de raies d'absorption dans une large gamme spectrale. Il est donc nécessaire de posséder une source large bande adaptée à la spectroscopie, suffisamment intense dans l'ensemble du domaine spectral et suffisamment stable pour être compatible avec la technique interférométrique.

En tant que gamme spectrale intermédiaire entre infrarouge et micro-ondes, le domaine THz a historiquement été produit par les techniques large bande de ses deux domaines voisins. Or, l'intensité de ces sources classiques devient souvent plus faible à l'approche de ce qui a été appelé "le fossé du Térahertz". En effet, les sources électroniques comme les transistors, les diodes à effet Gunn, ou autres dispositifs quantiques basés sur le transport d'électrons, sont limités en fréquence à environ 500 GHz (15 cm^{-1}); en ce qui concerne les sources optiques à large bande, telles que les sources à décharge de mercure ou le corps noir, leur intensité chute en $1/\lambda^4$, rendant leur exploitation ardue.

Le rayonnement Synchrotron dans l'infrarouge

Le critère d'une source large bande est rempli par la source synchrotron. Dans l'infrarouge et spécifiquement entre 10 et 5000 cm^{-1}, l'utilisation du rayonnement synchrotron pour la spectroscopie par transformation de Fourier a permis l'obtention de nombreux résultats et montré un avantage significatif par rapport à l'utilisation de sources thermiques. Un effort particulier sur la stabilité mécanique des anneaux de troisième génération et l'exploitation du rayonnement par bord d'aimant a mené à une amélioration de plus d'un ordre de grandeur de la sensibilité de la technique de spectroscopie à transformée de Fourier.

Les systèmes étudiés par spectroscopie infrarouge

Dans cette thèse, les effets du confinement sur la structure et les liaisons hydrogène entre molécules d'eau sont étudiés par spectroscopie infrarouge à transformée de Fourier (FTIR) qui permet d'identifier les vibrations intramoléculaires dans le moyen infrarouge (MIR: élongation O-H, 3000-3700 cm^{-1}; angle de pliage HOH, ~ 1650 cm^{-1}), et les modes de vibration intermoléculaires, dans l'infrarouge lointain (FIR: rotations frustrés, 300-900 cm^{-1}; translations frustrée des liaisons hydrogène, 30-300 cm^{-1}). L'utilisation de la source de rayonnement synchrotron infrarouge de la ligne de lumière AILES, au sein du synchrotron SOLEIL, a permis l'étude d'échantillons très absorbant avec un bon rapport signal sur bruit.

Des mesures d'hydratation par étapes ont été effectuées sur trois supports nanoporeux : le verre poreux Vycor®, la membrane Nafion® et les nanotubes de carbone à paroi unique (SWNT). Nous avons sélectionné ces trois échantillons, qui diffèrent par leur nature (respectivement hydrophile, amphiphile ou hydrophobe), la taille de leurs pores (de 1 à 5 nm) et leurs formes (pores cylindriques ou sujettes à gonflement), afin de déterminer les effets de la nature des parois et les limites stérique qui affectent les réseaux d'eau lors du confinement. S'ajoute à cela, un intérêt technologique pour ces systèmes dans des applications, telles que la purification et le dessalement de l'eau ainsi que la production d'énergie propre.

La cellule à hydratation

Dans le cadre de cette thèse, chacun des systèmes poreux a été placé à l'intérieur d'une cellule à hydratation conçue pour suivre *in situ* l'adsorption et la désorption des molécules d'eau. Il s'agit d'une cellule compatible ultra-vide (taux de fuite inférieur à $1 \cdot 10^{-9}$ mbar·l/s) équipée de deux fenêtres en diamant brazées sur une enceinte en cuivre permettant des mesures en transmission dans un large domaine spectral. L'ensemble est compatible avec le spectromètre présent sur la ligne de lumière AILES exploitant la source de rayonnement infrarouge produite au synchrotron SOLEIL. Un réglage fin soit de la pression de vapeur d'eau via une microfuite, contrôlée par une gauge capacitive thermostatée (P=0-100±0.02 mbar), soit de la température appliquée à l'échantillon, en contact rigide avec un cryostat à cycle fermé (T=40-380 ±0.1 K), optimise la reproductibilité des mesures en permettant l'acquisition d'un ensemble cohérent de données dans toute la gamme infrarouge. La configuration à T=350 K et $P<10^{-3}$ mbar, réalisée à l'aide d'une pompe turbomoléculaire et de l'application d'un faible chauffage, est utilisée dans un premier temps pour assécher les systèmes poreux puis l'eau est introduite à pression contrôlée afin de suivre les processus d'hydratation à partir de très faibles teneurs d'eau, en révélant progressivement les complexes transformations chimiques et physique qui ont lieu dans les systèmes.

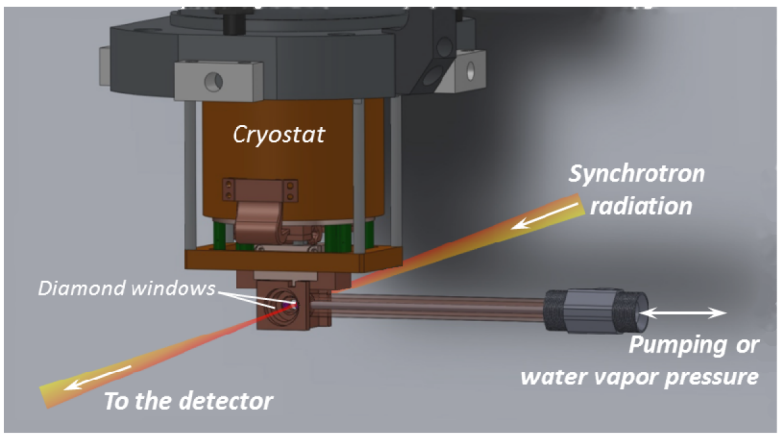

Figure R1 – Schéma de la cellule à hydratation conçue au sein de la ligne de lumière AILES. La cellule est connectée au cryostat à cycle fermé. L'optique de focalisation du faisceau modulé permet des mesures en transmission de l'échantillon qui est en contact avec une quantité contrôlée de gaz.

Lors des mesures d'hydratation, une ampoule contenant de l'eau liquide dégazée et déminéralisée (18,2 M Ω · cm à 25 ° C) est utilisée comme source de vapeur. Chaque étape d'hydratation se termine quand l'échantillon est à l'équilibre (c'est-à-dire lorsqu'il n'y a plus d'évolution des spectres infrarouges) pour une certaine valeur d'humidité relative (RH) définie par le rapport entre la pression effective de vapeur d'eau dans la cellule à hydratation, p, et la pression de vapeur de l'eau, p_0=31,7 mbar à 25 ° C, à une température donnée :

$$RH = \frac{p}{p_0} \cdot 100 \qquad \text{(R1)}$$

L'étude du Vycor

Le verre poreux utilisé dans les expériences présentées est le Vycor n°7930, un produit de Corning Glass Works. Il s'agit d'un verre poreux largement utilisé dans les procédés d'hydratation pour ces excellentes propriétés absorbantes. Il est constitué principalement de silice (96% de SiO_2), ce qui en fait un matériau hydrophile et caractérisé par un réseau tridimensionnel de pores cylindriques interconnectés d'environ 3 nm de rayon (Figure R2).

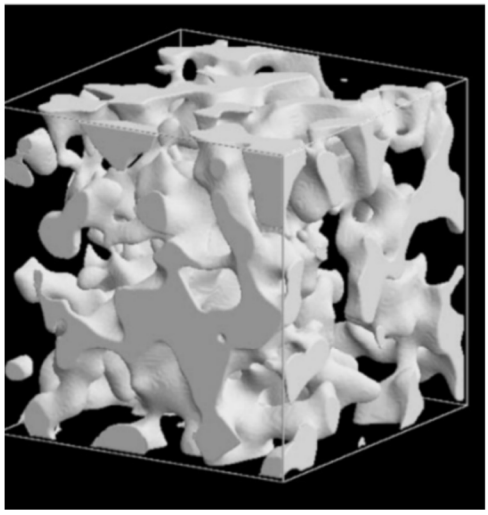

Figure R2 – Reconstruction numérique du Vycor. Un échantillon numérique de la section transversale du verre poreux de silice obtenu en utilisant un procédé de reconstruction « off-lattice », tirée de [86].

Les groupes silanol (Si-OH), qui se trouvent à l'interface air-solide sur les parois des pores, adsorbent facilement les molécules d'eau et, à pleine hydratation, le Vycor peut absorber une quantité d'eau égale à 25% de son poids sec. Lorsque le Vycor est en équilibre avec une pression de vapeur d'eau qui correspond à RH~30%, une monocouche d'eau est adsorbée et tous le groupes silanol accessibles sur les parois des pores établissent une liaison hydrogène avec une molécule d'eau adsorbée. En effet, dans les spectres infrarouges (Figure R3) on observe que les oscillateurs O-H des groupes silanol produisent une bande d'absorption à une fréquence spécifique (3695 cm^{-1}) qui disparaît lors de l'hydratation à environ 30% d'humidité relative.

L'effet d'une surface hydrophile sur la structure, la densité et la dynamique des molécules d'eau à l'interface a été étudié en utilisant une lamelle de Vycor, de 80 µm d'épaisseur, partiellement hydratée à l'équilibre avec une pression de vapeur d'eau de 9.1 mbar, ce qui correspond à une monocouche de molécules d'eau sur la surface des pores.

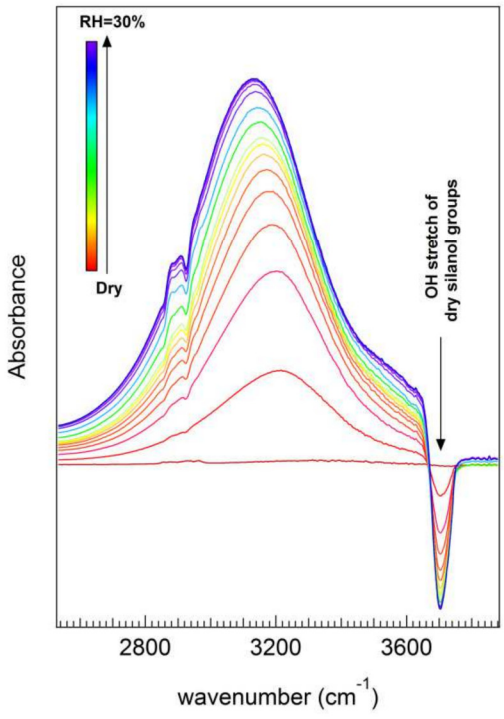

Figure R3 – Elongation OH pendant l'hydratation du Vycor (de sec à RH=30%). Spectres de différence lors de l'hydratation, de l'échantillon sec (courbe rouge) jusqu'à RH=30% (courbe bleu). Le Vycor sec est utilisé comme référence. Le bande d'élongation OH des groupes silanol disparaître quand l'eau est adsorbé dans les pores de Vycor.

La force de liaison hydrogène a été analysée par la bande de connectivité (100-250 cm^{-1}) et de la bande d'élongation O-H (de 2700 à 3600 cm^{-1}) entre T=70 K et T=300 K. Les spectres ont été comparés avec ceux de la glace amorphe et cristalline (précédemment mesurés avec une cellule pour les échantillons liquides), Figure R4 a,b. Nous en avons déduit que l'eau interfaciale à basse température n'est pas cristalline et qu'elle établit une forte liaison hydrogène avec la surface hydrophile.

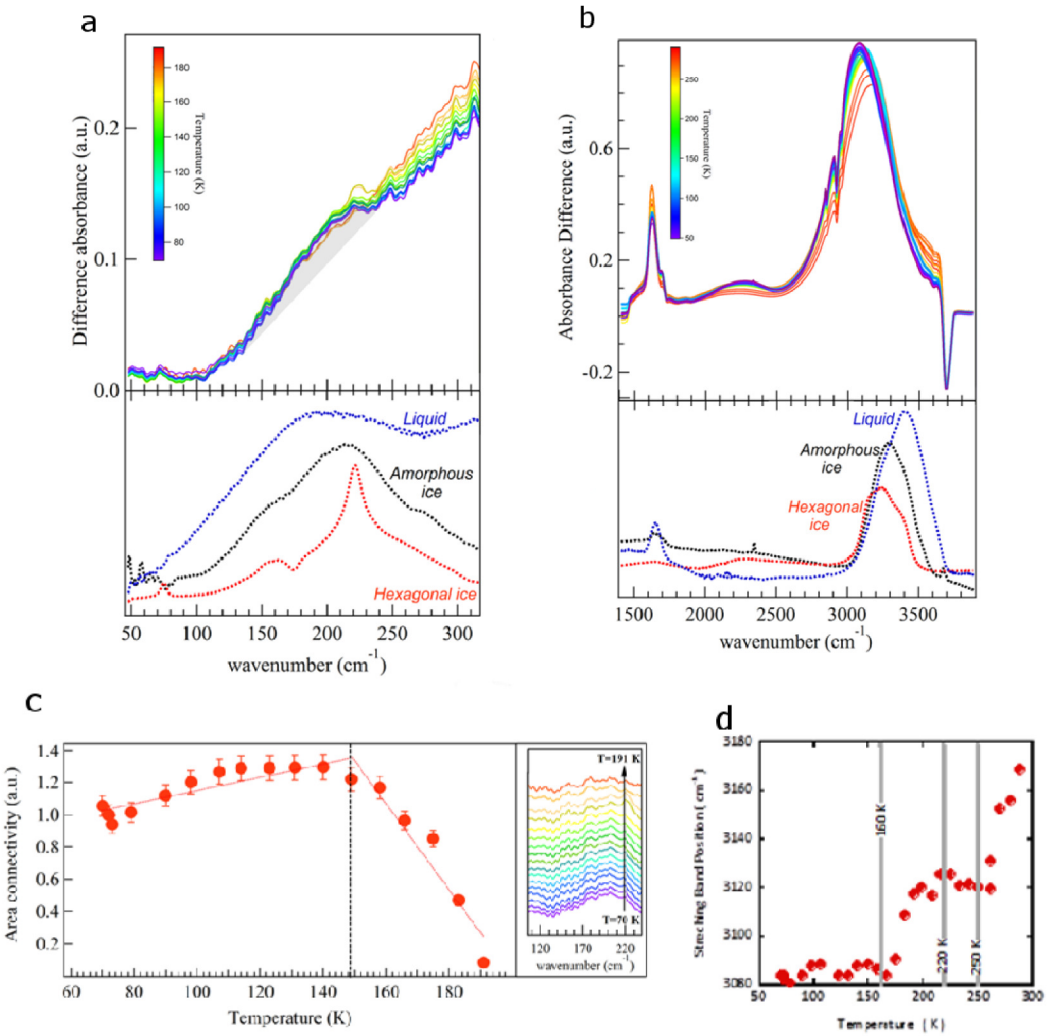

Figure R4 – Dépendance de la température de l'eau interfaciale dans le Vycor, de 70 à 300 K. Les spectres de la glace hexagonale ou amorphe (LDA) et de l'eau liquide sont présentés à titre comparatif. a) La bande de la connectivité, autour de 210 cm^{-1}, est superposée à la bande de libration, à partir de 250 cm^{-1}. b) La bande du pliage HOH à 1625 cm^{-1} et la région de l'élongation OH de l'eau 2700 à 3600 cm^{-1} et des groupes silanol à 3695 cm^{-1}. c) Surface du spectre représenté dans l'encadré sur la droite qui montre les spectres de différence de la connectivité (zone gris dans a)). d) Position du maximum de la bande d'élongation OH en fonction de la température.

Dans la figure R4 c,d, on observe les modifications de la bande de connectivité et un déplacement de la bande d'élongation O-H en fonction de la température qui indiquent des modifications dans le réseau de liaisons hydrogène. Aux températures plus élevées, aucune autre information ne peut être obtenue à partir de la bande de connectivité, qui est masquée par la bande de libration. Cependant, les paliers dans le déplacement des bandes d'élongation O-H montrent d'autres modifications dans le réseau d'eau à T ~ 220 K et T ~ 250 K (ces étapes intermédiaires ont également été observées par RMN et neutron).

Cette étude démontre l'importance des interactions d'une surface hydrophile sur l'eau interfaciale. Par conséquence, les transitions observées dans l'eau en surfusion piégé dans des petits pores ne peuvent pas être simplement considérées comme preuve directe du point critique à basse température, à T ~ 220 K, séparant deux phase liquides chacune ayant ses propres propriétés de densité et compressibilité, tel que suggéré dans la littérature.

L'étude du Nafion

Le deuxième système analysé est le Nafion®, un polymère perfluoré sulfoné composé d'un squelette fluoro-carboné (type Teflon®) sur lequel sont greffées des chaînes pendantes (perfluorovinyléther) terminées par un groupe ionique sulfonate (Figure R5). En conséquence, le squelette est de nature hydrophobe, tandis que les sites ioniques sont hydrophiles.

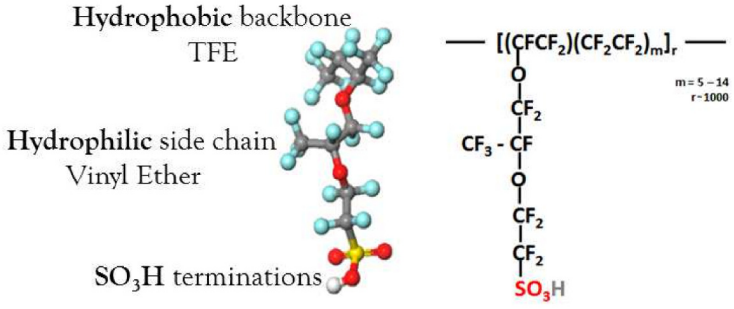

Figure R5 - Structure du Nafion®. Structure de la membrane Nafion acidifiée où les chaînes pendantes terminent pour les groupes SO_3H.

Ces membranes, inventées et brevetées par Dupont de Nemours en 1962, sont utilisées dans les piles à combustible à membrane échangeuse de protons (PEMFCs) comme source d'énergie propre et efficace, principalement pour le transport et les technologies portables. Leur stabilité et le transport sélectif d'ions en font d'excellents électrolytes permettant la conduction protonique de l'anode vers la cathode pour la production d'énergie électrique à partir d'un combustible chimique. Les performances des piles PEMFCs dépendent fortement de la morphologie et du niveau d'hydratation de l'électrolyte car ces dernières affectent la conduction protonique dans le Nafion. Au sein de la membrane, il existe deux modes de diffusion du proton H_3O^+ : une diffusion *véhiculaire*, pour laquelle le proton est transporté par la diffusion de l'eau, et une diffusion *structurale* (mécanisme de Grotthuss) qui correspond au déplacement de la charge sur les molécules d'eau par formation et rupture de la liaison hydrogène.

Une membrane Nafion N211, d'épaisseur 25 μm, a été utilisée pour analyser le processus d'hydratation des membranes acides perfluorosulfoniques en fonction du niveau d'hydratation (en équilibre avec le 0.7%, 1.8%, 3.5%, 6.8%, 12.1%, 17.8%, 24.5%, 32.4%, 47.7%, 66.9%, 76.5%, 89.7%, and 100% d'humidité relative). Le processus d'ionisation, la formation de l'ion hydronium (H_3O^+), la formation d'espèces protonique ($H_5O_2^+$ et $H_9O_4^+$), et les interactions moléculaires ont été mises en évidence par spectroscopie infrarouges dans le FIR [20-500 cm^{-1}] et le MIR [500-4000 cm^{-1}] et ont permis d'en déduire un processus d'hydratation en trois étapes.

Quand la membrane est déshydratée, les groupes sulfoniques sont liés entre eux par un réseau de liaison hydrogène caractérisé par trois modes de vibration intermoléculaires (à 250, 335 et 375 cm^{-1}) dans le FIR (Figure R6).

Le premier seuil d'hydratation est atteint quand l'intensité de plusieurs bandes augmente jusqu'à atteindre un maximum, tandis que simultanément l'intensité d'autres bandes diminue jusqu'à disparaître. Ce premier seuil d'hydratation est associé à la dissociation progressive des groupes SO_3H (associée aux bandes 912 et 1064 cm^{-1}, Figure R7) et à la formation de l'ion hydronium H_3O^+ (associée aux bandes 250 et 2700 cm^{-1}, Figure R7), qui se produit lorsqu'une molécule d'eau par groupe ionique est adsorbée (λ=1). Cette première étape d'ionisation est indépendante de la pression de vapeur en équilibre avec la membrane. On parle alors d'un processus dépendant de la cinétique.

Le deuxième seuil est atteint à λ=3 et correspond à l'intercalation de molécules d'eau entre H_3O^+ et les groupes SO_3^-. Ces groupes SO_3^- étant en contact avec l'eau n'interagissent plus avec les ions. Des complexes protoniques hydratés, Zundel ($H_5O_2^+$) et Eigen ($H_9O_4^+$), sont ensuite formés favorisant le transfert rapide de protons à l'intérieur de la membrane.

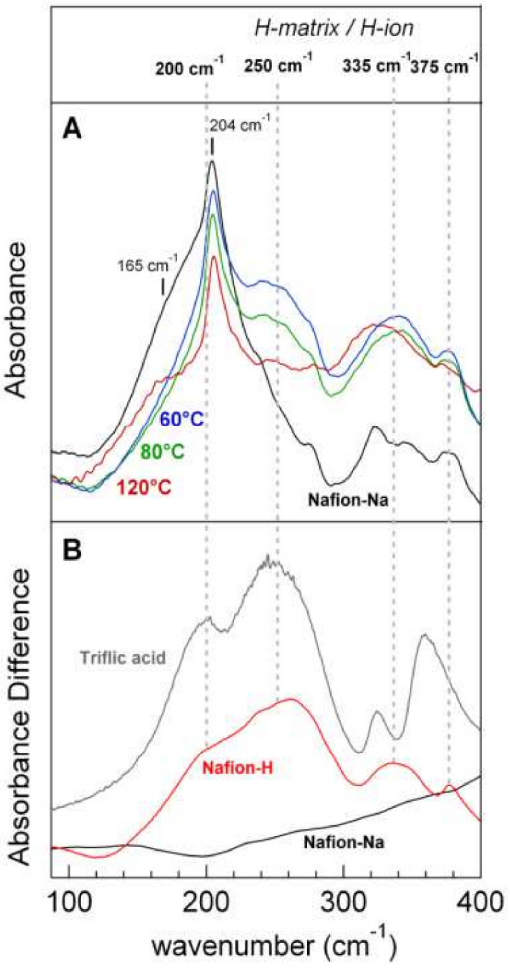

FIGURE R6 – Spectres FIR [100-400 cm^{-1}] des membranes déshydratées Nafion-H et Nafion-Na. (A) Nafion-H séché à 60, 80 et 120 °C, et Nafion-Na séché à 80 °C. (B) Spectre d'absorption d'une solution d'acide triflique très concentré (λ=H_2O/SO_3H~1); spectres de différence du Nafion-H et Nafion-Na obtenue en soustrayant les spectres des membranes sèches d'absorbance de celle à λ=1.

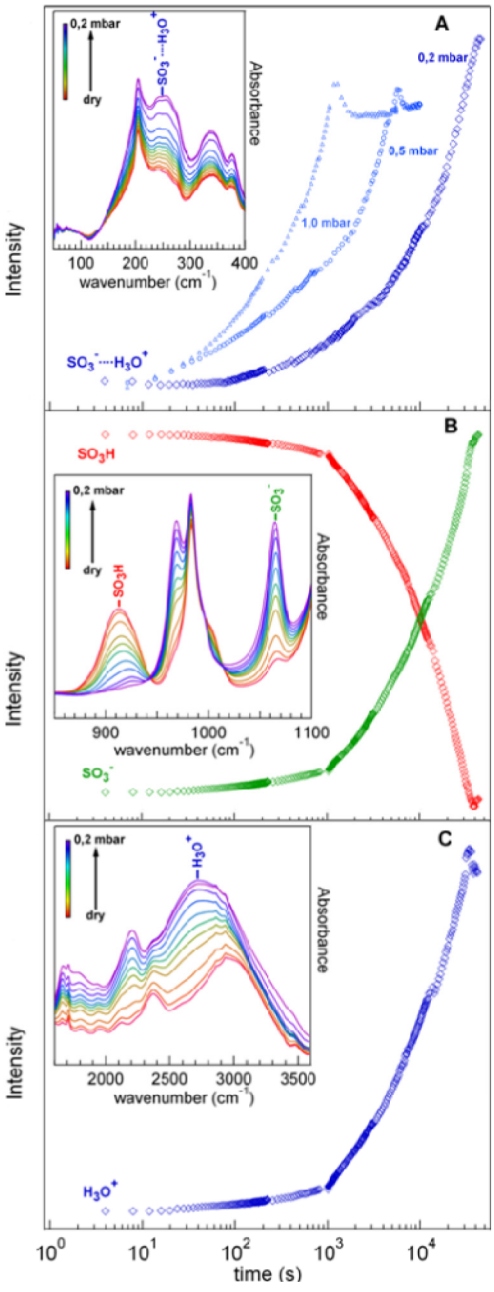

FIGURE R7 – Premier seuil d'hydratation. Evolution des spectres du Nafion et cinétique des bandes principales pendant l'hydratation, du sec à 0.2 mbar de pression de vapeur d'eau.

L'étude des nanotubes de carbone

Une première étude expérimentale sur l'hydratation des nanotubes de carbone à paroi unique (SWNT, ayant un diamètre de 14±5 Å) en pression de vapeur d'eau contrôlée a été réalisée. De façon contrintuitive, la nature hydrophobe de ce système n'empêche pas une adsorption significative d'eau (Figure R8) mais et, au contraire, des études ont montrées que l'on pouvait observer un déplacement rapide des molécules d'eau à l'intérieur des nanotubes (de 10 à 40 molécules d'eau nm^{-2} s^{-1}).

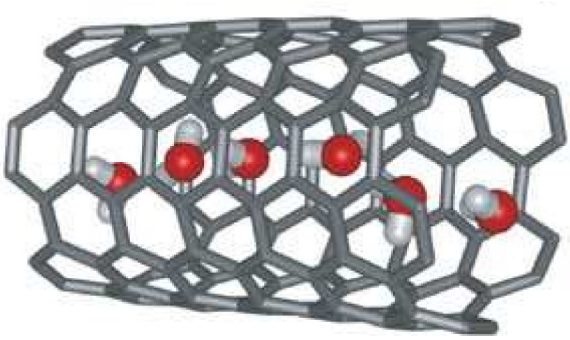

Figure R8 – Structure d'une chaîne d'eau dans un nanotube de carbone à paroi unique. Simulation numerique de l'hydratation d'un nanotube de carbone à paroi unique (8,8) par Hummer et al., tirée de [8].

Le processus d'hydratation des nanotubes de carbone a été révélé par un ensemble de données s'étendant du térahertz jusqu'au moyen infrarouge (25-4000 cm^{-1}), Figure R9. Dans cette gamme, les nanotubes de carbone présentent un coefficient d'absorption extrêmement élevé, cependant, l'utilisation de la source de rayonnement synchrotron a permis de détecter le faible signal infrarouge provenant des molécules confinée dans les tubes de carbone.

L'analyse quantitative de la bande d'élongation O-H de l'eau, nous a permis de déterminer l'organisation des molécules en réseau à l'intérieur des nanotubes de carbone en fonction de la pression de vapeur d'eau appliqué au système (Figure R10). Les données ont été interprétées en assumant que la force des oscillateurs O-H révèle le nombre de liaisons hydrogène établies par les molécules d'eau. De cette façon, chaque sous-composante de la bande d'élongation O-H est représentative des molécules d'eau impliquées dans un niveau de liaison hydrogène donné.

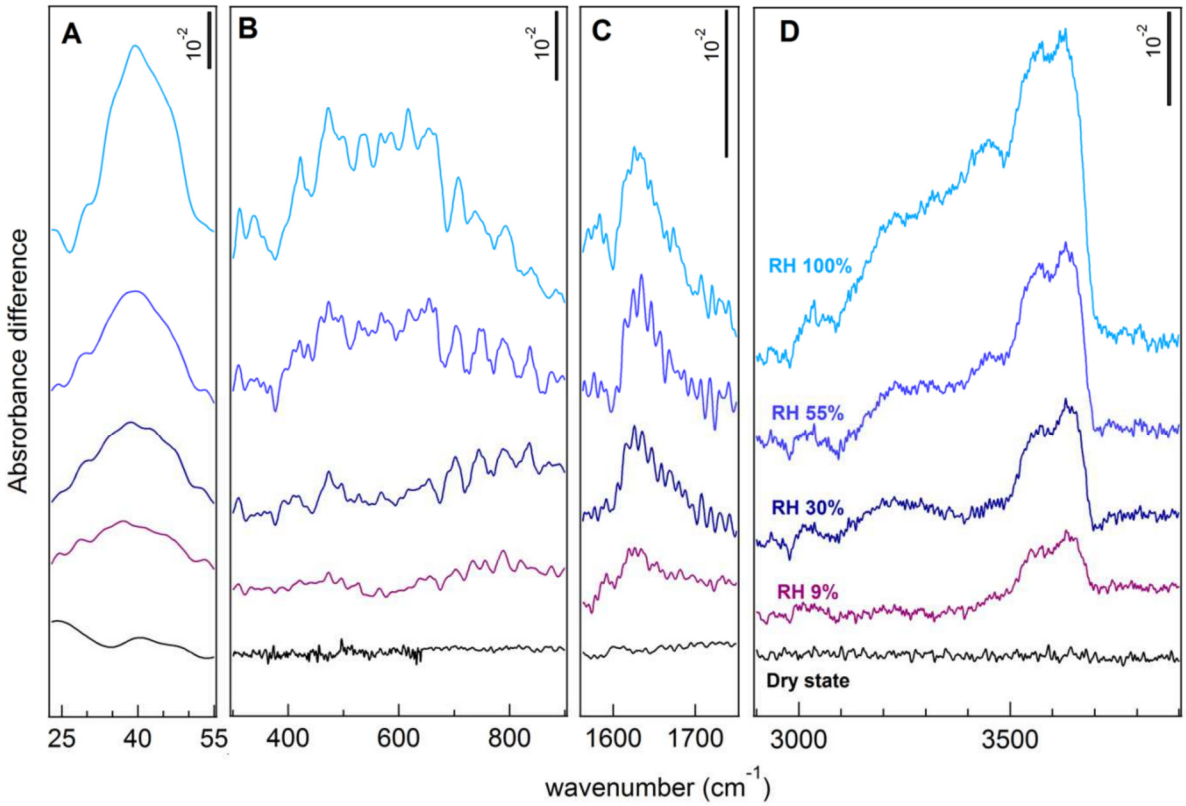

Figure R9 – Les spectres de l'eau dans les nanotubes de carbone à paroi unique pour différents niveaux d'hydratation. Spectres de différence de l'eau à l'intérieur de nanotubes de carbone à l'état sec et à 9%, 30%, 55% et 100% d'humidité relative. Les domaines spectrales montrent les modes de vibration de l'eau adsorbée pendant l'hydratation: (A) ~40 cm^{-1}, (B) autour de 560 cm^{-1}, (C) autour de 1625 cm^{-1}, (D) entre 3100 et 3700 cm^{-1}. Les spectres sont décalés pour clarté.

A faible hydratation, RH=9%, des molécules d'eau isolées ou peu connectées sont présentes dans les nanotubes. La signature infrarouge des liaisons pendantes O-H qui n'ont pas établi de liaisons avec une molécule voisine et font face aux parois hydrophobes a été identifiée dans les sous-composants à haute fréquence à 3560 et 3640 cm^{-1}.

A un niveau d'hydratation supérieur, RH=30%, des composantes à basse fréquence apparaissent à 3215 et 3340 cm^{-1} indiquant une organisation ordonnée des molécules d'eau dans les tubes de carbone. Ce résultat est la preuve expérimentale de ce qui a été prévu dans certaines études de simulations numériques: l'eau dans des pores petites tailles (~ 1.2 nm) s'organise de façon très ordonnée même à température ambiante.

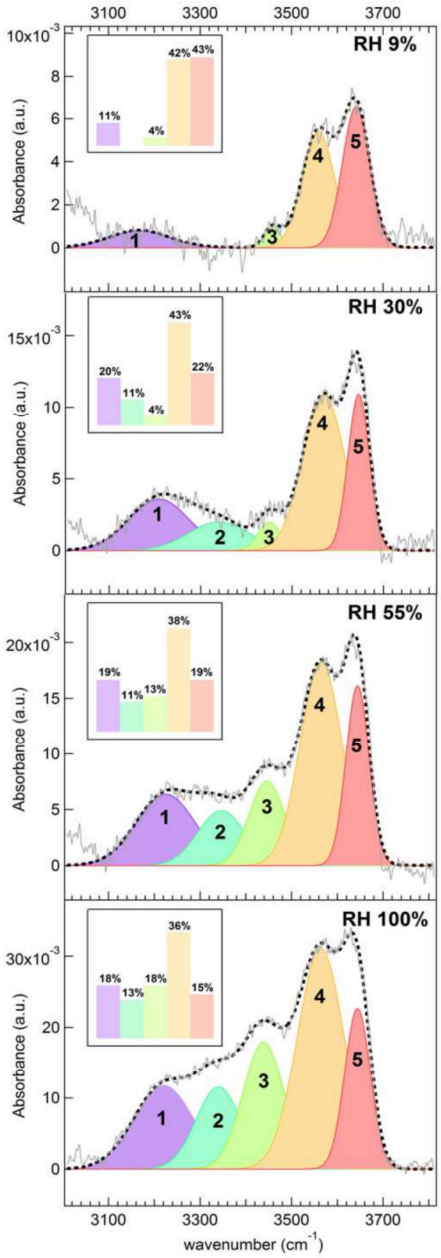

Figure R10 – Déconvolution de la bande d'élongation OH pour chaque niveau d'hydratation. La déconvolution par cinq gaussiennes de la bande d'élongation OH des spectres de différence à 9% (A), 30% (B), 55% (C) et 100% (D) d'humidité relative. Inset: proportion de chaque sous-composant.

Pendant les dernières étapes d'hydratation, RH=100%, les grands nanotubes sont remplis mais, dans ce cas-là, les molécules d'eau établissent un réseau plus désordonné.

Le réseau d'eau est fortement affecté par le confinement et, en particulier, des liaisons pendantes OH qui font face aux parois de carbone se développent dès les premiers stades et restent présents en grande quantité (~ 50%), même à pleine

hydratation. La présence des groupes OH pendants pour tous les remplissages joue vraisemblablement un rôle central dans le flux d'eau sans frottement. De plus, une structure solide peut faciliter un passage libre de turbulence. Ces deux propriétés, révélées par spectroscopie infrarouge, peuvent être à l'origine du déplacement rapide des molécules d'eau dans les nanotubes de carbone.

Discussion des résultats

En comparant les spectres infrarouges des trois échantillons, nous pouvons en tirer des conclusions concernant l'effet de la nature des interfaces (hydrophile comme le Vycor ou hydrophobe comme les nanotubes de carbone). On peut également évaluer l'effet de l'environnement stérique en scrutant les caractéristiques de l'eau pour différents volumes de confinement.

Nous avons établi que lorsque l'eau interfaciale interagit avec une surface hydrophile, elle forme des liaisons hydrogène fortes avec les parois du matériau poreux qui provoquent un affaiblissement des liaisons intramoléculaires O-H des molécules d'eau. En suivant l'évolution des spectres de l'eau à l'interface en fonction de la température, nous avons observé des changements dans le réseau de liaison hydrogène à des températures spécifiques (T=160, 220, 240 K). La bande d'élongation O-H de l'eau confinée se trouve à plus basse fréquence (~3230 cm^{-1}) que celle de l'eau en masse. Une telle fréquence est comparable à celle de la bande d'élongation OH de la glace hexagonale où chaque molécule forme quatre liaisons hydrogène.

Un comportement opposé est observé quand l'eau est confinée dans les nanotubes de carbone. Dans ce système, les molécules d'eau sont contraintes dans les tubes cylindriques mais n'interagissent pas directement avec les parois de carbone. Les groupes O-H pendants, qui font face aux parois, donnent lieu à des bandes d'élongations spécifiques, à 3560 et 3640 cm^{-1}, une fréquence très inhabituelle pour l'eau en masse ou lors qu'elle est piégée dans les systèmes hydrophiles. Des sous-composantes de la bande d'élongation OH à basses fréquences apparaissent à faible niveau d'hydratation. Ceci a été interprété comme la preuve expérimentale d'un arrangement ordonné singulier des molécules d'eau dans les petits nanotubes de carbone (~1 nm de diamètre) à température ambiante. Il est probable que les molécules d'eau s'organisent de façon à ce que les liaisons hydrogène forment soit

des chaines ou soit des anneaux empilées dans les tubes, comme prédit par simulation numérique.

Des trois systèmes analysés, l'eau adsorbée dans la membrane Nafion est celle qui ressemble le plus à l'eau en masse. En effet, la structure chimique du Nafion à l'échelle nanométrique présente une séparation de phase hydrophobe-hydrophile. Lorsque l'eau est adsorbée, les domaines hydrophobes se déforment et provoquent le gonflement des canaux. Par conséquence, les molécules d'eau peuvent se ranger dans un réseau à trois dimensions très peu affecté.

Concernant la bande de pliage HOH, elle semble affectée par le confinement stérique plutôt que par la nature de la surface. Nous avons observé un décalage vers les basses fréquences dans les spectres de l'eau confinée, aussi bien dans des systèmes hydrophiles qu'hydrophobes. En fait, que ce soit dans les pores hydrophiles du Vycor ou dans ceux hydrophobes des nanotubes de carbone, la bande de pliage de l'eau apparaît à 1625 cm^{-1}, au lieu de 1650 cm^{-1} comme pour l'eau en masse. Dans le cas du Nafion, L'eau adsorbée est moins affectée par le confinement (les pores sont plus larges) et la bande de pliage HOH est seulement décalée à 1634 cm^{-1}. Il a également été observé que l'intensité de la bande de pliage de l'eau devient plus grande suite au confinement. Il est probable que l'arrangement modifié adoptée par les molécules d'eau piégées dans les pores augmente le changement de moment dipolaire associé à ce mode.

Concernant les modes intermoléculaires, la plupart des informations est fournie par la bande de connectivité, car la bande de libration est souvent éclipsée par la forte absorbance de la matrice, comme dans le Vycor ou le Nafion. Dans le cas des nanotubes de carbone, la libration apparait à plus basse fréquence par rapport à l'eau en masse indiquant un faible réseau de liaison hydrogène.

La bande de connectivité de l'eau interfaciale dans les pores du Vycor révèle qu'à basse température, de la glace amorphe est formée et aucune forme cristalline n'est observée. Encore une fois, l'effet de la surface provoque une forte modification de la structure de l'eau.

L'eau confinée dans les nanotubes de carbone produit une bande de connectivité trop faible pour être détecté avec notre configuration. Cependant, un mode à basse fréquence, ~40 cm^{-1}, probablement associé au réseau des liaisons hydrogène, suggère que le nombre de liaisons hydrogène augmente à hauts niveaux

d'humidité relative, en correspondance avec le remplissage des plus grands tubes (diamètre compris entre 1.5 et ~2.0 nm).

L'interaction entre les molécules d'eau et les groupes acide sulfonique de la membrane Nafion à l'état sec a été suivie lorsque les premières molécules d'eau sont adsorbées. Les signatures des ions hydronium, H_3O^+, liés par liaison hydrogène aux groupes sulfoniques, SO_3^-, ont été identifiées à 250, 2210 et 2700 cm^{-1}. On peut également remarquer que la force de la liaison hydrogène entre ces deux espèces est comparable à la force de la liaison hydrogène établie entre deux groupes SO_3H avant la dissociation. Nos spectres infrarouges montrent aussi que le processus d'ionisation est un processus cinétique qui ne dépend pas de la pression de vapeur d'eau.

Conclusions et perspectives

En résumé, nous avons conçu une cellule à hydratation pour étudier l'adsorption de l'eau dans deux systèmes modèles chimiquement et dynamiquement inertes, soit le Vycor et les nanotubes de carbone à paroi unique, et le processus d'hydratation dans un système plus complexe, la membrane Nafion. Le couplage des données du moyen et lointain infrarouge nous a permis de mettre en évidence les processus complexes qui ont lieu dans les échantillons à l'étude. De toute évidence, cette étude n'a pas la prétention de donner une image exhaustive des innombrables interactions subies par les molécules d'eau lorsqu'elles sont confinées dans des systèmes biologiques, chimiques ou géophysiques. Néanmoins, elle apporte des nouvelles évidences expérimentales permettant d'améliorer la compréhension de l'eau confinée, qui seront également exploitables pour des applications technologiques. La présente étude ouvre la voie à de futures études de systèmes plus complexes, tels que les systèmes biologiques dans lesquels les réseaux d'eau jouent un rôle crucial.

REFERENCES

[1] J. Teixeira, The Physics of Liquid Water, *J Physique IV C1*, **3** (1993) 162-169.

[2] D. Eisenberg and W. Kauzmann, *The Structure and Properties of Water*, (Oxford, London, 1969).

[3] *Water Science Review*, ed Franks F (Cambridge Univ. Press.) **1-5** (195-90).

[4] *Correlations and Connectivity, Geometry Aspects of Physics, Chemistry and Biology,* eds. H. E. Stanley and N. Ostrowzky (Kluwer Acaedmic, Dordrecht, 1990).

[5] J.-B. Brubach, A. Mermet, A. Filabozzi, A. Gerschel and P. Roy, Signatures of the Hydrogen Bonding in the Infrared Bands of Water, *J. Chem. Phys.*, **122** (2005) 184509.

[6] A. Striolo, A. A. Chialvo, K. E. Gubbins and P. T. Cummings,Water in Carbon Nanotubes: Adsorption Isotherms and Thermodynamic Properties From Molecular Simulation, *J. Chem. Phys.*, **122** (2005) 234712.

[7] A. I. Kolesnikov, J. M. Zanotti, C. K. Loong, P. Thiyagarajan, A. P. Moravsky, R. O. Loufty and C. J. Burnham, Anomalously Soft Dynamics of Water in a Nanotube: A Revelation of nanoscale Confinement, *Phys. Rev. Lett.*, **93** (2004) 035503.

[8] G. Hummer, J. C. Rasaiah and J. P. Noworyta, Water Conduction Through the Hydrophobic Channel of a Carbon Nanotube, *Nature*, **414** (2001) 188.

[9] H. Tanaka and K. Koga, Formation of Ice Nanotube with Hydrophobic Guests Inside Carbon Nanotube, *J. Chem. Phys.*, **123** (2005) 094706.

[10] L. D. Gelb, K. E. Gubbins, R. Radhakrishnan and M. Sliwinska-Bartkowiak, Phase Separation in Confined Systems, *Rep. Progr. Phys.*, **62** (1999) 1573.

[11] C. Alba-Simionesco, B. Coasne, G. Dosseh, G. Dudziak, K. E. Gubbins, R. Radhakrishnan and M. Sliwinska-Bartkowiak, Effect of Confinement on Freezing and Melting, *J. Phys.: Condens. Matter*, **18** (2006) R15.

[12] D. Takaiwa, K. Koga and H. Tanaka, Structures of Filled Ice nanotubes Inside Carbon Nanotubes, *Mol. Simul.*, **33** (2007) 127-132(6).

[13] K. Koga, G. T. Gao, H. Tanaka and X. C. Zeng, Formation of Ordered Ice Nanotubes Inside Carbon Nanotubes, *Nature*, **412** (2002) 802-805.

[14] K. Koga and H. Tanaka, Phase Diagram of Water between Hydrophobic Surfaces, *J. Chem. Phys.*, **122** (2005) 104711.

[15] K. Koga and H. Tanaka, Close-packed Structures and Phase Diagram of Soft Spheres in Cylindrical Pores, *J. Chem. Phys.*, **124** (2006) 131103.

[16] J. Zheng, E. M. Lemmon, H. A. Tsao, H. J. Sheng and S. Jiag, transport of a Liquid Water and Methanol Mixture Through Carbon Nanotubes Under a Chemical Potential Gradient *J. Chem. Phys.*, **122** (2005) 214702.

[17] K. Matsuda, T. Hibi, H. Kadouaki, H. Kataura and Y.Maniwa, Water Dynamics Inside Single-Wall Carbon Nanotubes: NMR Observations, *Phys. Rev. B: Condens. Matter Mater. Phys.*, **74** (2006) 073415.

[18] G. Armstrong, Proton Transfer: Water Discovery, *Nature Chemistry*, doi:10.1038/nchem.865.

[19] Y. Zhang and Z. Xu, Atomic Radii of Noble Gas Elements in Condensed Phases, *American Mineralogist* **80** (1995) 670-675.

[20] B. Cabane and R. Vuillemier, The Physics of Liquid Water, *C. R. Geoscience*, **337** (2005).

[21] D. D. Kempand M. S. Gordon, An Interpretation of the Enhancement of the Water Dipole Moment Due to the Presence of Other Water Molecules, *J. Phys. Chem. A*, **112** (2008) 4885-4894.

[22] W. M. Latimer and W. H. Rodebush, Polarity and Ionization from the Standpoint of the Lewis Theory of Valence, *J. Am. Chem. Soc*., **42** (1920) 1419-1433.

[23] G. C. Pimentel and C. H. Sederholm, Correlation of Infrared Stretching Frequencies and Hydrogen Bond Distances in Crystals, *J. Chem. Phys.* **24** (1956) 639.

[24] S. J. Suresh and V. M. Naik, Hydrogen Bond Thermodynamic Properties of Water from Dielectric Constant Data, *J. Chem. Phys.* **113** (2000) 9727-9732.

[25] F. Bartha, O. Kapuy, C. Kozmutza and C. Van Alsenoy, Analysis of Weakly Bound Structures: Hydrogen Bond and the Electron Densitiy in a Water Dimer, *J. Mol. Str.: THEOCHEM*, **666-667** (2003) 117-122.

[26] A. G. Császár, G. Czakó, T. Furtenbacher, J. Tennyson, V. Szalay, S. V. Shirin, N. F. Zobov and O. L. Polyansky, On equilibrium structures of the water molecule, *J. Chem. Phys.*, **122** (2005) 214305.

[27] J. B. Hasted, *Water: A Comprehensive Treatise*, ed. Franks F (Plenum, New York), **1** (1972) 255-309.

[28] H. A. Stern and B. J. Berne, Quantum Effects in Liquid Water: Path-Integral Simulations of a Flexible and Polarizable Ab Initio Model, *J. Chem. Phys.*, **115** (2001) 7622-7628.

[29] G. S. Fanourgakis and S. S. Xantheas, The Bend Angle of Water in Ice Ih and Liquid Water: The Significance of Implementing the Nonlinear Dipole Moment Surface in Classical Interaction Potentials, *J. Chem. Phys*., **124** (2006) 174504.

[30] A. K. Soper, The radial distribution functions of water and ice from 220 to 673 K and at pressures up to 400 MPa, *Chem. Phys*., **258** (2000) 121-137.

[31] V. F. Petrenko and R. W. Whitworth, *Review of Physics of Ice*, Oxford Univ. Press (Oxford, 1999).

[32] M. Shiga and W. Shinoda, Calculation of Heat Capacities of Light and Heavy Water by Path-Integral Moleculare Dynamics, *J. Chem. Phys*., **123** (2005) 134502.

[33] K. Ichikawa, Y. Kameda, T. Yamaguchi, H. Wakita and M. Misawa, Neutron-Diffraction Investigation of the Intramolecular Structure of a Water Molecule in the Liquid-Phase at High-Temperature, *Mol. Phys*., **73** (1991) 79-86.

[34] M. A. Floriano, D. D. Klug, E. Whalley, E. C. Svensson, V. F. Sears and E. D. Hallman, Direct Determination of the Intermolecular O-D Distance in Ice Ih and Ic by Neutron Diffraction, *Nature*, **329** (1987) 821.

[35] W. F. Kuhs and M. S. Lehmann, The structure of the ice Ih by neutron diffraction, *J. Phys. Chem*., **87** (1983) 4312.

[36] C. A. Angell, Water: A Comprehensive Treatise, ed. Franks F (Plenum, New York), **7** (1982) 1-81.

[37] P. G. Debenedetti and H. E. Stanley, Supercooled and Glassy Water, *Phys. Today*, **56** (2003) 40-46.

[38] O. Mishima and H.E. Stanley,The Relationship Between Liquid, Supercooled and Glassy Water, *Nature,* **396** (1998) 329-334.

[39] L. Pauling, General Chemistry (Freeman, San Francisco, 1970), 3rd ed. republished by Dover, New York, 1988.

[40] N. Agmon, The Grotthuss Mechanism, *Chem. Phys. Lett.,* **244** (1995) 456-462.

[41] O. F. Mohammed, D. Pines, J. Dreyer, E. Pines and E. T. J. Nibbering, Sequential Proton Transfer Through Water Bridge in Acid-Base Reaction, *Science,* **310** (2005) 83-86.

[42] K. J. Tielooij, R. L. A. Timmer, H. J. Bakker and M. Bonn, Structure Dynamics of the Proton in Liquid Probed with Terahertz Time-Domain Spectroscopy, *Phys. Rev. Lett.* **102** (2009) 198303.

[43] C. Liang and T. L. C. Jansen, Proton Transport in a Binary Biomimetic Solution Revealed by Molecular Dynamics Simulation, *J. Chem. Phys.,* **135** (2011) 114502.

[44] B. L. D. Groot, T. Frigato, V. Helms and H. Grobmuller, The Mechanism of Proton Exclusion in the Aquaporin-1 Water Channel, *J. Mol. Bio*., **333** (2003) 279-293.

[45] E. Tajkhorshid, P. Nollert, M. O. Jensen, L. J. W. Miercke, J. O`Connel, R. M. Stroud and K. Schulten, Control of the Selectivity of the Aquaporin Water

Channel Family by Global Orientation Tuning, *Science*, **296** (2002) 525-530.

[46] H. E. Stanley and J. Teixeira, Interpretation of the Unusual Behavior of H2O and D2O at Low Temperatures: Tests of a Percolation Model, *J. Chem. Phys.*, **73** (1980) 3404.

[47] J. Zielkiewicz, Structural Properties of Water: Comparison of the SPC, SPCE, TIP4P, and TIP5P Models of Water, *J. Chem. Phys*, **123** (2005) 104501.

[48] A. Nilsson and L. G. M. Pettersson, Perspective on the Structure of the Liquid Water, *Chem. Phys.*, **389** (2011) 1-34.

[49] H. F. M. C. Martiniano and N. Galamba, Insights on Hydrogen-Bond Lifetimes in Liquid and Supercooled Water, *J. Chem. Phys. B*, **117** (2013) 16188-16195.

[50] I. Brovchenko, A. Oleinikova, Interfacial and Confined Water (Elsevier, Amsterdam, The Netherlands), 2008.

[51] D. Chandler, Interfaces and the Driving Force of Hydrophobic Assembly, *Nature*, **437** (2005) 640-647.

[52] M. D. Fayer, N. E. Levinger, Analysis of Water in Confined Geometries and at Interfaces, *Annu. Rev. Anal. Chem.*, **3** (2010) 89-107.

[53] C. Boissière, J. B. Brubach, A. Mermet, G. de Marzi, C. Bourgaux, E. Prouzet and P. Roy, Water Confined in Lamemmar Structures of AOT Surfactants : An Infrared Investifation, *J. Phys. Chem. B*, **106** (2002) 1032-1035.

[54] L. Liang, J. Zhang, Y. Zhou, J. Xie, X. Zhang, M. Guan, B. Pan and Y. Xie, High-Performance Flexible Electrochromic Device Based on Facile Semiconductor-to-Metal Transition Realized by $WO_3 \cdot 2H_2O$ Ultrathin Nanosheets, *Sci. Rep.*, **3** (2013) 1936.

[55] M. D. Fayer, Water in a Crowd, *Physiology*, **26** (2011) 381-392.

[56] B. Dreyfus, G. Gebel, P. Aldebert, M. Pineri, M. Escoubes and M. Thomas, Distribution of the Water Micelles in Hydrated Perfluorinated Ionomer Membrane from SANS Experiment, *J. de Physique*, **51** (1990) 1341-1354.

[57] G. Gebel, Structural Evolution of Water Swollen Perfluorosulfonated Ionomers from Dry Membrane to Solution, *Polymer*, **41** (2000), 5829.

[58] J. Liu, R. S. Andino, C. M. Miller, X. Chen, D. M. Wilkins, M. Ceriotti and D. Manolopoulos, A Surface-Specific Isotope Effect in Mixture of Light and Heavy Water, *J. Phys. Chem. C*, **117** (2013) 2944-2951.

[59] Y. Nagata, R. E. Pool, E. H. G. Backus and M. Bonn, Nuclear Quantum Effects Affect Bond Orientation of Water at the Water-Vapor Interface, *Phys. Rev. Lett.*, **109** (2012) 226101-5.

[60] J. J. Thomas and H. M. Jennings, Effects of D2O and Mixing Energy on the Early Hydration Kinetics of Tricalcium Silicate, *Chem. Mater*., **11** (1999) 1907-1914.

[61] B. Yaron, G. Dagan and J. Goldshmid, *Pollutants in Porous Media*, Springer-Verlag (Berlin Heidelberg 1984).

[62] R. L. Raymond, J. O. Hudson and V. W. Jamison, Oil Degradation in Soil, *Appl. Environ. Microbiol.*, **31** (1976) 522-535.

[63] H. J. Butt, K. Graf, M. Kappl, Physics and Chemistry of Interfaces, Wiley-VCH Verlag & Co. KGaA, (2003).

[64] K. S. W. Sing, D. H. Everett, R. A .W Haul, L. Moscou, R.A. Pierotti, J. Rouquérol, T. Siemieniewska, Reporting Physsisorption Data for Gas/Solid Systems, *Pure Appl. Chem*., **57**, (1985) 603-619.

[65] G. H. Findenegg, S. Jahnert, D. Akcakayiran and A. Schreiber, Freezing and Melting of Water Confined in Silica Nanopores, *Chem. Phys. Chem*., **9** (2008) 2651-2659.

[66] K. Overloop and L. Van Gerven, Freezing Phenomena in Adsorbed Water as Studied by NMR, *J. Magn. Reson. A*, **101** (1993) 179-187.

[67] K. Morishige and K. Kawano, Freezing and Melting of Water in a Single Cylindrical Pore: The Pore-Size Dependence of Freezing and Melting Behavior, *J. Chem. Phys*., **110** (1999) 4867-4872.

[68] K. Morishige and K. Nobuoka, X-Ray Diffraction Studies of Freezing and Melting of Water Confined in a Mesoporous Adsorbent (MCM-41), *J. Chem. Phys*., **107** (1997), 6965-6969.

[69] S. Jahnert, F. Vaca Chavez, G. E. Schaumann, A. Schreiber, M. Schonhoff and G. H. Findenegg, Melting and Freezing of Water in Cylindrical Silica Nanopores, *Phys. Chem. Chem. Phys*., **10** (2008) 6039-6051.

[70] D. T. Limmer and D. Chandler, Phase Diagram of Supercooled Water Confined to Hydrophilic Nanopores, *J. Chem. Phys*., **137** (2012) 044509.

[71] J. Jelassi, H. L. Castricum, M.-C. Bellissent-Funel, J. Dore, J. B. W. Webber and R. Sridi-Dorbez, Studies of Water and Ice in Hydrophilic and Hydrophobic Mesoporous Silicas: Pore Characterisation and Phase Transformations, *Phys. Chem. Chem. Phys*., **12** (2010) 2838-2849.

[72] J. M. Baker, J. C. Dore and P. Behrens, Nucleation of Ice in Confined Geometry, *J. Phys. Chem. B*, **101** (1997) 6226-6229.

[73] K. Morishige, H. Yasunaga and H. Uematsu, Stability of Cubic Ice in Mesopores, *J. Phys. Chem. C*, **113** (2009) 3056-3061.

[74] P. H. Poole, F. Sciortino, U. Essman and H. E. Stanley, Phase Behaviour of Metastable Water, *Nature*, **360** (1992) 324-328.

[75] R. J. Speedy and C. A. Angell, Isothermal Compressibility of Supercooled Water and Evidence for a Thermodynamic Singularity at -45 degrees C, *J. Chem. Phys.*, **65** (1976) 851-858.

[76] R. Mancinelli, The Effect of Confinement on Water Structure, *J. Phys.: Condens. Matter*, **22** (2010) 404213.

[77] M. Sliwinska-Bartkowiak, M. Jazdzewska, L. L. Huang and K. E. Gubbins, Melting Behavior of Water in Cylindrical Pores: Carbon Nanotubes and Silica Glasses, *Phys. Chem. Chem. Phys.*, **10** (2008) 4909-4919.

[78] T. Iiyama, K. Nishikawa, T. Suzuki and K. Kaneko, Study of the Structure of a Water Molecular Assembly in a Hydrophobic Nanospace at Low Temperature With In Situ X-Ray Diffraction, *Chem. Phys. Lett.*, **274** (1997) 152-158.

[79] Y. Maniwa, H. Kataura, M. Abe, A. Udaka, S. Suzuki, Y. Achiba, H. Kira, K. Matsuda, H. Kadowaki and Y. Okaba, Ordered Water Inside Carbon Nanotubes: Formation of Pentagonal to Octagonal Ice-Nanotubes, *Chem. Phys. Lett.*, **401** (2005) 534-538.

[80] E. Tombari, G. Salvetti, C. Ferrari and G. P. Johari, Thermodynamic Functions of Water and Ice Confined to 2 nm Radius Pores, *J. Chem. Phys.*, **122** (2005) 104712.

[81] S. Senapati and A. Chandra, Dielectric Constant of Water Confined in a Nanocavity, *J. Phys. Chem. B*, **105** (2001) 5106-5109.

[82] G. Cicero, J. C. Grossman, E. Schwegler, F. Gygi and G. Galli, Water Confined in Nanotubes and between Graphene Sheets: A First Principle Study, *J. Am. Chem. Soc.*, **130** (2008) 1871-1878.

[83] G. Cicero, J. C. Grossman, A. Catellani and A. Galli, Water at a Hydrophilic Solid Surface Probed by Ab Initio Molecular Dynamics: Inhomogeneous Thin Layers of Dense Fluid, *J. Am. Chem. Soc.*, **127** (2005) 6830.

[84] Z. Cao, Y. Peng, T. Yan, S. Li, A. Li and G. A. Voth, Mechanism of Fast Transport along One-Dimensional Water Chains Confined in Carbon Nanotubes, *J. Am. Chem. Soc.*, **132** (2010) 11395-11397.

[85] H. P. Hood and M. E. Nordberg, *Treated Borosilicate Glass*, U. S. patent 2,106,744, Feb 1938.

[86] R. J. M. Pellenq, B. Rousseau, and P. E. Levitz. A grand canonical monte carlo study of argon adsorption/condensation in mesoporous silica glasses, *Phys. Chem. Chem. Phys.*, **3(7)** (2001) 1207–1212.

[87] M.-C. Bellissent-Funel, *Hydration Processes in Biology: Theoretical and Experimental Approaches*, ed. IOS Press (Les Houces, 1999).

[88] J. Larminie and A. Dick, *Fuel Cell Systems Explained*, 2nd ed. Wiley (New York, 2003).

[89] D. E. Curtin, R. D. Lousenberg, T. J. Henry, P. C. Tangeman and M. E. Tisack, Advanced Materials for Improved PEMFC Performance and Life, *J. Power Sources,* **113** (2004) 41-48.

[90] L. Rubatat, A.-L. Rollet, G. Gebel and O. Diat, Evidence of Elongated Polymeric Aggregates in Nafion, *Macromolecules*, **35** (2002) 4050-4055.

[91] F. J. Waller and R. W. Van Scoyoc, Catalysis with Nafion, *Chemtech*, **17** (1987) 438-441

[92] D. E. Moilanen, D. B. Spry and M. D. Fayer, Water Dynamics and Proton Transfer in Nafion Fuel Cell Memnbranes, *Langmuir*, **24** (2008) 3690-3698.

[93] S. Iijima, Helical microtubulus of graphitic carbon, *Nature,* **354** (1991) 56-58.

[94] N. Grobert, Carbon Nanotube – Becoming Clean, *Materials Today*, **10** (2007) 28-35.

[95] A. Oberlin, M. Endo and T. Koyama, Filamentous Growth of Carbon through Benzene Decomposition, *J. Cryst. Growth*, **32** (1976) 335.

[96] S. Iijima and T. Ichihashi, Single-shell carbon nanotubes of 1-nm diameter, *Nature* **363** (1993) 603–605.

[97] D. S. Bethune, C. H. Kiang, M. S. De Vries, G. Gorman, R. Savoy, J. Vazquez and R. Beyers,. Cobalt-Catalysed Growth of Carbon Nanotubes with Single-Atomic-Layer Walls, *Nature* **363** (1993) 605–607.

[98] M. Kumar and Y. Ando, Chemical Vapor Deposition of Carbon Nanotubes: A review on Growth Mechanism and Mass Production, *J. Nanosci. Nanotechnol.,* **10** (2010) 3739-3758.

[99] N. Hamada, S. Sawada and A. Oshiyama, New One-Dimensional Conductors: Graphitic Microtubules, *Phys. Rev. Lett.*, **68** (1992) 1579.

[100] M.-F. Yu, B. S. Files, S. Arepalli and R. S. Ruoff, Tensile Loading of Ropes of Single Walled Carbon Nanotubes and their Mechanical Properties, *Phys. Rev. Lett.*, **84** (2000) 5552-5555.

[101] J. K. Holt, H. G. Park, Y. Wang, M. Stadermann, A. B. Artyukhin,, C. P. Grigoropoulos, A. Noy and O. Bakajin, Fast Mass Transport through Sub-2-Nanometer Carbon Nanotubes, *Science*, **312** (2006) 1034-1037.

[102] F. R. Elder, A. Gurewitsch, R. V. Langmuir and H. C. Pollock, *Phys. Rev.*, **71** (1948) 52.

[103] J. Larmor, A Dynamical Theory of the Electric and Luminiferous Medium. Part III. Relations with Material Media, *Philosophical Transactions of the Royal Society A: Mathematical, Physical and Engineering Sciences,* **190** (1987) 205.

[104] A. Lienard, Champ Electrique et Magnetique Produit par une Charge Electrique Concentrée en un Point et Animée d'un Mouvement Quelconque, *L'Eclairage Elect.*, 16, 5, (1898)

[105] P. Roy, M. Rouzières, Z. Qi and O. Chubar, The AILES Infrared Beamline on the Third Generation Synchrotron Radiation Facility SOLEIL, *Infrared Physics & Technology*, **49** (2006) 139-146.

[106] G. L. Carr, M. Hanfland, G. P. Williams, Mid-infrared beamline at the National Synchrotron Light Source port U2B, *Rev. Sci. Instrum.*, **66(2)** (1995) 1643-1645.

[107] S. N. Mikhailenko, VI. G. Tyuterev, K. A. Keppler, B. P. Winnewisser, M. Winnewuisser, G. Mellau, S. Klee and K. Narahari Rao, The $2\nu_2$ Band of Water: Analysis of new FTS Measurements and High-K_a Transitions and Energy Levels, *J. Mol. Spectr.*, **184** (1997) 330-349.

[108] L. Pauling, The Structure and Entropy of Ice and of Other Crystals with Some Randomness of Atomic Arrangement, *J. Am. Chem. Soc.*, **58** (1935) 2680-2684.

[109] I. Bergonzi, L. Mercury, J.-B. Brubach and P. Roy, Gibbs Free Energy of Liquid Water Derived From Infrared Measurements. *Phys. Chem. Chem. Phys.* **16** (2014) 24830-24840.

[110] S. Y. Venyaminov and F. G. Prendergast, Water (H2O and D2O) Molar Absorbtivity in the 1000 − 4000cm−1 Range and Quantitative Infrared Spectroscopy of Aqueous Solutions, *Anal. Biochem.*, **248** (1997) 234–245.

[111] P. A. Kollman and L. C. Allen, Theory of the hydrogen bond: electronic structure and properties of the water dimer, J. Chem. Phys., 51 (1969) 3286-3293.

[112] G. Profeta and S. Scandolo, Far-Infrared Spectrum of Ice Ih: A First Principle Study, *Phys. Rev. B*, **84** (2011) 024103.

[113] G. S. Bordonskiy and A. O. Orlov, Investigation of Ferroelectric Phase Transitions of Water in Nanoporous Silicates in Simultaneous Electrical Noise and Calorimetric Measurements, *Phys. Solid State*, **56** (2014) 1626-1633.

[114] K. Kobayashi and H. Yasuda, Phase Transition of Ice Ic to Ice XI Under Electron Beam Irradiation, *Chem. Phys. Lett.*, **547** (2012) 9-12.

[115] J. E. Bertie and E. Whalley, Optical Spectra of Orientationally Disordered Crystals. II. Infrared Spectrum of Ice Ih and Ic from 360 to 50cm-1, *J. Chem. Phys.*, **46** (1966) 1271-1284.

[116] H. Fukazawa, A. Hoshikawa, Y. Ishii, B.C. Chakoumakos and J. A. Fernandez-Baca, Existence of Ferroelctric Ice in the Universe, *Astrophys. J.*, **652** (2006) L57-L50.

[117] Y. Tajima, T. Matsuo and H. Suga, Phase Transition in KOH-doped hexagonal ice, *Nature* **299** (1982) 810-812.

[118] T. L. Malkin, B. J. Murray, A. V. Brukhno, J. Anwar and C. G. Salzmann, Structure of Ice Crystallized from Supercooled Water, *Proc Natl Acad Sci USA*, **109** (2011) 1041-1045.

[119] I. Kohl, E. Mayer and A. Hallbrucker, The Glassy Water-Cubic Ice System: A Comparative Study by X-ray Diffraction and Differential Scanning Calorimetry, *Phys. Chem. Chem. Phys*., **2** (2000) 1579-1586.

[120] P. Geiger, C. Dellago, M. Macher, C. Franchini, G. Kresse, J. Bernard, J. N. Stern and T. Loerting, Proton Ordering of Cubic Ice Ic: Spectroscopy and Computer Simulations, *J. Phys. Chem. C*, **118** (2014) 10989-10997.

[121] M. Arakawa, H. Kagi and H. Fukazawa, Laboratory Measurements of Infrared Absorption Spectra of Hydrogen-Ordered Ice: A Step to the Exploration of Ice XI in Space, *ApJS*, **184** (2009) 361-365.

[122] G. Hummer, J. C. Rasaiah and J. P. Noworyta, Water conduction through the hydrophobic channel of a carbon nanotube, *Nature*, **414** (2001)188-190.

[123] M. Sadeghi and G. A. Parsafar, Density-induced molecular arrangements of water inside carbon nanotubes. *Phys. Chem. Chem. Phys.,* **15** (2013) 7379.

[124] R. J. Mashl, S. Joseph, N. R. Aluru and E. Jakobsson, Anomalously immobilized water: a new phase induced by confinement in nanotubes, Nano Lett. **3**, 589-592 (2003).

[125] G. Pérez-Hernandez and B. Schmidt, Anysotropy of the water-carbon interaction: molecular simulations of water in low-diameter carbon nanotubes, *Phys. Chem. Chem. Phys.*, **15** (2013) 4995-5006.

[126] M. Danilczuk, A. J. Perkowski and S. Schlick, Ranking the Stability of Perfluorinated Membranes Used in Fuel Cells to Attack by Hydroxyl Radicals and the Effect of Ce(III): A Competitive Kinetics Approach Based on Spin Trapping ESR, *Macromolecules*, **43** (2010) 3352-3358.

[127] K. D. Kreuer, M. Schuster, B. Obliers, O. Diat, U. Traub, A. Fuchs, U. Klock, S. J. Paddison and J. Maier, Short-side-chain proton conducting perfluorosulfonic acid ionomers: Why they perform better in PEM fuel cells, *J. Power Sources*, **178** (2008) 499-509.

[128] S. A. Hodge, M. K. Bayakit, K. S. Coleman and M. S. P. Shaffer, Unweaving the Rainbow: a Review of the Relationship between Single-Walled Carbon Nanotube Molecular Structures and their Chemical Reactivity, *Chem. Soc. Rev*., **41** (2012) 4409-4429.